KELLI-ANNE JOHNSON – MASTER'S THESIS – MCMASTER UNIVERSITY

CROSSLINKING AND CHARACTERIZATION OF PRESSURIZED GAS EXPANDED LIQUID POLYMER MORPHOLOGIES TO CREATE MACROPOROUS HYDROGEL SCAFFOLDS FOR DRUG DELIVERY AND WOUND HEALING

By Kelli-anne Johnson

A Thesis Submitted to the School of Graduate Studies
In Partial Fulfillment of the Requirements for the
Degree Master of Applied Science

MASTER OF APPLIED SCIENCE (2018)

Department of Chemical Engineering

McMaster University

Hamilton, Ontario

TITLE: Crosslinking and Characterization of Pressurized Gas Expanded Liquid Polymer Morphologies to create Macroporous Hydrogel Scaffolds for Drug Delivery and Wound Healing

AUTHOR: Kelli-anne Johnson
B.Sc.(Eng.) in Engineering Chemistry (Queen's University)

SUPERVISOR: Dr. Todd Hoare (Department of Chemical Engineering, McMaster University)

COMMITTEE: Dr. David Latulippe (Department of Chemical Engineering, McMaster University)
Dr. Ryan Wylie (Department of Chemistry, McMaster University)

NUMBER OF PAGES: 197

ABSTRACT

The development of structured macroporous hydrogels are of great interest in many industries due to their high permeabilities, large surface areas and large pore volumes. In drug delivery and wound healing applications, these macropores may theoretically be utilized as large drug reservoirs to deliver anti-inflammatory drugs to a wound site, while simultaneously absorbing exudate and maintaining a hydrated environment in which the wound may heal. However, current methods of generating macroporous structured hydrogels are low-throughput, expensive, and require the use of organic solvents, salts, and other additives that are difficult to remove from the crosslinked hydrogel scaffold. In contrast, the Pressurized Gas eXpanded liquid (PGX) processing technology, patented by the University of Alberta and licensed for all industrial applications by Ceapro Inc., has been shown to generate purified and exfoliated biopolymer scaffolds in a less expensive and more efficient way.

Herein, the tunability of the PGX processing method was investigated in depth, varying solvent/anti-solvent ratios, nozzle mixing volume, polymer molecular weight, and polymer concentration to examine the resulting effects on produced polymer morphologies. PGX-processed chitosan and alginate scaffolds were stabilized as bulk hydrogels through post-processing crosslinking methods using anti-solvents, solid-state chemistries, and/or rapid gelation kinetics. The mechanical strength, swelling/degradation kinetics, affinity for protein uptake, and cytotoxicity of these stabilized scaffolds were subsequently examined and compared to hydrogels produced without the use of PGX processing. Furthermore, in situ crosslinking methods were explored, in which alginate and poly(oligoethylene glycol methacrylate) polymers were shown to form stable aerogels during the standard PGX processing method. Finally, the PGX apparatus was reconfigured to enable the impregnation of a model hydrophobic drug into

pre-processed polymer scaffolds via circulation of supercritical CO_2. The total loading was calculated and the release kinetics from loaded-scaffolds examined.

In conclusion, this work outlines a novel method of creating structured macroporous hydrogels from PGX processed biopolymers with the potential to provide improved drug loadings and sustained release profiles. It is expected that this work will provide a basis for a great deal of research into the further stabilization of scaffolds for use in other applications, the investigation of a larger range of bioactive molecules for impregnation and release, and the exploration of PGX hydrogel scaffolds for in vivo wound healing.

ACKNOWLEDGEMENTS

This work would not have been possible without the guidance and support of a great many people. First and foremost, I need to thank my supervisor Dr. Todd Hoare. I can sincerely say that Dr. Hoare is one of the most brilliant, compassionate, and dedicated individuals that I have ever had the opportunity to work with. Despite some initial struggles adapting to this project, he consistently made me feel supported, and encouraged me to make my own research decisions. I would also like to thank Dr. David Latulippe, Dr. Bernhard Seifried, Dr. Paul Moquin, Dr. Byron Yepez, and Nick Kudeba who collaborated on this project and provided helpful advice and feedback throughout my degree.

That being said, my experience in graduate school would not have been as memorable, entertaining, or exciting without the advice and friendship of my colleagues. Throughout this degree I was blessed with the opportunity to work with a truly stellar group of individuals who never failed to challenge me, make me laugh, and provide valuable insight when things weren't going to plan. In particular, I would like to thank Nicola Muzzin, Eva Mueller, Madeline Simpson, Angus Lam, and Jonathan Dorogin, whose friendship I will treasure for years to come.

Finally, I would like to acknowledge my family for their encouragement and reassurance. Whenever I felt discouraged they were the first ones lifting my spirits and restoring my excitement in my research. Of course, this includes my fiancé, Mac Wootton, who has been with me (either in person or over the phone) through every single day of this degree. He has supported me unconditionally through countless trips to Edmonton, late night visits to the lab, varsity athletics, *way* too many extracurricular activities, and all the stress that came along with them. Mac, I love you more than words can describe and your support has been invaluable throughout this experience!

TABLE OF CONTENTS

LIST OF FIGURES

LIST OF TABLES

LIST OF ABBREVIATIONS

3T3 – mouse fibroblast cells (3T3 = "3-day transfer, inoculum 3×10^5 cells")

AA – acetic acid

ABPR – automatic back-pressure regulator

AIBMe - Dimethyl 2,2'-azobis(2-methylpropionate)

BAU – bioactive units

BET – Brunauer–Emmett–Teller theory

BSA – bovine serum albumin

CO_2 – carbon dioxide

DIW – deionized water, Mill-Q water

DMEM – Dulbecco's modified eagle media

EDTA – ethylenediaminetetraacetic acid

ELAS – expanded liquid antisolvent

ESI – electrospray ionization

EtOH – 99% anhydrous ethanol

FBS – fetal bovine serum

FITC – fluorescein isothiocyanate

FTMS – Fourier transform mass spectrometry

GDL – glucono-delta-lactone

HCl – hydrochloric acid

HEPES – (4-(2-hydroxyethyl)-1-piperazineethanesulfonic acid)

HiM – helium ion microscopy

HIPE – high internal phase emulsion

HPLC – high performance liquid chromatography

M – mole per litre

mmu – millimass units (mass spectrometry)

MS – mass spectrometer

NaOH – sodium hydroxide

OEGMA – oligoethylene glycol methacrylate

PBS – phosphate buffered saline

PEG – poly(ethylene glycol)

PEGDA – poly(ethylene glycol dimethacrylate)

PGSS – particles from gas-saturated solution

PGX – Pressurized Gas eXpanded liquid technology

PNIPAAm – poly(N-isopropylacrylamide)

POEGMA – poly(oligoethylene glycol methacrylate)

RESS – rapid expansion of supercritical solution

SAA – supercritical assisted atomization

SAS – supercritical antisolvent

$scCO_2$ – supercritical carbon dioxide

SEM – scanning electron microscopy

TIC – total ion chromatogram

UV – ultraviolet

DECLARATION OF ACADEMIC ACHIEVEMENT

The work presented in this thesis was completed by the author, with the guidance and consultation of Dr. Todd Hoare and Dr. David Latulippe, except for the following contributions:

Nicola Muzzin and Vishrut Panchal assisted in the growth of cells for in vitro cytotoxicity assays, listed in Figure 57, Figure 58, and Figure 70. Alan Mo assisted in the collection of swelling and degradation data from which Figure 64, Figure 65, Figure 82, and Figure 85 are generated, as well as collecting the light microscopy images presented in Figure 11, Figure 16, Figure 20, and Figure 24. Ibuprofen impregnations into chitosan and alginate were conducted by employees of Ceapro Inc, due to conflicting travel arrangements, and HiM images were collected by Ricardo Tomas Do Couto with the assistance of Dr. Feral Temelli at the University of Alberta.

Chapter 1 – Introduction

At the most basic level, hydrogels may be described as any three-dimensional, crosslinked polymeric network that has been swollen in aqueous media. More specifically, a hydrogel is any viscoelastic polymeric network that is water-soluble in its uncrosslinked form, but is able to resist dissolution and absorb a mass fraction of water typically much higher than the polymer mass fraction when crosslinked [1]. The hydrophilicity of these materials stems from the functional groups present on the backbone of the polymer, while the resistance to dissolution is the result of chemical crosslinks or physical entanglements that hold polymer chains tightly together and prevent chain reorganization.

Due to their unique physical and chemical properties, hydrogels have gained tremendous popularity in recent decades for their great potential in applications like tissue engineering [2], agriculture [3], bio-separations [4], and drug delivery [5], among others. These properties may be tuned according to the desired application: mechanical strength is easily modified by varying the degree of crosslinking, while the functionality on the backbone of the polymer may be altered to tune hydrophilicity, thereby customizing swelling behaviour in aqueous solvent systems.

The polymeric material from which hydrogels are based may consist of either naturally-sourced (carbohydrate-based) or synthetically manufactured polymers. Particularly in the case of carbohydrate-based scaffolds, their composition and mechanical/interfacial properties often mimic that of native extracellular matrix (ECM), improving their biocompatibility [5]. However, recent advances in synthetic polymer synthesis have allowed scientists to achieve a similar degree of biocompatibility as natural biopolymers. These synthetically generated scaffolds provide a degree of control over polymer structure and molecular weight, while allowing for the incorporation of stimuli responsive behaviour to control drug release or tune degradation rate [6].

1.1 Development of Macroporous Hydrogels

Macroporous hydrogels have been highly sought after in several industries, primarily biomedical [2] [5] and environmental [3] [4], due to their large pore volumes, large surface areas, and high permeabilities. These properties make them well suited for use as adsorbents, drug/bioactive delivery vehicles, biofiltration monoliths, and tissue engineering scaffolds.

Most effective tissue engineering scaffolds are macroporous (with pores greater than 50 nm) [7], and rely on highly interconnected pore structures for the transportation of oxygen and nutrients throughout the scaffold. While pore sizes with a minimum diameter of 3-12 μm (approximately the diameter of a single cell) are often targeted [8], optimal pore size depends on the type of tissue being engineered. For example, tissue engineering scaffolds designed for trabecular bone tissue regeneration can have porosities of 75-85% with pore sizes in the range of several hundred micrometres [9]. In contrast, scaffolds intended to mimic vascular tissues require small macropores (<38 μm) in order for microvascular epithelial cells to adhere and proliferate [8].

In drug delivery applications, hydrogels with structured macropores provide several advantages, namely their ability to offer large drug reservoirs (which likely result in larger drug loadings), while their high surface-to-volume ratios increase the potential for drug-surface interactions through ionic, electrostatic, or hydrophobic forces. Particularly in diffusion-controlled release mechanisms, drug release rate may be somewhat tuned based on pore size, with delivery rate increasing with increased pore size [7].

In all applications, the requisite pore size and interconnectivity of a crosslinked scaffold must be balanced with its degradability, mechanical strength, and permeability. A high degree of

porosity and/or large pore diameters will result in scaffolds with higher surface areas and permeabilities but more compressible hydrogel structures, resulting in generally less durable scaffolds. Similarly, higher surface areas result in faster enzymatic/hydrolytic degradation rates due to the reduced mass transfer resistances to enzyme or water transport, resulting in shortened gel lifespans. As such, a great deal of work has been dedicated to the creation of stable, macroporous hydrogels with tunable pore sizes and pore structures, as summarized in Figure 1.

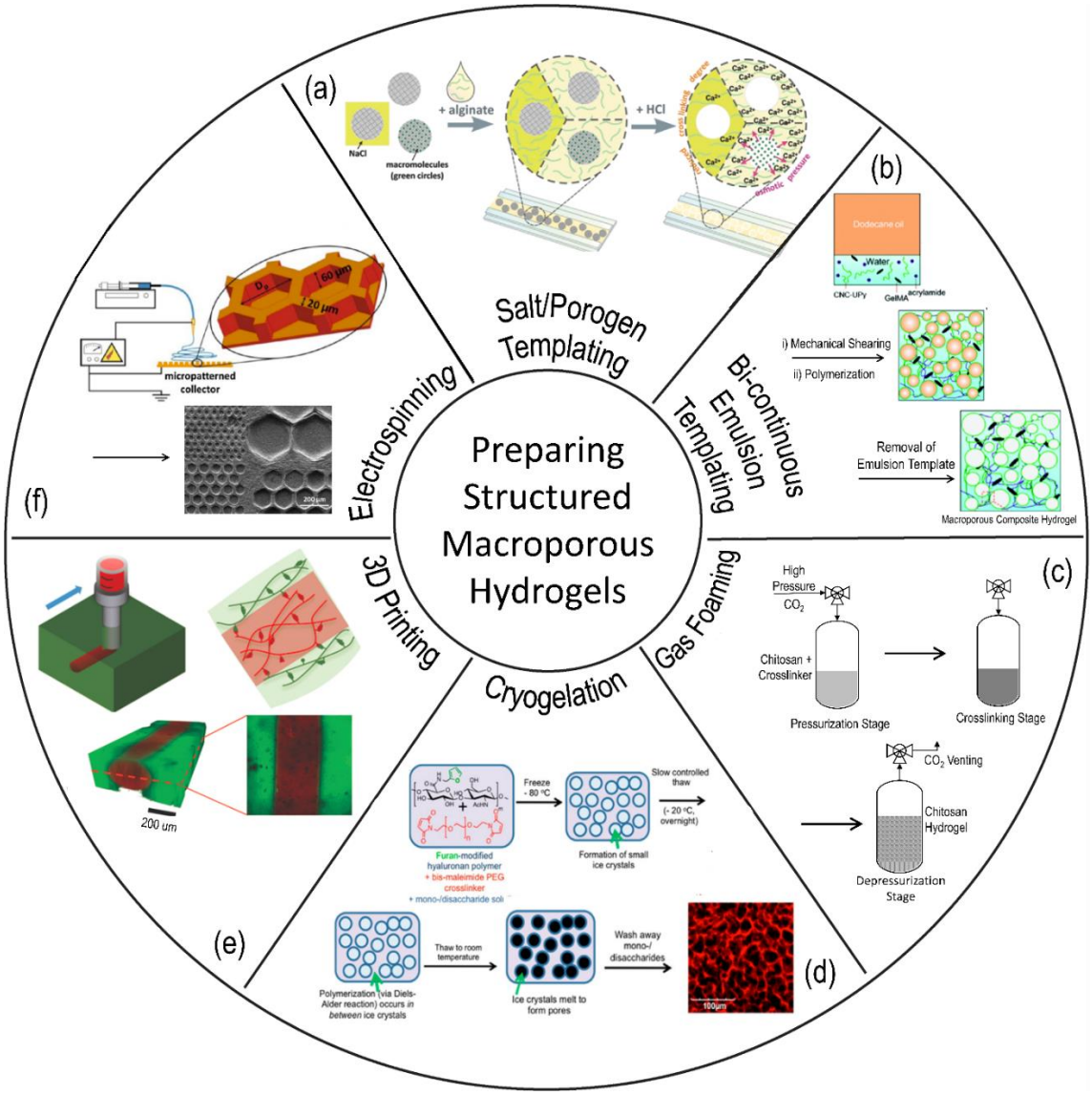

Figure 1: Conventional methods of preparing structured macroporous hydrogels: (a) porogen templating, (b) bicontinuous emulsion templating, (c) gas foaming, (d) cryogelation, (e) 3D printing, (f) electrospinning. Reproduced with permission [10]. Copyright 2018, John Wiley & Sons, Inc.

1.1.1 *Porogen Templating*

A common method of generating macropores within hydrogel structures is through porogen templating. In a typical porogen templating reaction, the desired polymer scaffold is dissolved in solution and mixed with a particulate material, called a "porogen". The polymer scaffold is subsequently crosslinked and/or precipitated, and the porogen is dissolved/degraded away to leave porogen-templated voids behind in the gel. Preferably, the size, geometry, and molecular structure of porogens should by highly tunable, to allow for the development of materials that mimic variable biological tissues or are able to target specific molecules in a separations application [11].

Salt leaching methods are used to prepare porous polymer scaffolds by casting polymer around inorganic salt particles. Sodium chloride is the most commonly used porogen material [12], with particle size and size distribution resulting from the sequence of grinding and sieving steps used to generate the particles. Sodium chloride particles obtained through sieving typically have large particle size distributions but can generate a wide range of porogen sizes (from 15 – 500 um) for diverse applications [12, 13]. Nucleation and crystallization techniques have also been developed, to generate smaller sodium chloride porogens with narrower particle size distributions on the order of tens of microns [12].

Once the polymer has been stabilized, the salt particles may be removed by dissolution in water; however, removal is never 100% effective (particularly for unconnected pores). In tissue engineering applications, this residual salt can limit the potential for cell loading into the scaffold, as it will affect the osmolarity of the extracellular fluid in the gel. Ultimately, the hypotonic conditions will result in the swelling and cytolysis of cells.

To resolve issues associated with the high osmolarity from leached salts, other hydrogel-based microparticles have been investigated for use as porogens. Calcium alginate microbeads developed using two inkjet printing techniques exhibited highly controllable particle sizes and distributions of 48 ± 4 and 248 ± 42 μm respectively [11], while alginate porogens created using emulsion methods were shown to have much larger diameters and distributions of 450-900 μm [14]. In both cases, the alginate porogens may be removed from the polymer scaffold by using a calcium-binding ligand such as ethylenediaminetetraacetic acid (EDTA), followed by subsequent dissolution of the alginate in water. Gelatin microparticle porogens have also been created through emulsification methods, yielding particles ranging in size from 100-500 μm after equilibration in water [15]. The same techniques were applied to poly(ε-caprolactone fumarate)-based microparticles, with control over pore-size demonstrated based on the ratio of poly(ethylene glycol) sebacic acid diacrylate incorporated into the beads [15]. Porogens were subsequently degraded using a sodium hydroxide solution and leached from the scaffold in aqueous solution.

The simplicity of salt leaching and porogen templating methods, along with the precise control over pore size and the overall degree of porosity, has caused this technique to remain relevant in the field of structured macroporous hydrogels, despite several obvious shortcomings. Complete removal of any porogen from a polymer scaffold is challenging, leaving residual pore-templates behind in the macroporous polymer scaffold. Due to the discrete nature of porogen particles, a consistent distribution of pores, and/or high interconnectivity of the pore network within the polymer scaffold are virtually impossible to achieve. For bioseparations or environmental applications that require the transport of a fluid through the polymer scaffold, this discontinuous pore structure can cause significant challenges [10]. Lastly, the extraction of

porogens from a polymer scaffold is a lengthy process, often involving several equilibrium steps, and is highly dependent on mass transfer kinetics. As a result, the scale-up of porogen templated scaffolds is extremely difficult, limiting their use in industrial applications.

1.1.2 *3D Printing*

The concept of printing three-dimensional hydrogel scaffolds has only become a reality in the past two decades, due to rapid improvements in printing technologies [16], including the ability of users to define precise morphologies and geometries using computer-aided modelling software. Two primary printing methods exist for bioinks: extrusion and stereolithography.

Extrusion-based technologies are the most common, likely because of their simplicity and reproducibility [17]. During printing, an automated extruder head moves in XYZ cartesian planes, while bioink/polymer solution is fed through a microneedle, deposited on a build plate, and gelled in situ. Crosslinking reactions will often be thermally initiated, with the microneedle heated to temperatures necessary for the decomposition of a thermal initiator. Extrusion-based printers have also been adapted to print cells directly into polymer matrices with up to 97% cell viability [18], as well as printing matrices out of cells themselves [19]. Advantages of this method include the speed with which printing can occur, as well as the variety of bioinks that are compatible with extrusion-based systems. However, printing of low viscosity polymer solutions is not possible, resolution is limited to features on a scale of 100 μm [17], and shear forces at the needle tip can affect the viability of printed cells, particularly when working with higher speeds and/or cell densities [20].

Stereolithography functions based on the premise of photopolymerization or photo-crosslinking, involving the exposure of a basin containing liquid monomer or polymer solution to

a highly concentrated beam of light that autonomously moves along XY-axes according to a digital model. The polymerization/crosslinking happens layer-by-layer, while the system gradually pulls the precipitated scaffold upwards out of the bath. However, traditional stereolithography, which uses UV-light beams for crosslinking, has been shown to cause mutations in encapsulated cells [21], causing visual light methods to gain attention. Several visible light methods have since been developed, including the use of eosin Y as a photoinitiator to crosslink functionalized gelatins such as gelatin-methacrylate [22] or gelatin methacryloyl [23]. Stereolithography offers high accuracies, printing speeds and cell viabilities, but is still confined to resolutions of approximately 100 μm and cannot accommodate the high cell densities achieved through extrusion-based printing methods.

All 3D printing methods are capable of manufacturing scaffolds with highly interconnected, user-defined pore structures and shapes without the concern of leaving behind pore templates. These technologies have also made tremendous progress towards the rapid creation of anatomically accurate and mechanically heterogeneous artificial tissues, like the 3D printed aortic valve scaffolds made from poly(ethylene glycol diacrylate) to mimic the geometries and mechanics of a fixed porcine tricuspid valve [24]. However, ongoing challenges exist relating to the resolution of printed polymeric fibres, limiting these methods to the production of macroscale systems [17].

1.1.3 *Gas Foaming*

Gas foaming methods of pore formation involve the incorporation of gas bubbles into polymeric matrices. This may be done using one of two methods: gas entrapment or gas generation. In gas entrapment, solid polymer structures are exposed to high pressure gas,

typically CO_2, for a period of several days. When the pressure is relieved, the rapid expansion of gas causes bubbles to form. In contrast, gas generation relies on a foaming agent that is added to the polymer and forms gas bubbles in situ as the result of chemical oxidation/decomposition.

The most common foaming agents are bicarbonate salts, particularly sodium bicarbonate, due to their minimal toxicity and ability to readily react with mild acids to produce carbon dioxide (CO_2) [25]. Sodium bicarbonate was employed as a foaming agent during the gelation of acrylic acid and acrylamide graft co-polymers in a study of swelling in super-porous hydrogels, generating circular pores averaging 100-250 μm in diameter [26]. The resulting porous structures were highly interconnected due to the proximity of bubbles, allowing for rapid swelling of the polymer scaffold due to the mobility of water through its interconnected capillary channels. Ammonium bicarbonate and sodium nitrite have also been employed as gas foaming agents, producing either CO_2 and ammonia gas (NH_3) or nitrogen gas (N_2) respectively, with pore sizes up to 20 μm in diameter [27, 28].

A distinct advantage of the gas entrapment method over gas generation, is that it avoids the deposition of chemical residues by conventional foaming agents. Instead, polymer solutions are placed in a pressure vessel and saturated with high pressure carbon dioxide at near supercritical conditions, called 'dense' CO_2 [29]. A chemical-crosslinking reaction is then facilitated, followed by the release of pressure and nucleation of entrapped CO_2 gas [28]. Dense CO_2 gas entrapped at 60 bar into recombinant tropoelastin/α-elastin hydrogels successfully generated internal pores of 35 ± 9 μm diameter and surface pores of 78 ± 17 μm diameter, while CO_2-saturated hydrogels at ambient pressure generated internal pores of 20 ± 5 μm with little to no pores generated at the surface [29]. This indicates that the increased solubility of dense CO_2 gas in the polymer provides increased interconnectivity of pores. However, even at near-

supercritical conditions, the overall porosity of these foamed scaffolds remains limited by the low solubility of CO_2 in aqueous solution.

Advantages of both gas foaming techniques include the speed of scaffold production, the potential to scale-up systems to generate larger batches of material, and the general cost-effectiveness of the process [10]. However, this technique suffers from a general lack of control over pore size and interconnectivity, resulting in randomly distributed pore networks of varying sizes. In gels with slower crosslinking kinetics, surfactants may also be required to stabilize foams and prevent bubble coalescence, resulting in the accumulation of unwanted chemical residues on the scaffold [28].

1.1.4 *Bicontinuous Emulsion Templating*

Emulsion pore templating techniques involve the combination of two different phases, typically a polymer-containing aqueous solution and a water-immiscible organic solvent. These two phases are mixed to form a water in oil-emulsion, and subsequently cast into a mold and rapidly frozen. Once frozen, the water is removed from the matrix through lyophilization, leaving behind macropores. By controlling the relative ratios of water-phase and oil-phase, as well as the mixing/homogenization regime, the size and interconnectivity of the resulting pore structure may be controlled.

To create macroporous hydrogels, emulsions with a volume fraction of dispersed phase greater than 74%, high internal phase emulsions (HIPEs), are used [30], with polymerizations/crosslinking reactions usually occurring in the continuous phase. Macropores are subsequently created by removal of the dispersed phase, often through flash-freezing and lyophilization, to leave behind open cellular structures [31]. An additional advantage of the

HIPE technique is the ability to pour an emulsification directly into a mold of any geometry prior to curing, enabling the creation of highly customized macroporous bulk hydrogels [32].

However, most bicontinuous emulsions require a large amount of surfactant for stabilization, presenting both economic and environmental challenges [32]. As a result, a great deal of research has been done using "Pickering-HIPEs" that use colloidal particles as opposed to conventional surfactants for interface stabilization, reducing the concentration of surfactant required and exhibiting enhanced anti-coalescence properties [31]. This method has been employed to create macroporous polyacrylamide (crosslinked with potassium persulfate and stabilized with Tween 80) to generate open-cell porous structures with pore sizes ranging from 10-40 μm and total porosities of 80% [31]. Similarly, poly(acrylic acid) porous monoliths were prepared using an oil-in-water bicontinuous emulsion to generate scaffolds with 80% porosity and an average pore size of 1 μm [32].

Advantages of using HIPE systems include their simplicity, the potential to generate continuous pore structures, the high speed of scaffold creation, and the potential to scale-up the system. However, it is difficult to precisely control pore size, and emulsion systems require additives like emulsifiers/surfactants as well as immiscible organic solvent that can reduce both the incorporation of cells during the gelation process and cell viability after scaffold creation.

1.1.5 *Cryogelation*

Cryogels are crosslinked macroporous polymeric materials that have been generated by subjecting a polymer in aqueous solution to a series of controlled freeze-thaw cycles. Cryogelation is typically done by holding an aqueous solution of polymer at a temperature just below its melting point (between -5 and -20^{o}C), initiating the formation of ice crystals within the

solvent [33]. As the crystalline phase continues to grow, it will gradually concentrate the polymer phase, isolating it into a continuous, nanofibrous network. Ice crystals will continue to grow until they encounter a crystal from another nucleation site, resulting in a highly interconnected pore structure. Once gelation is complete, removal of pore templates is done simply by returning the gel to temperatures exceeding the solvent melting point. When fully hydrated, the pores within the polymer scaffold will take on a smooth, rounded geometry, as a result of the surface tension at the polymer-solvent interface, eliminating the often sharp and triangular structures templated by the ice crystals [33].

Like other hydrogels, cryogels may be formed through a variety of crosslinking chemistries or physical entanglements. The formation of stable glutaraldehyde-crosslinked poly(vinyl alcohol) cryogels has been widely reported, with irregular pore diameters between 10-150 μm [34]. Similarly, laminin-containing gelatin cryogels, also stabilized through glutaraldehyde crosslinking, exhibited average pore sizes of 80-120 μm with a broad pore size distribution ranging from 20-160 μm [35], while poly(N-isopropyl acrylamide) cryogels crosslinked with N,N-methylene bis(acrylamide) exhibited a smaller pore size distribution with a mean pore size of 20-30 μm [36]. Combinations of pore templating methods have also been used in an effort to minimize the shortcomings of each individual method. For example, Thomas and Shea [37] successfully prepared porous hydrogels through the photopolymerization of poly(ethylene glycol) (PEG) around cryotemplated ice crystals. Through the use of micropatterned photomasks, they were subsequently able to create porous cryogels with diverse and customizable architectures [37].

Pore size may be adjusted through tuning of process variables such as polymer type, temperature, rate of phase change, number of freeze/thaw cycles and crosslinker composition.

An optimization of PVA-based cryogels indicated a decrease in pore size with an increasing number of freeze thaw cycles, as well as an increase in pore size with faster freezing rates. Furthermore, slower thawing rates produced cryogels with higher mechanical strengths, due to the increased time for polymer chain reorganization, but had little effect on pore size, while higher polymer concentrations in the initial solution resulted in denser fibres but smaller pore diameters [38].

Cryogelation methods have shown significant advantages over other methods, by utilizing the general approach of porogen templating, but eliminating the necessity of a difficult porogen-removal step [10, 33]. The resulting scaffolds possess inherently interconnected pore networks that are easily permeable by aqueous solutions and have great potential to be scaled up for large-scale industrial production. Their unique viscoelastic properties and mechanical stability also make them desirable for tissue engineering applications [39]. However, the sub-zero processing temperatures limit the types of gelation chemistries that may be performed (e.g. thermally activated crosslinking), as well as the potential for incorporating cells into the matrix during gelation without using a cryoprotectant like dimethyl sulfoxide (DMSO) [40]. Furthermore, this method lacks a degree of control over the pore size and pore geometry.

1.1.6 *Electrospinning*

A typical electrospinning apparatus consists of a syringe pump with a metallic needle, a high voltage supply, and a grounded collection plate. A polymer solution or melt is loaded into the syringe pump and a high voltage (between 2 and 30 kV) is applied to the metallic ejection needle. As the charged polymer is extruded through the needle, the electric potential acting on the solution is able to overcome forces due to surface tension, and the spherical droplet formed at the end of the needle will deform into a cone, referred to as a Taylor cone [41]. As the polymer

solution or melt passes through the air towards the collector, it undergoes a whipping motion resulting from the presence of an electric field, causing solvent to evaporate (or the polymer to solidify in the case of a melt), creating nanofibrous structures that eventually get deposited on the collection plate [42].

The process of electrospinning is highly tuneable, with variations in both solution characteristics and processing parameters resulting in significantly different fibre structures. Solution characteristics like viscosity, polymer concentration, and conductivity can affect the uniaxial stretching of the polymer fibres as they are ejected from the needle, resulting in changes to the fibre diameter. Lower polymer concentrations, higher surface charge, lower flowrates, and longer distances between the needle and collection plate will typically result in thinner fibres [41]. Solvent characteristics must also be tuned to achieve the desired polymer solubility while maintaining sufficient volatility to evaporate prior to the collection plate.

A great deal of work has been done by researchers to tune and optimize the technique of electrospinning. Boland et. al. modified their electrospinning process to include a cylindrical collection system, rotating at 1000 rpm, to achieve aligned poly(glycolic acid) fibres (from 0.15 to 1.5 μm in diameter), with anisotropic mechanical properties [43]. Targeted deposition of fibres was also exhibited by controlling the chaotic whipping motions of the polymer as the fibres move towards the collection vessel, enabling the production of poly(ethylene oxide) fibres with diameters less than 300 nm [44]. From a tissue engineering perspective, electrospun tubular scaffolds have been developed by depositing fibres around a rotating mandrel of poly(ethylene glycol) [45]. The resulting hollow structure with nanofibrous surface characteristics is well suited for applications in tissue engineered vascular grafts.

Advantages of electrospinning include its moderate control over pore size and fibre diameter, as well as its ability to produce hierarchical, nanostructured materials such as hollow fibres [42]. The process also enables the incorporation and immobilization of drug and/or cells directly into the polymer scaffold, with little effect on cell viability. However, the creation of large pores within an electrospun scaffold is challenging, and stabilization of electrospun fibres is only possible by rapid in situ chemical gelation or physical entanglement with high molecular weight support materials [10]. Process throughput is also very slow, with scale-up of this technique limited by the achievable size of a collection plate and the safety of operating a high voltage system at a much larger scale.

1.2 Current Challenges in Making Macroporous Hydrogels

Despite the many advances in the creation of macroporous hydrogels, significant drawbacks still exist. Templating and gas foaming methods often leave residual pore templates or gas by-products behind within the crosslinked gel, while methods not relying on pore templates lack a degree of control over both the interconnectivity and size of pores within the network. 3D printing/lithography-based methods have made significant advances towards solving this problem, allowing for the creation of user-defined pore structures and geometries, but are both inherently slow processes that are severely limited in terms of resolution (based on the minimum dimensions of an extruder head or a focused light source). Electrospinning has been shown to be very effective at creating macroporous polymer scaffolds, but is expensive, requires the use of high voltage, and is limited to viscous, high molecular weight polymer solutions.

A common challenge among all methods of macroporous hydrogel creation is the lack of mechanical stability of the macroporous 3D structure, as the increase in pore volume is typically associated with a decrease in overall mechanical strength [10]. Techniques to improve mechanical strength include increasing the crosslink density [46], increasing the connectivity of polymer fibres and pore networks [47], increasing the mass percentages of polymer in the hydrogel scaffold [48], and/or using unique crosslinkers to produce nanocomposite gels [49]. However, further improvements are required to allow for the use of hydrogels as substitutes for load-bearing tissues or as monoliths for high pressure separation processes.

1.3 Pressurized Gas eXpanded Liquid (PGX) Technology

Many requisite properties of an effective macroporous hydrogel scaffold may be achieved less expensively and more efficiently using the Pressurized Gas eXpanded liquid (PGX) processing method, developed by the University of Alverta and Ceapro, Inc. Unlike the methods discussed in section 1.1, this process is relatively high throughput, operating at five or twenty litre batch volumes, with the potential to increase process throughput even further by adapting the process to function in a semi-batch regime. In further contrast to conventional templating methods, the PGX process is able to purify and sterilize polymer scaffolds, removing water or ethanol soluble impurities during processing as opposed to leaving residual impurities behind in the macroporous scaffold.

The PGX process was originally developed to dry high molecular weight, water-soluble biopolymers using supercritical CO_2 and gas expanded ethanol. The system utilizes relatively mild temperatures (40^oC) and moderate pressures (approx. 100 bar), resulting in relatively low energy expenditure compared to conventional supercritical fluid processing systems [50].

In the PGX system, the polymer is pumped into a pressurized vessel as an aqueous solution, where it is injected through a co-axial needle and combined with supercritical CO_2 and gas expanded ethanol. The gas expanded ethanol acts as an antisolvent – rapidly precipitating the polymer out of its original aqueous solution and depositing it in the holding vessel – while simultaneously increasing CO_2 solubility and allowing for higher CO_2 ratios in the single-phase gas expanded liquid region. These increased CO_2 concentrations allow for higher penetrability of the CO_2 into the polymer scaffold, resulting in a subsequent increase in volume and decrease in viscosity.

Once pumping of aqueous solution is complete, two washing steps are performed; the first washing step flushes residual water from the system using CO_2 and ethanol, while the second removes the remainder of the ethanol from the system using only supercritical CO_2. When residual water and ethanol have been eliminated from the system, the apparatus is slowly returned to ambient pressure, allowing the supercritical CO_2 to vaporize. The gradual transition of supercritical CO_2 back to its gaseous state maintains the pore structure of the precipitated polymer, resulting in highly-exfoliated macroporous networks with extremely low bulk densities and high surface areas. Furthermore, the ability of all processing solvents to remain miscible throughout the solvent exchange process provides additional advantages over other precipitation/solvent exchange methods, as it avoids drastic changes to the polymer structure as a result of rapid swelling/deswelling behaviour in immiscible solvent systems.

An additional advantage of the PGX system is its ability to be reconfigured to circulate supercritical CO_2 ($scCO_2$) through the pressure vessel, carrying $scCO_2$ soluble drugs and bioactives into the system and depositing them on a pre-processed polymer scaffold. This technique will be discussed in further detail in Chapter 4.

1.4 Applications of Structured Macroporous Hydrogels in Drug Delivery

Traditionally, hydrogels intended for the delivery of drugs are formed into a desired shape and loaded with drug in vitro, prior to being placed in the body. A multitude of different chemistries may be used to synthesize these materials, with the potential to purify (or remove toxic reagents) prior to exposure to the body. Bulk hydrogels also offer a great deal of flexibility in regard to their size/shape, as they may be molded into virtually any geometry. The primary drawback of this method is that pre-formed hydrogels are confined to the specific size and shape in which they were cured, limiting their ability to be extruded through a needle. Therefore, these bulk hydrogels must either be implanted in the body through surgical methods [5] or used for transdermal drug delivery through close contact with the skin [51].

Several different chemistries have been developed with the aim of eliminating the invasive surgical placement of hydrogels in vivo. One such method is referred to as in situ crosslinking, in which the polymers are co-injected through a static mixer as two un-crosslinked precursor solutions, one (or both) of which is loaded with drug. These precursor solutions crosslink rapidly when mixed to form drug-loaded bulk hydrogels in vivo [52]. Common in situ gelation methods include Schiff base formation, hydrazone bonding, Michael addition of an acrylate and primary amine to form a secondary amine, or Michael addition of an acrylate and thiol to form a sulfide, as shown in Figure 2.

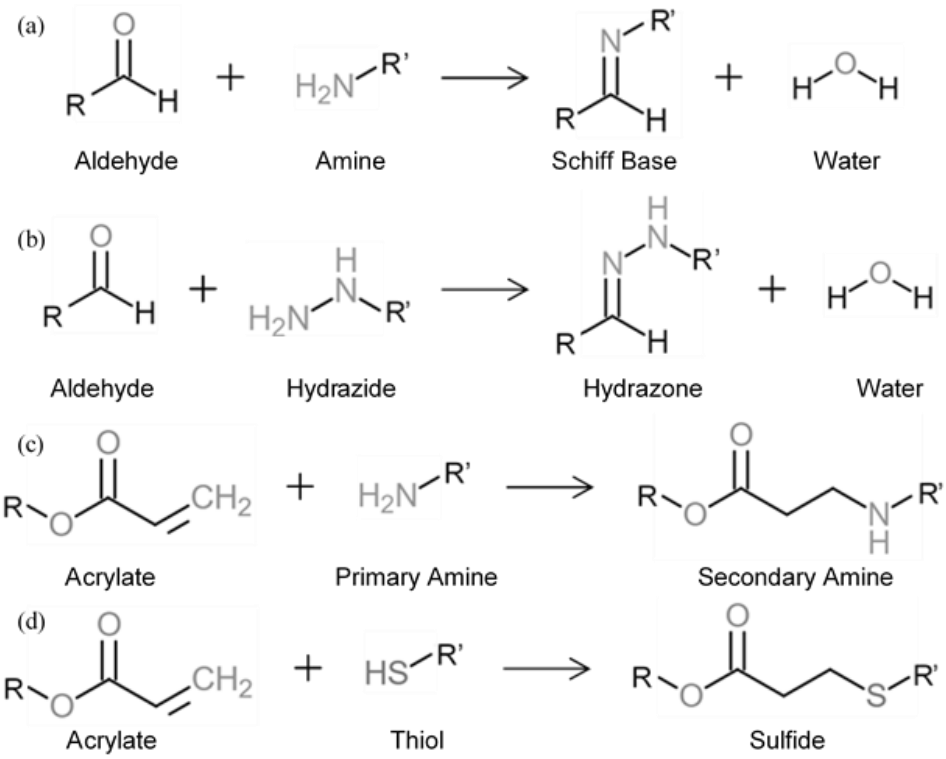

Figure 2: Mechanisms of common in situ gelation reactions: (a) Schiff base formation between an aldehyde and amine, (b) reaction between aldehyde and hydrazide to form a hydrazone bond, (c) Michael addition between an acrylate and primary amine, (d) Michael addition between an acrylate and thiol. Figure adapted from [5].

Pre-gelled formulations may also be appropriate for injection if the hydrogel exhibits shear thinning behaviour, allowing for passage through a needle and recovery of mechanical strength when returned to low shear conditions [51]. Alternatively, hydrogels may be preformed into nano-sized or micron-sized particles or capsules (called nanogels or microgels) that may be loaded with drug, suspended in buffer solution, and injected/sprayed to their target site in vivo. For example, poly(oligoethylene glycol methacrylate) nanogels were successfully delivered intranasally, transporting anti-psychotic drugs through the blood brain barrier to the brain [53].

1.4.1 *Empirical Modelling of Drug Release Mechanisms*

Drug release profiles from hydrogel systems are dependent on many different compounding variables, including the physiochemical properties of the solutes, the structural and

chemical characteristics of the polymer matrix, the release media, as well as any potential interactions between these variables. However, the primary forces driving the rate of drug release in most hydrogel systems are solute diffusion, matrix swelling effects, and polymer degradation rate [54]. For non-degradable hydrogel networks with low swellability, the release rate of solutes is primarily controlled by diffusion of drug through the polymer matrix, often exhibiting a zero-order release rate that remains relatively constant with time [54]. In contrast, drug release from swellable, macroporous matrices tend to be driven by Fickian diffusion, with release rates highly dependent on the concentration gradient, diffusion distance, and degree of swelling [54]. Empirically, these phenomena may be modelled using one of several power law-equations that have been developed for such solute-in-polymer-matrix systems, as shown in Table 1. In these equations, the diffusional exponent, n, depends on the type of transport (i.e. Fickian vs. non-Fickian diffusion) and hydrogel geometry [51]. When the diffusional exponent is equal to one (n=1), the transport mechanism is referred to as case II transport and the release rate is zero-order, meaning that the release of solute is constant and controlled primarily by polymer relaxation [55].

Table 1: Empirical formulas describing the general release profile of drug from a swollen polymer matrix, where M_t is the mass of drug released at time t, M_∞ is the total amount of drug released, k_x are kinetic constants, and n is the diffusional exponent [54].

Model Name	**Model Equation**	**Restrictions**
Higuchi	$\frac{M_t}{M_\infty} = kt^{1/2}$	Suitable for Fickian diffusion only
Ritger-Peppas	$\frac{M_t}{M_\infty} = k_1 t^n$	n=1: Case II transport n=0.5: Fickian diffusion 0.5 < n < 1: Non-Fickian diffusion
Peppas-Sahlin	$\frac{M_t}{M_\infty} = k_1 t^m + k_2 t^{2m}$	Suitable for non-Fickian diffusion only

While these equations are easy to use and may help to model simple drug release mechanisms, it is difficult to elucidate many of the more complex transport mechanisms and, therefore, important to recognize the shortcomings of these models.

Polymer systems have also been developed to respond to external stimuli, such as temperature, pH, magnetic fields, ultrasound, etc [49]. Drug release rates from many of these methods are controlled by the triggered swelling/de-swelling and/or controlled degradation of the hydrogel structure and, as such, do not follow typical solute-release models.

1.4.2 *PGX Materials for Drug Delivery Systems*

A distinct advantage of using PGX-processed materials for drug loading/delivery is their extremely high pore volumes that can act as large reservoirs to hold bioactives and/or drugs and substantially increase the drug-loading capacity of the scaffold. The large surface areas of PGX materials also increase the potential for physical and chemical interactions to occur between the drug and the polymer matrix, allowing for delayed or prolonged drug release profiles. For example, charge interactions between a 4-vinylpyridine and N-(3-aminopropyl)methacrylamide co-polymer and two non-steroidal anti-inflammatory drugs, resulted in 10-fold and 20-fold increases in the drug loading of ibuprofen and diclofenac, respectively [56]. The acid-base interactions between the amino group on the polymer and the anionic drug also allowed for extended drug release, providing sustained release of ibuprofen for at least 24 hours and sustained release of diclofenac for over one week.

Another significant advantage of using the PGX system lies in its ability to impregnate hydrophobic and/or thermally-sensitive drugs into polymeric scaffolds through the use of $scCO_2$. By reconfiguring the processing system, $scCO_2$ may be circulated through a vessel at high

pressures and moderate temperatures, carrying $scCO_2$ soluble drugs and depositing them on the pre-dried polymer scaffold. Upon depressurization of the vessel, drugs are re-precipitated in micronized or nano-crystalline form, providing a large active interface between the drug particle and surrounding media [57]. The high surface-to-volume ratios of these tiny crystals/particles can drastically increase their solubility/dissolution profiles and dispersion stability, improving their overall bioavailability and pharmacokinetic properties [57].

1.5 Applications of Structured Macroporous Hydrogels in Wound Healing

A typical wound healing process consists of five stages: haemostasis, inflammation, migration, proliferation, and remodelling. Haemostasis and inflammation occur immediately upon wound creation, driving vasoconstriction and blood clotting to prevent excessive blood loss at the wound site. Platelets also travel to the wound site and form platelet plugs to temporary block open blood vessels while simultaneously secreting growth factors and cytokines that attract neutrophils and macrophages to the site. Fibrinogen, a circulating blood protein, is enzymatically converted to insoluble fibrin, which acts to strengthen the clot by binding red blood cells and facilitating subsequent coagulation [58].

Acute inflammation processes are initiated by either pathogen recognition or tissue damage and may last up to 7 days after wound creation. This phase is primarily characterized by swelling, pain, redness, and elevated temperatures at the wound site, as well as the presence of neutrophils and other phagocytic cells. Neutrophils release a variety of bioactive species (such as reactive oxygen and proteases) to prevent bacterial contamination and remove debris, after which monocytes are recruited from the blood to become macrophages that act primarily to phagocytose bacteria and necrotic tissue [59]. Macrophages are also responsible for the release

of growth factors, (e.g. vascular endothelial growth factor, or VEGF) and other cytokines to recruit fibroblasts, endothelial cells and keratinocytes that work to promote angiogenesis [60]. Typically, it is the failure to progress past the inflammatory phase that classifies a wound as chronic [59].

The end of the inflammatory phase is characterized by the apoptosis of immune cells and the commencement of the proliferation phase. This phase is responsible for tissue granulation, angiogenesis, as well as re-epithelialization of the wound site [59] and is initially marked by the formation of a disorganized matrix of granulation tissue that consists largely of procollagen and elastin and fills the wound site to allow for the ingrowth of new blood vessels [61]. The subsequent remodelling of the wound site consists of the reorganization of the collagen matrix into small parallel bundles, culminating in wound contracture and scar formation. The entire remodelling process can take up to a year to complete, as the damaged tissue regains its structural integrity [61].

While many researchers believe that inflammation is necessary for subsequent wound healing to proceed, Szpaderska and DiPietro have hypothesized that reduced inflammation may slow the healing process but ultimately provide superior wound healing [62]. They observed the phenomenon of "scarless" wound healing in early fetal skin, where wounds are known to exhibit a negligible inflammatory response relative to adult wounds that generally resolve as scars [63, 64]. Furthermore, mucosal tissues in the tongue and skin tend to heal rapidly and with minimal scar formation, correlating with significantly lower numbers of neutrophils, macrophages, and T-cells as well as reduced levels of relevant cytokines at these sites, indicating a reduced degree of inflammation [62]. However, it must be noted that these wounds were surgically inflicted and

occurred in near aseptic conditions without the mass tissue damage and microbial contamination present in many traumatic wounds that may confound interpretation of the results.

In practice, a moderate inflammatory response is necessary for haemostasis, as well as the recruitment of the innate immune system to the wound site [65]. This process ensures that pathogens and necrotic tissue are metabolized, preparing the wound site for subsequent healing processes. In clinical practice, the inflammation stage may even be utilized for degradation of implanted materials. This is especially true for materials like resorbable sutures, as cells such as monocytes and macrophages will produce hydrolyzing agents (such as enzymes) and oxidizing agents (like nitric oxide) during inflammation [66]. This allows for the controlled degradation of the biomaterial and the regrowth of healthy tissue in the place of the degraded implant. However, a prolonged inflammatory response at a wound site (whether caused by a biomaterial implant or untreated infection) could cause mass destruction to the surrounding tissues as a result of elevated immune and phagocytotic cell activity [65].

1.5.1 *Polymeric Wound Healing Systems*

Many polymeric wound healing scaffolds have been designed to moderate the inflammatory response while simultaneously treating infection. These scaffolds should ideally mimic the properties and functions of human skin (protecting the wound from pathogens and dehydration) and include drugs to treat inflammation, with the option to include cells, biological signalling molecules, or any combination thereof to further enhance the healing response [67]. Ultimately, successful wound dressings should be able to absorb wound exudate, treat/protect from bacterial infections, moderate inflammation and encourage haemostasis.

Historically, wound dressings were fabricated from unprocessed plant fibres and animal fats to simply cover and protect wounds [68]. Modern methods have evolved to include active treatment at the wound site, but many promising biomaterial scaffolds are still prepared from naturally-sourced biopolymers due to their non-toxic, non-immunogenic, and biodegradable properties, as well as ready availability. Biological polymers such as collagen, fibrin, gelatin, elastin, chitosan, alginate, and hyaluronic acid are commonly seen in both wound healing and tissue engineering applications [69].

Several commercial engineering allograft scaffolds exist. Apligraf ® (composed of a bovine type I collagen matrix) and Dermagraft ® (a bioresorbable scaffold composed of PLGA with 90% G-units and 10% L-units) are both pre-seeded with human neonatal fibroblasts, while scaffolds like Talymed ® and Hyalomatrix ®, are acellular biopolymeric scaffolds composed of poly(N-acetyl glucosamine) and poly(hyaluronic acid), respectively [70]. While these dressings are effective at either sealing/protecting the wound or seeding cells into the wound site, multi-functional wound dressings that target multiple avenues of wound healing are not readily available for consumers. Academic labs are now targeting such multi-active wound healing scaffolds. For example, Kumbar et. al. prepared an electrospun poly(lactic-co-glycolic acid) matrix with the same tensile strength as native skin (40-80 MPa) onto which human fibroblasts were seeded, supporting cell proliferation as well as the expression of collagen I, collagen III, and elastin expression in the matrix [67]. Alternately, Li et. al. prepared zinc (Zn^{2+}) and calcium (Ca^{2+}) crosslinked alginate hydrogels that released both Zn^{2+} and Ca^{2+} into a wound site, inhibiting bacterial growth and stimulating cell proliferation/migration in vivo [71]. Histological results from these scaffolds suggest that they are also capable of promoting blood vessel formation and regeneration of epithelial tissue [71].

1.5.2 *PGX Materials for Wound Healing Systems*

Many of the requisite properties of an effective wound healing scaffold can be obtained more efficiently using PGX-generated morphologies. For example, the PGX has been shown to produce morphologies similar to electrospun mats, whose highly-porous, nanofibrous structures are known to accelerate wound healing and mimic natural tissues [68]. PGX-dried polymers are also highly absorbent, which may be coupled with the unique drug impregnation capabilities of PGX materials to facilitate the production of scaffolds suitable for the simultaneous delivery of anti-inflammatory drugs and absorption of wound exudate to/from a large wound site. By tuning PGX processing conditions, scaffolds containing both macropores and micropores may be fabricated, which have been shown to provide improved cell proliferation and adhesion over scaffolds containing only macropores [72]. Furthermore, promising methods for developing PGX composite materials have been developed, that allow for the co-drying (and co-structuring) of two different polymer materials in a very homogeneous manner. For example, the known anti-inflammatory properties of beta-glucan [73] may be combined with the haemostatic and anti-microbial properties of chitosan [74] to target multiple facets of the wound healing process.

Chapter 2 – Pressurized Gas eXpanded Liquid Processing Methods

2.1 Introduction

2.1.1 *Supercritical Fluid Processing*

A supercritical fluid may be formed from any substance that is either liquid or gas at ambient conditions when it is raised above its critical temperature and pressure, as shown in Figure 3. These conditions are typically achieved at moderately high pressures and temperatures, at which liquids become less dense and gases become more dense until phase-distinctions between liquid and gas do not exist at all [75].

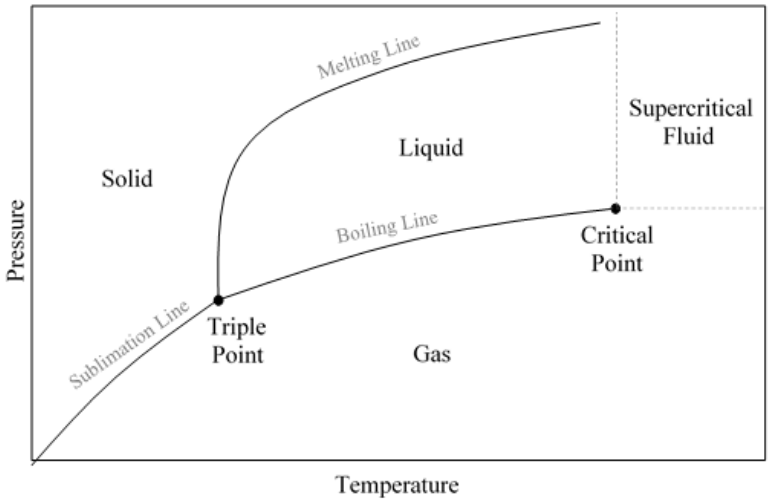

Figure 3: Typical phase diagram for an arbitrary substance, illustrating the presence of a supercritical fluid at high termperature and pressure

Supercritical fluids exhibit gas-like viscosities but liquid-like densities, as well as large compressibility, high permeability, and low surface tension, making them ideal for extractions or purifications of solvent-sensitive biological molecules, and the processing of biopolymer systems. Supercritical carbon dioxide ($scCO_2$) is the most common supercritical fluid used for processing and extractions, due to its availability, low cost, and net zero emissions production

[75]. In polymer processing, $scCO_2$ also provides the distinct advantage of being a gas at ambient conditions, allowing for its easy removal from the polymer phase with negligible disruption to the pore structure and/or polymer morphology.

Supercritical fluid technologies are currently being applied to biopolymer processing through a variety of extrusion and gas foaming processes. For example, Cotugno et. al performed a microcellular foaming reaction of poly(ε-caprolactone) using $scCO_2$, by placing molten polymer in a sealed vessel and pressurizing the system at various temperatures, both above and below the critical point [76]. They observed a dramatic increase in the diffusion coefficients and solubility of CO_2 in the polymer phase above the critical point, producing polymer foams with significantly lower densities when depressurized. In extrusion technology, $scCO_2$ may be injected into a pressurized extruder alongside a polymer melt, resulting in the solubilization of CO_2 by the molten polymer, and subsequent decrease in polymer viscosity, melting point and glass transition temperature [77]. In this application, dissolved $scCO_2$ offers the benefits of a plasticizer (allowing for the processing of molecules that would otherwise degrade when subjected to the shear forces of an extruder), while simultaneously acting as a gas foaming agent (generating large pores in the polymer network as it is expanded through a die and returned to ambient pressures) [77]. Alavi et. al. examined the $scCO_2$ extrusion of thermoplastic starch and observed expansion ratio increases of up to 140% and bulk density decreases up to 70% relative to steam-based expansion methods [78].

The use of supercritical fluids in spray drying technologies have also attracted significant research attention, much of which is focused around supercritical fluid-assisted atomization (SAA) of components through a high shear nozzle, and their subsequent precipitation into uniformly-distributed particles [79]. Four primary processing techniques based on supercritical

fluids have been developed for generating small and uniform particles: rapid expansion of supercritical solution (RESS), supercritical anti-solvent (SAS), supercritical assisted atomization (SAA), and particles from gas saturated solution (PGSS) [80]. In these methods, $scCO_2$ may be utilized as a solvent (as in RESS), co-solute (as in PGSS and SAA), or anti-solvent (as in SAS). Particular to the SAS method, a solute is dissolved in organic solvent and then combined with CO_2 at supercritical conditions in which the $scCO_2$ and organic solvent are miscible, rapidly precipitating the solute [80]. The miscible organic solvent-$scCO_2$ phase in this system is referred to as a gas expanded liquid.

2.1.2 *Gas Expanded Liquid Processing*

A gas expanded liquid is a mixed solvent system composed of a compressible gas (e.g. CO_2 or ethane) at supercritical conditions, dissolved in an organic solvent to form a single-phase system [81]. The organic solvent undergoes a significant volumetric expansion due to the dissolution of the gas and, when used for processing of polymers or small molecules, combines the advantages of a supercritical fluid (high permeability, low viscosity, favourable transport properties), with those of an organic solvent (modified solubilities). The incorporation of an organic solvent often affects the solubility/miscibility of the $scCO_2$ with other liquid components, allowing for ternary systems like CO_2-EtOH-H_2O with larger mole fractions of water and ethanol than would otherwise be possible at single-phase conditions [81].

De Marco et. al. utilized an expanded liquid anti-solvent (ELAS) system to precipitate yttrium acetate and BSA from aqueous solution into micro- and nano-sized particles, by passing them through a nozzle and into a collection vessel, in which they were combined with gas expanded ethanol and CO_2. By varying certain processing conditions, they demonstrated the

production of both stable BSA nanoparticles (0.2-2 μm in diameter from concentrations <50 mg/mL in aqueous solution) and fibrous networks (1-5 μm in diameter, from concentrations <100 mg/mL in aqueous solution) [80]. Other researchers have investigated the concept of gas expanded liquids as they apply to the preparation of fine powders (often in pharmaceuticals, pigments, or nutraceuticals) [82]. However, utilizing gas expanded liquids to generate super-porous or nanofibrous polymeric networks has largely been unexplored.

2.1.3 *Advantages of the PGX System*

Similar to methods discussed in section 2.1.2, CO_2 and ethanol are the chosen gas expanded liquid solvents in the PGX system. These solvents significantly enhance water solubility/miscibility, allowing for significantly higher water concentrations (and therefore, polymer concentrations) in the single-phase processing regime. These higher polymer concentrations, in combination with the unique mechanisms of mixing and precipitation within the PGX system (discussed in section 2.1.3.1), provide favourable conditions for the generation of multi-porous structures and nanofibrous networks, as opposed to nanoparticles. Such morphologies exhibit extremely high surface areas and bulk densities, as shown in Table 2 and Figure 4, and possess great potential for use in many different industries, including tissue engineering, drug delivery, and bioseparations.

Table 2: Bulk densities and surface areas of PGX-processed biopolymers (processed according to 2.2.2.6)

Sample ID	Specific Surface Area (m^2/g)	Bulk Density (g/mL)
PGX-Processed Chitosan	192 ± 37	0.0140 ± 0.0036
PGX Processed Alginate	165 ± 27	0.0126 ± 0.0039
PGX Processed Corn Starch	65 ± 1	0.0109 ± 0.0019
PGX Processed Citrus Pectin	305 ± 6	0.0483 ± 0.0643

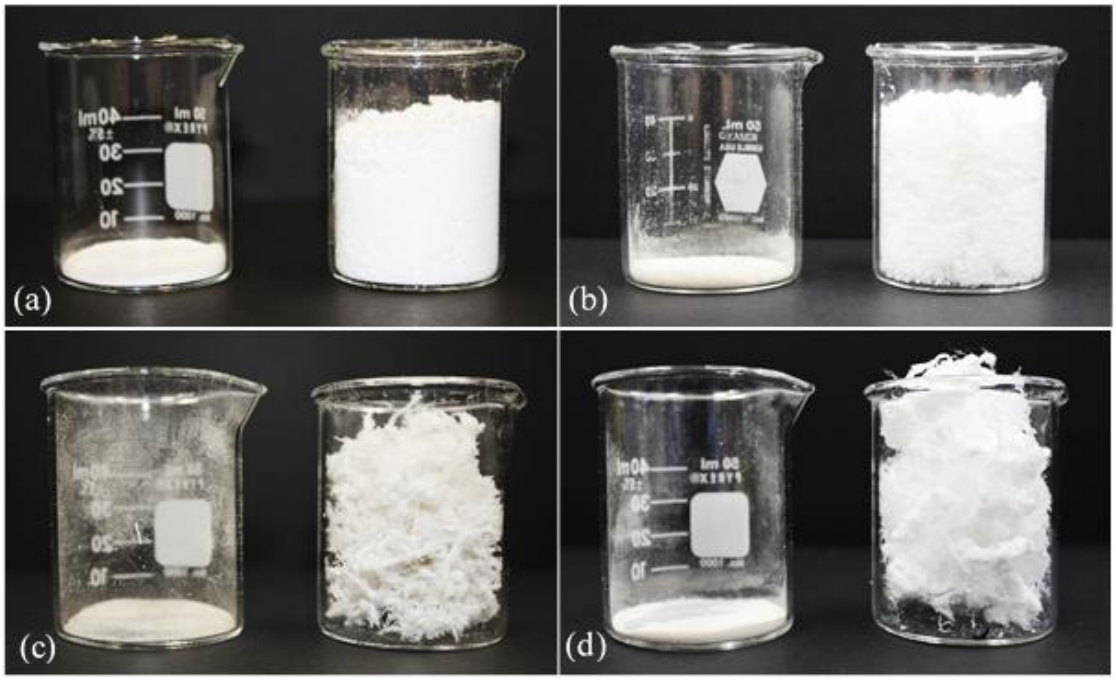

Figure 4: Equal masses of PGX-processed polymer (right beaker) and unprocessed polymer (left beaker) to illustrate the significant increase in bulk density of (a) starch from corn (b) chitosan (c) citrus pectin (d) sodium alginate due to PGX processing.

2.1.3.1 Mechanisms Responsible for the Generation of PGX-Morphologies

Three primary mechanisms contribute to the ability of the PGX to generate highly-exfoliated, macroporous and/or nanofibrous structures. First, the unique co-axial nozzle design in the PGX system results in the turbulent mixing of the aqueous solution and gas expanded liquid streams as they pass through the mixing chamber and into the vessel. Second, the gas expanded liquid EtOH-CO_2 has favourable transport properties (high permeability, low viscosity) and can rapidly form a miscible single-phase system with water, acting as an anti-solvent to instantaneously precipitate the polymer from solution. Finally, the $scCO_2$ acts as a solvent for the water, reducing its viscosity and interfacial tension during polymer precipitation and allowing for an immediate solvent exchange within the polymer network. The combination of these mechanisms results in the formation and precipitation of highly porous, nanofibrous

polymer structures, and the subsequent removal of water from the polymer network without the collapse of pore structures due to capillary forces.

2.2 Materials and Methods

2.2.1 *Materials*

Starch from corn (Sigma Aldrich, practical grade), unmodified waxy corn starch of essentially pure amylopectin (Sigma Aldrich, contains only trace amounts of amylose), and pectin from citrus peel (Sigma Aldrich, Galacturonic acid ≥ 74.0 %) were used to assess the operational tuneability of the PGX system. To generate samples with different molecular weight but the same basic chemical composition, starch from corn (Sigma Aldrich, practical grade) was degraded with α-amylase (MP Biomedical, ~165,000 BAU/gram). Anhydrous ethanol (Les Alcools de Commerce, 99%) and compressed CO_2 equipped with a liquid withdrawal tube (Air Liquide Canada, 99.5%) were used as the solvents for PGX processing.

2.2.2 *Methods*

2.2.2.1 *Gelatinization/Dissolution of Starch for Processing*

Base method starch samples were suspended to 10wt% in DIW and transferred into a Smart BT 6Qt Pressure Cooker (Instant Pot). The starch was heated from room temperature to 110^{o}C and held at high pressure for ten minutes. The dissolved starch was pumped directly into the PGX system upon removal from the pressure cooker.

2.2.2.2 *Controlled Degradation of Starch for PGX Processing*

Starch was gelatinized as described in section 2.2.2.1, removed from the pressure cooker and allowed to cool to 60^{o}C. For the most degraded starch, 20mg of α-amylase (165,000

BAU/gram) was added and the mixture was allowed to incubate for 6 minutes. For the intermediate molecular weight, 5 mg of α-amylase was added, and the mixture was incubated for 3 minutes. After the designated incubation period, the starch/amylase mixture was heated to 80°C over the course of 3 minutes to denature the enzyme. The degraded starch was pumped directly into the PGX system after heating, with the anhydrous EtOH solvent effectively denaturing any residual active enzyme [83].

2.2.2.3 Preparation of Pectin for PGX Processing

Base method pectin samples were suspended to 5wt% in DIW and heated to 80°C with magnetic stirring to dissolve. The dissolved pectin was pumped directly into the PGX system upon removal from the hot plate.

2.2.2.4 Degradation of Pectin for Processing

Pectin samples were suspended to 5wt% in DIW and heated to 80°C under constant stirring. The solution was adjusted to pH = 10 using sodium hydroxide (NaOH) and allowed to stir for four hours, facilitating the base-catalyzed hydrolysis of the glycosidic linkages. Degradation was quenched by neutralizing the reaction solution with hydrochloric acid and transferring it into dialysis tubing. The salts and low molecular weight components were subsequently removed through 6 (6+ hour) cycles of dialysis against DIW, after which the degraded product was lyophilized to dryness.

2.2.2.5 Determination of Viscosity-Average Molecular Weight of Degraded Samples

Degraded starch samples were dissolved to 10 wt% in DIW and gelatinized according to the process described in section 2.2.2.1. Similarly, dissolved pectin samples were prepared according to methods described in section 2.2.2.3. The viscosity of dissolved polymer solutions

was measured using a Discovery HR-2 rheometer (TA Instruments), fitted with an advanced Peltier plate and 40 mm diameter upper cone geometry with a 1° cone angle. Viscosity measurements were conducted over a 60 second integration time at a temperature of 85°C and testing gap of 150 µm. Apparent viscosity was determined according to a Herschel-Bulkley fit, as calculated by the discovery HR-2 software, and intrinsic viscosity was estimated by subtracting the measured viscosity of pure solvent from that of solvent containing either degraded or undegraded polymer. The relative viscosity-average molecular weights of degraded starch samples were estimated using the Mark-Houwink equation: $[\eta] = kM^{\alpha}$, where η is the intrinsic viscosity of the polymer solution, k and α are constants for a given polymer-solvent system, and M is the viscosity-average molecular weight. The estimated relative molecular weight values of the degraded samples were used for the primary purpose of morphological comparisons (relative to the non-degraded standard).

2.2.2.6 *Standard PGX Processing Method*

A process flow diagram of the PGX processing method in its standard spray drying configuration is provided in Figure 5. The primary components of the system are a positive displacement pump (Hydra-Cell, MT8 Low Flow/High Pressure Triplex Metering Pump) to modulate ethanol flow, a pneumatic metering pump (Williams, V-Series Hi Pressure Dual Seal Plunger) to control a syringe injection system for aqueous polymer solutions, and a high-pressure positive displacement pump (Thar Technologies Inc, High Pressure P-Series Pump) for CO_2. The solvents are combined at a static mixing tee with a 90° mixing angle and pumped through a custom-machined coaxial nozzle into a 5L pressure vessel equipped with a heating jacket (Thar Technologies Inc.). The system also includes a heat exchanger (Thar Technologies Inc, SFE2000M1) to regulate temperature, an automated back pressure regulator (Thar Technologies

Inc, SFE2000M1) to control vessel pressure, and a 500mL separation vessel to separate gaseous and liquid waste streams at ambient temperature and pressure.

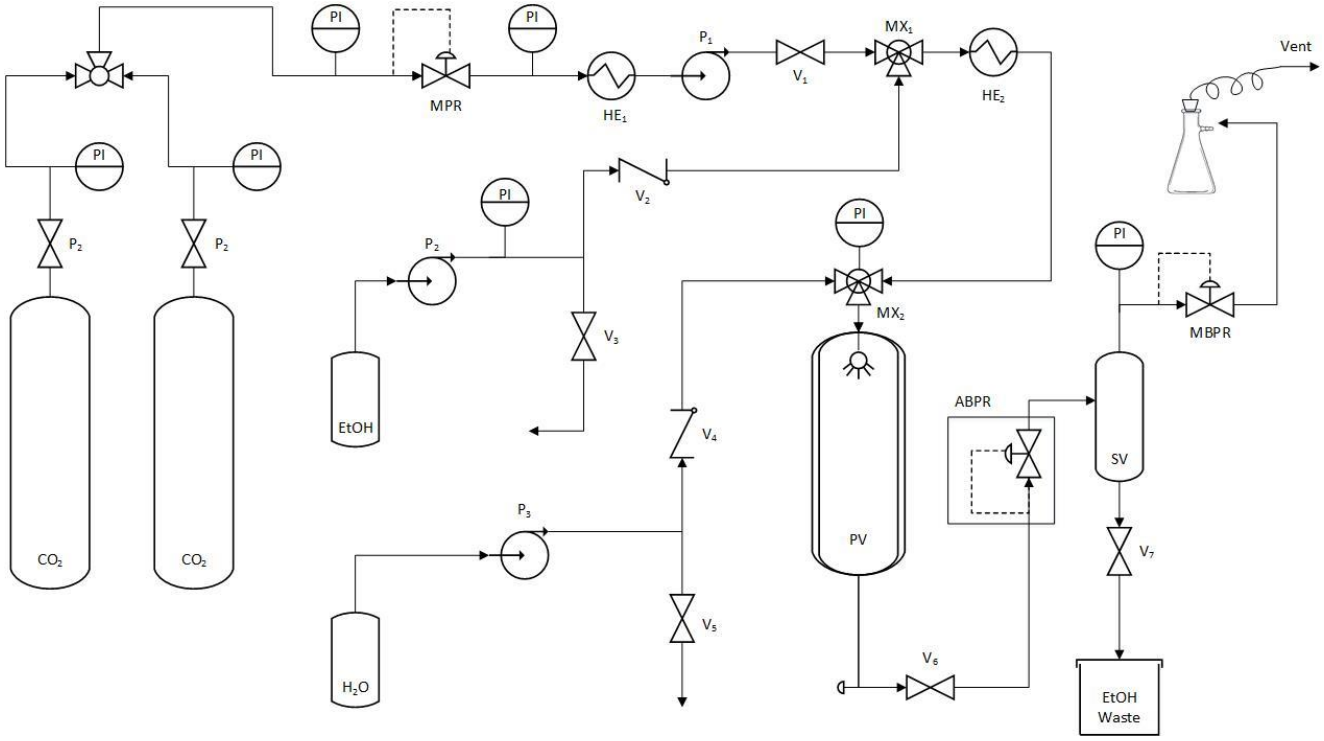

Figure 5: Process flow diagram of the PGX in its spray drying configuration, showing the PV (pressure vessel), SV (separation vessel), ABPR (automatic back pressure regulator), MBPR (manual back pressure regulator) and mixing valves (MX_1 and MX_2).

The PGX system was pressurized by pumping ethanol (EtOH) and CO_2 through a static mixing tee (MX1) and heat exchanger (HE_2) into the pressurized collection vessel (PV) at 45 mL/min and 15 mL/min, respectively. These flowrates were maintained while the system equilibrated to reach a single-phase gas expanded liquid mixture at 40°C and 100 bar. While equilibrating, the isolated syringe pump was filled with aqueous polymer solution using a peristaltic laboratory pump, and the pneumatic metering pump was engaged to build pressure in the syringe. When the system was equilibrated and the pressure in the syringe was large enough to overcome that of the vessel, the polymer solution was pumped into the system, maintaining the flow at 15 mL/min. The polymer solution flows through the inner tube of a coaxial nozzle

(1/4" diameter inner tube and 3/8" diameter outer tube, with tube thicknesses of 0.035" and 0.049" respectively) while the CO_2 and EtOH flow through the outer tube. The aqueous polymer solution is rapidly combined with the gas expanded CO_2/EtOH in a small mixing chamber at the end of the nozzle before being co-ejected into the vessel through a 1/8" diameter hole. The polymer is rapidly precipitated as it passes through the nozzle and is deposited at the bottom of the pressure vessel. The now ternary gas expanded liquid solvent system is washed through several filter discs, as shown in Figure 6, into the separation vessel and, ultimately, out of the system and into the waste collector.

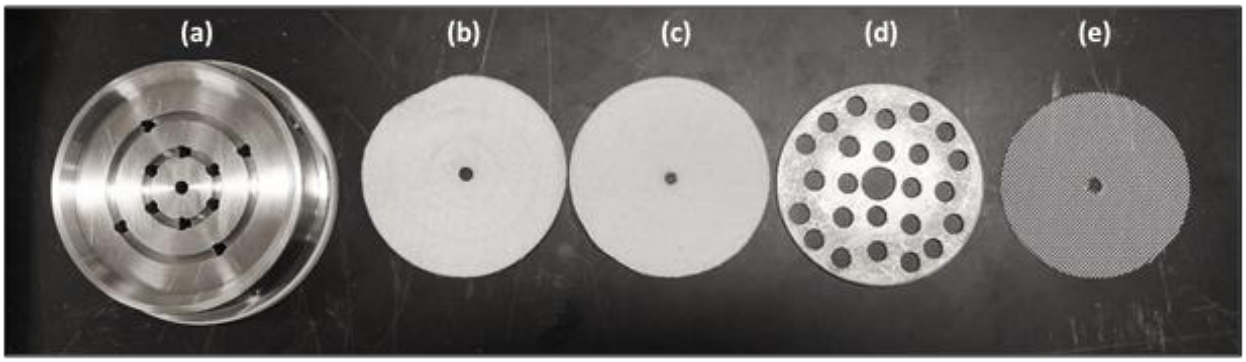

Figure 6: Configuration of filter discs at the base of the pressurized collection vessel. From bottom to top: (a) metal base of collection basket, (b) 5 micron felt filter pad, (c) 5 micron felt filter pad, (d) metal reinforcement disc, (e) coarse nylon filter pad.

Once the aqueous polymer solution was finished pumping, the system was directed through two washing steps. First, the residual water was flushed from the system using gas expanded EtOH/CO_2, as illustrated in step (1) on the ternary phase diagram in Figure 7. The flowrate of EtOH was then gradually decreased while the CO_2 flowrate was increased, maintaining a constant overall flowrate of 60 mL/min as the residual EtOH was flushed from the system (shown by step (2) in Figure 7).

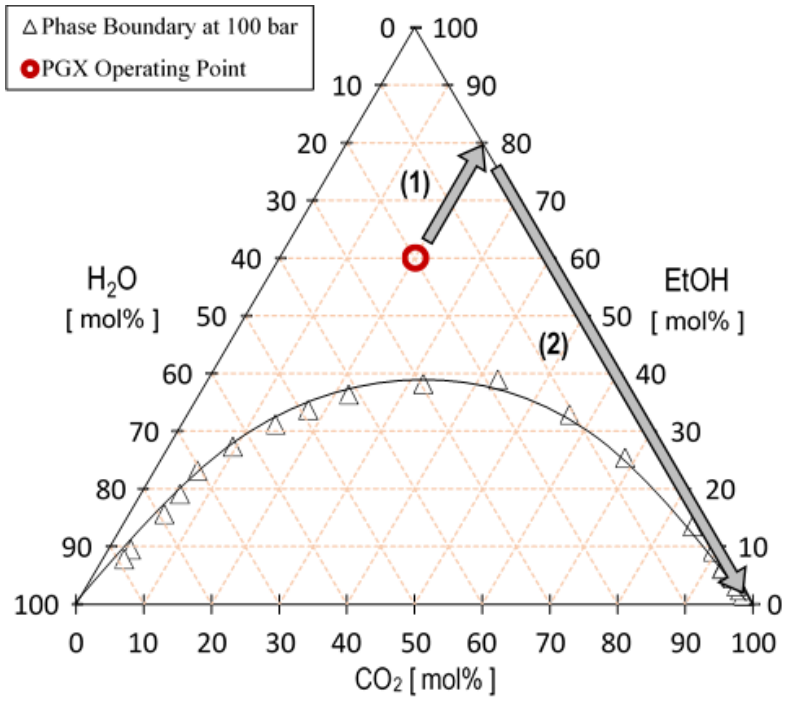

Figure 7: Ternary phase diagram showing flow ratios for standard PGX processing at 100 bar and 40°C. Step (1) illustrates flow ratios during the first washing step, while step (2) illustrates flow ratios during the second washing step. Phase data obtained from Durling et. al. [84]

When only $scCO_2$ remained in the PGX system, all flow to the vessel was stopped, the ABPR was controlled manually, and the pressure from the system was gradually released, allowing CO_2 to return to its gaseous state and exit the system without affecting the morphology of the processed polymer. The pressure vessel, now at ambient pressure and temperature, was opened and the collection basket removed to recover the PGX-processed polymer.

2.2.2.7 *BET Analysis of Specific Surface Area and Pore Size*

PGX-dried and/or unprocessed polymer samples intended for BET analysis were degassed for 24 hours at 105°C using an Autosorb-iQ-MP/XR gas sorption analyzer (Quantachrome Instruments). The degassing temperature of 105°C was selected to preserve the polymer structure and prevent thermal degradation prior to surface area analysis. The 24 hour outgassing time was selected by gravimetrically assessing a representative sample to determine

when all residual water/solvent had been removed from the sample. The Autosorb-iQ-MP/XR physisorption gas sorption analyzer (Quantachrome Instruments) was then used to measure adsorbed and desorbed amounts of nitrogen gas to/from the sample at relative pressures (P/P_0) from 0.05 to 0.9. Quantachrome ASiQwin software was used to analyze adsorption and desorption isotherms and specific surface areas were calculated using multi-point Brunauer-Emmett-Teller equations, while pore sizes were calculated from a Monte Carlo pore size model.

2.2.2.8 *SEM Imaging of PGX Morphologies*

PGX-processed samples were affixed to stainless steel specimen stubs (12.5 mm or 25 mm diameter) with electrically conductive, non-porous carbon tape and subsequently sputter coated with gold or platinum to prevent charging. Samples were imaged using a Tescan Vega-II XMU (Tescan Instruments) or FEI Magellan 400 (FEI Company) scanning electron microscope at 500, 1000, 5000, 50 000 times magnification and voltages of 10 or 20 kV

2.2.2.9 *Light Microscopy Imaging of PGX Starch and Calculation of Particle Size Distribution*

Starch samples intended for bright field microscopy imaging were suspended to 0.01wt% in anhydrous ethanol and sonicated in an ultrasonicator bath (Cole-Parmer, 115V) for twenty minutes to break up aggregates. A 200 μL volume of sonicated solution was subsequently deposited on a microscope slide, blown dry with nitrogen, and imaged on a Zeiss Axiovert 200M microscope. Brightfield images were converted to a binary mask using ImageJ software, followed by editing of the binary photo to separate aggregate particles. The edited photos were then used to calculate area using the "analyze particles" algorithm in ImageJ, from which individual particle diameters were calculated assuming a perfectly spherical particle. Three microscope slides were prepared and analyzed for each sample and the results combined for presentation, with error bars representing the standard deviation of all particles analyzed (n=100-150).

2.3 Tunability of the PGX Operating System

2.3.1 *PGX-Processed Starch Polymers*

A set of experiments was conducted on the PGX system to determine the effects of varying different processing parameters on the polymer morphology obtained. Starch was selected as the primary biopolymer to study in these experiments, based on its ready availability, with the potential for different chain structures at a low cost.

Starch is a naturally-sourced carbohydrate, derived from cereal crops like corn, potato, and pea, that is a co-polymer of linear amylose and highly branched amylopectin, with monomer units connected through α-1,4-glycosidic linkages, and branch-points stemming from the presence of α-1,6-glycosidic linkages [85]. However, native starches are unique in their ability to form water-insoluble semi-crystalline granule structures, composed of concentric, ordered arrays of alternating crystalline linear units and amorphous branched units, as shown in Figure 8.

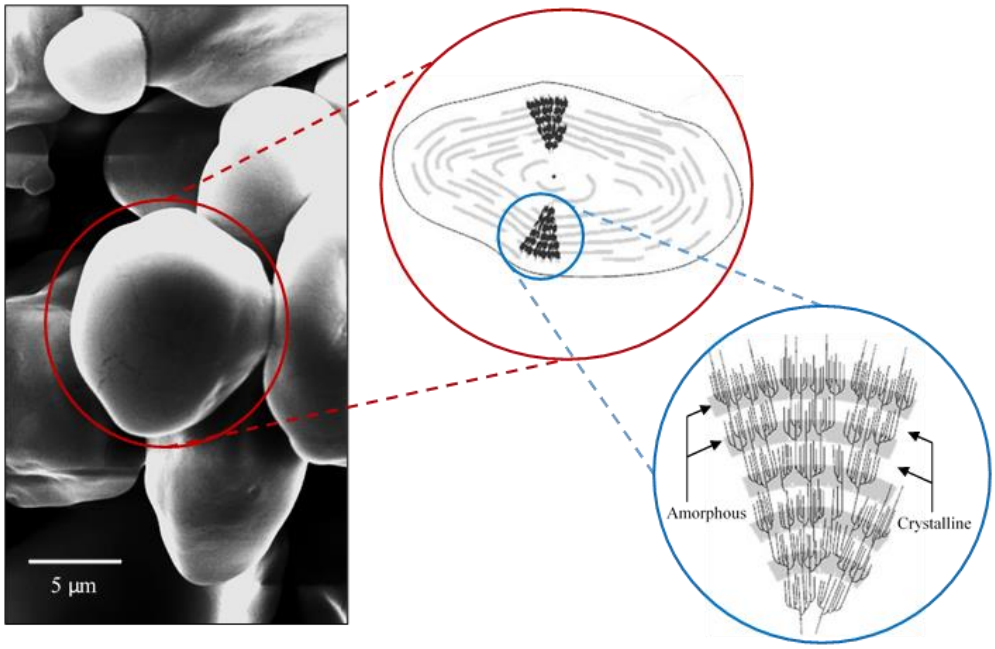

Figure 8: SEM Image of a starch granule with illustrations showing granule structure. Portions of this image were reproduced from [86].

Such granules may range from 1-100 µm in diameter, depending on their source [87], and are only broken down through a process known as starch gelatinization. To induce gelatinization, starch granules must be suspended in water and heated to over 110^{o}C. This thermal treatment facilitates absorption of water into the granule, resulting in granular swelling, disruption of hydrogen bonding/molecular order, melting of crystalline components, and ultimate solubilization [88]. As the solubilized starch cools, it subsequently goes through the process of retrogradation by which the polymer chains reorganize/recrystallize back into a partially crystalline, gel-like structure. Based on the rate of cooling, the extent to which crystalline domains re-associate may be modified [89].

For PGX tuning experiments, the temperature and pressure within the PGX system were held constant at 40^{o}C and 100 bar, respectively. The dimensions of the coaxial nozzle remained constant, with a 1/8" injection hole into the collection vessel. The base experimental set-up for the system was defined by a CO_2 flowrate of 15 g/min, an EtOH flowrate of 45 g/min, an aqueous solution flowrate of 15 g/min and a polymer concentration of 10 wt%. The mixing chamber size (defined as the distance from the tip of the inner coaxial tube to the injection hole) was set by screwing on the nozzle cap until it contacted the inner coaxial tube (0 mm mixing distance) and then turning it back one full turn (1/8" mixing distance).

The resulting polymer morphologies were characterized using four quantitative metrics (bulk density, particle size, specific surface area, and pore volume) in addition to their qualitative appearance, as assessed via both photography and brightfield microscopy.

2.3.1.1 Effect of Mixing Distance on Polymer Morphology

A series of processing runs were conducted to determine the effect of mixing chamber size and mixing distance on polymer morphology by manually adjusting the tightness of the nozzle cap on the coaxial injection tubes, as shown in Figure 9. Trials were conducted according to the method described in section 2.2.2.6 using three different mixing distances, or "gaps", ranging from 1/16" to 3/16". Upon removal of the precipitated samples from the collection vessel, process efficiencies (defined as the amount of dried polymer obtained relative to the initial amount of polymer pumped into the system in aqueous solution) and bulk densities were measured gravimetrically, with the results shown in Table 3.

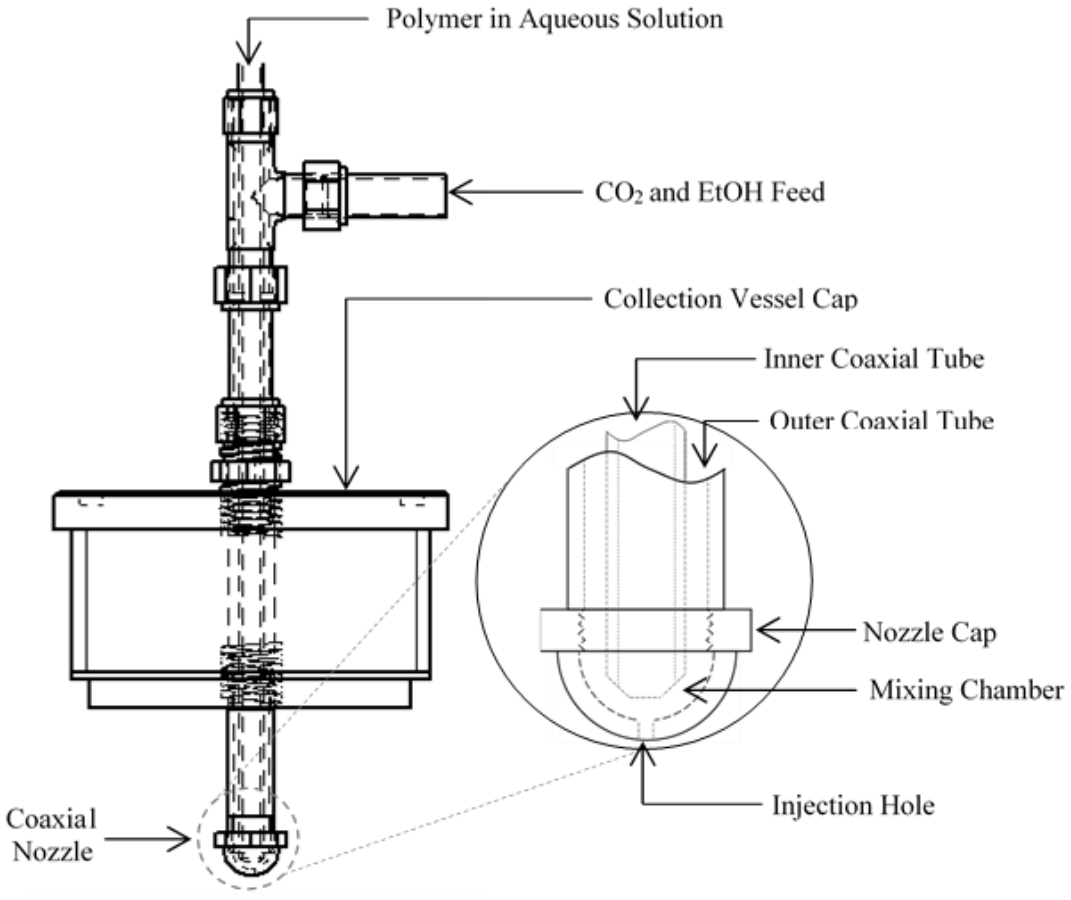

Figure 9: Schematic diagram of the coaxial nozzle on the PGX collection vessel with emphasis on the mixing chamber and injection hole.

Table 3: Process efficiencies and bulk densities of PGX-processed starch samples with varying gap size

Sample ID	Mixing Distance	Process Efficiency	Bulk Density (mg/mL)
Small Gap	1/16”	38%	50 ± 1
Base Method	1/8”	50%	47 ± 1
Large Gap	3/16”	50%	38 ± 1

To better analyze particle size and shape, samples were photographed and examined under a brightfield microscope. Visually, all processed starch samples were observed as non-spherical particles, with an apparent increase in void volume for samples processed with larger mixing distances, as shown in Figure 10. These images were subsequently analyzed in ImageJ, particle area was determined, and an average particle diameter was calculated based on the assumption of a spherical particle as shown in Figure 11 and Figure 12.

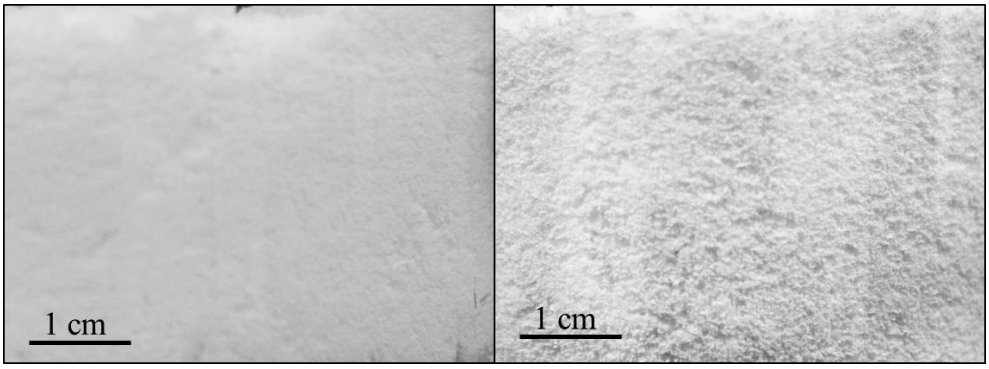

Figure 10: Photographs of corn starch after PGX-processing with either a 1/6" mixing distance (left) or a 3/16" mixing distance (right).

.

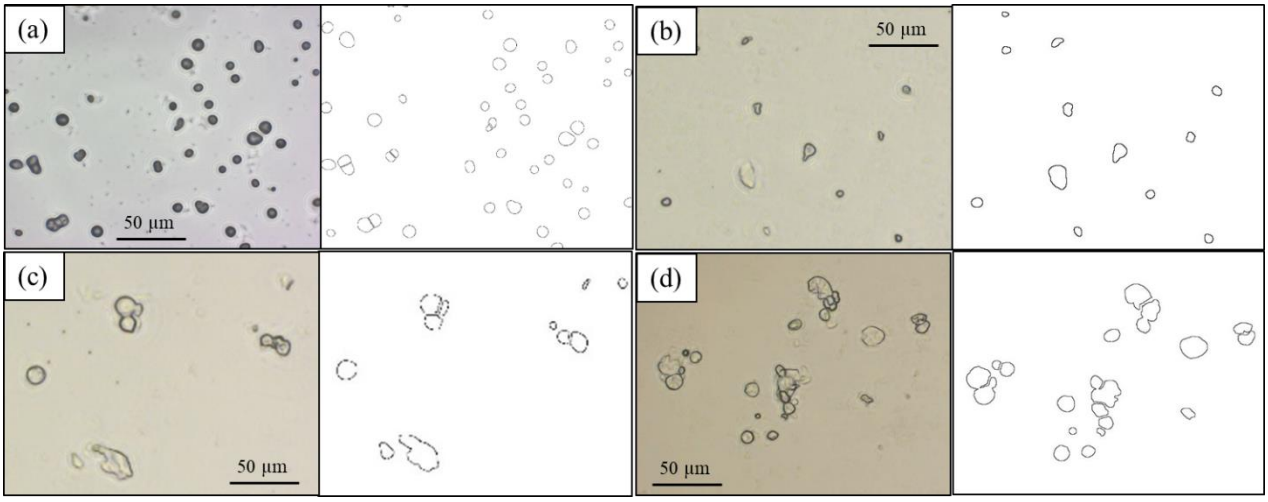

Figure 11: Bright field microscopy images (left) and ImageJ processed photos for analysis of particle size (right) of starch morphologies generated with varying mixing distances: (a) Unprocessed starch, (b) 1/16" mixing distance, (c) 1/8" mixing distance, (d) 3/16" mixing distance.

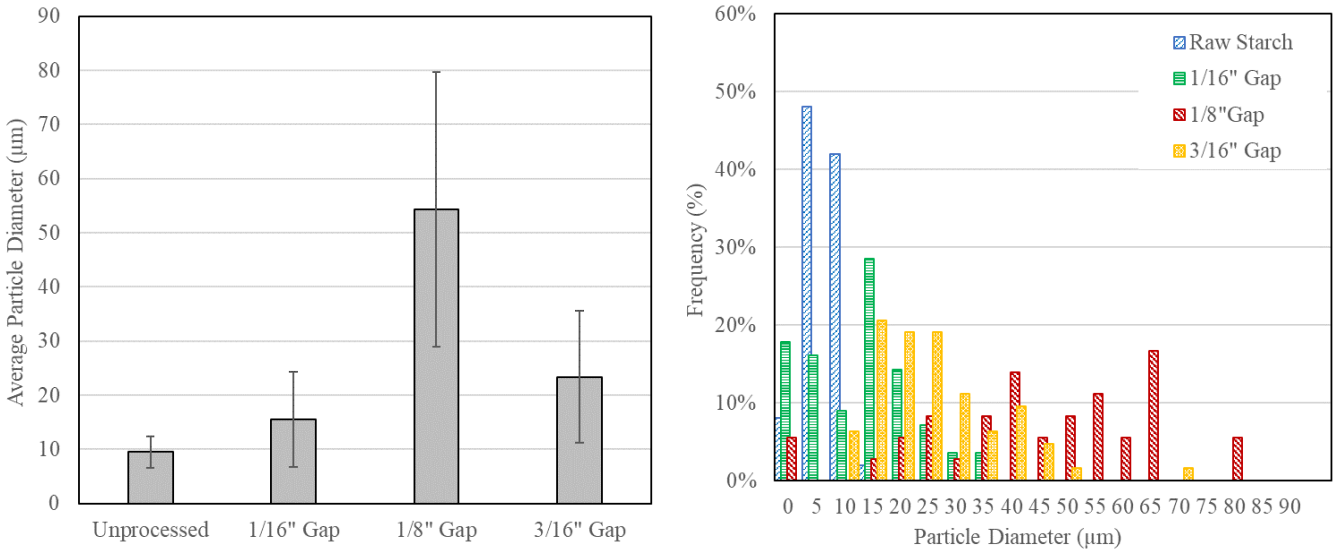

Figure 12: Average particle diameters (left) and particle size distributions (right) of starch samples PGX-processed with varying gap sizes.

While the unprocessed starch particles are generally spherical and well-dispersed, all of the PGX-processed samples appear as aggregates of smaller particles, with very large particle size distributions. Interestingly, samples processed with a large nozzle gap (3/16" mixing distance) also appeared to have smaller average particle sizes than those processed using the base method (1/8" mixing distance). For particulate samples in the PGX system, their size and size

distributions are largely dependent on the turbulence within the mixing chamber and shear forces within the nozzle cap. Since the nozzle cap is somewhat conical in shape, the diameter of the mixing chamber will increase as the mixing distance is increased, increasing the Reynold's number and therefore, the turbulence. In this case, it is hypothesized that more turbulent mixing regimes would result in more rapid mixing with anti-solvent, precipitating the polymer out of aqueous solution faster and thus generating smaller aggregate particles. In contrast, when the nozzle cap is installed more tightly on the coaxial tubes, the shear forces will increase as the polymer passes at higher velocities through the mixing chamber and injection hole. These shear forces are potentially high enough to micronize the polymer, resulting in generally less-aggregated particles with a more consistent particle size distribution.

Specific surface area and total pore volume (for pores <1582 Å radius) were also collected for these samples on a per mass basis, with the results shown in Figure 13.

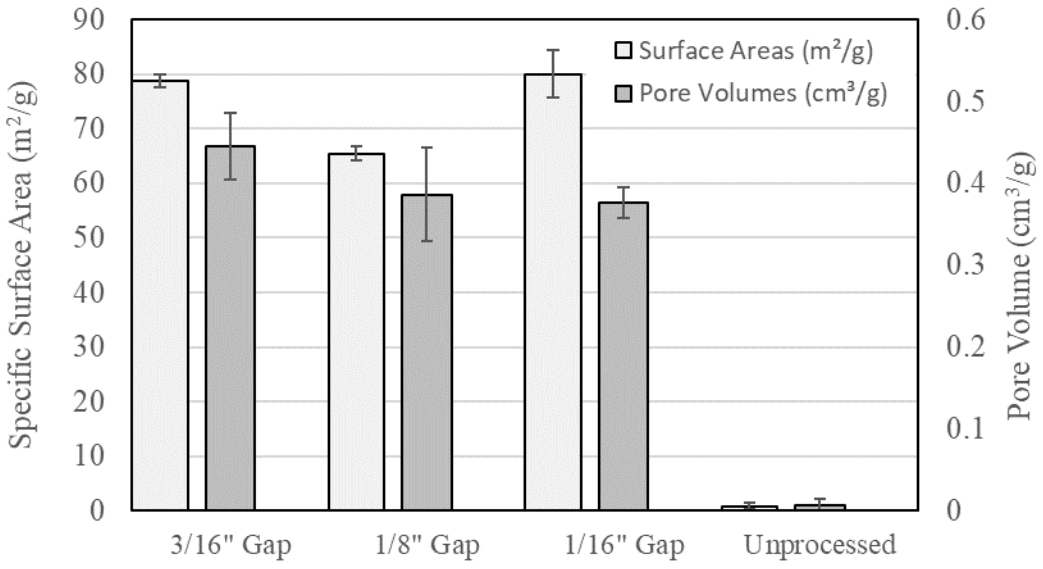

Figure 13: Measured specific surface areas (m^2/g) and pore volumes of PGX-processed starch samples with nozzle gap sizes of 1/16", 1/8", and 3/16"

Assuming particles are relatively spherical with homogeneous densities, their surface areas should increase as the square of the diameter, while their volume (and thus mass) should increase as the cube of diameter. As such, it was hypothesized that smaller particles with little-to-no porosity should have significantly larger surface areas when normalized for mass. This hypothesis was reflected in the BET data, where the smaller particles from trials conducted with gap sizes of 1/16" and 3/16" resulted in significantly higher surface areas, despite relatively consistent pore volumes between all three processed samples.

2.3.1.2 *Effect of Operating Point on Polymer Morphology*

Solvent flow ratios within the PGX system were varied to determine the effect of operating point on final polymer morphology. This change in the mole fraction of fluid components within the vessel was expected to affect variables like density and viscosity, which decrease with increasing CO_2 content, as well as the solubility of aqueous solutes, which decrease with increasing EtOH mole fraction. Processing runs were attempted at three different operating points: the standard PGX operating point (20 mol% H_2O, 60 mol% EtOH, 20 mol% CO_2), operating point #1 (10 mol% H_2O, 80 mol% EtOH, 10 mol% CO_2), and operating point #2 (30 mol% H_2O, 40 mol% EtOH, 30 mol% CO_2), as shown in Figure 14. It was hypothesized that operating point #1 would provide an aggressive mixing regime to precipitate the polymer with smaller/less aggregated features, while operating point #2 would allow for faster pumping of aqueous solution, but was expected to result in the coalescence of precipitated features, resulting in larger aggregates.

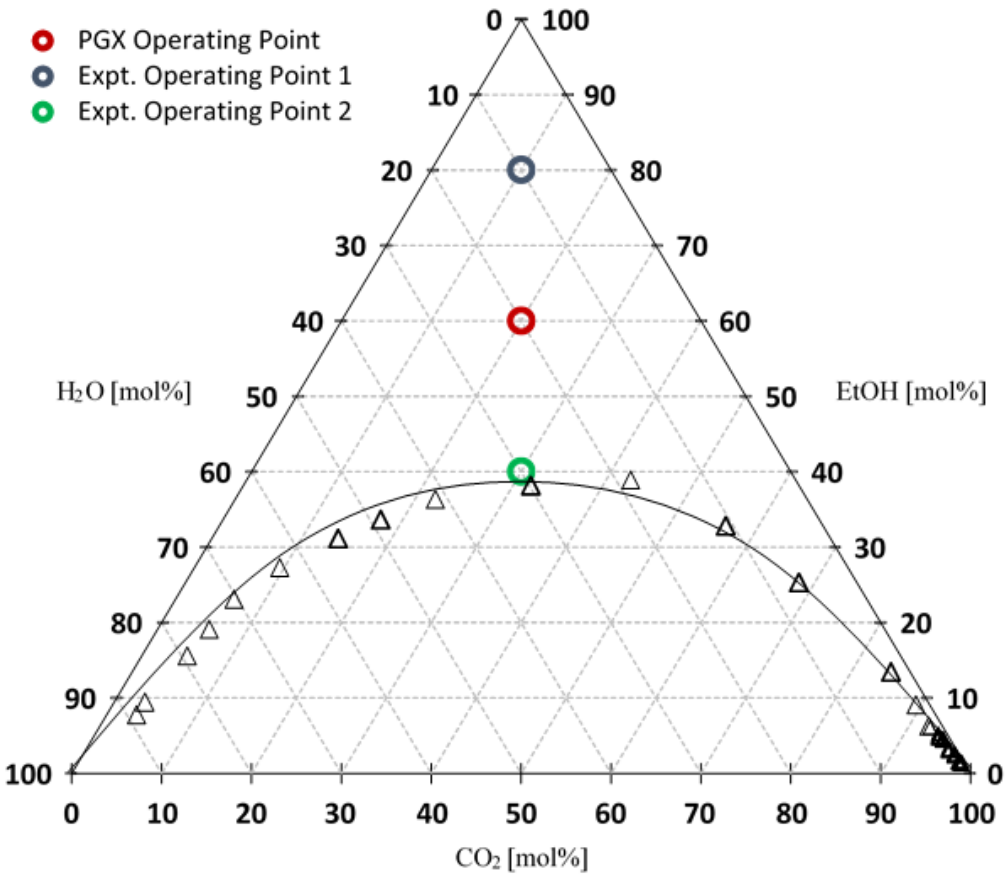

Figure 14: Ternary phase diagram showing the flow ratios corresponding to each experimental operating point at 100 bar and 40°C. Phase data obtained from Durling et. al. [84].

Samples processed at all three operating points were collected and analyzed gravimetrically to determine process efficiency (i.e. PGX-processed polymer obtained relative to polymer initially pumped into the system) and bulk density, as displayed in Table 3. In addition, samples were photographed to visually compare the void volume and sample texture, with results shown in Figure 15. Process efficiencies and bulk densities recorded for the three different operating points failed to exhibit substantial differences between trials, but visual distinctions in packing density were observed, with operating point #1 appearing to consist of smaller and/or less aggregated particles than operating point #2.

Table 4: Process efficiencies and bulk densities of PGX-processed starch samples produced with varying co-solvent mole fractions.

Sample ID	Mol% H_2O	Mol% EtOH	Mol% CO_2	Efficiency	Bulk Density (mg/mL)
Operating Point #1	10	80	10	63%	53 ± 1
Base Method	20	60	20	51%	47 ± 1
Operating Point #2	30	40	30	62%	45 ± 1

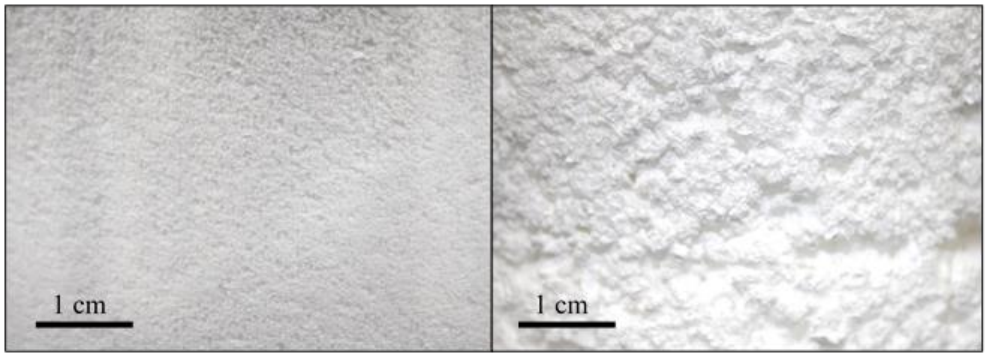

Figure 15: Photographs of corn starch after PGX-processing at either operating point #1 (left) or operating point #2 (right).

To further elucidate the sample structure and its correlation to operating point, samples were imaged on a bright field microscope to observe particle size and aggregation tendencies. Images collected from the microscope were subsequently analyzed using ImageJ software to calculate an average particle area, from which average particle diameters were calculated based on the assumption of a spherical particle. Bright field microscopy images are displayed in Figure 16 and calculated particle diameters compared in Figure 17.

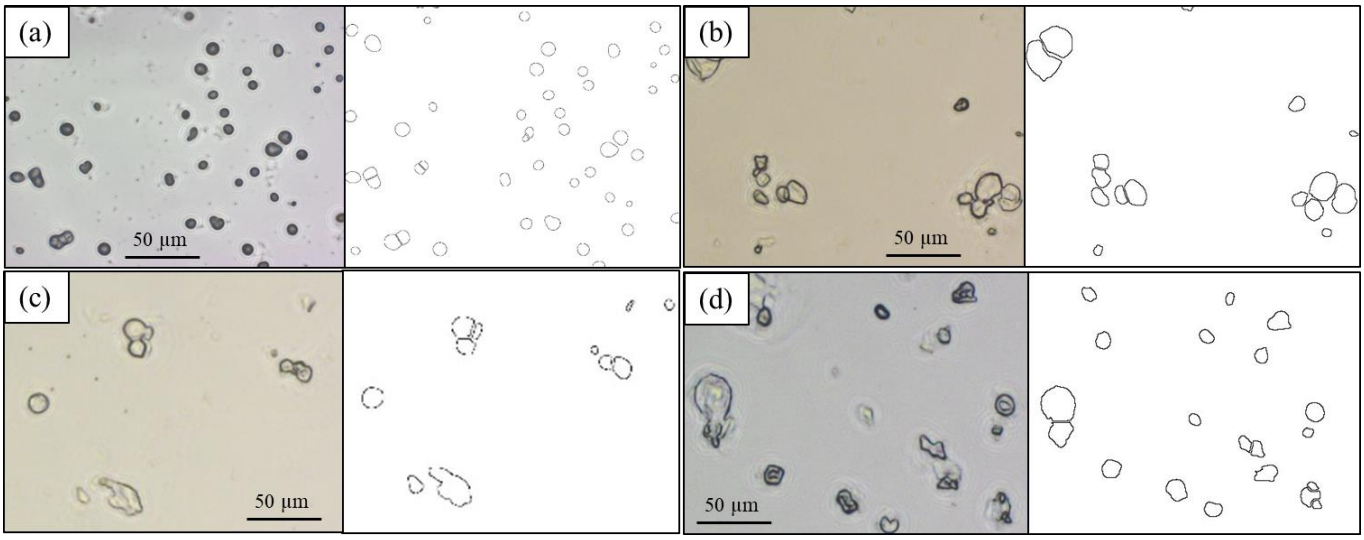

Figure 16: Bright field microscopy images (left) and ImageJ processed photos for analysis of particle size (right) of starch morphologies generated with varying solvent mole fractions: (a) unprocessed starch, (b) operating point #1, (c) base method, (d) operating point #2

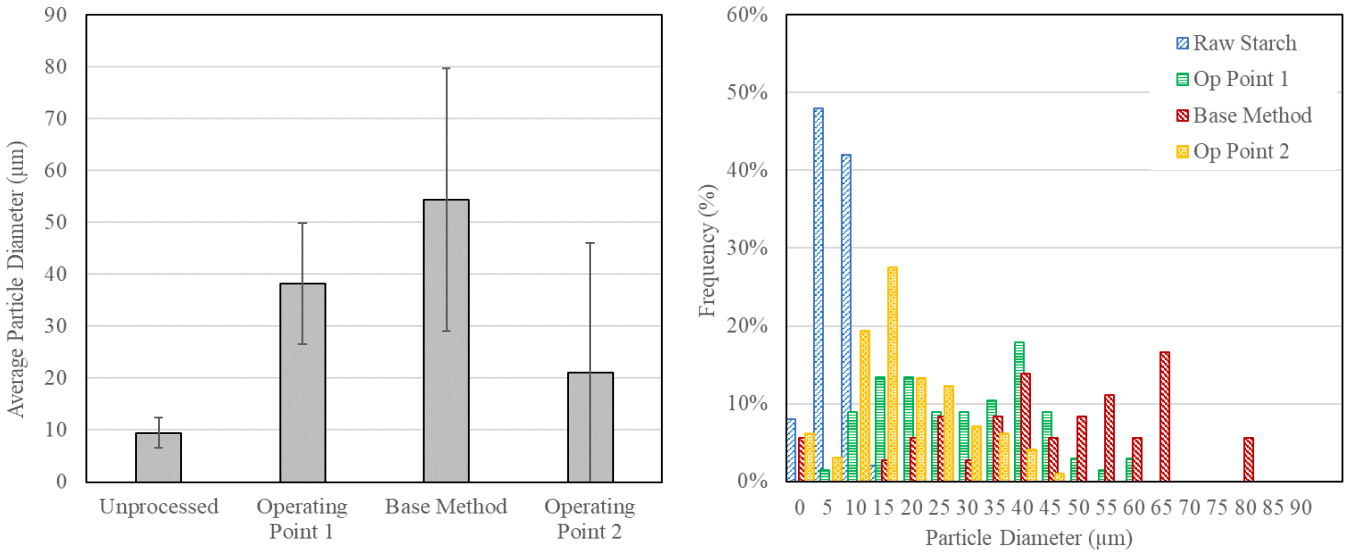

Figure 17: Average particle diameters (left) and particle size distributions (right) of PGX-processed starch samples with varying co-solvent molar ratios (where operating point #1 is 10:80:10 H_2O:EtOH:CO_2, base method is 20:60:20 H_2O:EtOH:CO_2, and operating point 2 is 30:40:30 of H_2O:EtOH:CO_2)

Several conclusions can be made based on the analysis of these images. First, changes in the mixing and precipitation mechanisms from varying the co-solvent ratios between operating point #1 and operating point #2 do not generate statistically different particle sizes in starch. However, operating point #2 has a significantly higher incidence of particle coalescence and,

therefore, aggregation after passing through the nozzle, which results in larger void space when aggregated particles are packed in a container together. The coalescence observed in samples processed at operating point #2 was attributed to the larger molar ratios of water present in the ternary co-solvent system, facilitating a small residual solubility of the polymer in the single-phase gas expanded liquid solution once it had entered the vessel. This residual solubility allows for a softening of polymer at particle interfaces, resulting in the eventual attachment of particles as the water is flushed from the system and complete precipitation is achieved.

Specific surface area and total pore volume (for pores <1582 Å radius) measurements were also collected for these samples on a per mass basis, as shown in Figure 18.

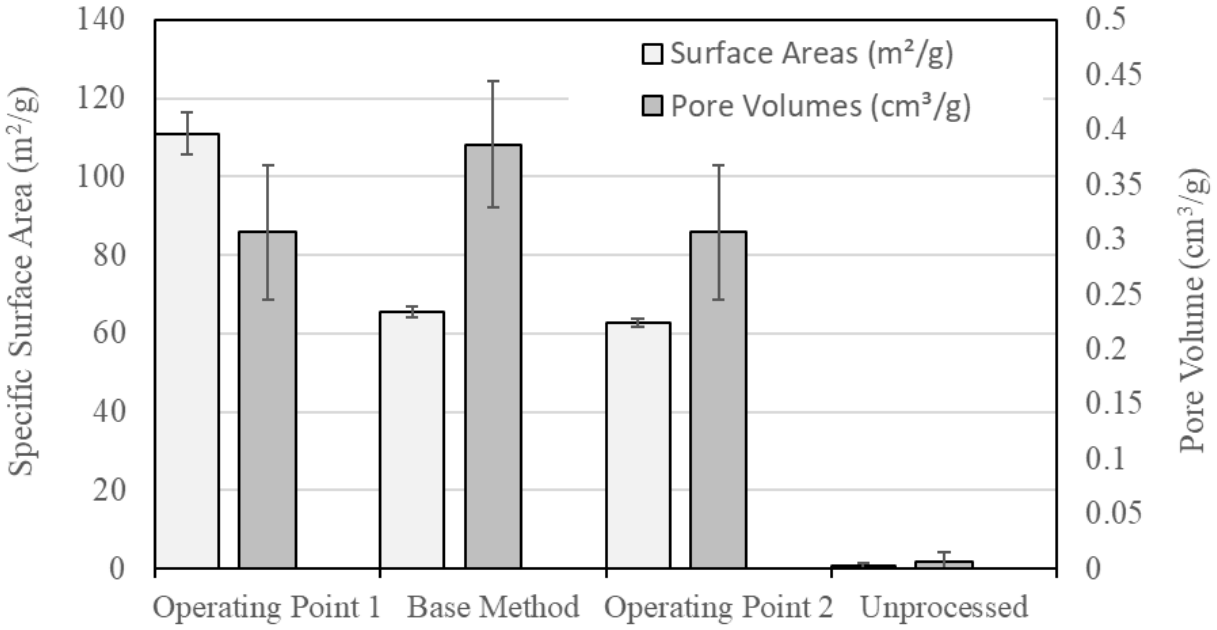

Figure 18: Measured specific surface areas of PGX-processed starch samples with varying molar ratios of co-solvent (where operating point #1 is 10:80:10, base method is 20:60:20, and operating point #2 is 30:40:30 of H_2O:EtOH:CO_2)

At operating point #1, the ternary solvent system was located well outside of the two-phase conditions and consisted of a high concentration of anti-solvent. This operating point was expected to induce aggressive precipitation (due to the increase in EtOH mole fraction) with

more turbulent flow regimes (due to lower CO_2 mole fractions and thus decreased volumetric expansion, increased fluid density, and decreased fluid velocity). In contrast, operating point 2 was located almost inside the two-phase condition, driving less aggressive precipitation as well as decreased turbulence within the mixing chamber. These theories are reinforced by the surface area data, with samples processed at operating point #1 displaying a significantly higher surface area than those collected using the base method and operating point #2. However, no statistical difference in pore volume was observed between the three trials. We hypothesize that these results stem from a combination of factors that occur during processing, samples processed at operating point #1 consisting of particles with a more uniform size and shape, explaining their higher specific surface areas and ability to pack more tightly in a bulk container, while samples processed at operating point #2 do not appear to precipitate fully in the vessel, causing particle coalescence to occur and lowering the overall surface area of the polymer.

2.3.1.3 *Effect of Polymer Molecular Weight on Polymer Morphology*

Additional experiments were conducted to understand the effect of inherent material properties on the generated PGX-processed morphologies. Of particular interest was the effect of polymer molecular weight on the resulting polymer structure. These experiments were conducted by degrading starch from its initial molecular weight as described in sections 2.2.2.2. The apparent viscosity was measured using the Herschel-Bulkley model (R^2 >0.99) and the viscosity-average molecular weights calculated using the Mark-Houwink equation. Relative molecular weights and associated processing metrics are displayed in Table 5.

Table 5: Viscosities, relative molecular weights, process efficiencies, and bulk densities of PGX-processed starch samples PGX-processed before and/or after degradation.

Sample ID	Viscosity ($Pa{\cdot}s \times 10^3$)	Relative Molecular Weight	Process Efficiency	Bulk Density (mg/mL)
Non-Degraded Starch	45.7	MW_1	50%	47 ± 1
Degraded Starch	4.7	$(0.10)MW_1$	65%	48 ± 1
Most Degraded Starch	0.23	$(0.005)MW_1$	18%	98 ± 6

Initially, it was noted that the degraded materials had significantly lower process efficiencies. It is hypothesized that this resulted from the generation of much smaller particles which were able to pass through the filter pads at the bottom of the collection vessel. Furthermore, degraded starches showed higher bulk densities, indicating the presence of smaller particles with the ability to pack much more tightly together. To verify these observations, starch samples were photographed to examine void space, and inspected using a brightfield microscope, as shown in Figure 19 and Figure 20. Particle diameters were calculated using brightfield microscopy images and the results are presented in Figure 21.

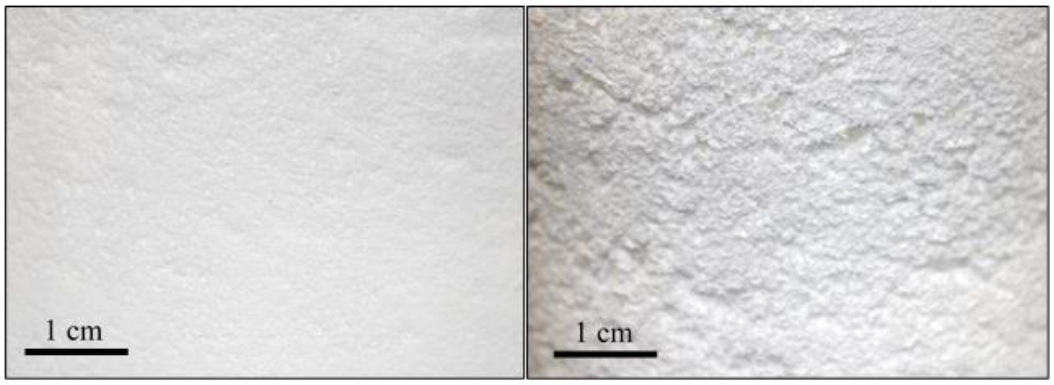

Figure 19: Photographs of degraded/low-molecular weight (left) and non-degraded (high-molecular weight (right) corn starch after PGX-processing.

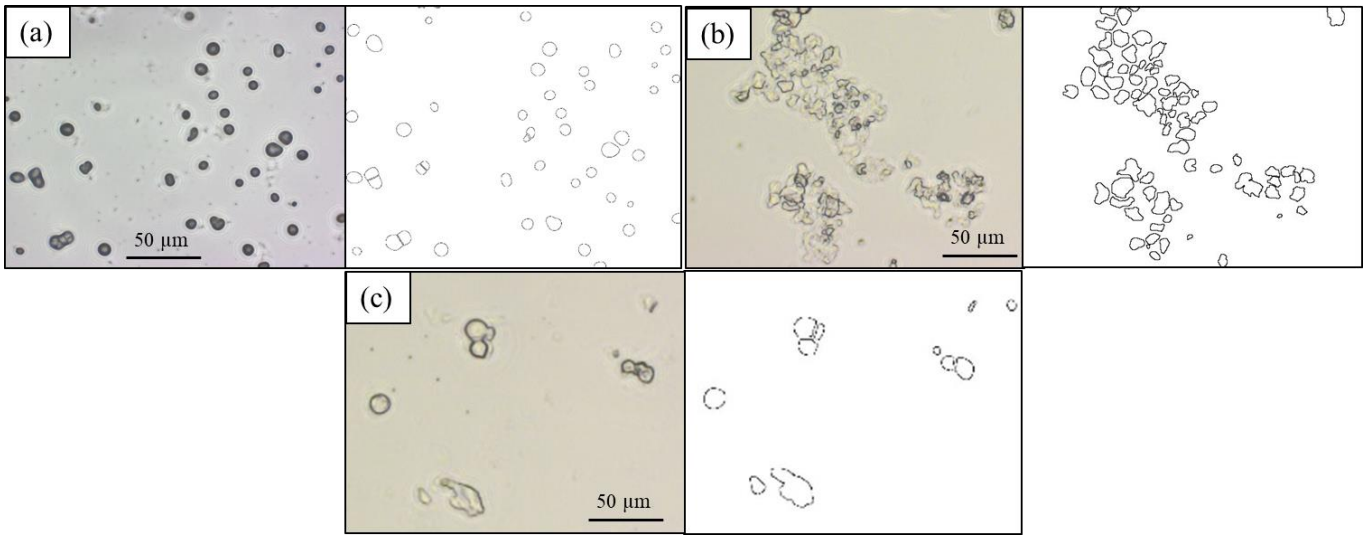

Figure 20: Bright field microscopy images (left) and ImageJ processed photos for analysis of particle size (right) of morphologies generated from: (a) Unprocessed, (b) Most Degraded, (c) Non-Degraded

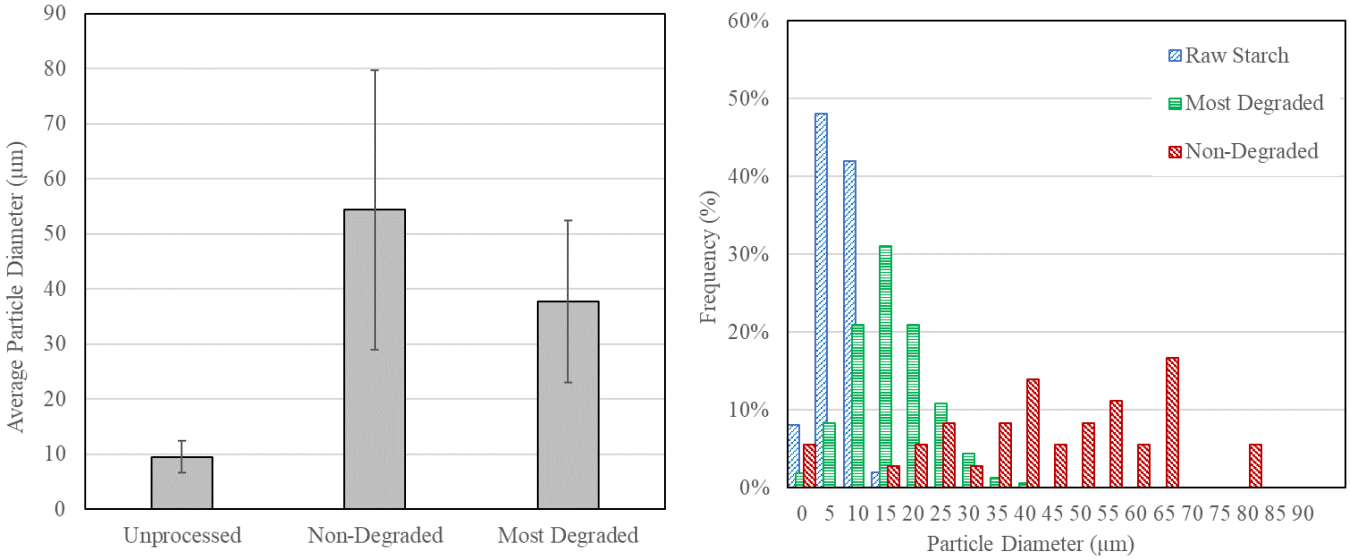

Figure 21: Average particle diameters (left) and particle size distributions (right) of PGX-processed starch samples with varying molecular weight (where non-degraded = base method).

Consistent with earlier observations, these results indicate that degraded samples form smaller particles as they are precipitated in the PGX-system. It is expected that this decrease in particle size is due to two mechanisms. First, the decrease in viscosity of the aqueous feed in the lower molecular weight polymers would result in an increase in turbulence through the nozzle, likely creating a more aggressive mixing and precipitation regime. Second, the ability of shorter-

chain molecules to form highly ordered granules during retrogradation is significantly hindered, likely causing polymer chains to remain more disperse in solution.

To observe the effect of molecular weight on pore volume and surface area, BET data was collected, as shown in Figure 22.

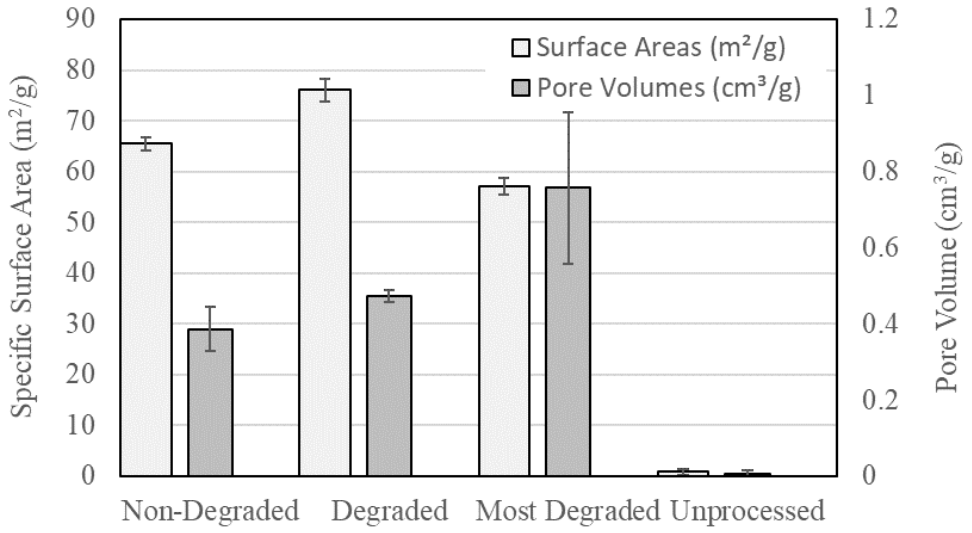

Figure 22: Measured specific surface areas of PGX-processed corn starch with varying molecular weight

From this data it is apparent that the measured specific surface areas from high molecular weight starch samples originated primarily from the external surface of particles and not from extensive internal porosity. In contrast, the low molecular weight samples appear to have extensive internal pore volume in addition to smaller particle sizes. The structural differences observed for degraded samples were hypothesized to be the result of a decrease in intramolecular bonding due to shorter chain lengths and, hence, less ordering of crystalline and amorphous regions during retrogradation.

2.3.1.4 *Effect of Polymer Concentration on Polymer Morphology*

A set of processing runs were conducted to determine the effect of polymer concentration on the PGX-generated morphology. Runs were conducted by adjusting the initial concentration

of polymer in aqueous solution to 0.5 and 1.5 times that of the base method. Samples processed at all three concentrations were collected and analyzed gravimetrically to determine process efficiency and bulk density, as displayed in Table 6. In addition, samples were photographed to visually compare the void volume and sample texture, as shown in Figure 23.

Table 6: Process efficiencies and bulk densities of PGX-processed starch samples produced with varying polymer concentrations in the aqueous feed.

Sample ID	Concentration	Process Efficiency	Bulk Density (mg/mL)
Starch Low Concentration	5 g/mL	31%	50 ± 2
Starch Base Method	10 g/mL	50%	47 ± 1
Starch High Concentration	15 g/mL	57%	47 ± 1

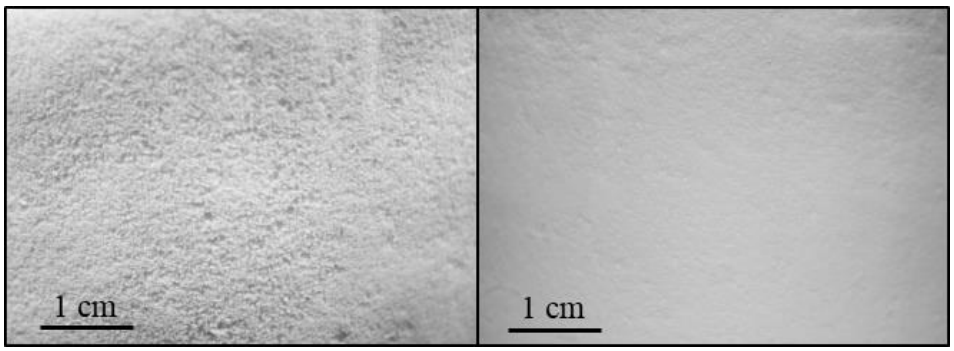

Figure 23: Photographs of PGX starch that has been processed at high concentration (15 g/mL) on the left and low concentration (5 g/mL) on the right.

Visually, the materials processed at a lower concentration appear more consistent and are made up of smaller particles than those processed at higher concentrations. It may also be noted that the process efficiencies decrease for these low concentration runs, again indicating that smaller particles are formed and subsequently passed through the filter pads at the bottom of the collection vessel. However, examination of starch samples under brightfield microscopy shows no statistical difference between the particle size in the low concentration and high concentration samples, illustrated by Figure 24 and Figure 25. As such, it may be concluded that the higher

void volumes and large particle sizes observed at higher processing concentrations are the result of aggregated particles that are loosely held together and, thus, broken up during the sonication step prior to imaging on the brightfield microscope.

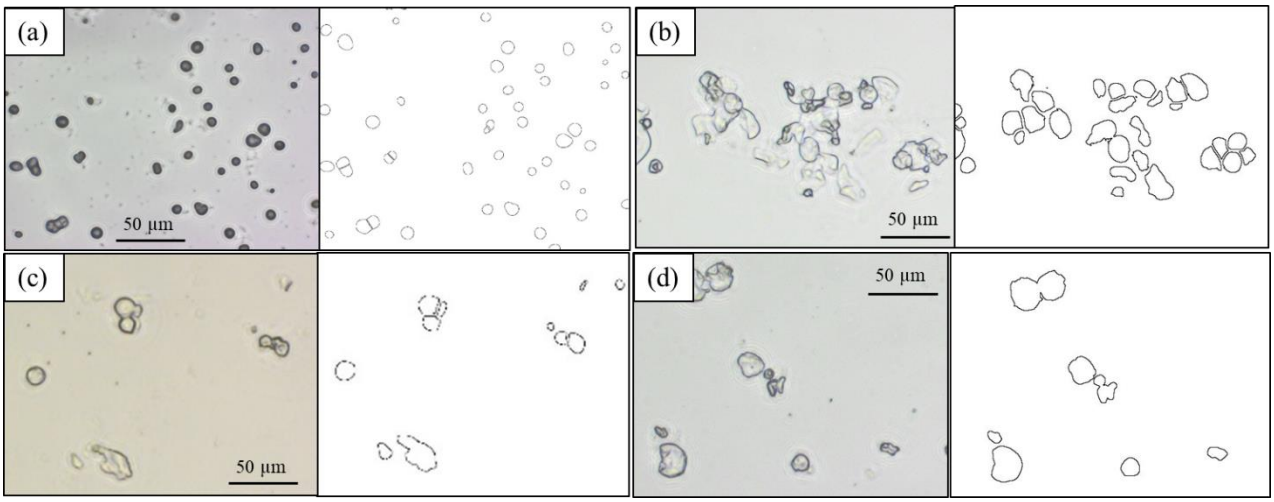

Figure 24: Bright field microscopy images (left) and ImageJ processed photos for analysis of particle size (right) of morphologies generated from starch at: (a) unprocessed, (b) low concentration (c) base method, (d) high concentration.

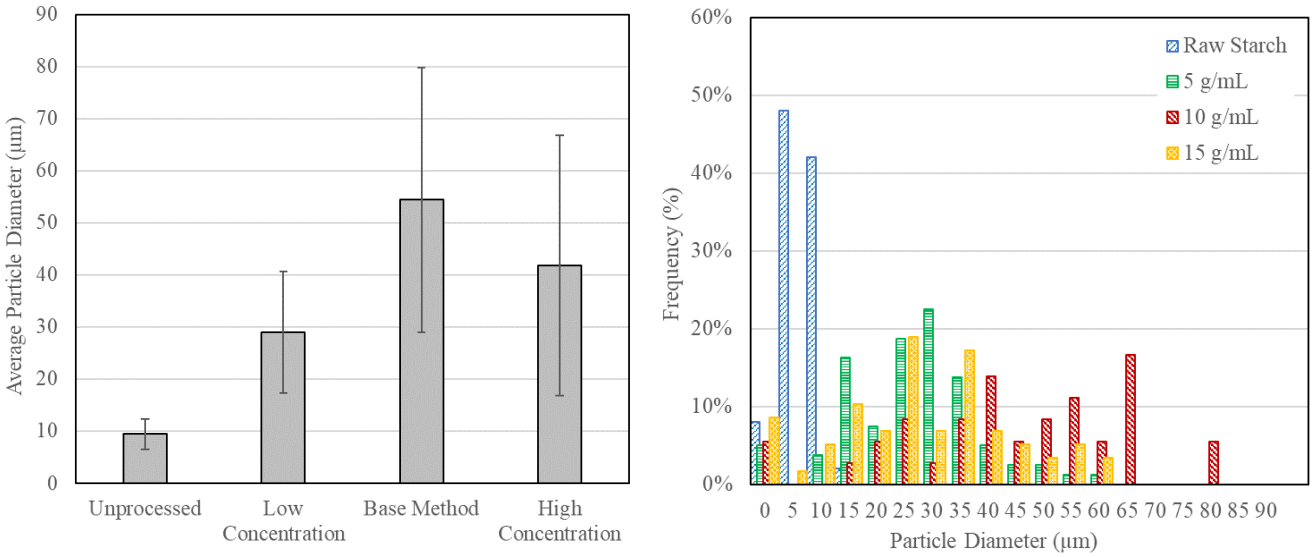

Figure 25: Average particle diameters (left) and particle size distributions (right) of starch that has been PGX processed at different concentrations in aqueous solution (low concentration = 5 g/mL, base method = 10 g/mL, high concentration = 15 g/mL)

It is hypothesized that the mixing regimes displayed by solutions with lower polymer concentrations will be more turbulent as a result of their lower viscosities. Furthermore, polymer

at lower concentrations is expected to be more dispersed in its initial solution (i.e. less polymer passing through the nozzle at any given time) and is expected to precipitate more rapidly than at higher concentrations, resulting in smaller particles. In contrast, higher concentrations are expected to precipitate more slowly as the result of a less turbulent flow regime, retaining water for a slightly longer period of time and exhibiting a heightened tendency to coalesce as they are deposited into the vessel. This theory could account for the aggregation observed in Figure 23 and the visual appearance of larger particle sizes in the sample processed at 15 g/min.

BET data showed that starch samples pumped at lower concentrations displayed lower overall surface areas despite their smaller particle sizes, indicating that the sample processed at a higher concentration must have substantial internal porosity to achieve a higher overall surface area. Indeed, the sample processed at a concentration of 15 g/min had significantly higher pore volumes than the samples processed at a concentration of 5 g/min, as seen in Figure 26. Depending on the number and diameter of these pores, the resulting difference in surface area could be substantial and account for the majority of the sample's surface area.

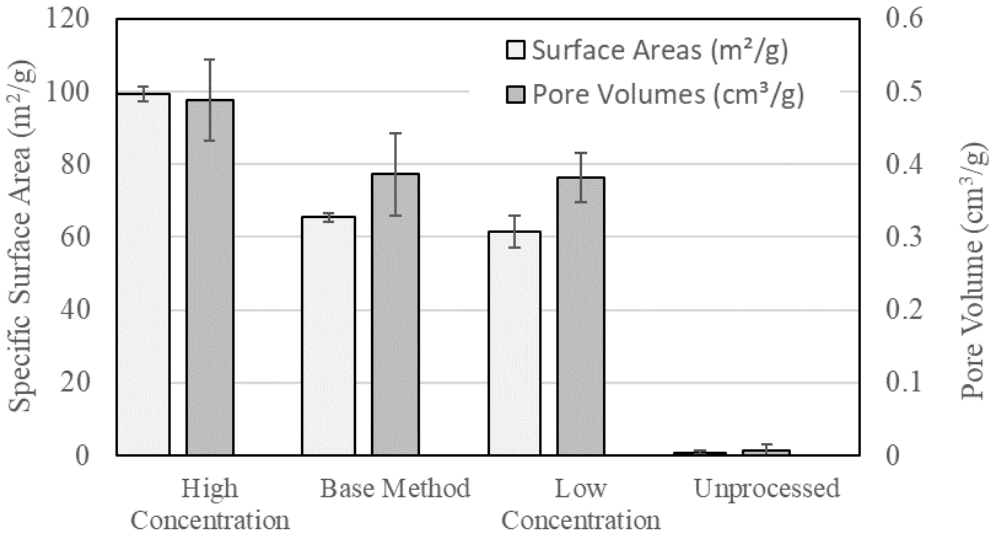

Figure 26: Measured specific surface areas of PGX-processed starch samples pumped at varying concentrations (where high = 15 g/mL, base method = 10 g/mL, and low = 5 g/mL)

2.3.2 *PGX Processing of Pectin*

For trials relying on the intrinsic properties of the polymer itself (i.e. the effect of polymer molecular weight and the effect of polymer concentration) PGX morphologies obtained from corn starch were compared to those observed by processing pectin at the same conditions. In contrast to corn starch, pectin is readily water-soluble at both moderately high temperatures (less than <100^{o}C) or in dilute acid (pH ≤ 3.6) and is primarily homopolymeric, consisting of linear repeating α-(1,4) linked D-galacturonic acid units with varying degrees of methyl esterification [90]. The carboxylic acid moieties on pectin form polyanions at neutral pH, resulting in a significant negative charge on low methoxy pectin due to the presence of larger ratios of carboxylate groups. Many of these low methoxy fibres are also partially amidated, allowing for both intermolecular and intramolecular acid-base or hydrogen bonding interactions in aqueous solution [91].

The use of pectin as a comparative tool stemmed from the similarity of its monomer structure to that of starch without the presence of highly-branched co-polymer units that self-assemble into organized crystalline regions. As a result, granule formation does not occur and the PGX-processed polymer morphologies are assumed to be largely related to processing conditions without the added variable of retrogradation kinetics. Furthermore, preliminary experiments involving the PGX-processing of pectin indicated that an interconnected fibrous morphology was generated as opposed to aggregated particles. Since this PGX-generated morphology was so distinct from that of starch, the effects of varying polymer concentration and polymer molecular weight were investigated to determine how the PGX morphology was affected and whether similar trends were observed for both starch and pectin.

All pectin trials were conducted with the same experimental set-up and process flowrates as the starch samples, with variations existing only in concentration and molecular weight. The resulting polymer morphologies were characterized using three quantitative metrics (bulk density, specific surface area, and pore volume) in addition to their qualitative appearance, as assessed via photography and SEM.

2.3.2.1 Effect of Molecular Weight on Polymer Morphology

Previously, PGX processed high molecular weight pectin had been shown to generate unique networks of highly-interconnected multi-scale fibres. Of particular interest to this study, was whether similar PGX morphologies would exist for lower molecular weight samples, and if trends would agree with those observed for starch. Pectin materials were degraded according to methods described in 2.2.2.4, with the resulting relative molecular weights calculated experimentally according to 2.2.2.5 and shown in Table 7 along with the associated process efficiency and measured bulk density of each sample. Similar to degraded starch samples, PGX-processed low MW pectin exhibited a low process efficiency of 29%, which is hypothesized to be the result of smaller precipitates passing through the filter discs and into the waste.

Table 7: Viscosities, relative molecular weights, process efficiencies, and bulk densities of pectin samples PGX-processed with and without degradation.

Sample ID	Viscosity (Pa·s $\times 10^{-3}$)	Relative Molecular Weight	Process Efficiency	Bulk Density (mg/mL)
Non-Degraded Pectin	33.7	MW_P	78%	13 ± 1
Degraded Pectin	1.7	$(0.005)MW_P$	29%	27 ± 1

Visually, the presence of a fibrous network was maintained for both degraded and non-degraded pectin samples, but the morphologies of the fibres were significantly different. PGX processed low MW pectin consisted of smaller, “fluffier” and more evenly-distributed fibres,

while high MW PGX pectin appeared to create hierarchical fibres of varying sizes, as shown in Figure 27. Specific surface areas and pore volumes of these scaffolds were also measured and the results shown in Figure 28.

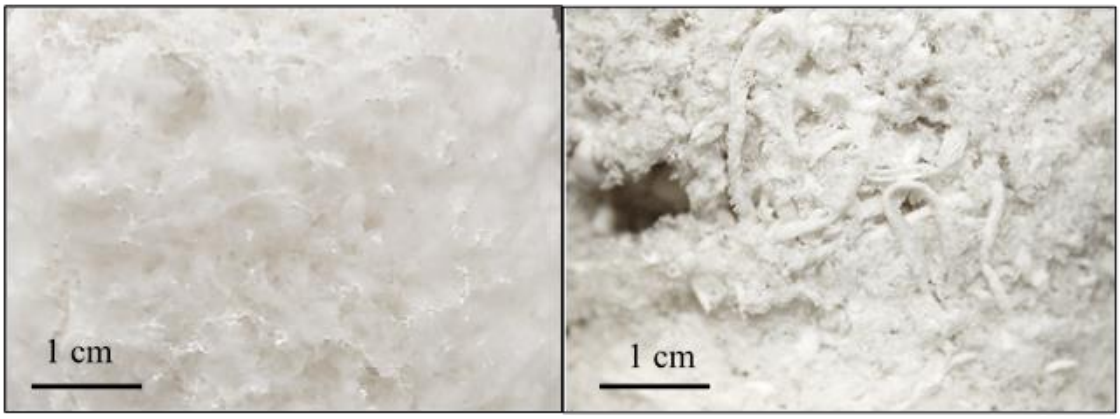

Figure 27: Photographs of PGX-processed pectin at: (a) low molecular weight/degraded, (b) high molecular weight/non-degraded.

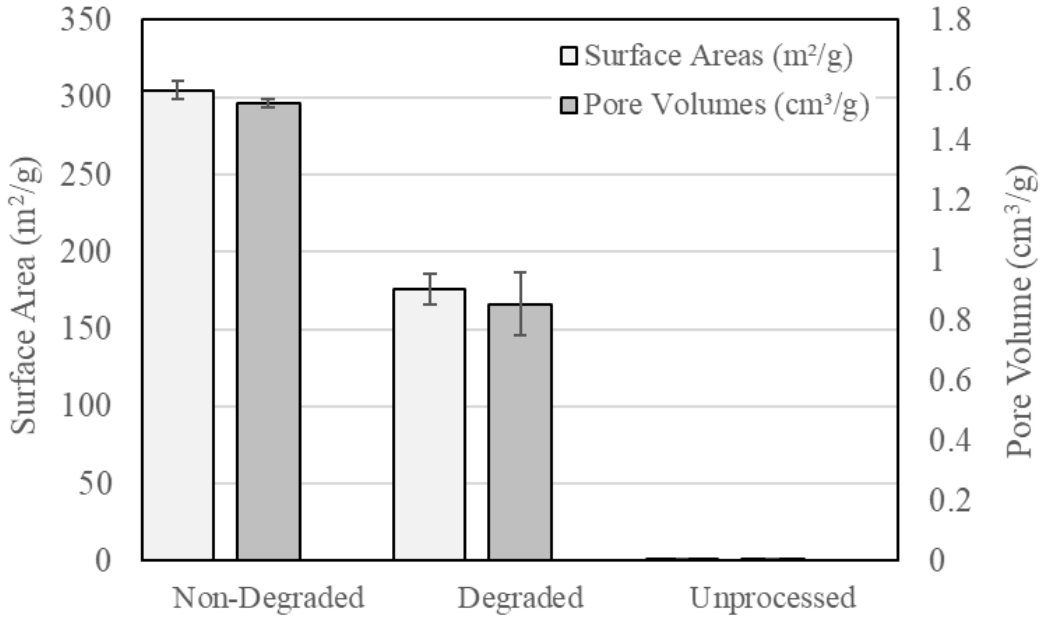

Figure 28: Measured specific surface areas and pore volumes of non-degraded and degraded PGX-processed pectin samples relative to unprocessed pectin.

Interestingly, the porosity of starch samples was shown in section 2.3.1.3 to increase with decreasing molecular weight, while pectin samples show a clear decrease in porosity after

degradation. This is hypothesized to be the result of more turbulent mixing regimes for degraded samples (due to their significantly decreased viscosity in solution), while the increased viscosity of the higher molecular weight polymers lowered turbulence and restricted the collapse of fibre structures upon drying to effectively increase the internal porosity of the sample. Similar to starch, the measured surface area of pectin decreases at lower molecular weights, which is thought to originate primarily from the decrease in internal pore volume and corresponding reduction in internal surface area.

2.3.2.2 *Effect of Polymer Concentration on Polymer Morphology*

A set of processing trials were conducted on pectin by adjusting the initial concentration of polymer in aqueous solution to 0.5 and 1.5 times that of the base method and observing the resultant changes in polymer morphology. In particular, samples processed at all three concentrations were collected and analyzed gravimetrically to determine process efficiency and bulk density (Table 8), and the visual appearance inspected through photography (Figure 29) and SEM (Figure 30).

Table 8: Process efficiencies and bulk densities of PGX-processed pectin samples produced with varying polymer concentrations in the aqueous feed.

Sample ID	Concentration	Process Efficiency	Bulk Density (mg/mL)
Pectin Low Concentration	2.5 g/mL	14 %	10 ± 1
Pectin Base Method	5 g/mL	31%	13 ± 1
Pectin High Concentration	10 g/mL	30%	15 ± 1

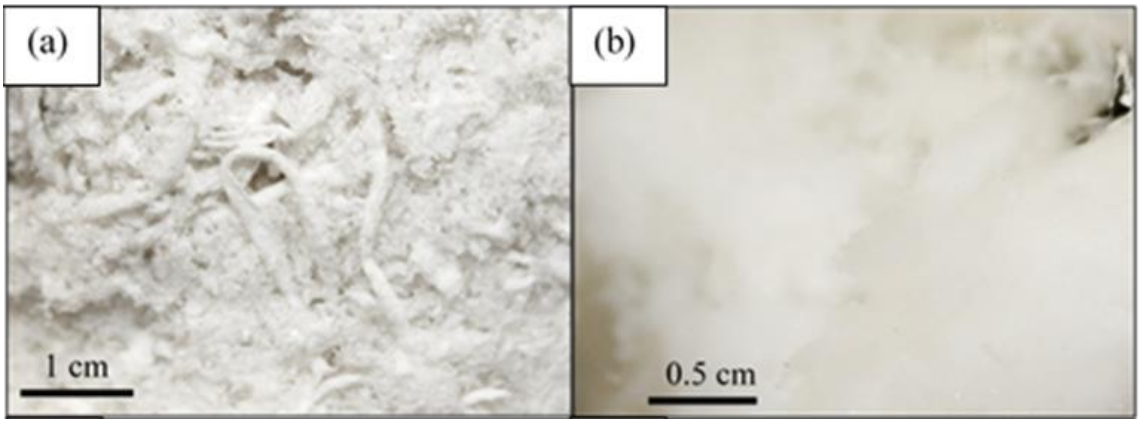

Figure 29: Photographs of PGX-processed: (a) Pectin at high concentration (10 g/mL), (b) Pectin at low concentration (2.5 g/mL)

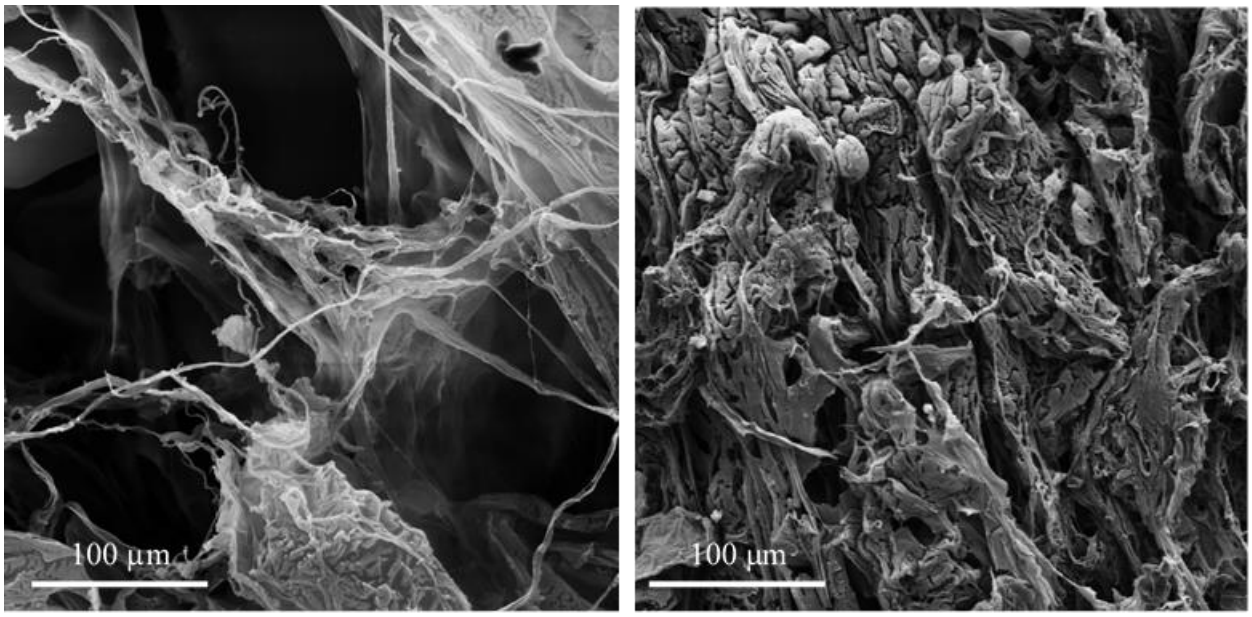

Figure 30: SEM images of pectin processed at low concentration (left) and high concentration (right)

Visual results were similar to those obtained in section 2.3.2.1, with the pectin sample pumped at low concentration (2.5 g/mL) exhibiting much smaller and more consistent fibres than the sample processed at a high concentration. SEM showed that low concentration samples consisted of fibres with diameters in the range of tens of microns, while the diameters of fibres from the high concentration sample consistently exceeded several hundred microns. Both

process efficiencies and bulk densities were decreased as the diameter of precipitated features decreased, consistent with previous results.

An analysis of BET data collected from these samples and shown in Figure 31 exhibited different trends than those observed in section 2.3.2.1, with pectin samples showing significantly higher total pore volumes when pumped at lower concentrations. However, total surface area remained constant within all pectin samples, either signifying the presence of pores larger than 1582 Å radius at higher concentrations (which would be unmeasurable via BET) or significantly lower internal porosity in samples pumped at higher concentrations.

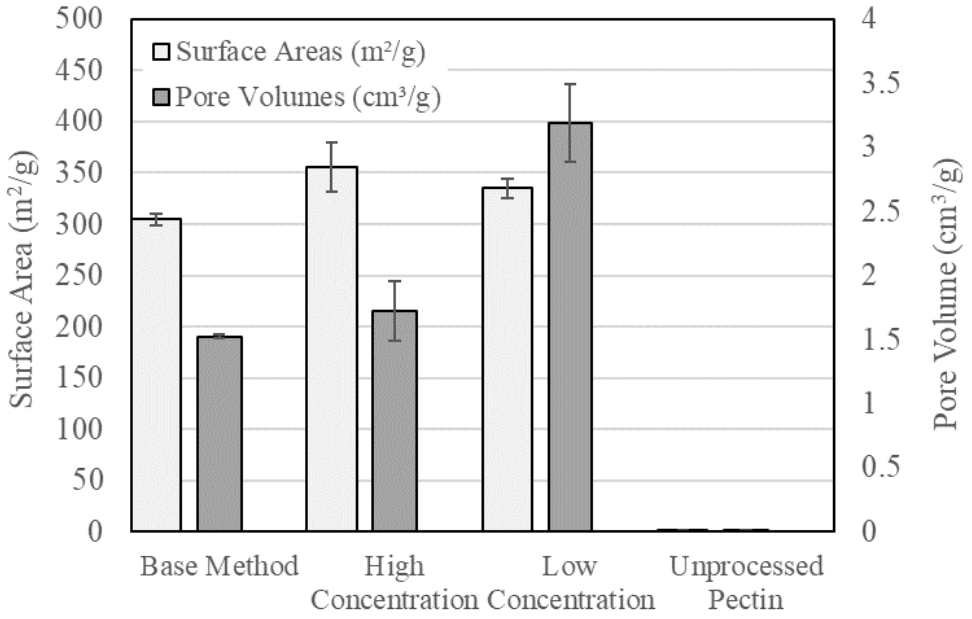

Figure 31: Measured specific surface areas of PGX-processed pectin samples pumped at varying concentrations (where high = 10 g/mL, base method = 5 g/mL, and low = 2.5 g/mL)

It is expected that the significantly larger pore volumes observed in the polymer sample processed at 2.5 g/mL are the result of a significantly more interconnected network structure than that observed in the low molecular weight materials processed in section 2.3.2.1, despite their comparable bulk densities. This concept would be consistent with the idea of a longer chain

length, where polymers at low concentration would be more dispersed in solution (with less solid per unit volume so smaller features formed on the timescale of solvent removal), but have a greater potential for physical entanglements and surface interactions as a result of its longer chain lengths. As such, pores would exist between the junction points of the polymer fibres as opposed to within the polymer fibres themselves.

The significantly higher pore volumes of PGX-processed pectin when compared to the starch samples examined in section 2.3.1 are thought to be the result of significantly decreased chain interactions in the precipitated state and the inability of pectin to tightly pack into crystalline regions like those found in a native starch granule.

2.3.3 *Conclusions*

In all cases, the average particle diameter of starch samples was shown to increase upon PGX processing while optical microscopy indicated that PGX-processed particles had more irregular shapes with higher transmittance of light. BET measurements reinforced these observations, showing significant increases in both surface area and pore volume after PGX processing. However, starch consistently formed particulate structures as opposed to interconnected networks, which is thought to be the result of moderated re-crystallization/retrogradation as the starch is re-precipitated in the collection vessel. While the presence of spherical starch granules is not observed to the same extent post-processing, the tendency to form particles indicates significant inter- and intramolecular bonding between starch molecules even after exfoliation in the PGX process. In contrast, pectin materials (which are not known to form granules or have significant intramolecular bonding mechanisms), successfully formed interconnected matrix structures, with fibre diameters somewhat dependent on

processing conditions, and consistently higher surface areas and pore volumes than starch processed at the same conditions.

It is nearly impossible to formulate conclusions about how these processing conditions affected polymer morphology by looking primarily at starch results, as the high driving force for starch to form semi-crystalline granule structures conflicted with the ability to isolate variables on the processing system. In order to fully elucidate the effects of these variables, additional trials would be required using a different polymer.

Chapter 3 Post-Processing Stabilization Methods for Chitosan and Alginate PGX-Morphologies

3.1 Introduction

The ultimate goal in using the PGX system for processing biopolymers is to stabilize the PGX-generated morphologies to obtain covalently/ionically-crosslinked aerogels or hydrogels for extended use in diverse applications. Stabilization of PGX-generated morphologies may be achieved by crosslinking polymer scaffolds through two different methods. The first requires a reconfigured PGX apparatus to allow for the co-extrusion of two aqueous feeds, co-delivering either two different polymers that participate in "click"-crosslinking chemistries, or one polymer and one or more crosslinker. This method can be highly advantageous, due to its efficiency and ability to generate sterile crosslinked products without additional crosslinking reactions, solvent exchanges, and/or time-consuming purification steps. However, the success of this method is dependent on the ability to tune gelation kinetics to achieve in situ crosslinking within the PGX collection vessel, as discussed in Chapter 5.

As such, in situ crosslinking reactions are not always achievable due to issues regarding reaction kinetics, solubility, temperature, or solvent incompatibilities of the polymer and/or crosslinker. In the case that polymer systems cannot be gelled in situ, post-processing stabilization methods may be pursued to maintain PGX-generated morphologies in the form of a structured macroporous hydrogels. These reactions must be conducted in a solid or partially-solubilized state, to not dissolve the PGX-generated networks, relying on unfavourable solvent systems or rapid gelation kinetics to preserve polymer structure. Gelation kinetics may subsequently be tuned to achieve a balance between the solubilization required to perform

effective crosslinking (with higher solubilities/slower gelation typically providing higher crosslinking efficiencies) and the preservation of the PGX-generated structure.

3.1.1 *Chitosan Structure and Properties*

Chitosan is the deacetylated product of chitin, a linear polysaccharide derived from crustacean exoskeletons. Similar to many carbohydrate polymers, the polymer backbone is composed of repeating hexose units with unique functional groups. In the case of chitosan, the polymer consists of repeating units of β-1,4 linked D-glucosamine, randomly interspersed with residual N-acetylglucosamine groups [92]. Depending on the source and preparation methods, polymer molecular weights typically range from 50 to 1000 kDa with degrees of deacetylation between 50 and 90% [93].

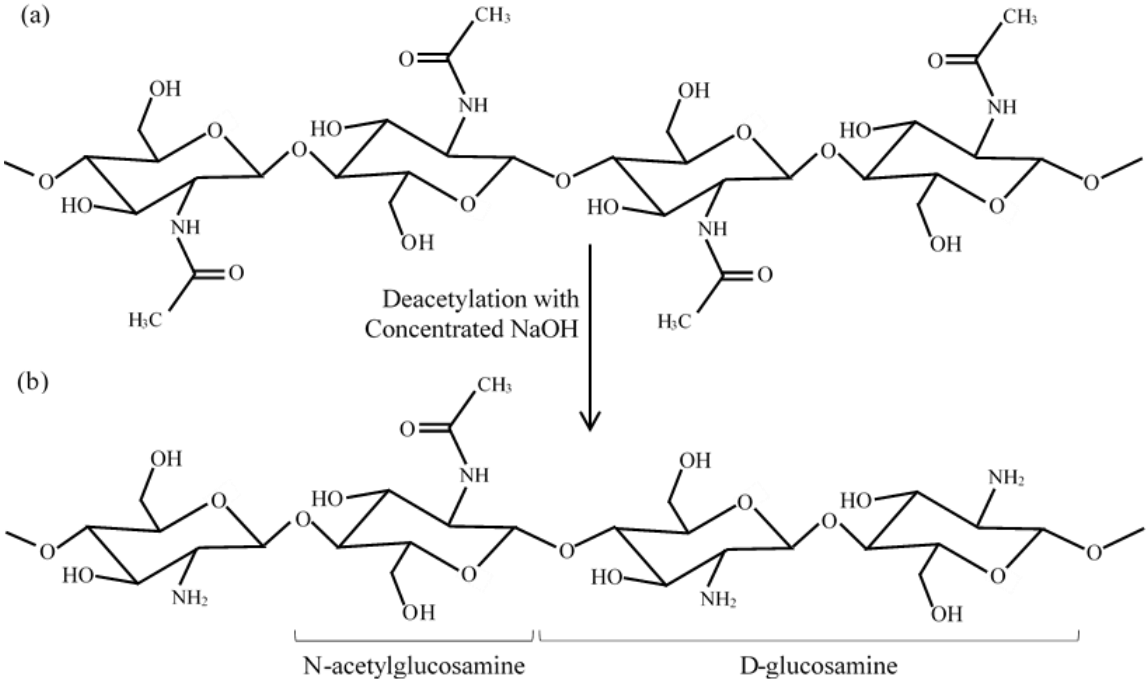

Figure 32: Chemical structure of (a) chitin, and (b) chitosan, the deacetylation product of chitin

Depending on the degree of deacetylation achieved, chitosan can form stable, hydrogen-bonded crystalline domains, with maximum crystallinity occurring at 0% and 100% deacetylated

product (i.e. pure chitin or pure chitosan) [94]. The presence of this crystalline structure invokes noticeable differences in the solubility behaviour of chitosan polymers, causing them to remain primarily insoluble in aqueous solutions at neutral pH [93]. In an attempt to improve the solubility of highly-deacetylated chitosan, a variety of functionalization reactions have been developed to disrupt the crystalline structure. O- and N-carboxymethyl functionalized chitosans have become the most common, showing increased water-solubility up to pH 7 [95], while unfunctionalized and highly-deacetylated chitosan is reliant on the protonation of free amino groups to facilitate solubility. Since the pK_a of the amine groups on chitosan is ~ 6.5 [96], complete solubility occurs around pH 1.5. Alternatively, the amine-group on chitosan may be quaternized, to yield the cationic derivative, trimethylchitosan ammonium, which is water soluble at nearly any pH [97]. N-methylene phosphonic chitosans, 6-O-sulfate chitosan, and carbohydrate-branched chitosans have also garnered attention due to their increased water solubilities and unique properties [97].

Because of the reactivity of the amines/amides on the chitosan backbone, there is huge potential for the functionalization of other side groups to obtain desired properties, as well as a great variety of potential crosslinking chemistries to yield stable, hydrogel scaffolds. Glutaraldehyde is by far the most common crosslinking agent [98], but other aldehyde-containing covalent crosslinkers, as well as ionic crosslinkers with dense negative charges (like tripolyphosphate) have also been reported to be effective crosslinkers [99, 100].

The rate of enzymatic degradation of chitosan for in vivo applications has been inversely related to the degree of crystallinity (percentage of deacetylation), with more crystalline structures exhibiting slower degradation [101]. Adsorption of lysozyme, particularly onto acetylated residues, is known to degrade the polymer enzymatically into shorter chain chitosan

oligosaccharides [102]; consequently, due to their relative lack of enzymatic lability, highly-deacetylated versions of chitosan possess the slowest degradation rates.

3.1.2 *Chitosan as Wound Healing Scaffolds and Delivery Vehicles*

The appropriateness of chitosan as a biomaterial has been extensively investigated, both in vitro and in vivo. A great deal of the interest in chitosan stems from its cationic nature and high charge density in solution, allowing it to form complexes with dissolved anionic polymers like heparin and alginate, as well as synthetic polyanions like poly(acrylic acid) [94]. Chitosan's positive charges also allow for a variety of non-specific binding interactions between the polymer and blood proteins, which are mostly negatively charged at physiological pH [94].

An additional aspect of chitosan that has attracted interest is the similarity of residual N-acetyl-glucosamine monomers to glycosaminoglycans (GAGs), a common structural molecule found in the extracellular matrix (ECM) [93]. Since GAGs are known to have specific interactions with various growth factors, enzymes, and adhesion proteins, the corresponding moieties on chitosan are expected to show similar effects [94].

In a wound healing application, the effect of biomaterials on macrophage stimulation and phenotypic expression are particularly important given the role of macrophages in mediating inflammation, tissue remodelling/regeneration, removing of foreign species, producing pro-inflammatory or anti-inflammatory cytokines and chemokines [103]. Peluso et. al. demonstrated significantly enhanced macrophage activation both in vitro (culturing rat peritoneal macrophages on a chitosan substrate) and in vivo (implanting chitosan pellets subcutaneously) in response to chitosan [104], while Oliveira et al. concluded that macrophages take on an M2c

(anti-inflammatory) phenotype upon contact with chitosan to promote tissue regeneration and remodelling [103].

In addition, both chitosan and chitin have been shown on numerous occasions to possess haemostatic, antimicrobial, and mucoadhesive properties [105]. Two main mechanisms are thought to be responsible for the antibacterial and antifungal properties of chitosan: (1) the positively charged amino-groups of chitosan that can interact with the anionic part of a cell membrane, altering its permeability; and (2) the ability of chitosan to bind to animal cell DNA and thus inhibit the synthesis of microbial RNA [105]. The mucoadhesive and haemostatic properties of chitosan can also be easily explained by the density of positive charge on the polymer surface [105]. These positive charges attract the negatively charged residues in mucin (in the case of mucoadhesion) while also interacting with the negatively charged membranes of red blood cells, allowing for the collection of red blood cells at the site of hemorrhage and the prompt formation of a thrombus to prevent further bleeding. These theories have been reinforced experimentally via demonstrations of the antibacterial [106, 107], mucoadhesive [108], and haemostatic [106] properties of chitosan.

Many of the properties that make chitosan desirable for wound healing applications are also advantageous for drug delivery. For example, the interactions of positively charged chitosan with cell membranes have been shown to enhance the translocation of tight junction proteins from the membrane to the cytoskeleton, increasing cell permeability and cellular drug uptake. This mechanism has been confirmed with in vivo studies, in which the presence of chitosan increased cellular uptake of horseradish peroxidase up to 18-fold in epithelial cells [109]. Furthermore, chitosan can be used for the controlled release of anionic drugs, with the charge-interactions between the chitosan matrix and the drug resulting in significantly slower

release profiles. For example, Bhise et al. confirmed that polyelectrolyte complex formation between chitosan and an anionic drug (naproxen) facilitated greatly sustained release profiles when compared to those achieved with cationic drugs [110].

3.1.3 *Sodium Alginate Structure and Properties*

Sodium alginate is a naturally occurring polysaccharide, composed of β-D-mannuronic acid (M-unit) and α-L-guluronic acid (G-unit) monomer units. The alginate macromolecule is a linear block co-polymer, consisting of sections of repeating M-units (MMMM) and sections of repeating G-units (GGGG) interspersed with atactic regions of random M- and G-units (MGMMGMGG). The frequency and distribution of M- and G- units within the polymer chain may vary depending on the source of the alginate, the season, and the growth conditions of the plant [111]. The most common commercial source for alginates is brown algae, with alginate polysaccharides residing in the plant cell walls and contributing to almost 40% of the dry mass of the algae [111].

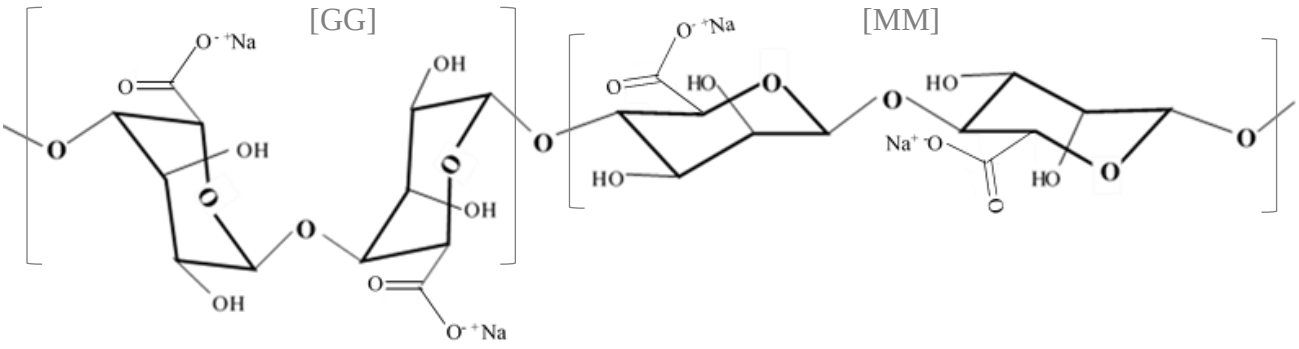

Figure 33: Molecular structure of sodium alginate, showing folded guluronate and linear mannuronate monomer units.

Alginate is able to form non-covalent crosslinks instantaneously when it comes into contact with easily dissociable bivalent metal ions, that can interact with carboxylic acid groups accessible on the backbone of guluronic acid residues [112]. When a homopolymer unit of

guluronic acid comes in contact with free bivalent cations like calcium (Ca^{2+}), the carboxylic acid and (to a lesser extent via lone pair interactions) hydroxyl groups on the tetrahydropyran ring of the α-L-guluronic acid monomers chelate to the calcium ion, forming a buckled shape, referred to as an 'egg box' in which Ca^{2+} ions are tightly packed [113]. Hence, four guluronic acid monomers per calcium ion are required to form a single crosslink.

Using this method, researchers have successfully developed many formulations of calcium chloride ($CaCl_2$) crosslinked fibres and microgels. Often, these formulations involve extruding an alginate solution dropwise through a small-diameter needle into a stirring bath saturated with calcium chloride, forming spherical beads less than one millimetre in diameter [114]. Alternatively, pre-treated alginate that has been dried into fibres or particles may be submerged in a saturated calcium chloride bath, crosslinking instantaneously upon contact with the calcium ions, and preserving the shape of the dry polymer.

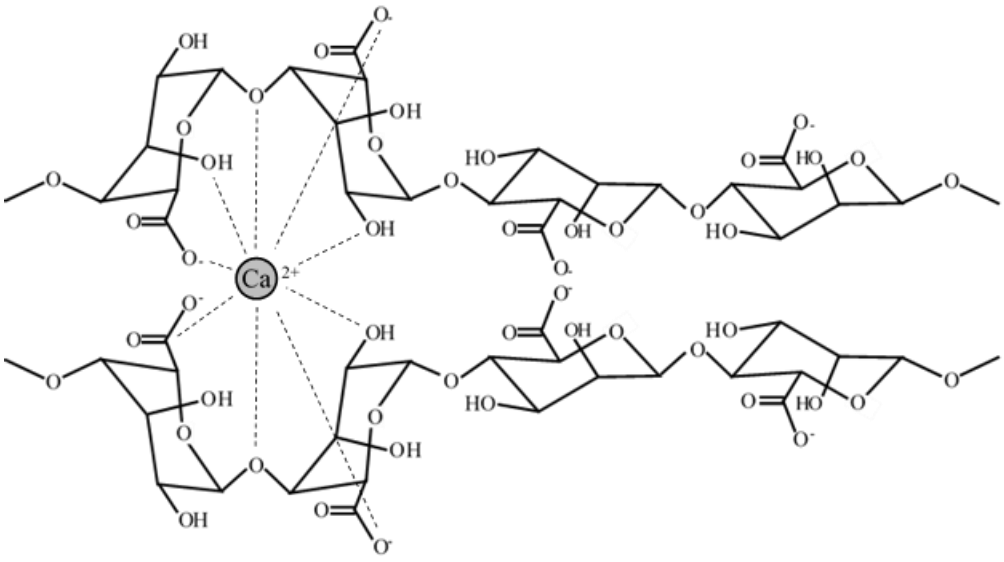

Figure 34: Structure of calcium-ion crosslinked alginate

A significant disadvantage to the conventional method of alginate-crosslinking with $CaCl_2$, is the speed with which this crosslinking occurs, limiting the potential for curing the gel

into useful shapes or providing injectable gel formulations. The rapid gelation also inhibits subsequent diffusion of calcium ions past the interface at which the alginate solution meets the calcium ion solution, due to the compaction of the polymer chains upon exposure to excess Ca^{2+} ions [115]. As a result, gels cured using this method often exhibit inconsistent shapes and mechanical strengths as well as inhomogeneous swelling patterns.

Alginate cure times may be extended by utilizing a less freely-available bivalent ion like calcium carbonate. Using this method, the concentration of free Ca^{2+} may be tuned by introducing controlled dissociation through counter-ion stabilization according to the following equilibrium reaction: $CaCO_3 + H_3O^+ \rightleftharpoons [Ca]^{2+} + [HCO_3]^- + H_2O$. By employing a slowly hydrolyzing acid like glucono-δ-lactone, a common food additive that hydrolyzes into gluconic acid at a rate dependent on pH and temperature [115], bulk hydrogels in more useable shapes as well as in situ gelling formulations may be obtained. Cellularization of these gels has also been demonstrated using human dermal fibroblasts, with improved live:dead ratios than can be achieved using the $CaCl_2$ crosslinked controls. This increase in cell viability is attributed to the increased swellability and porosity in the slow-gelling formulations [115], which allow for improved ordering of polymer chains during the crosslinking process, as well as increased diffusivity of calcium ions throughout the entire gel network. Both of these attributes are expected to facilitate more repeatable mechanical properties and more consistent swelling profiles. Subsequently, alginates with higher G-block content will exhibit higher Young's modulus, since G-residues are the only crosslinking monomer groups.

However, a significant shortcoming of Ca^{2+} crosslinked alginate gels is their lack of long-term stability in physiological conditions, as these gels will gradually lose mechanical stability in vivo through the exchange of calcium ions from the crosslinked alginate network. As such,

several methods of enhancing the stability of alginate gels have been investigated to inhibit this degradation. Most often, this is done through the introduction of a bivalent crosslinker, like poly(ethylene glycol) diamine (PEGDA) or adipic acid dihydrazide, to form covalent crosslinks with alginate bound -COOH groups via the formation of amide (effectively non-degradable) or hydrazone (slowly degradable) crosslinks [116]. Once covalently crosslinked, calcium ions may be removed from the scaffold using a calcium-scavenger like ethylenediaminetetraacetic acid (EDTA), that can chelate to calcium more strongly than alginate does [117]. The same covalent bonding may be employed with a multi-functional crosslinker like hydrazide-functionalized poly(acrylamide), that has more than two reactive hydrazide groups per crosslinker molecule, resulting in more tightly bound gel networks, as well as more tunable mechanics and degradation rates [116]. This tunability stems from the potential to regulate the degree of functionality of the crosslinker and provide multiple attachment points between the crosslinker and the gel.

3.1.4 *Alginate as Wound Healing Scaffolds and Delivery Vehicles*

The use of alginate hydrogels as wound dressings dates back to the early 20th century, when a method of fabricating calcium alginate fibres was first patented [118]. More recently, alginate wound dressings have become available commercially for the treatment of diabetic and trophic ulcers (Sorbsan ®) or to achieve haemostasis after surgical procedures (Kaltostat ®, Jelonet ®) [118]. In this application, alginate was shown to remove up to 20 times its own weight of bacterially infected wound exudate and promote the early development of healthy granulation tissue [119]. It is hypothesized that this is a result of the ion exchange reaction that takes place between the calcium ions in the dressing and sodium ions in blood serum and wound exudate. In the wound site, Ca^{2+} stimulates the calcium signalling pathway, activating the genes responsible for inducing resting cells to re-enter the cell cycle [120] and stimulating events

throughout mitosis and interphase [121]. Ion exchanges from the alginate scaffold result in partial degradation of the dressing, allowing it to swell further and absorb additional fluid [122].

Combining this calcium delivery feature with the delivery of other drugs further improves outcomes. A study of alginate hydrogels for the sustained release of dibutyryl cyclic adenosine monophosphate, demonstrated complete re-epithelialization of full-thickness wounds in a rat model in only ten days [123]. Alginate gel dressings delivering stromal cell-derived factor-1 were also shown to be effective at accelerating wound closure and minimizing scar formation in pigs with acute surgically-induced scars [124].

In pharmaceuticals, alginate has been considered for both immediate and sustained drug release of small molecules. Conventional alginate hydrogels are nanoporous, with pores in the range of 5nm [125], allowing for diffusion-controlled release of small molecules throughout the scaffold. Macroporous alginate hydrogel formulations have since been developed for delivery of active components; however, the majority of drug-delivering alginate scaffolds are in the form of microbeads or microcapsules [126], with little experimental evidence of the effectiveness of alginate as a macroporous bulk hydrogel for transdermal drug delivery. Covalent crosslinking has also been demonstrated to enhance long-term drug release from alginate scaffolds. For example, release of an ibuprofen-derivative from alginate microparticles was almost complete in 1.5 hours, while covalent crosslinking of the microgels using ADH resulted in continuous drug release for up to 8 hours in phosphate buffer solution [127].

In this chapter, multiple post-processing stabilization techniques will be discussed to create PGX-structured chitosan and alginate hydrogels, taking advantage of both the inherently useful biological properties of such polymers as well as their compatibility with various post-gelation strategies that have the potential to largely retain the PGX structure.

3.2 Materials and Methods

3.2.1 *Materials*

Sodium alginate (alginic acid sodium salt, Sigma Aldrich, M_n = 16722 by GPC) and chitosan (deacetylated chitin, Sigma Aldrich, ≥ 75 % deacetylated, with molecular weights of 310,000-375,000 Da) were PGX-processed and subsequently used for gelation. Solvents used for PGX processing were anhydrous ethanol (Les Alcools de Commerce, 99%) and compressed CO_2 equipped with a liquid withdrawal tube (Air Liquide Canada, 99.5%). Glacial acetic acid (LabChem Inc, ACS Grade, ≥ 99.7%), genipin (Wako Chemicals USA, 98%), concentrated glutaraldehyde solution (Sigma Aldrich, Grade II, 25% in H_2O), sodium carbonate buffer, calcium carbonate (Fisher Chemical, ≥ 97%), calcium chloride (Caledon Laboratory Chemicals, reagent grade), and D-(+)-glucono-delta-lactone (Sigma Aldrich, reagent grade) were used for various gelation chemistries. Carbonate buffer solutions were prepared using sodium bicarbonate (Caledon Laboratories) and sodium carbonate (Sigma Aldrich). Bovine serum albumin (MilliporeSigma, ≥96%), and fibrinogen from human plasma (Sigma Aldrich, 50-70% protein) were labelled with fluorescein-isothiocyanate isomer I (Sigma-Aldrich, ≥90%) for protein adsorption studies. 3T3 mouse fibroblasts (ATCC/Cedarlane Laboratories), cell culture media (Gibco©/Thermo Fisher), and trypsin-EDTA (Sigma Aldrich, 1x solution) were used for cell culture. Cell culture media was composed of Dulbecco's Modified Eagle Medium-high glucose (DMEM), fetal bovine serum (FBS), and penicillin streptomycin, all of which were purchased from Gibco©/Thermo Fisher (Burlington, ON). 3-(4,5-dimethylthiazol-2-yl)-5-(3-carboxymethoxyphenyl)-2-(4-sulfophenyl)-2H-tetrazolium dye (MTS) for metabolic assays was acquired from Abcam (Toronto, ON). Hydrochloric acid (HCl, 1M) and sodium hydroxide (NaOH, 1M) were obtained from LabChem Inc. (Pittsburgh, PA). All experiments used Milli-Q

grade distilled deionized water (DIW). When necessary, dialysis tubing (Thermo Fisher Scientific, 3.5 kDa) was used for purifications.

3.2.2 *Methods*

3.2.2.1 *Preparation of Chitosan for PGX Processing*

Chitosan was prepared for PGX processing through sequential dissolution in acid, precipitation in base, and re-suspension into EtOH. Chitosan was dissolved in 0.05M hydrochloric acid (HCl) solution to a total chitosan concentration of ~ 1wt% and subsequently reprecipitated by adjusting the acidity of the solution to pH 9. The resulting precipitate was isolated using centrifugation, after which the supernatant was neutralized and disposed of. The centrifuged pellet was resuspended in anhydrous EtOH to ~ 1wt%, or until solvent ratios of approximately 25:75 DIW: EtOH were obtained. The chitosan suspension was homogenized using an L4R homogenizer (Silverson) outfitted with a square hole high shear screen, at 4000 RPM for two minutes. Due to incompatibilities of the PGX piping network with excessively high or low pH, the final 75% EtOH slurry was pumped into the PGX system in place of an aqueous solution.

3.2.2.2 *Preparation of Alginate for PGX Processing*

Sodium alginate polymer was dissolved to a concentration of 1.5wt% in DIW at room temperature via constant magnetic stirring. If undissolved polymer chunks remained after magnetic stirring, the solution was processed using an L4R homogenizer (Silverson) outfitted with a square hole high shear screen at 2000 RPM for two minutes to break up solids and accelerate the dissolution process. When undissolved polymer chunks were no longer visible, the alginate solution was pumped directly into the PGX system as a viscous aqueous solution.

3.2.2.3 Synthesis of Genipin-Crosslinked Chitosan Hydrogels

A genipin stock solution was prepared by dissolving genipin to 4 wt% in a 60% EtOH/40% water solution. Acetic acid solutions were subsequently prepared at pH 2.95 (0.5% acetic acid) and pH 2.75 (1% acetic acid) by diluting glacial acetic acid. Gels were prepared by first weighing 16.7 mg (0.0821 mmol N-acetylglucosamine units) of either unprocessed or PGX-processed chitosan into a polystyrene weigh boat. Genipin stock solution (3.8 μL, 0.00067 mmol genipin), and acetic acid solution (329 μL) were combined and pipetted into the plastic weigh boat containing the pre-weighed chitosan sample. The gel components were mechanically mixed using a metal spatula and transferred into a silicone mold (12.5 diameter and 1.5 mm height), covered with a glass coverslip, and allowed to cure for a predetermined length of time at either 37^{o}C or 85^{o}C. During both curing and storage, gels were kept in a sealed container at 100% humidity, to prevent gel dehydration.

3.2.2.4 Synthesis Glutaraldehyde-Crosslinked Chitosan Hydrogels

Dilute acetic acid solutions were prepared at pH 2.95 (0.5% acetic acid) and pH 2.75 (1% acetic acid) by diluting glacial acetic acid. A glutaraldehyde stock solution was subsequently prepared by diluting concentrated glutaraldehyde solution to 1 wt% in either the previously prepared pH 2.95 or pH 2.75 acetic acid solutions. Gels were prepared by first weighing 16.7 mg (0.0821 mmol N-acetylglucosamine units) of either unprocessed or PGX-processed chitosan into a polystyrene weigh boat. The selected concentration of diluted acetic acid solution (266 μL) was pipetted into the plastic weigh boat containing the pre-weighed chitosan sample, the components were mechanically mixed using a metal spatula and transferred into a silicone mold (12.5 diameter and 1.5 mm height). Glutaraldehyde stock solution (67 μL, 0.0067 mmol glutaraldehyde) was pipetted over the top of the gel mixture, the mold was covered with a glass

coverslip, and the gels were cured for 12-24 hours at room temperature. During both curing and storage, gels were kept in a sealed container at 100% humidity, to prevent gel dehydration.

3.2.2.5 Synthesis of Calcium Carbonate-Crosslinked Alginate Hydrogels

Calcium carbonate ($CaCO_3$) and glucono-δ-lactone (GDL) stock solutions were prepared by dissolving calcium carbonate and D-(+)-glucono- δ-lactone to designated concentrations in DIW, as shown in Table 9 of section 3.4. Gels were prepared by first weighing 16.7 mg (0.0948 mmol of β-D-mannuronic/L-guluronic acid units) of either unprocessed or PGX-processed sodium alginate into a polystyrene weigh boat. Prepared stock solutions of $CaCO_3$ and GDL were combined and pipetted into the plastic weigh boat containing the pre-weighed alginate sample. The gel components were mechanically mixed using a metal spatula and transferred into a silicone mold (12.5 diameter and 1.5 mm height), covered with a glass coverslip, and allowed to cure for 12-24 hours at room temperature. During both curing and storage, gels were kept in a sealed container at 100% humidity, to prevent gel dehydration.

3.2.2.6 Synthesis of Calcium Chloride-Crosslinked Alginate Hydrogels

Calcium chloride ($CaCl_2$) stock solution was prepared by dissolving predetermined amounts of calcium chloride (Caledon Laboratory Chemicals, reagent grade) in 30 µL of DIW, as shown in Table 10 of section 3.4. Gels were prepared by first weighing 16.7 mg (0.0948 mmol of β-D-mannuronic/L-guluronic acid units) of either unprocessed or PGX-processed sodium alginate into a polystyrene weigh boat. DIW (300 µL) was pipetted into the plastic weigh boat containing the pre-weighed chitosan sample, after which the components were mechanically mixed using a metal spatula and transferred into a silicone mold (12.5 diameter and 1.5 mm height). Calcium chloride stock solution (33 µL) was pipetted over the top of the gel mixture, the mold was covered with a glass coverslip, and the gels were allowed to cure for 12-

24 hours at room temperature. During both curing and storage, gels were kept in a sealed container at 100% humidity, to prevent gel dehydration.

3.2.2.7 Analysis of Hydrogel Swelling and/or Degradation Kinetics

The swelling kinetics of hydrogels were measured at 37ºC in 10 mM buffer solution at physiological pH (pH = 7.4). Cell strainers were numbered, tared, and assigned to a 6-well plate filled with buffer solution (~ 10 mL/well). Fully cured hydrogel discs (12.5 mm diameter and 1.5 mm height) were transferred into cell strainers and an initial mass was determined by gravimetric analysis. The gels were subsequently submerged in buffer solution and their masses measured at pre-determined time intervals. Each time a measurement was taken, the cell strainer was removed from the well, drained of buffer solution, and gently surface-dried using a Kim wipe prior to being placed on the analytical balance. After each measurement, the well was refilled to its original volume with DIW to account for evaporation, while every 24 hours the buffer solution was completely replaced. Measurements were continued for at least 200 hours or until the gels reached equilibrium swelling and then subsequently began to degrade. The swelling ratio was determined by dividing the dry mass of the gel (at time = 0) to the swollen mass at each respective time point. All samples were conducted in quadruplicate, with the error bars representing the standard deviation of the replicate measurements.

Swelling and degradation kinetics of chitosan gels were measured in phosphate buffered saline solution, while swelling and degradation kinetics of alginate gels were measured in HEPES buffered saline (according to the Cold Springs Harbor Protocol [128]). Phosphates are known to induce an ion exchange with crosslinking calcium ions, accelerating the degradation of calcium-crosslinked alginate structures [129]. As such, this buffer was selected for work involving alginate gels due to its low phosphate content.

3.2.2.8 *Measurement of Hydrogel Mechanical Strength*

The mechanical properties of hydrogels were measured using a Mach-1 V500CST mechanical tester (Biomomentum, Inc.), operating with parallel circular plates (12.5 mm in diameter). Once fully cured, hydrogel discs (12.5 mm diameter and 1.5 mm height) were transferred onto the bottom plate of the tester and their precise height measured by bringing the head into contact with the top surface of the gel. The gel was subsequently compressed to 75% of their original height (i.e. 25% compression) by lowering the head of the tester at a rate of 3% compression per second. Once compressed, the linear viscoelastic range of each sample was determined by conducting a strain sweep from 0.1-100% strain at a frequency of 0.5 Hz. A set amplitude was selected within the viscoelastic range, after which the gels were put through a dynamic frequency sweep from 0.1 to 2.15 Hz, to determine shear storage (G') and loss (G") moduli. All experiments were repeated in quadruplicate at 22^{o}C, with error bars representing the standard deviation of replicate measurements.

3.2.2.9 *Synthesis of Fluorescein-Isothiocyanate Labelled Proteins*

Fluorescein-isothiocyanate (FITC) labelled bovine serum albumin (BSA) and fibrinogen were prepared by dissolving 200 mg of protein in 450 mL of carbonate buffer at pH 9. A stock solution of FITC was prepared in carbonate buffer by dissolving 5 mg of FITC to a volume of 50 mL. All 50 mL of FITC-stock was added to the protein solution, after which the reaction was incubated in the dark at room temperature for at least 12 hours under gentle magnetic stirring. The FITC-labelled protein was subsequently transferred into dialysis tubing and purified against DIW for a minimum of 6 (6+ hour) cycles. Once purified, the protein was lyophilized to dryness, transferred into an airtight container, and stored in the dark at -20^{o}C. For both BSA and fibrinogen, calibration curves were prepared in buffer solution to determine the relationship

between fluorescence and concentration. Fluorescence values (excitation λ = 495nm and emission λ = 525 nm) were recorded on an Infinite M200 Pro plate reader (Tecan Group Ltd.), with the fluorescence values converted to protein concentrations based on a calibration curve prepared over a concentration range of 0 to 200 μg/mL (with $R^2 \geq 0.99$).

3.2.2.10 *In Vitro Protein Uptake Assay*

FITC-labelled BSA and fibrinogen were prepared according to the method described in section 3.2.2.9. The uptake of these proteins was determined by punching out chitosan and alginate hydrogels to match the exact diameter of a 96-well plate. The gel discs were subsequently placed in the plate to completely fill the bottom of each well and swollen in 10 mM buffer solution. Simultaneously, stock solutions of each protein were prepared at a concentration of 2000 μg/mL in 10 mM buffer solution, from which serial dilutions were performed to obtain protein solution concentrations of 1000 μg/mL, 500 μg/mL, and 250 μg/mL. When equilibrium swelling was achieved (typically within 2 hours), the wells were drained and replaced with 200 μL of protein stock solution. Samples were incubated at 37°C, with 15 μL samples collected from each well at 24 and 72 hours. Collected samples were diluted to 150 uL and their fluorescence measured on an Infinite M200 Pro plate reader (Tecan Group Ltd.) at excitation and emission wavelengths of λ = 495nm and λ = 525nm, respectively. Protein uptake was subsequently calculated by subtracting the total mass of protein experimentally measured to remain in solution from the initial protein mass added. Each gel formulation was measured in triplicate for both BSA and fibrinogen at all four concentrations, with error bars representing the standard error of all samples measured.

3.2.2.11 *In Vitro Cytotoxicity Assay*

The cytotoxicity of viable cells when exposed to chitosan and alginate hydrogel leachates was determined using an MTS assay. Mouse 3T3 fibroblasts were first plated in a 24-well plate at a density of 20,000 cells/well and cultured in DMEM media supplemented with 10% FBS and 1% penicillin streptomycin. Hydrogels were simultaneously cured and placed in cell strainers, after which they were subjected to either zero or three (6+ hour) cycles of dialysis against DIW. After allowing the cells to incubate for 24 hours, the cell inserts containing the hydrogels were added to the wells with cultured cells and the culture media volume was increased to 2 mL to ensure that the gels were submerged. Cells were cultured for an additional 24 hours with continued exposure to the hydrogels and their leachates. Resulting cell viability was subsequently characterized by removing the gels from the well plate, adding the MTS assay, and allowing it to incubate for at least four hours. The metabolism of the MTS tetrazolium compound by viable cells produced a coloured compound that was subsequently read on an Infinite M200 Pro plate reader (Tecan Group Ltd.) at λ = 490 nm. The metabolic conversion of cells in contact with hydrogels was compared to a positive control of cells in growth media (with no hydrogel) and a negative control of growth media only (with no cells and no hydrogel) to calculate % cell viability. Each hydrogel formulation was tested in triplicate, with error bars representing the standard deviation of the cell viability percentages calculated.

3.3 Formulation and Characterization of PGX Chitosan Hydrogel Scaffolds

In many applications, the insolubility of chitosan in neutral media is a significant disadvantage. However, in our application, the poor solubility of chitosan is ideal to maintain the PGX-generated morphologies during subsequent functionalization and/or crosslinking reactions. Furthermore, the potential tuning of chitosan's solubility kinetics by varying the

acidity of the reaction solution from completely insoluble (above pH 6) to completely soluble (below pH 1.5) [130] offers potential to finely balance the crosslinking kinetics, solubility, and mass transfer kinetics on the timescale of the reaction to achieve sufficient crosslinking of the polymer without dissolving the PGX-generated macroporous structure.

3.3.1 *Chitosan Crosslinked via Schiff Base Reaction*

A Schiff base is classified by the nucleophilic addition of a nitrogen, often from an amine or hydrazide group, to the carbonyl functional group of an aldehyde or ketone [131] to form an imine bond [132]. These chemistries formed the basis for the first set of crosslinking reactions conducted by reacting chitosan with glutaraldehyde, a linear 5-carbon dialdehyde molecule [133] selected as a crosslinker in this application due to its ability to react rapidly with the amine groups on the backbone of chitosan at a range of pH values and without a catalyst. Glutaraldehyde has also been shown to generate more thermally, biologically and chemically stable crosslinks than other aldehyde-functionalized molecules [134], generating more hydrolytically and enzymatically stable hydrogels with slower in vivo degradation rates. The proposed mechanism for the glutaraldehyde-crosslinking of chitosan is shown in Figure 35.

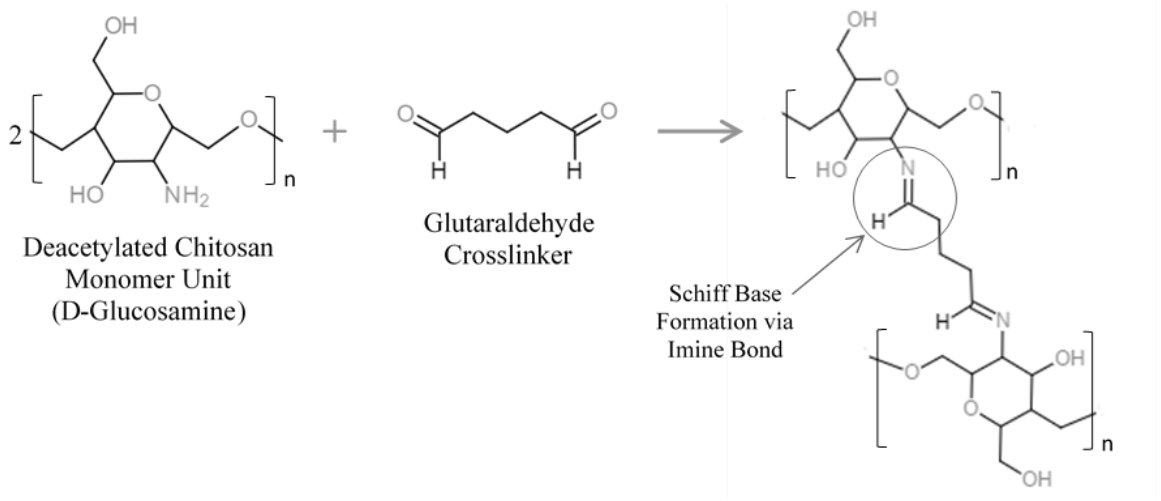

Figure 35: Proposed crosslinking reaction of glutaraldehyde and chitosan via Schiff base formation

However, glutaraldehyde has been shown to undergo a series of complex chemistries in aqueous solutions to create a variety of molecular forms, many of which are less available to participate in crosslinking reactions [133]. For example, in neutral and acidic conditions, glutaraldehyde has been shown to exist in an equilibrium mixture of free dialdehyde monomer, a corresponding cyclic hemiacetal, and polymers of the cyclic hemiacetal. Specifically, Kawahara et al. investigated the structure of glutaraldehyde in dilute solution by UV absorption and light scattering and found that, while glutaraldehyde was primarily monomeric between pH 3.0-8.0, its primary form was a cyclic hemiacetal and not a free dialdehyde [135], as shown in Figure 36.

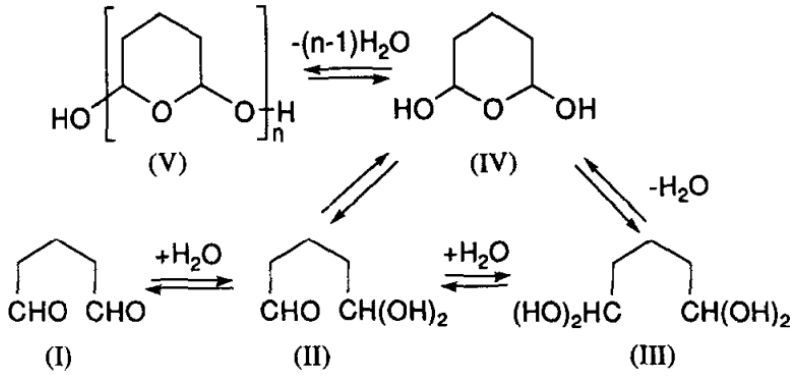

Figure 36: Possible molecular forms of glutaraldehyde in neutral to acidic dilute aqueous solutions. Reproduced with permission [135]. Copyright © 2018, Elsevier.

Conversely, above pH 10 and in concentrated solutions, glutaraldehyde has been shown to self-polymerize, existing as primarily insoluble oligomers of glutaraldehyde's cyclic and/or linear forms with significantly reduced presence of free aldehyde groups [133]. As such, glutaraldehyde exhibits significantly reduced participation in crosslinking under these conditions.

In the following work, molar ratios of glutaraldehyde crosslinker were increased 10-fold relative to other crosslinking methods to account for this unavailability of free glutaraldehyde and the subsequent inefficiencies associated with glutaraldehyde crosslinking.

3.3.2 *Chitosan Crosslinked via Reduction of Genipin*

To reduce issues often associated with the cytotoxicity of glutaraldehyde in biological applications, crosslinking of chitosan was also pursued via the reduction of genipin. Traditionally used as a small molecule in oriental medicine, genipin is extracted in its glycosidic form from gardenia fruit, and subsequently isolated via β-glucosidase catalyzed hydrolysis [136]. Genipin also exhibits unique properties as a small molecule, with studies presenting compelling evidence towards its pharmaceutical activity as an anti-inflammatory, antioxidant, and choleretic agent [136]. As a crosslinker, genipin's negligible cytotoxicity [137] provides a distinct advantage over glutaraldehyde, eliminating the need for post-crosslinking purifications steps to remove unreacted crosslinkers and toxic biproducts.

The actual mechanism of chitosan-crosslinking by genipin is known to differ depending on the pH of solution in which the reaction is conducted [137]. At acidic and neutral conditions, the crosslinking reaction proceeds via nucleophilic attack of chitosan's amino group on the unsaturated C3 carbon of genipin's dihydropyran ring. This facilitates a ring opening reaction, allowing another of chitosan's amino groups to attack the newly formed aldehyde. In this mechanism, genipin's ring-opened product essentially functions as a dialdehyde, but with significantly more stable condensation products than glutaraldehyde, and without the concern of self-polymerization or significant molecular structural changes [137].

At alkaline pH, the ring opening reaction of genipin progresses via nucleophilic attack by the hydroxyl ions in aqueous solution. This allows genipin to form intermediate aldehyde moieties that can subsequently undergo either a base-catalyzed aldol condensation reaction to form oligomers of genipin, or undergo Schiff base formation with the amine groups on chitosan to form a crosslink [137].

For the purposes of this work, genipin crosslinking reactions were conducted in dilute solutions of acetic acid to promote the acid-catalyzed mechanism and thus allow for better control over the crosslinking products, as well as the rate of solubilization of chitosan throughout crosslinking reactions. The proposed crosslinking reaction of chitosan and genipin in acidic solution is shown in Figure 37.

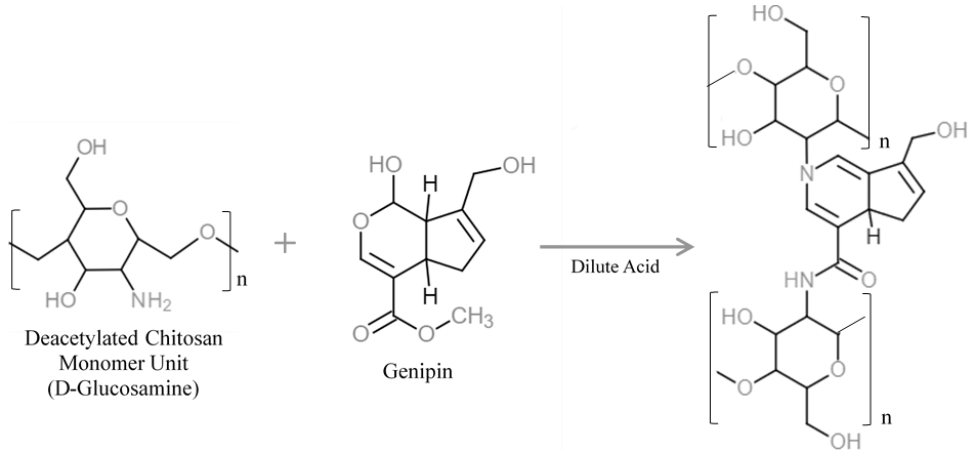

Figure 37: Proposed crosslinking reaction of chitosan and genipin in acidic conditions.

3.3.3 *Hydrogel Rheology*

3.3.3.1 *Glutaraldehyde-Crosslinked Chitosan Gels*

The effectiveness of glutaraldehyde as a crosslinker was verified by formulating a series of hydrogels by crosslinking PGX chitosan with different glutaraldehyde concentrations and measuring their elastic storage modulus, the results of which are shown in Figure 38. Observed plateau moduli for gels containing 4wt%, 2wt% and 1wt% glutaraldehyde (relative to the mass of chitosan) were 18-20 kPa, 15-17 kPa, and 12-13 kPa, respectively, exhibiting a proportional increase in mechanical strength with increasing crosslinker concentration. This proportional change in recorded G' indicates that the crosslinking reaction was progressing as intended, and that a degree of tuneability exists within these gel formulations to target a desired elastic modulus by varying crosslinker concentration.

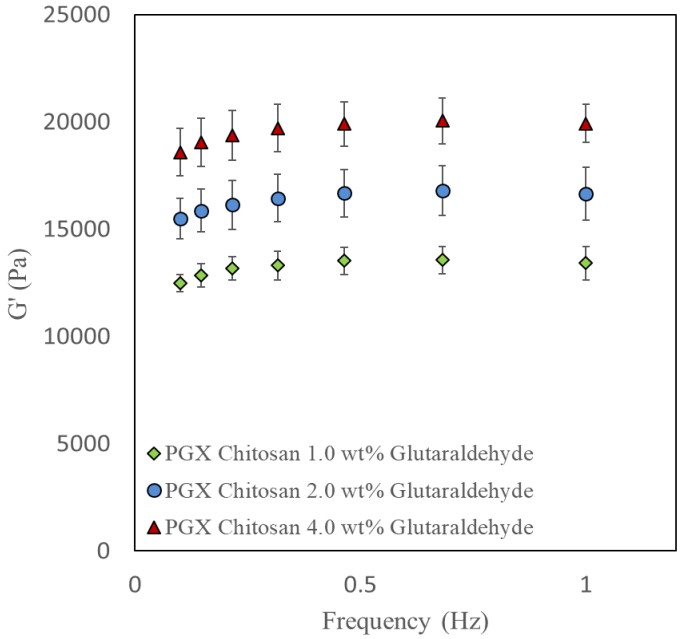

Figure 38: Elastic storage modulus (G') as a function of frequency for glutaraldehyde-crosslinked chitosan gels with varying crosslinker concentrations. Reaction solution pH and polymer concentration were held at 2.95 and 5wt%, respectively. Total gel volume was controlled at 333 µL.

Gels with the highest crosslinker concentration were subsequently formed under a variety of pH conditions and compared to gels formulated from non-PGX processed materials, as shown in Figure 39. In acidic media, decreases in pH were expected to increase chitosan solubilization kinetics, resulting in greater solubility of the polymer on the timescale of the reaction. This increased solubility at lower pH resulted in enhanced overall crosslinking, but slower crosslinking kinetics (due to lower localized polymer concentrations upon dissolution), and less maintenance of the PGX structure. Furthermore, an equilibrium between protonated and unprotonated amine groups on the chitosan backbone was expected, with higher ratios of the protonated form present at lower pH conditions. These protonated amine functionalities are unable to initiate crosslinking via nucleophilic attack on an aldehyde, resulting in potentially lower degrees of crosslinking than reactions conducted at higher pH. As such, changes in the structure (and thus mechanics) of the hydrogel were considered to be the result of balances

between the ionization and solubilization states of chitosan at the time the network is locked in place by crosslinking, which respectively affect both the efficiency and the local concentration of polymer at the time of crosslinking.

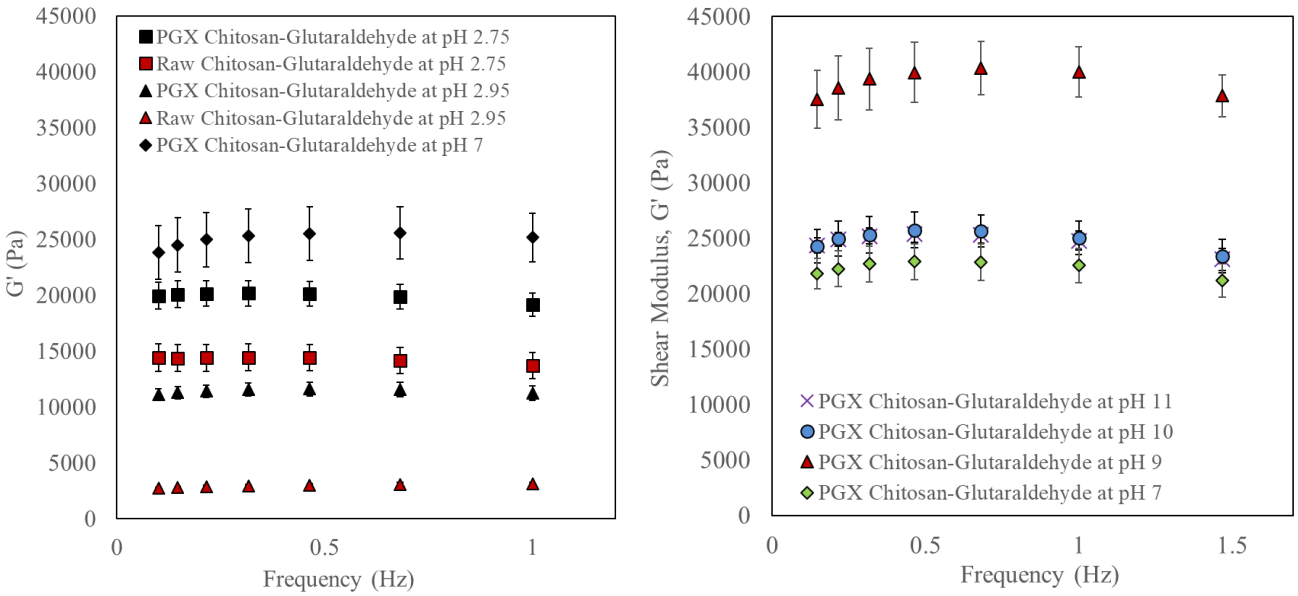

Figure 39: Elastic storage modulus (G') as a function of frequency for glutaraldehyde-crosslinked chitosan gels formulated from both PGX and unprocessed polymers in solutions with varying pH. Polymer and crosslinker concentrations were held constant at 5wt% and 4wt% respectively. Total gel volume was controlled at 333µL.

The increase in mechanical strength observed from gels prepared at pH 2.95 to those prepared at pH 2.75 is consistent with the increased rate of solubilization of chitosan at the lower pH, although a small increase in the fraction of protonated amine groups upon lowering the pH to 2.75 may also in part cause a slight reduction in the mechanical strength achieved. However, the significantly higher elastic storage moduli of gels formulated from PGX-processed precursors was unexpected, with the PGX-processed hydrogels exhibiting modulus increases of ~ 6 kPa at pH 2.75 and ~ 10 kPa at pH 2.95 relative to non-PGX controls. Two conclusions were drawn from this observation: (1) the increased surface area of PGX-processed precursors allows for a greater extent of crosslinking when chemistries are conducted in a partially precipitated

state (i.e. reactions proceed primarily through surface interactions); and (2) the smaller difference observed in mechanical strength at lower pH suggests the loss of PGX-generated morphologies under conditions in which chitosan is more soluble, making the final PGX-processed hydrogel more morphologically similar to conventional non-PGX hydrogels.

Gels prepared in neutral or basic conditions were significantly stronger than those prepared in acidic conditions. It is postulated that this phenomenon is primarily due to the insolubility of chitosan at these conditions, resulting in stiffer networks due to the deswelling of the polymer in an unfavourable solvent and the inability of the solvent to plasticize the polymer chains and thus allow them to move freely past each other in response to shear stress. As such, it is not believed that this increase in mechanical strength is due to an increase in the overall degree of crosslinking within the gels but rather the relative lack of solvation of the networks under these testing conditions, consistent with dewatering that was observed upon pre-compression of these neutral or basic gels prior to shear modulus measurement.

Upon examination of exclusively the basic formulations on the left, it was interesting to note that the elastic storage modulus values for the gels crosslinked in pH 9 buffer were significantly higher than those of any other trial. This is attributed to the structural changes of glutaraldehyde in aqueous solution at different pH conditions, as discussed in section 3.3.1. Below pH 8, glutaraldehyde exists primarily as a cyclic hemiacetal structure with significantly lower reactivity to amines than linear glutaraldehyde, while above pH 10, glutaraldehyde undergoes a base-catalyzed self-polymerization and thus experiences significantly hindered diffusivity through the hydrogel scaffold as a result of its longer chain length, with steric inhibition limiting the degree of crosslinking. Note that, due to the complete insolubility of chitosan in basic solution, synthesizing comparable homogeneous gel formulations from

unprocessed polymers was not possible, as the unprocessed polymer was too dispersed in solution to crosslink in the precipitated state.

3.3.3.2 Genipin-Crosslinked Chitosan Graphs

Genipin-crosslinked chitosan gels were designed to be thermally cured at physiological temperature (37°C) to allow for the incorporation of cells during gelation. However, the duration of the crosslinking reaction at this temperature was unknown, and the gelation kinetics could not practically be tracked by a test-tube inversion test due to the high viscosity of pre-crosslinked gel mixtures. Instead, the gelation kinetics were semi-quantitatively tracked by measuring the elastic storage modulus (G') of the gels as a function of crosslinking time, as shown in Figure 40.

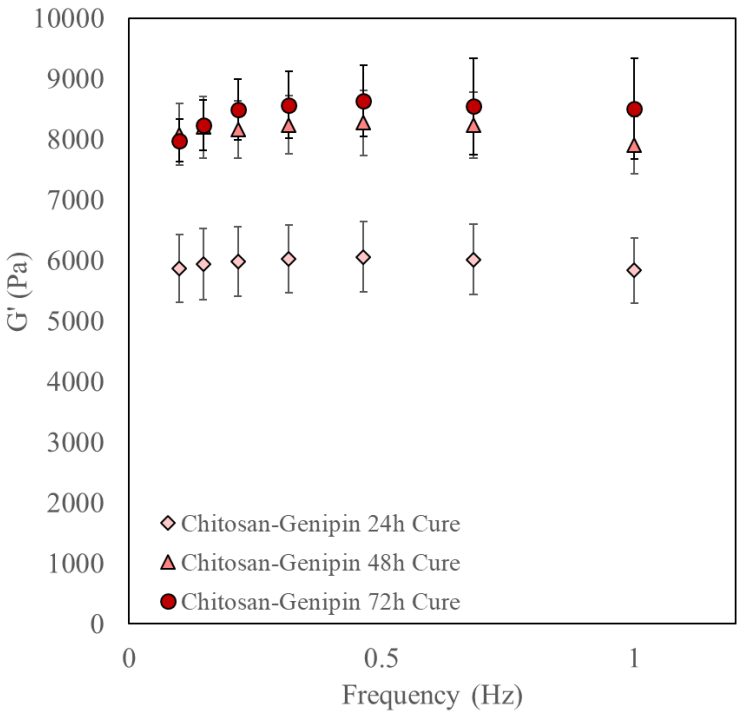

Figure 40: Elastic storage modulus (G') as a function of frequency for genipin-crosslinked chitosan gels with varying cure times at 37°C. Polymer and crosslinker concentrations were held constant at 5wt% and 0.9wt% respectively. Total gel volume was 333µL at pH 2.95.

While there was a noticeable difference in the gel stiffness between 24 and 48 hours, there was no significant difference between trials conducted after 48 hours or 72 hours of curing,

indicating that the crosslinking reaction was complete at/before 48 hours. As such, all subsequent trials were conducted after curing at 37ºC for a minimum of 48 hours, unless otherwise stated.

The efficiency of genipin as a crosslinker for chitosan was subsequently examined by varying the crosslinker percentage from 0.3wt% to 0.9wt%, relative to the mass of chitosan. The stiffness of the resulting hydrogels was tracked by monitoring the resulting change in elastic storage modulus, as seen in Figure 40. Observed plateau moduli for gels containing 0.9wt%, 0.6wt% and 0.3wt% genipin were 7.5-8.5 kPa, 6-6.1 kPa, and 4.1-5.9 kPa, respectively, exhibiting a proportional increase in mechanical strength with increasing crosslinker concentration. Like the glutaraldehyde formulations, this proportional change in recorded G' indicates that a degree of tuneability exists within these gel formulations to target a desired elastic modulus by varying crosslinker concentration. However, it must be noted that the lowest genipin-crosslinking ratio investigated here exhibited lower reproducibility, as indicated by the larger standard deviations when compared to chitosan gels with higher genipin content. It is hypothesized that this higher variability is the result of inhomogeneities in the dry PGX-scaffold, with the lower ratio crosslinker forming separate domains of tightly crosslinked gel (in sections with high chitosan concentration) and loosely crosslinked gel (in areas where chitosan chains are more dispersed). The presence of such inhomogeneities likely indicates the lower limit to which the mechanical properties of these gels may be adjusted.

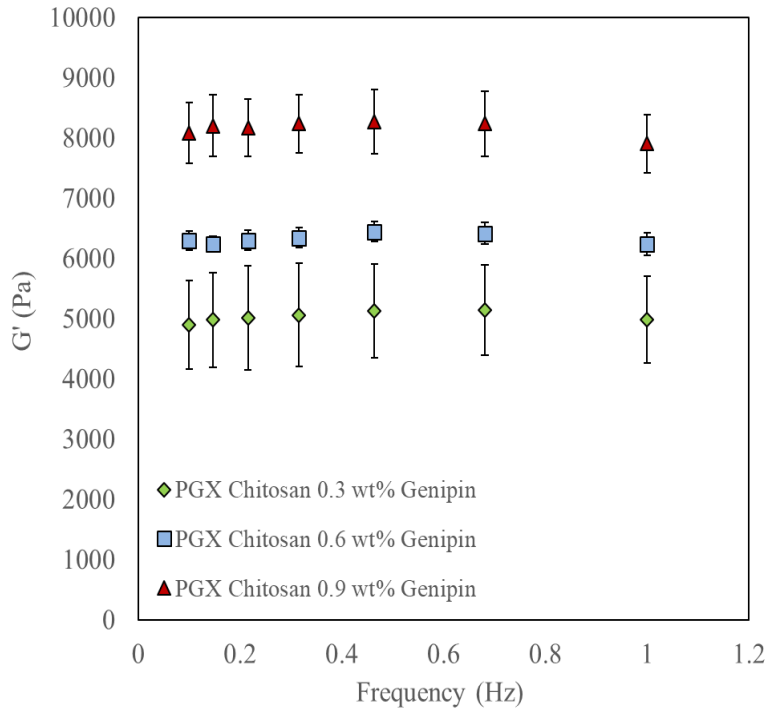

Figure 41: Elastic storage modulus (G') as a function of frequency for genipin-crosslinked chitosan gels with varying crosslinker percentage. Polymer concentration, reaction pH, and total gel volume were held constant at 5wt%, pH 2.95, and 333µL, respectively.

The effect of pH on the properties of genipin-crosslinked chitosan formulations were subsequently assessed by maintaining the polymer and crosslinker concentrations at 5wt% and 0.9wt% respectively, and varying the acidity of the reaction solution from pH 2.75 (1% acetic acid) to pH 7 (0% acetic acid). Similar to the glutaraldehyde formulations, gels prepared from PGX-processed precursors were significantly stronger than those formulated from unprocessed polymers, with PGX gels showing increases in G' of 10-11 kPa (at pH 2.75) and 5-7 kPa (at pH 2.95) compared to their non-PGX equivalents prepared under the same conditions. As with glutaraldehyde crosslinking, the smaller difference in G' achieved between PGX and unprocessed gels at lower pH is indicative of the chitosan becoming more soluble during the reaction, reducing the degree to which the PGX-generated interconnected network is maintained during crosslinking and decreasing the localized crosslink density within the scaffold (due to

lower localized polymer concentrations in the dissolved state). Note that, as before, no non-PGX gels could be fabricated at pH 7 due to the lack of chitosan solubility under these conditions.

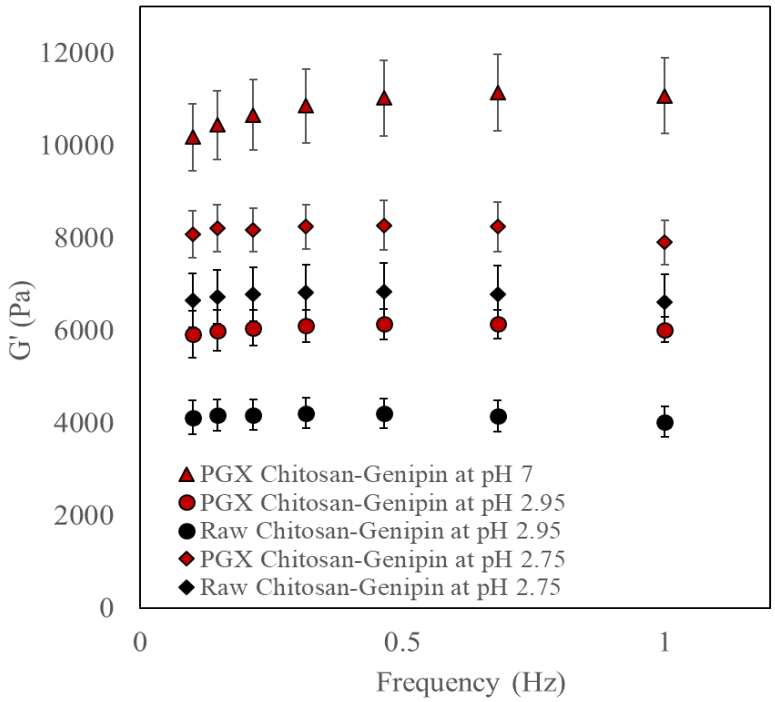

Figure 42: Elastic storage modulus (G') as a function of frequency for genipin-crosslinked chitosan gels with varying solution pH. Polymer and crosslinker concentrations were held constant at 5wt% and 0.9wt% respectively with a total reaction volume of 333µL.

Finally, the potential utility of faster-gelling formulations was assessed by curing 0.9wt% genipin-crosslinked PGX chitosan gels at 85ºC for 1.5 hours and 3 hours. According to the Arrhenius equation, the rate of the reaction should approximately double with every 10ºK increase in temperature [138]. As such, it was expected that, at 85ºC, the crosslinking reaction would be complete after only 1.5 hours. This hypothesis was tested by analyzing the elastic storage modulus under shear stress at each time point and comparing the results to the same gel formulation cured at 37ºC for 48 hours, as seen in Figure 43.

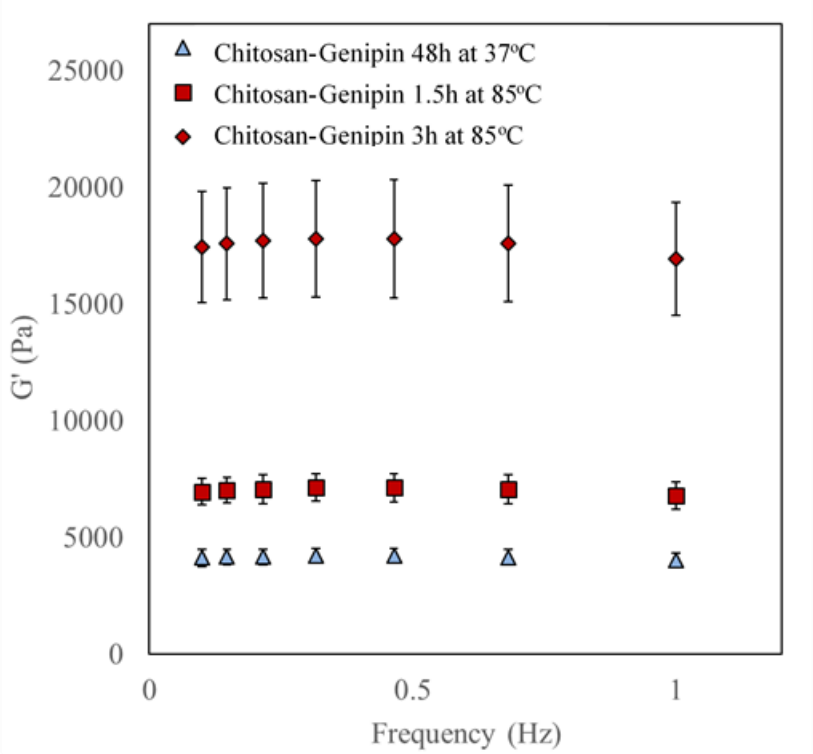

Figure 43: Elastic storage modulus (G') as a function of frequency for genipin-crosslinked chitosan gels cured at different temperatures. Gels were made with PGX-processed chitosan, with polymer and crosslinker concentrations of 5wt% and 0.9wt%.

Interestingly, gels cured for 1.5 hours at 85°C exhibited a G' of ~ 4.5 kPa, which is comparable to the G' of gels cured for 48 hours at 37°C (~ 7-8 kPa); furthermore, the stiffness of gels cured for twice the time at 85°C continued to increase, exhibiting a significantly greater plateau modulus of 15-20 kPa. These unique mechanical properties are attributed to the decreased ability of the polymer to reorganize and become soluble on the timescale of the crosslinking reaction at higher temperatures. Faster crosslinking allows for the maintenance of additional PGX structure and the presence of higher localized concentrations of polymer (originating from the initial PGX template), which therefore enable the formation of higher local mass concentration and thus stronger gels. For applications that do not require the encapsulation of cells, fast-gelling formulations provide significantly reduced gelation times, as well as the potential to target higher G' with lower crosslinker concentrations.

3.3.4 *Imaging of PGX Chitosan and its Hydrogel Scaffolds*

PGX-processed chitosan (in the dry state prior to crosslinking) was analyzed by several imaging techniques and compared to hydrogel scaffolds formulated from PGX chitosan materials in an attempt to determine which formulations best maintained the original PGX-generated polymer morphologies. Figure 44 shows the results of such visualization experiments (prior to hydration and crosslinking) using photography (in comparison to a non-PGX processed chitosan control), scanning electron microscopy (SEM) and helium ion microscopy (HiM).

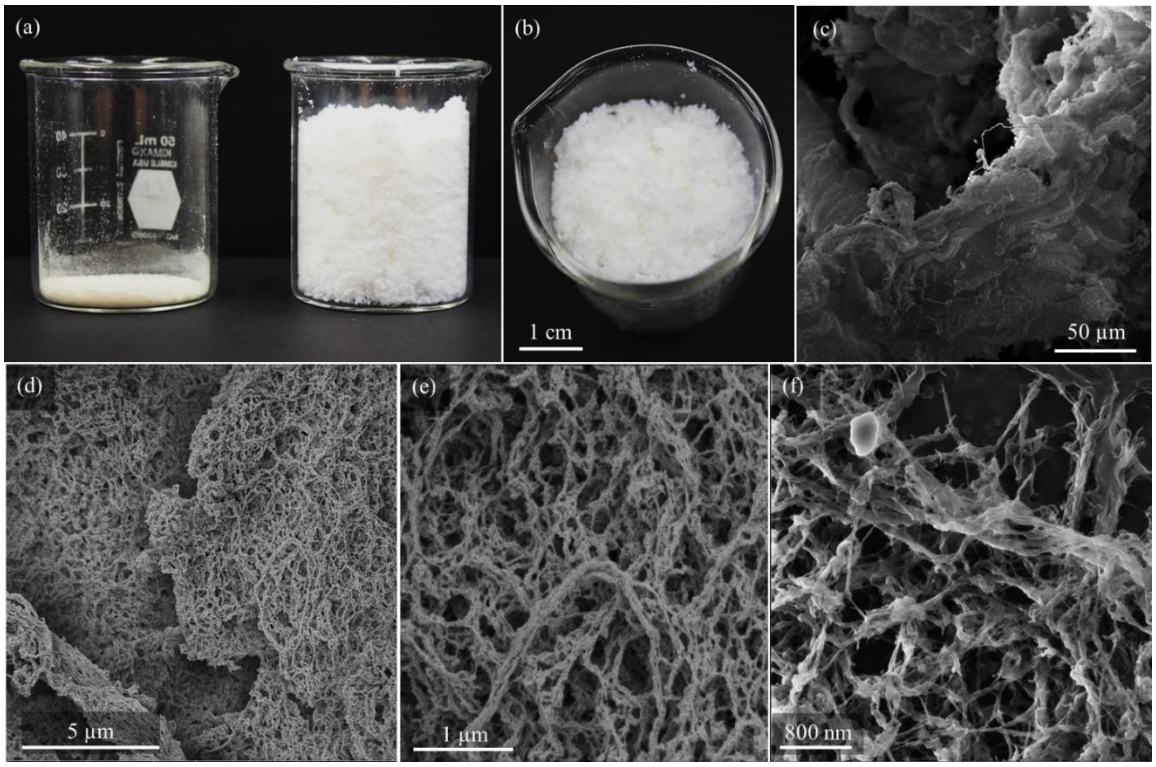

Figure 44: (a-b) photographs of PGX-processed chitosan compared to the same mass of unprocessed polymer, (c-e) SEM images of PGX chitosan at 1000x, 15,000x, 50,000x magnification, and (f) HiM image of PGX Chitosan.

Upon imaging, it was apparent that the pore structure of PGX-processed chitosan was not visible to the naked eye and that any visible void space originated primarily from the highly irregular shape of chitosan particulates. These observed particulates were determined to be a result of the precipitation and homogenisation steps conducted prior to PGX-processing, and not

from the actual PGX processing method (like those observed for starch). From further observation of Figure 44(c-f), it was concluded that, on a microscopic scale, PGX chitosan is highly exfoliated with pores in the range of 100nm - 1μm that are the result of a highly interconnected network of fibres with diameters on the scale of several hundred nanometres.

3.3.4.1 *Scanning Electron Microscopy of Lyophilized Hydrogel Scaffolds*

Both glutaraldehyde-crosslinked and genipin-crosslinked chitosan gels made from PGX-processed precurusors were flash-frozen, lyophilized, and imaged using SEM in an attempt to visualize the residual pore structure after hydration and crosslinking in different solvent systems, as shown in Figure 45. Gels formulated from PGX-processed chitosan were also compared to control gels prepared from unprocessed chitosan, as shown in Figure 47 and Figure 48. While it must be noted that the flash-freezing and lyophilization process used to dry hydrogel scaffolds for SEM imaging has the potential to alter pores structures due to pore expansion during ice crystal formation (particularly in the case of macropores), any differences observed between gel formulations via SEM were assumed to originate from stuctural differences in a wet state.

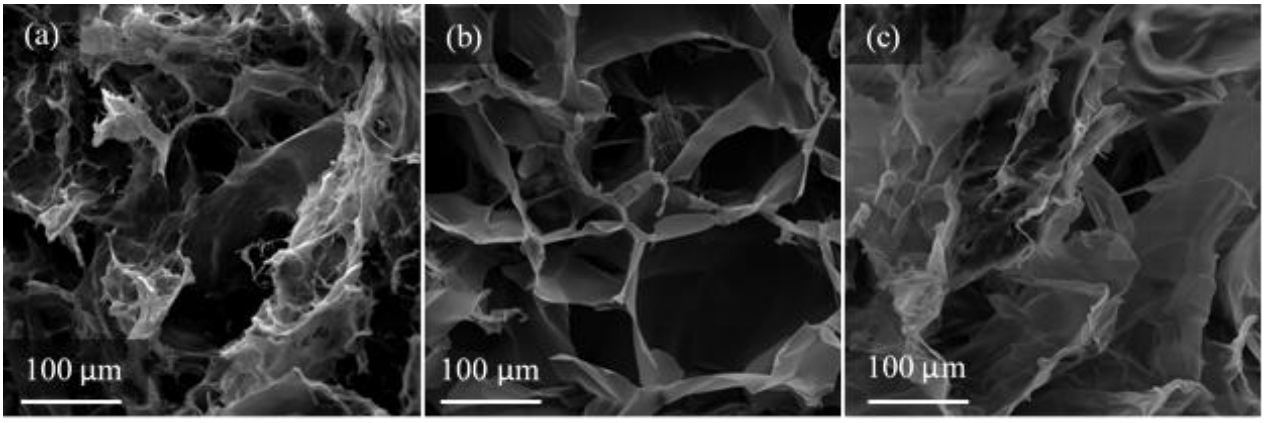

Figure 45: SEM images of glutaraldehyde-crosslinked chitosan gels at 1000x magnification made from PGX-precursors at (a) pH 9, (b) pH 2.95, (c) pH 2.75. Gels were prepared at 4wt% glutaraldehyde.

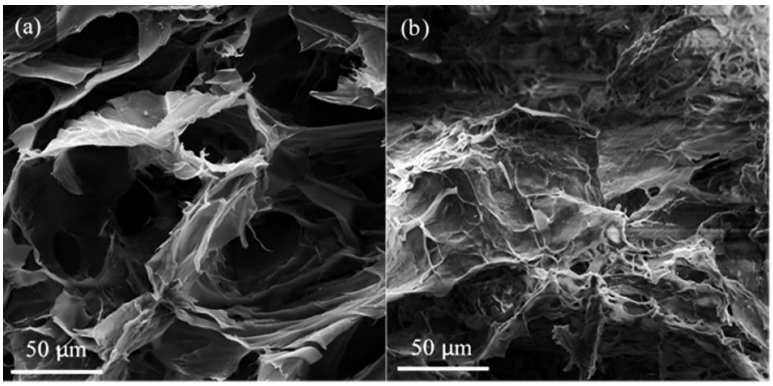

Figure 46: SEM images of genipin-crosslinked chitosan gels at 1000x magnification made from PGX-precursors at (a) pH 2.95 and (b) pH 2.75. Gels were prepared at 37°C for 48 hours.

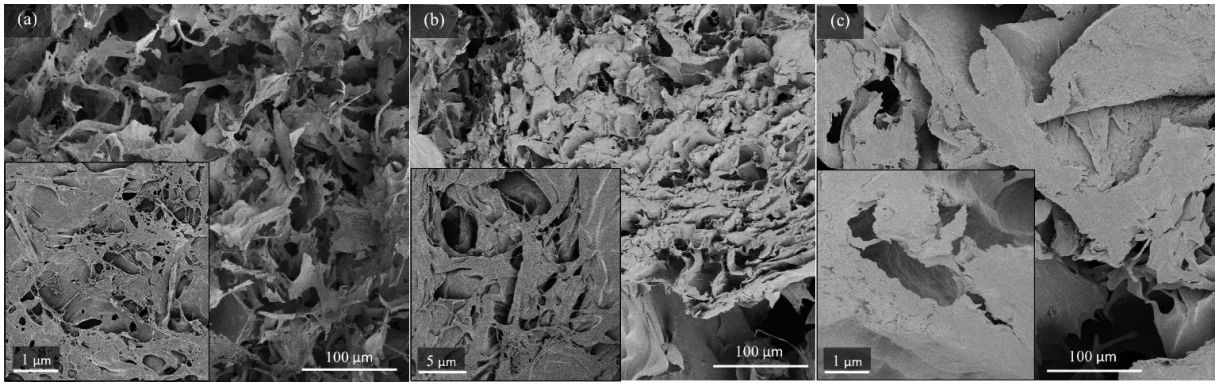

Figure 47: SEM images of glutaraldehyde-crosslinked chitosan gels using (a) PGX-chitosan in pH 9, (b) PGX-chitosan in pH 2.95, (c) unprocessed chitosan in pH 2.95.

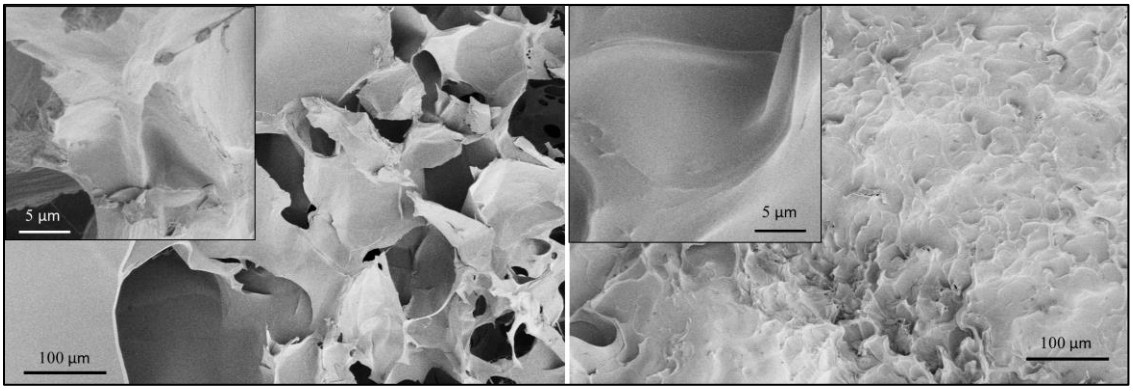

Figure 48: SEM images of genipin-crosslinked chitosan gels using PGX-processed polymer (left) and unprocessed polymer (right) at pH 2.95.

From Figure 45, the glutaraldehyde crosslinked gel clearly maintains the most of the original fibrous network of chitosan, attributable to the complete insolubility of chitosan in this

reaction media. The acidic formulations appeared to lose some of that fibrous network but maintained a significant degree of porosity, although it is likely that at least the larger pores may have originating from the freezing/lyophilization process used for sample preparation. It is believed that the increased rate of solubilization of chitosan at lower pH resulted in further dissolution of the original PGX-network, creating a structure closer to that of a conventional chitosan hydrogel. From Figure 46, many of the same conclusions may be drawn, with both gels appearing to lose aspects of the fibrous structure, and the pH 2.75 gel exhibiting relatively little porosity. This contrast was exacerbated by the significantly slower rate of the genipin crosslinking kinetics at 37^{o}C, allowing the pH 2.75 formulations to become almost completely re-solubilized on the time scale of the gelation reaction. The net effect of this solubility was an almost complete loss of pore structure at lower pH values, leaving polymer sheets with negligible macroporosity behind. As such, the criteria of maintaining PGX structure was determined to have not been met in pH 2.75, and gel formulations at pH 2.95 and pH 9 were used for all future experimentation. Note that it was not possible to access the high-resolution SEM to collect images for Figure 45 and Figure 46, so the presence of pores on a length scale less than 10 μm could not be confirmed.

While it appeared that a significant portion of the original PGX-generated porosity (in the range of 100nm – 1μm) was lost, all gels formulated from PGX-processed chitosan showed significantly greater porosity than gels formulated from unprocessed precursors, as shown in Figure 47 and Figure 48. This indicated that a portion of PGX morphology was retained in all formulations, and a significant difference in structure exists between PGX formulations and unprocessed controls. This result is consistent with the uniformly higher modulus values of PGX-processed gels compared to unprocessed gels (Figure 39 and Figure 42).

3.3.4.2 Confocal Imaging of Hydrated Gel Scaffolds

To exclude the possibility of changes in pore structure initiated by freezing and lyophilization as the principle reason for the differences between gel morphologies analyzed via SEM, gels were imaged in a hydrated state using confocal microscopy, the results of which are shown in Figure 49 and Figure 50. The primary goal was to ensure that gels formulated from PGX-chitosan still showed significantly different structures and/or higher porosity than gels prepared with unprocessed chitosan in the swollen state.

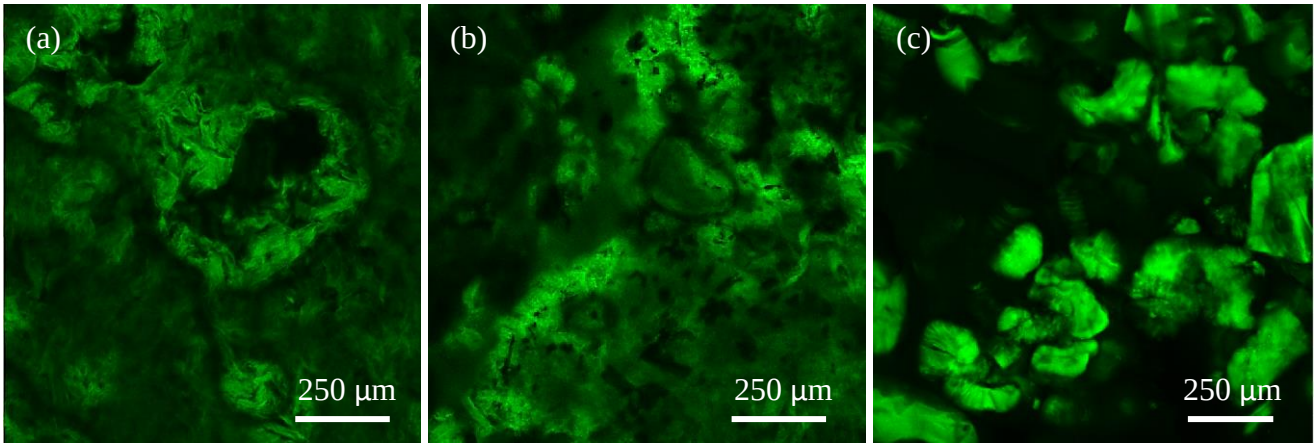

Figure 49: Confocal microscopy images of gels prepared using glutaraldehyde-crosslinked (a) PGX-chitosan in pH 9 buffer, (b) PGX-chitosan in pH 2.95 solution, (c) Unprocessed chitosan in pH 2.95 solution

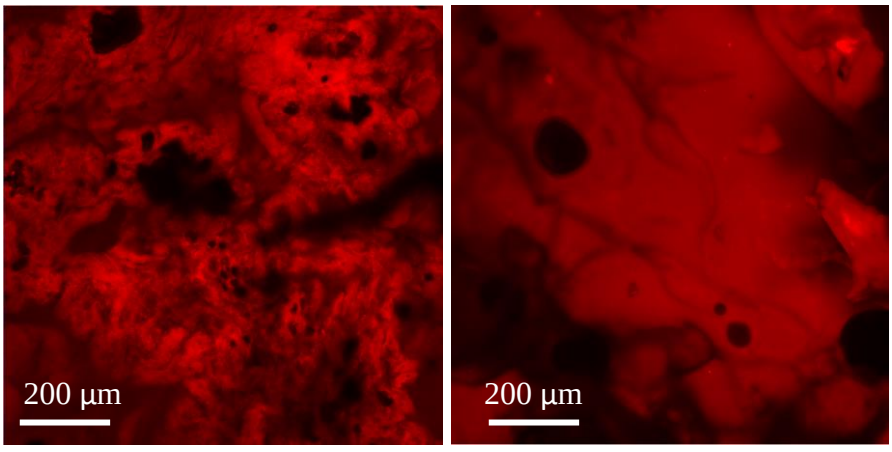

Figure 50: Confocal microscopy images of gels prepared using genipin-crosslinked PGX-chitosan (left) and non-PGX-chitosan (right) in pH 2.95 solution

The confocal images show clear differences between PGX and unprocessed gel morphologies in the swollen state. Genipin-crosslinked PGX gels show a highly interconnected network structure, (consistent with the original PGX-generated morphologies), with multiple pores on the range of tens of microns distributed throughout the gel while gels made under the same conditions from unprocessed chitosan show no obvious porosity on this length scale (note that the visible isolated spherical pores originate from entrapped air bubbles). Similar results are observed for glutaraldehyde-crosslinked gels, with the unprocessed chitosan in this case appearing as largely isolated polymer granules, consistent with the faster gelation times of glutaraldehyde crosslinking (i.e. the granules are only weakly solubilized during the crosslinking reaction). This observed morphology of weakly connected granules in unprocessed chitosan-glutaraldehyde gels relative to the network structure in PGX gels is consistent with the lower G' values measured for unprocessed versus PGX processed gels (Figure 39).

3.3.5 *Swelling and Degradation Kinetics*

Swelling and degradation kinetics for chitosan gels were conducted at 37^{o}C in 10 mM HCl, conditions in which chitosan polymer is soluble. The final extent of hydrogel swelling is often correlated to its degree of crosslinking (with highly crosslinked gels resisting swelling more strongly than those with fewer crosslinks), while the degradation kinetics are indicative of the hydrolytic stability of the polymer and its crosslinks. Interestingly, chitosan gels formulated at different conditions showed significantly different swelling profiles, as seen in Figure 51.

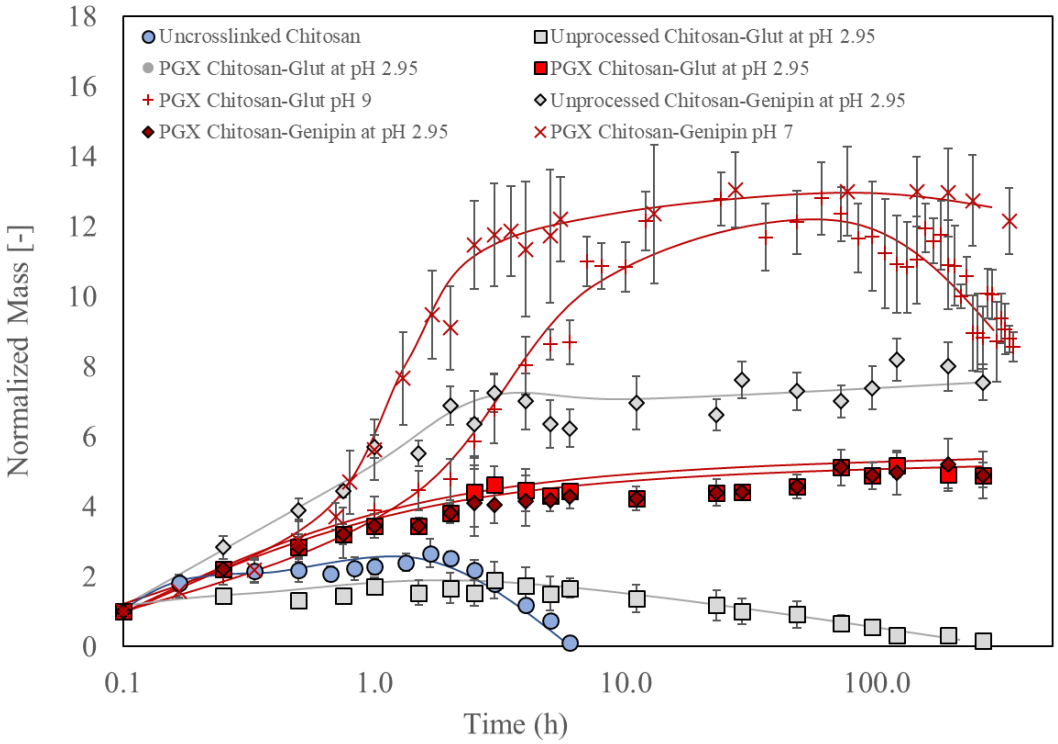

Figure 51: Swelling and degradation kinetics of both glutaraldehyde and genipin-crosslinked chitosan gels measured in comparison to an uncrosslinked PGX chitosan sample (blue) in 10 mM HCl at 37°C.

Gels crosslinked in basic media (in which the chitosan was completely insoluble) showed significant swelling within the first ten hours, resulting in a 10-fold increase in mass. This high degree of observed swelling suggests that the measured mechanical strength of basic formulations was a result of the intrinsic strength of the precipitated carbohydrate instead of being indicative of a high degree of crosslinking within the gel network which, if present, would have significantly suppressed this observed swelling. PGX chitosan crosslinked in pH 9 with glutaraldehyde also began to decrease in mass after 100 hours, indicating that lower crosslinking densities result in the onset of solubilization/gel degradation on the timescale of this experiment.

PGX gels prepared in acidic media showed significantly lower equilibrium swelling of 4-fold their original mass, with no indication of degradation over the test period, consistent with a higher internal degree of crosslinking within these gels. In contrast, gels formed from

unprocessed chitosan exhibited both more swelling and faster degradation than PGX-processed gels prepared under the same conditions; for example, genipin-crosslinked gels prepared with unprocessed chitosan swelled almost twice as much as their PGX equivalent. Similarly, the unprocessed glutaraldehyde-crosslinked gel never reached an equilibrium swelling ratio and began to degrade after only three hours. This result is consistent with the less networked morphology and weaker mechanics of the unprocessed hydrogels previously discussed. A completely uncrosslinked PGX chitosan control (blue) dissolved within ten hours and confirmed that all formulations subjected to glutaraldehyde or genipin reactions resulted in hydrogel structures with varying degrees of crosslinking.

3.3.6 *Protein Uptake*

The capacity of hydrogels prepared with and without PGX processing to uptake proteins was assessed to probe both the internal porosity/surface area of the various hydrogels as well as the practical potential utility of such hydrogels for protein release applications. Two model proteins of different molecular weights were chosen for this analysis: bovine serum albumin and human plasma fibrinogen. Albumin is the most abundant blood protein, comprising > 50% of total blood proteins, with a molecular weight of 66.5 kDa and a hydrodynamic radius of ~ 2.8 nm [139]. Conversely, fibrinogen comprises ~ 7% of blood proteins and has a molecular weight of 340 kDa and a hydrodynamic radius of ~ 10.7 nm [140]. Both proteins have an isoelectric point < pH 7.4 so are anionic at physiological pH and thus electrostatically attracted to chitosan.

Due to the highly porous nature of PGX hydrogels, protein adsorption versus absorption would be virtually impossible to decouple. As such, data was presented as a ‘protein uptake’ value per unit gel mass, as seen after 24 hours and 72 hours of incubation in protein-loaded solution, presented in Figure 52 and Figure 53 respectively.

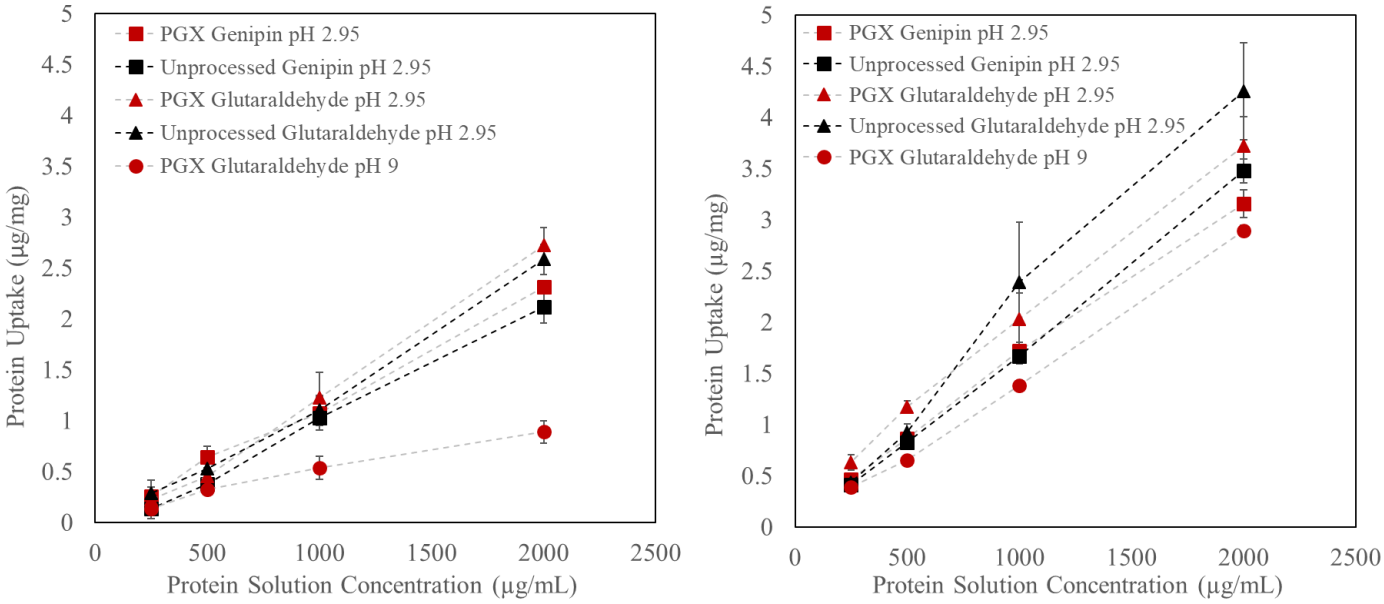

Figure 52: Protein uptake of albumin (left) and fibrinogen (right) by both PGX and unprocessed chitosan gels after 24 hours of incubation at 37°C in protein buffer solution at pH 7.4.

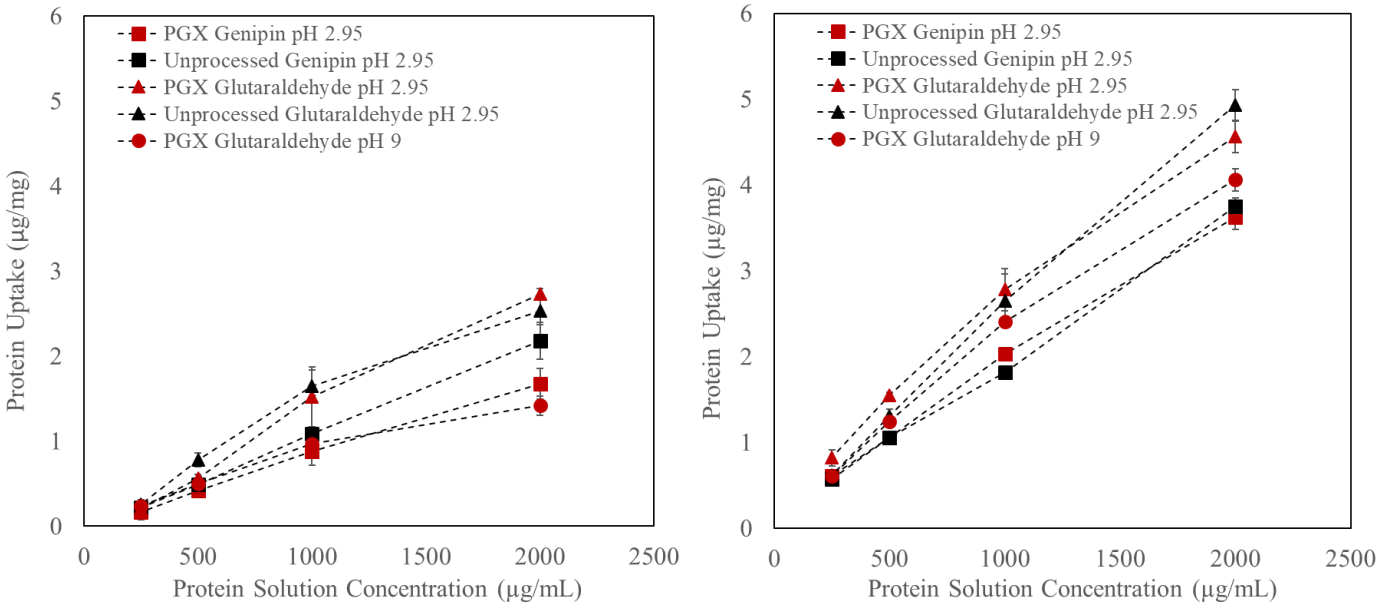

Figure 53: Protein uptake of albumin (left) and fibrinogen (right) by both PGX and unprocessed chitosan gels after 72 hours of incubation at 37°C in protein buffer solution at pH 7.4.

Increased protein uptake was observed with increasing protein solution concentration, with fibrinogen consistently exhibiting higher loadings than albumin for all formulations, despite its larger size which would likely reduce non-specific absorption into the gel matrix. We

attribute this increased uptake to the higher molecular weight of fibrinogen and, thus, the increased probability of interactions between the protein and the polymer scaffold. For both fibrinogen and albumin, there were only small and non-systematic difference between gels formulated using PGX-processed polymer and those prepared using unprocessed polymer, as well as between all of the different crosslinking chemistries chosen. One notable exception was the glutaraldehyde-crosslinked chitosan gel prepared at pH 9, which exhibited much lower uptake of BSA than the other gels at the 24-hour timepoint. It is hypothesized that this is due to residual carbonate buffer within the gel network, which acts as a poor solvent and causes the polymer to resist swelling (i.e. the network remains denser), making it more difficult for proteins to penetrate into the polymer matrix. By 72 hours, the PBS from the protein solution had sufficient time to diffuse into and neutralize the gel scaffold, at which point the BSA uptake of the chitosan-glutaraldehyde pH 9 gels were seen to catch up to the other formulations. Due to the significantly larger size of fibrinogen, absorption into polymer scaffolds is inherently more difficult, so the kinetic delay in protein uptake was not as notable.

In an attempt to elucidate the degree of absorption vs. adsorption of proteins in these gel networks, protein release from the scaffold was also tracked. We hypothesized that, upon placing gels into milli-Q water, adsorbed proteins would remain within the scaffold, while absorbed proteins would be free to diffuse out. Protein release from these gels was measured, as shown in Figure 54, while confocal microscopy images of the gels 24 hours after exposure to protein solution (to visualize the location of the protein within the polymer scaffold), are shown in Figure 55 and Figure 56 (with the polymer scaffold shown in red and the protein in green).

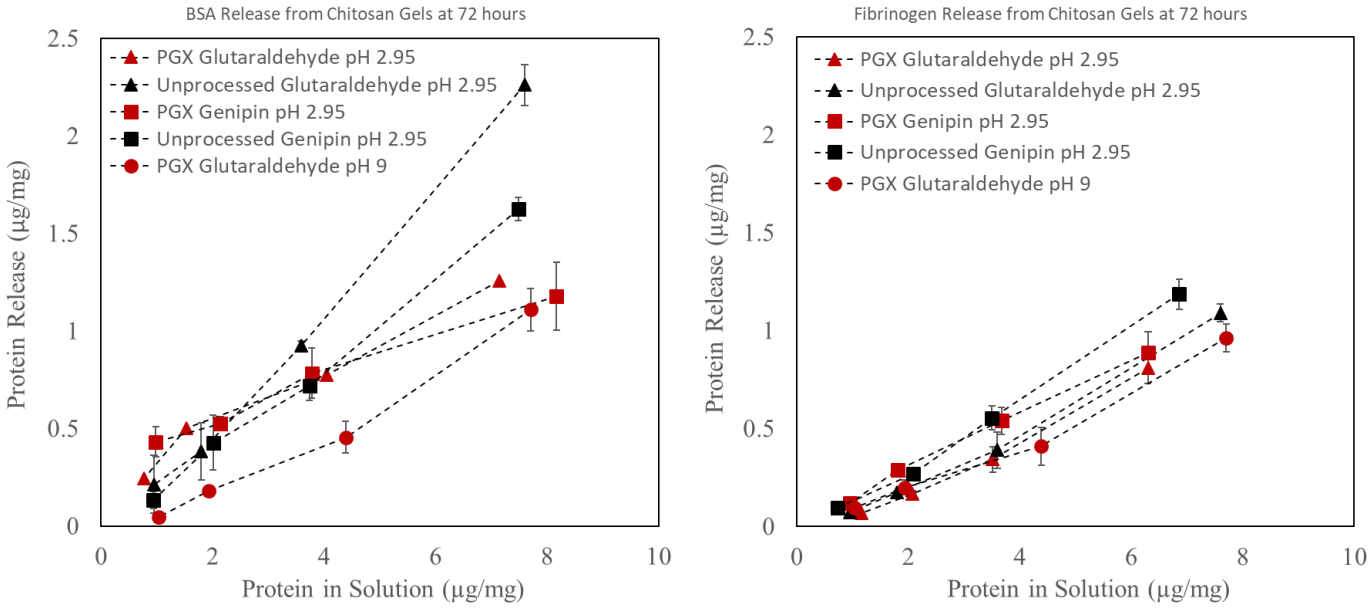

Figure 54: Protein release of albumin (left) and fibrinogen (right) for both PGX and unprocessed chitosan gels after 72 hours of incubation at 37°C in Milli-Q water. Reported protein masses on both axes are normalized by per mass unit of un-swollen alginate gel.

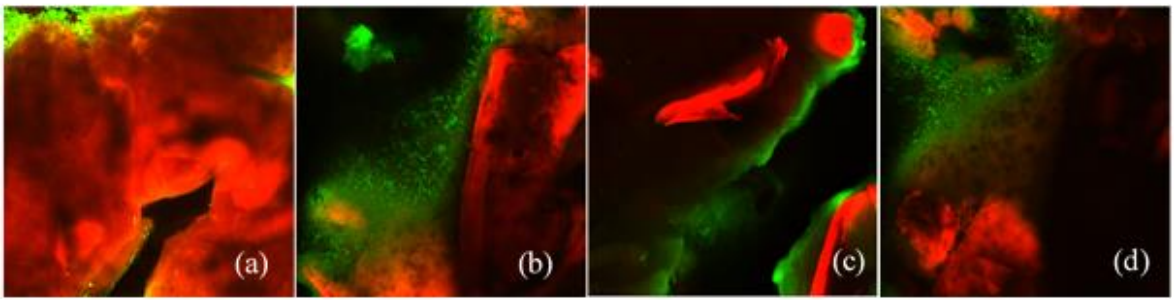

Figure 55: Protein uptake on PGX chitosan gels visualized via confocal microscopy after 24 hours of incubation in protein buffer solution (500 µg/mL): (a) fibrinogen in chitosan-genipin, (b) fibrinogen in chitosan-glutaraldehyde, (c) albumin in chitosan-glutaraldehyde, (d) albumin in chitosan-genipin.

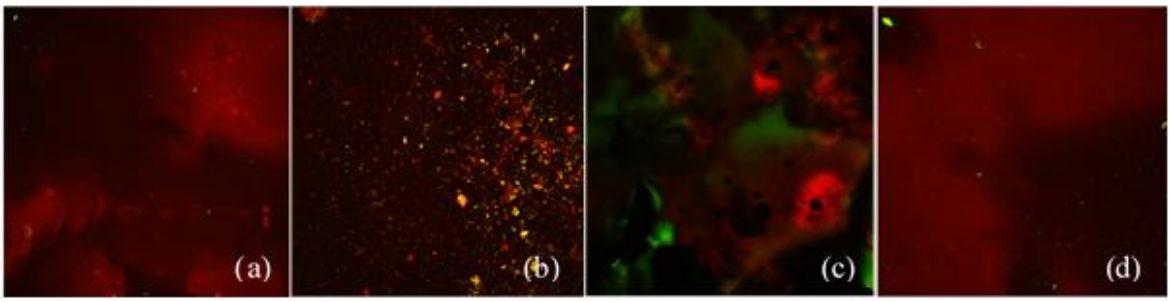

Figure 56: Protein uptake on unprocessed chitosan gels visualized via confocal microscopy after 24 hours of incubation in protein buffer solution (500 µg/mL): (a) fibrinogen in chitosan-genipin, (b) fibrinogen in chitosan-glutaraldehyde, (c) albumin in chitosan-glutaraldehyde, (d) albumin in chitosan-genipin.

The PGX processed scaffolds showed significantly slower protein release and a corresponding higher residual protein-derived fluorescence compared to unprocessed scaffolds, with very concentrated protein on the surface of the gel and relatively little elsewhere. In contrast, the protein location for unprocessed hydrogels was harder to assess via confocal microscopy, since the protein did not concentrate in specific areas of the scaffold and was overshadowed by the fluorescence from the polymer itself. Collectively, these results suggest that the majority of protein uptake observed for the PGX gels originated from protein adsorption (consistent with the micro/macroporous structure of PGX gels that yield higher internal surface areas), while a larger portion of the protein uptake measured for the non-PGX gels appeared to be from protein absorption into the scaffold. This result would mean that absorption is easier into unprocessed chitosan gels, which would be consistent with the locally higher polymer concentrations (and thus likely locally higher crosslink densities) achieved in the PGX gels. This conclusion is further supported by the larger release of protein from unprocessed versus PGX scaffolds seen in Figure 54, which is consistent with the presence of absorbed instead of adsorbed proteins.

3.3.7 *In Vitro Cytotoxicity*

The in vitro cytotoxicity of chitosan gel formulations was assessed using an MTS assay and 3T3 mouse fibroblasts cells. The results of the assay indicate that none of the gel formulations exhibit significant cytotoxicity ($p > 0.05$ in comparison to the positive control), and there was no significant difference between PGX and non-PGX formulations.

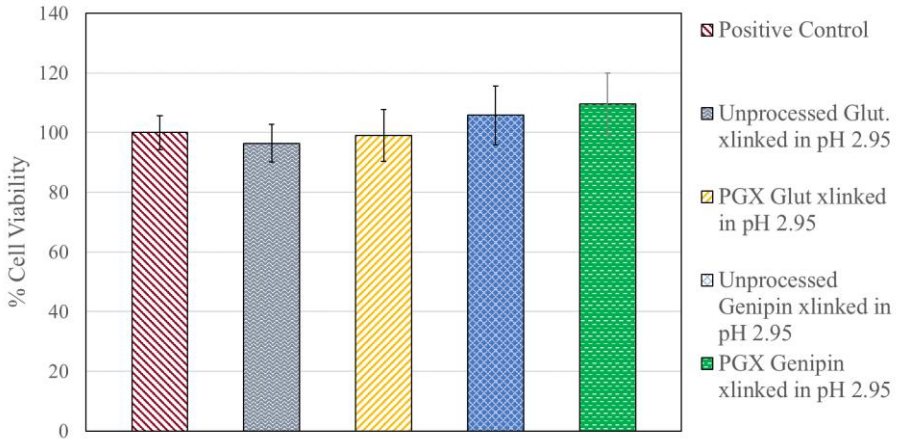

Figure 57: Relative viability of 3T3 mouse fibroblasts after exposure to chitosan gel formulations for 24 hours. All gel formulations were purified through dialysis for four rounds of 6+ hours prior to this study.

However, in larger scale production of these gels, the undoubted holdup would be the required dialysis of gels to remove unreacted toxic crosslinkers, namely glutaraldehyde. To eliminate the need for post-gelation purification, an aldehyde-functionalized long-chain POEGMA crosslinker was synthesized according to the method described in section 5.1.2.2. This aldehyde-functionalized polymer was subsequently used as an equivalent crosslinker to glutaraldehyde in pH 2.95 media, with the resulting gels subsequently exposed to 3T3 mouse fibroblast cells (without purification), alongside their glutaraldehyde-equivalent. As seen in Figure 58, the long chain crosslinker exhibited a significantly reduced cytotoxicity, eliminating the need for a purification step prior to in vitro or in vivo applications.

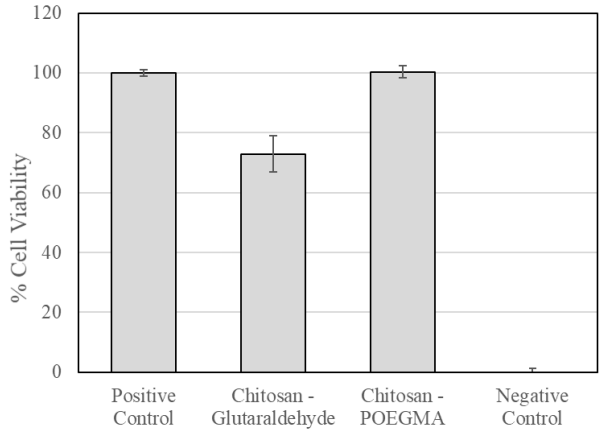

Figure 58: Relative viability of 3T3 mouse fibroblasts after exposure to unpurified PGX chitosan-POEGMA and PGX chitosan-glutaraldehyde gel formulations for 24 hours.

Similar to the effects observed for the glutaraldehyde trials conducted at pH ≥10 (Figure 39), in which glutaraldehyde polymerizes into a longer chain molecule that was sterically less accessible for crosslinking, the long-chain POEGMA crosslinker appeared to exhibit significant mass transfer problems. As a result, it was challenging to incorporate the amount of long-chain crosslinker necessary to reach the same extent of crosslinking as the glutaraldehyde gel formulation at pH 9. This was manifested as a decrease in mechanical strength when using the long-chain crosslinker, as seen in Figure 59.

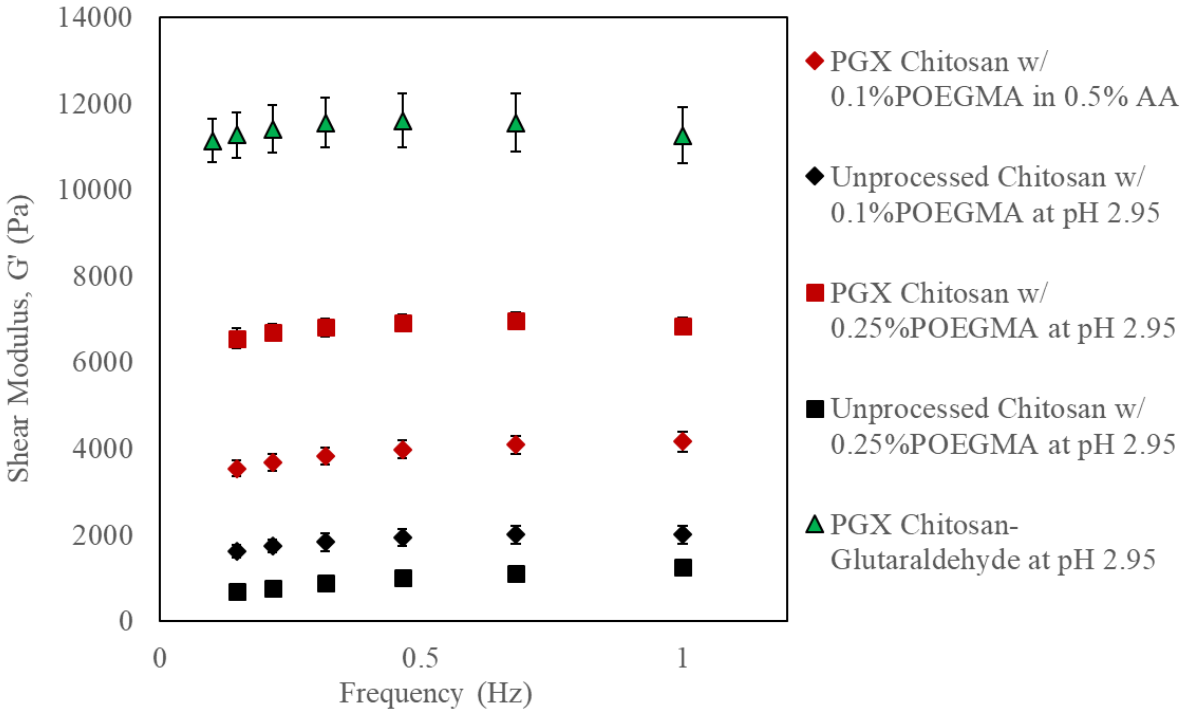

Figure 59: Elastic storage modulus (G') as a function of frequency for POEGMA-crosslinked chitosan gels, in comparison to chitosan gels crosslinked with glutaraldehyde.

In this context, while the POEGMA-aldehyde crosslinked gels are highly suitable for lower modulus biomedical applications, development of a long-chain crosslinker as an alternative to glutaraldehyde for higher modulus gels remain a work in progress. Particular effort will be invested into the development of a shorter chain length version of aldehyde-

POEGMA to lower the viscosity of the polymer solution and reduce mass-transfer related limitations.

3.4 Formulation and Characterization of PGX Alginate Hydrogel Scaffolds

Slow-gelling methods using $CaCO_3$ and GDL were employed to crosslink PGX morphologies via the chelation of calcium ions, as described in section 3.1.3. While ratios of G:M-units in alginate extracted from brown algae can vary from 60-70% [141], an average value of 70% G-units was considered in calculations of the molar equivalence of crosslinker. Theoretical degrees of crosslinking ranging from 50% to 200% were screened, with the former corresponding to one mole Ca^{2+} per two G-units. A 1:2 molar equivalence of $CaCO_3$:GDL was utilized in all formulations to maintain a neutral pH as the GDL hydrolyzes to free Ca^{2+} ions for crosslinking [142] . Increasing the crosslinker concentrations resulted in significantly faster gelation kinetics. While the gelation kinetics of semi-solubilized PGX-alginate could not be measured directly via test tube inversion, similar formulations investigated by Growney Kalaf et al. determined gelation times of 3 minutes (for the highest concentration of crosslinker) to 78 minutes (for the lowest concentration of crosslinker) over a similar range [115].

Table 9: Recipes for slow-gelling alginate formulations, with amounts and volumes reported for a single gel of 12.5 mm diameter and 1.5 mm height. Total polymer concentration and gel volume were held constant at 5wt% and 333 uL, respectively.

Alginate Gel Identification Code	**Theoretical Degree of Crosslinking**	**Amount of $CaCO_3$ [mg (mmol)]**	**Vol. $CaCO_3$ Solution (µL)**	**Amount of GDL [mg (mmol)]**	**Vol GDL Solution (µL)**
2:1 Alg:$CaCO_3$	50%	0.835 (0.0084)	283	2.97 (0.0167)	50
1:1 Alg:$CaCO_3$	100%	1.67 (0.0167)	232	5.95 (0.0334)	101
2:3 Alg:$CaCO_3$	150%	2.51 (0.0250)	182	8.92 (0.0501)	151
1:2 Alg:$CaCO_3$	200%	3.34 (0.0334)	131	11.9 (0.0668)	202

As a basis for comparison, rapid gelation methods using free calcium ions from $CaCl_2$ were also adapted to stabilize PGX morphologies and create useable gel shapes. This was done by filling a silicone mold, hydrating the scaffold with DIW, and subsequently pipetting the $CaCl_2$ solution over the top of the mold. Molar amounts of $CaCl_2$ were matched to make equivalent formulations to the $CaCO_3$ crosslinked gels with theoretical degrees crosslinking degrees of 150% and 200%, as seen in Table 10.

Table 10: Fast-gelling alginate recipes to form single gels of 12.5 mm diameter and 1.5 mm height. Total polymer concentration and gel volume were held constant at 5wt% and 333 uL respectively.

Alginate Gel Identification Code	**Theoretical Degree of Crosslinking**	**Amount of $CaCl_2$ [mg (mmol)]**	**Vol. $CaCl_2$ Solution (uL)**
2:3 Alg:$CaCO_3$	150%	2.77 (0.0250)	33
1:2 Alg:$CaCO_3$	200%	3.71 (0.0334)	33

3.4.1 *Hydrogel Rheology*

Since calcium-crosslinked alginate gels were formulated in DIW and alginate is readily soluble in DIW, the primary variable with respect to maintaining PGX structure was the gelation time. $CaCO_3$-crosslinked gels were produced from PGX-processed alginate and their shear elastic modulus was compared to the equivalent scaffolds formulated from non-PGX precursor polymers, as seen in Figure 60.

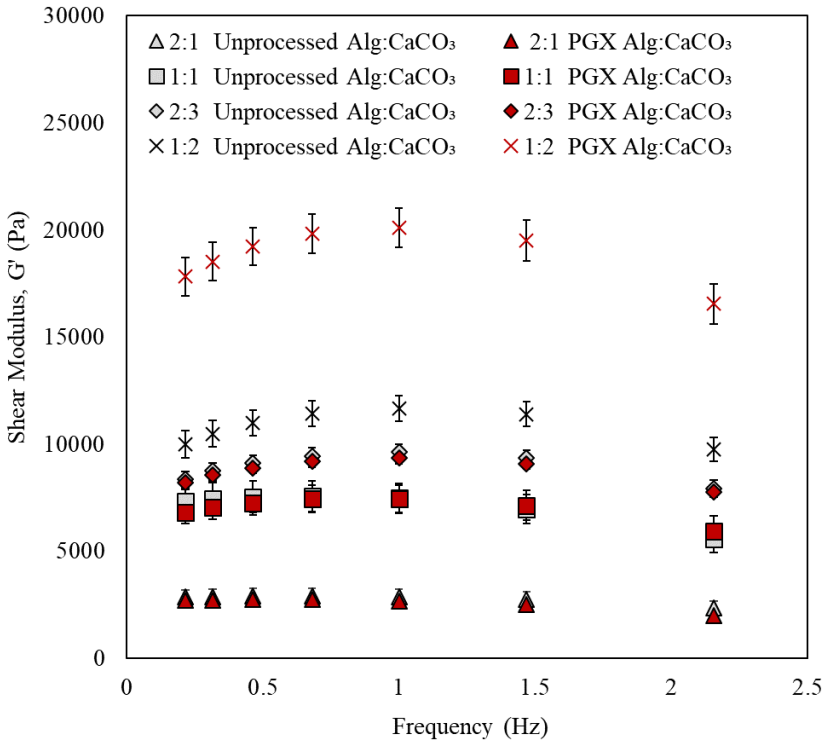

Figure 60: Elastic storage modulus (G') as a function of frequency for PGX and unprocessed $CaCO_3$-crosslinked alginate gels prepared with different crosslinker concentrations and gelation times.

Notably, there is no significant difference between the gels formulated using PGX alginate and those prepared using unprocessed alginate in the three slower gelling formulations (2:1 Alg:$CaCO_3$, 1:1 Alg:$CaCO_3$, and 2:3 Alg:$CaCO_3$), while the fastest-gelling formulation (1:2 Alg:$CaCO_3$) shows a significant increase in strength for the PGX gel with a G' ~ 10 kPa greater than its unprocessed equivalent. This increase in strength suggests that much of the PGX structure is preserved in the fastest-gelling formulation while the majority of the PGX structure appears to be lost in reactions with slower gelation kinetics, making such gels structurally similar or equivalent to gels prepared directly from alginate solutions. In particular, the much higher mechanical strength of the 1:2 Alg:$CaCO_3$ formulation suggests that the high interconnectivity of the PGX alginate network (when maintained) allows for the tight binding of calcium ions within

PGX micro- and nano-fibres, resulting in hydrogels that are much stronger than the homogeneously crosslinked alternatives.

$CaCl_2$ crosslinking facilitates the fabrication of even stiffer gels (Figure 61), exhibiting G' values at minimum ~ 30 kPa greater than those of the strongest $CaCO_3$-crosslinked formulation and, at the 2:3 Alg:$CaCl_2$ ratio, shear storage moduli as high as ~50 kPa. However, they also showed much greater variability, with standard errors on the range of 0.5-1 kPa compared to the <0.1 kPa errors shown by $CaCO_3$ crosslinked formulations. This is indicative of the much less consistent gelation patterns during the rapid binding of free calcium ions from $CaCl_2$, with the diffusivity of subsequent calcium ions past the rapidly gelled interface and into the gel structure drastically inhibited and thus the crosslink densities (and ultimately mechanics) of the gel much more dependent on the local structuring of the PGX product.

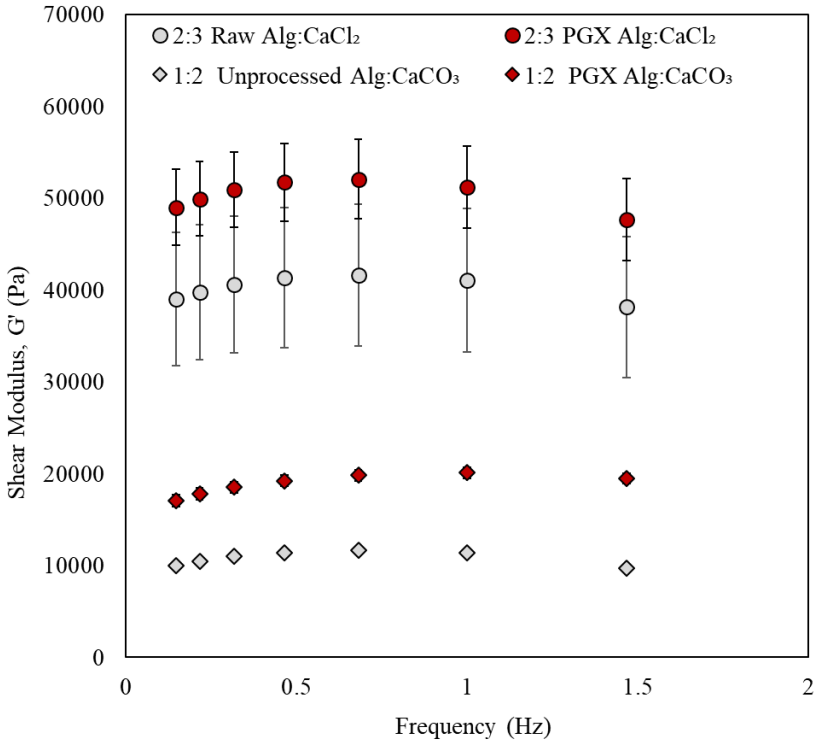

Figure 61: Elastic storage modulus (G') as a function of frequency for PGX and unprocessed $CaCl_2$-crosslinked alginate gels plotted in comparison to the strongest $CaCO_3$-crosslinked formulation.

3.4.2 *Imaging of PGX Alginate and its Hydrogel Scaffolds*

The structure of PGX-processed alginate (in a dry state prior to crosslinking reactions) was analyzed by photography and scanning electron microscopy (SEM), the results of which are shown in Figure 62.

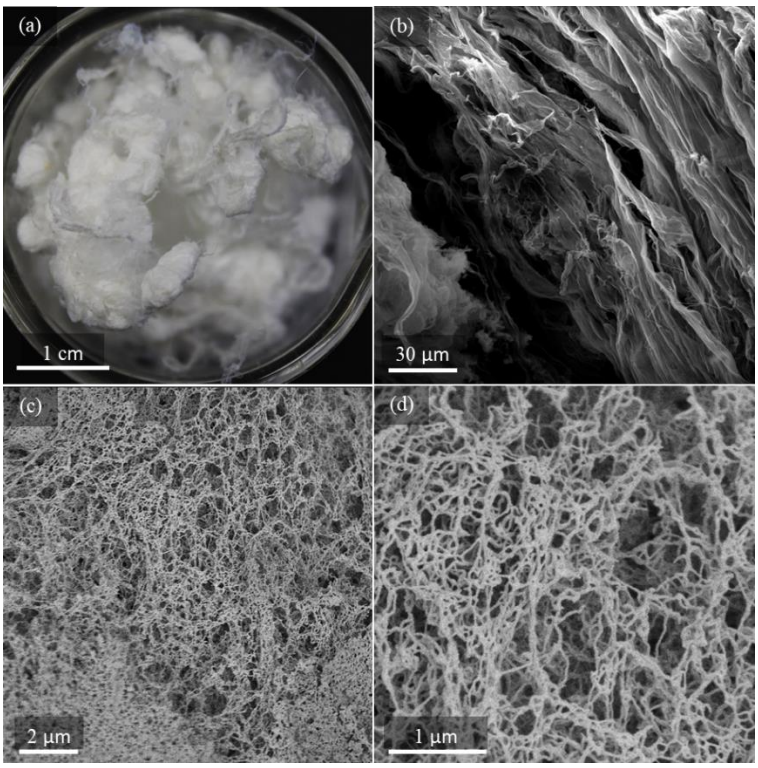

Figure 62: Structure of PGX-processed alginate prior to crosslinking: (a) photograph of PGX processed sodium alginate, (b-d) SEM images of PGX sodium alginate at 1000x, 15,000x, and 50,000x magnification.

In comparison to the PGX-structure of chitosan, processed alginate exhibits a much more fibrillar structure on a macro-scale, featuring highly-exfoliated, irregular fibres with diameters on a 1-5 mm length scale (Figure 62a). SEM imaging shows that these visible fibres are comprised of successive hierarchical bundles of smaller fibres of discrete sizes, with nanofibres of 50-100 nm diameters (Figure 67d) organizing into micro-scale fibrous assemblies on the order of ~50µm in diameter. Hence, PGX-alginate is both highly networked and highly porous, with very high apparent surface areas (Table 2).

3.4.2.1 *Scanning Electron Microscopy of Lyophilized Hydrogel Scaffolds*

The fastest gelling $CaCO_3$-crosslinked alginate gels (1:2 Alg:$CaCO_3$) made from both PGX-processed and unprocessed precursor polymers, were flash-frozen, lyophilized, and imaged using SEM in an attempt to visualize the residual pore structure after hydration and crosslinking in DIW, again with the caveat that the freeze drying process often produces artefactual macroporosity in hydrogels due to ice crystal formation; as such, the goal of this work was to compare the residual structures with and without PGX processing rather than to confidently report the quantitative porosities of each hydrogel system. Despite their stiffer mechanics (which would typically inhibit pore generation via ice crystal formation), PGX gels exhibited significantly greater porosity than the unprocessed gels, featuring highly interconnected pore networks of multi-scale sizes (Figure 63).

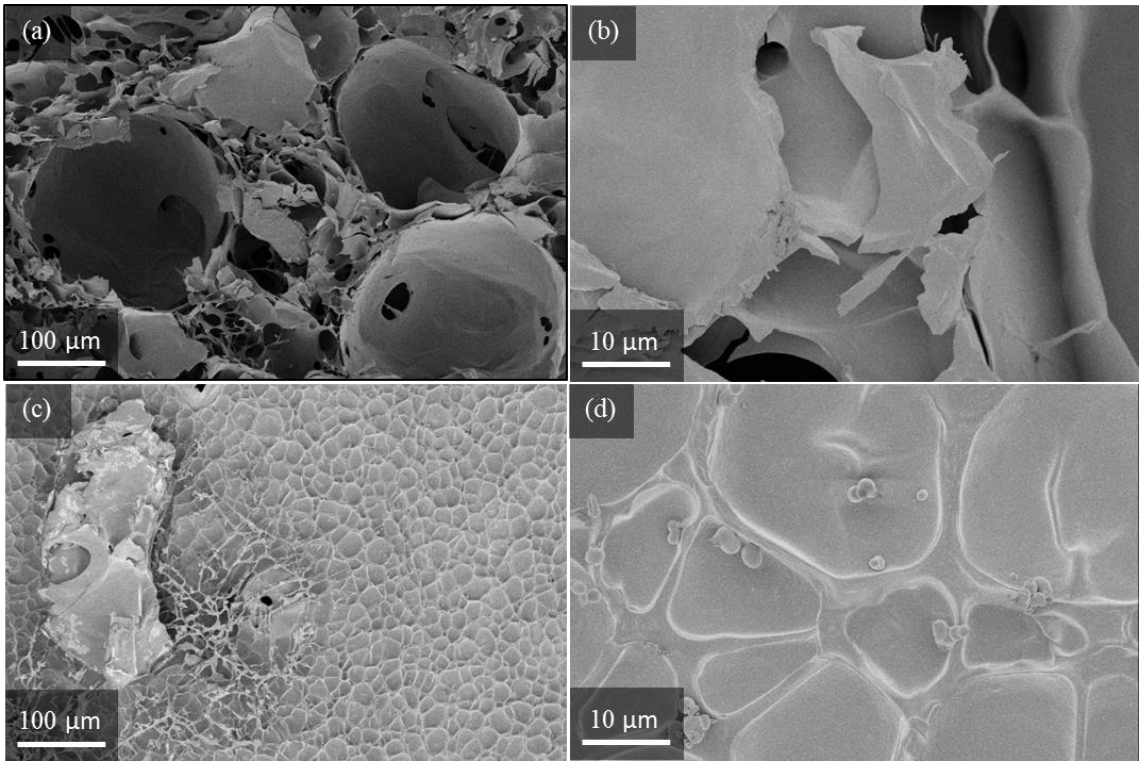

Figure 63: SEM images of calcium carbonate crosslinked alginate gels prepared using a 1:2 ratio of Alg:$CaCO_3$: (a-b) gels prepared from PGX-processed alginate at 500x, and 5000x magnification, (c-d) gels prepared with unprocessed alginate at 500x, and 5000x magnification.

It must be noted that the crosslinking reaction generates bicarbonate and/or carbonic acid gas, resulting in the formation of air bubbles in addition to the existing porosity of the PGX-generated network; in this context, the ~100-200 µm diameter highly spherical pores observed in Figure 63(a-b) were assumed to be the result of entrapped gas while the smaller pores (~ 10-50 µm in diameter) were thought to have been templated by the original PGX-processed scaffold. In comparison, the unprocessed alginate gels exhibit circular imprints (Figure 63(e)) that are hypothesized to correlate with the discrete and poorly interconnected air bubbles trapped within the dried network. Of note, the 10-40 µm diameter of the air bubbles observed in the unprocessed alginate gels are significantly smaller than those observed in the PGX-processed gels. This contrast was likely caused by the increased initial porosity in the PGX alginate gels, allowing generated gas to diffuse through the scaffold and coalesce, while movement of generated gas in the non-PGX scaffold is highly restricted by surface tension and viscosity. Neither scaffold exhibited the nanoscale fibrosity observed in the uncrosslinked and unhydrated PGX-alginate, consistent with, at minimum, small degrees of hydration prior to gelation that would very quickly result in the dissolution of the nanoscale fibres.

3.4.3 *Swelling and Degradation Kinetics*

Swelling and degradation kinetics for alginate gels were conducted at 37^{o}C in DIW, as well as 10 mM HEPES buffered saline solution. This buffer solution was selected for use in alginate trials instead of PBS due to the known ability of phosphate ions to precipitate with crosslink-forming Ca^{2+}, effectively reducing the concentration of Ca^{2+} available for crosslinking and thus accelerating the degradation of calcium-crosslinked alginate structures [129]. Interestingly, alginate gels formulated with PGX-processed or unprocessed polymers (as well as with different sources of calcium ion) all showed relatively similar swelling profiles in DIW, as

seen in Figure 64, while PGX-processed and unprocessed formulations behaved differently in HEPES buffered saline (Figure 65).

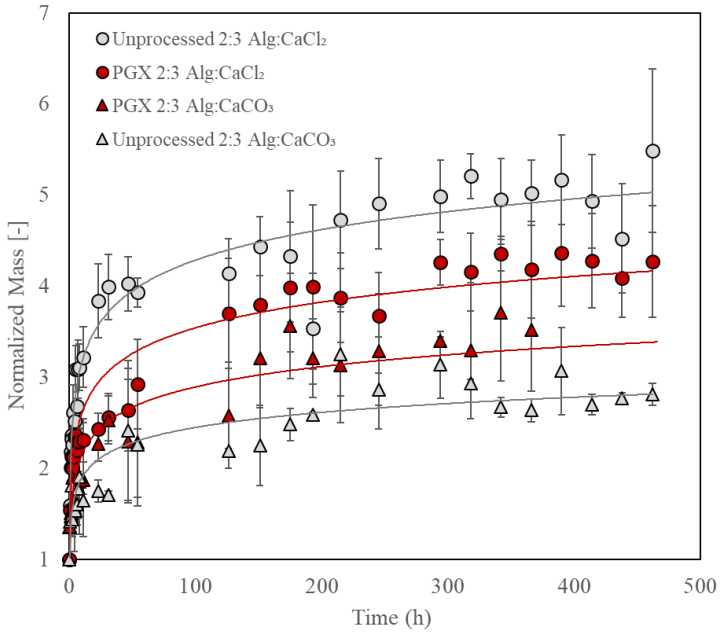

Figure 64: Swelling and degradation kinetics of alginate gels measured in DIW at 37°C and fit with logarithmic trendlines

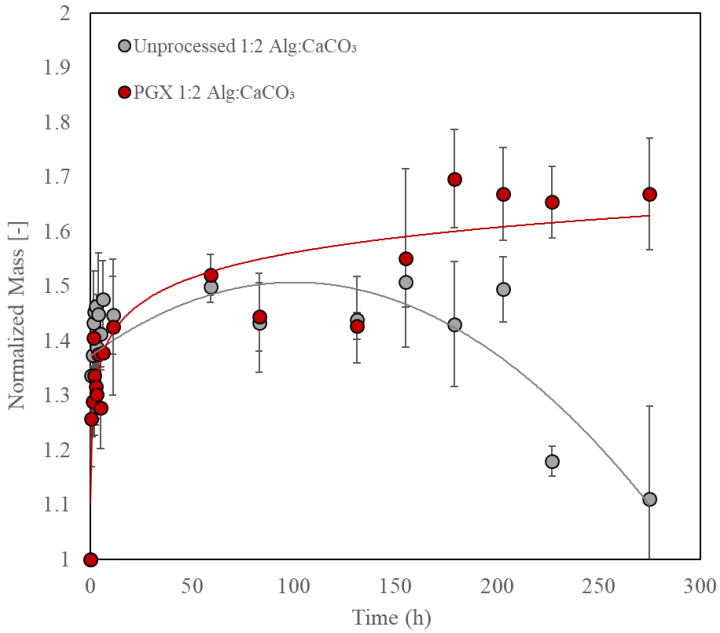

Figure 65: Swelling and degradation kinetics of alginate gels, measured in 10 mM HEPES buffered saline at 37°C and fit with logarithmic (PGX) and polynomial (unprocessed) trendlines.

As expected, gel degradation in DIW was not observed (even after 500 hours), as there were very few ions in solution with which to undergo ion exchange processes with the calcium ion crosslinker. $CaCl_2$ crosslinked gels swelled more than $CaCO_3$ crosslinked gels, but also underwent substantially more inhomogeneous swelling, including the loss of the original disc-shape of the gels. This was indicative of the tendency for $CaCl_2$-crosslinked gels to very tightly bind calcium in some sections but not at all in others due to the extremely fast kinetics of the crosslinking interaction, as previously discussed in section 3.1.3. Furthermore, $CaCO_3$-crosslinked gels prepared using PGX-processed alginate exhibited a slightly higher degree of swelling than those formulated using unprocessed alginate. This was attributed to the high interconnectivity of the PGX pore structure, and thus, the ease with which water could diffuse into the scaffold, accelerating swelling responses even in what appears to be a more highly crosslinked local network.

In HEPES buffered saline solution, PGX gels again exhibited a higher overall degree of swelling. However, PGX gels remained stable past 300 hours, while the non-PGX gels began to degrade after 200 hours. This data supported the conclusion that the interconnectivity and localized polymer density of the PGX alginate network allows for tighter binding of calcium ions within PGX fibres, resulting in stronger and more durable hydrogels.

3.4.4 *Protein Uptake*

Protein uptake by alginate hydrogel scaffolds from PBS was subsequently measured to assess differences in the pore structure and macromolecular affinity of various network structures of alginate. As with chitosan, the highly porous nature of PGX hydrogels makes protein adsorption versus absorption virtually impossible to decouple; as such, data was presented as a

'protein uptake' value, normalized by gel mass, as seen in Figure 66 (after 24 hours of incubation) and Figure 67 (after 72 hours of incubation).

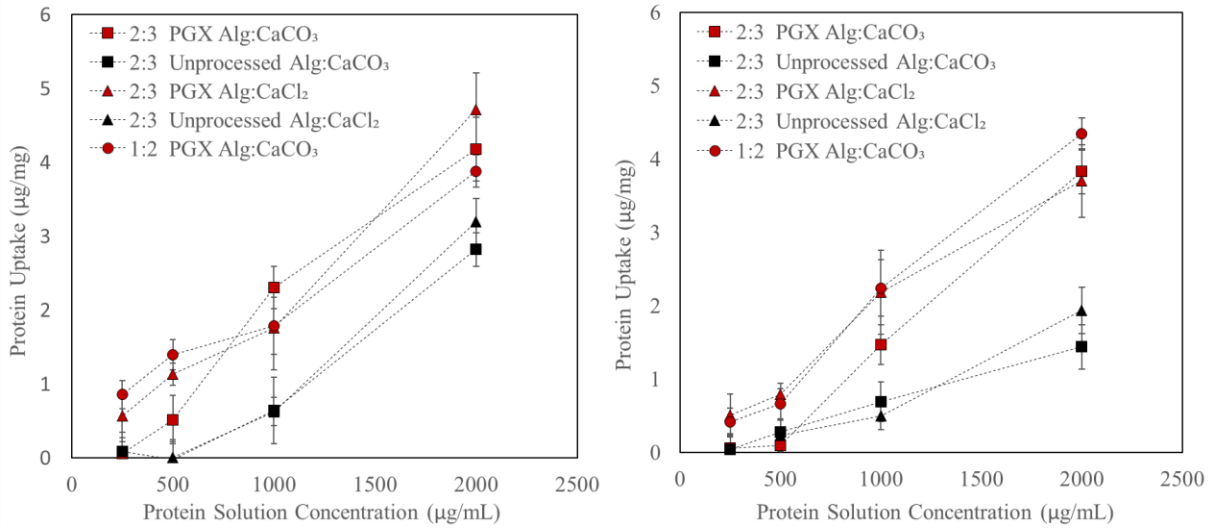

Figure 66: Protein uptake of albumin (left) and fibrinogen (right) by both PGX and unprocessed alginate gels after 24 hours of incubation at 37°C in protein buffer solution.

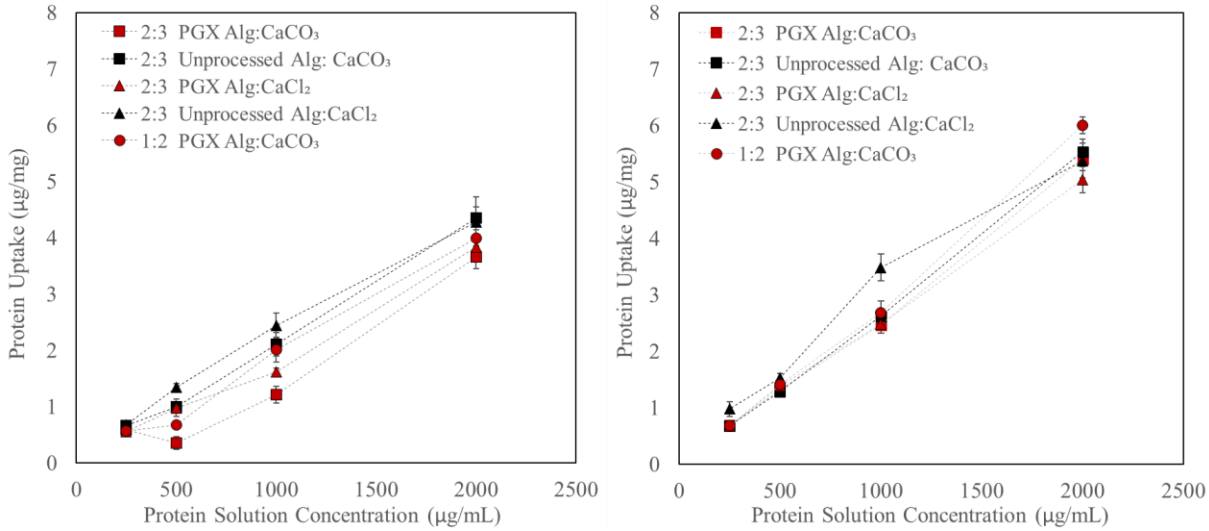

Figure 67: Protein uptake of albumin (left) and fibrinogen (right) by both PGX and unprocessed alginate gels after 72 hours of incubation at 37°C in protein buffer solution.

Increased protein uptakes were observed with increasing protein solution concentration, with albumin and fibrinogen showing relatively similar loadings into both scaffolds. Protein uptakes of both fibrinogen and albumin after 24 hours were observed to be significantly higher in

the gels formulated using PGX-processed alginate than those prepared from unprocessed alginate. We hypothesized that this result is related to the interconnectivity of the PGX-templated pore network and the ease with which proteins are able to diffuse through the pores and into the hydrogel, although the increased surface area of the macroporous PGX gels is also likely to enhance local adsorption of protein (both on and within the hydrogel network). After 72 hours however, no significant difference in protein uptake was observed between the unprocessed and PGX hydrogels, likely the result of enough time being provided for protein to diffuse into the less porous (and thus less accessible) network of the unprocessed scaffolds.

In an attempt to understand the absorption vs. adsorption tendencies of proteins in these gel networks, protein release from the scaffold was also tracked, as shown in Figure 68. Gels were incubated in HEPES buffered saline following protein uptake, allowing release of absorbed protein but likely significant retention of adsorbed protein. Confocal microscopy images of the gels were collected in conjunction with the quantitative release analysis to visualize the location of the protein within the polymer scaffold, the results of which are shown in Figure 69.

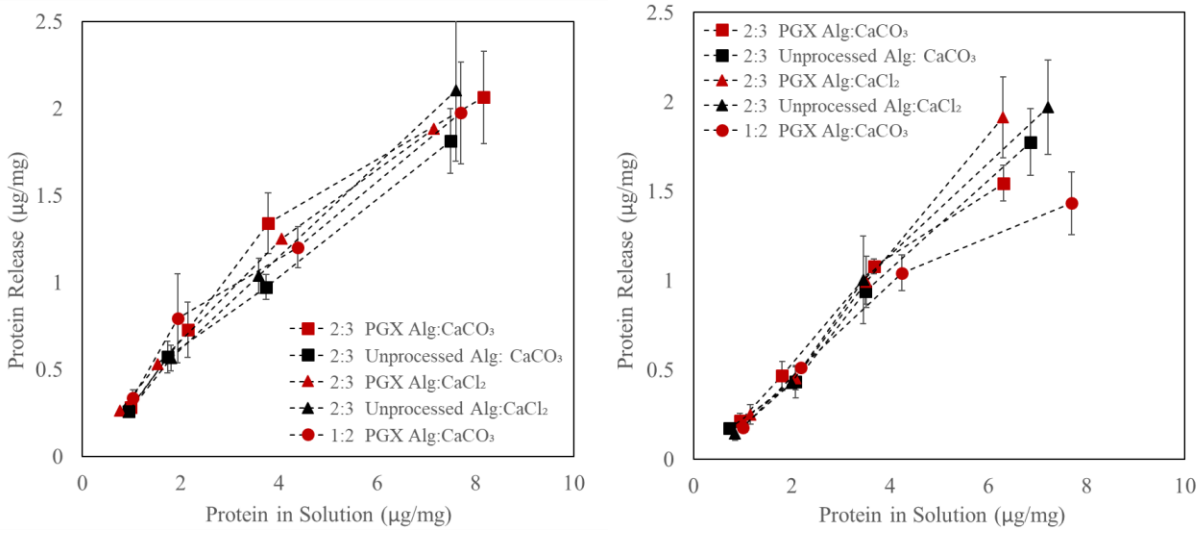

Figure 68: Protein release of albumin (left) and fibrinogen (right) from both PGX and unprocessed alginate gels after 72 hours of incubation at 37°C in DIW. Reported protein masses on both axes are normalized by per mass unit of un-swollen alginate gel.

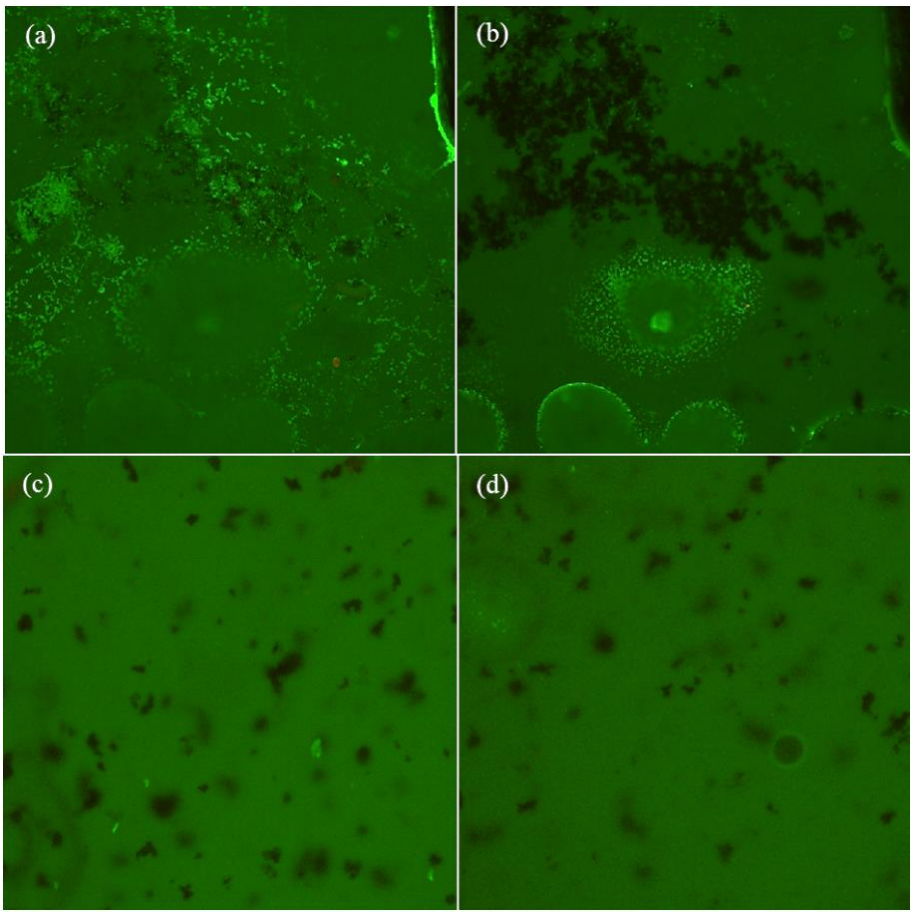

Figure 69: Protein uptake on PGX and unprocessed alginate scaffolds visualized via confocal microscopy after 24 hours of incubation in protein buffer solution (500 µg/mL): (a) PGX 2:1 $CaCO_3$:Alg in albumin (b) PGX 2:1 $CaCO_3$:Alg in fibrinogen (c) Unprocessed 2:1 $CaCO_3$:Alg in albumin, (d) Unprocessed 2:1 $CaCO_3$:Alg in fibrinogen

Contrary to what was expected, protein release data did not show any significant difference between the release from PGX scaffolds and from non-PGX scaffolds (Figure 68) and the release in each case was directly proportional to the loading, suggestive of a purely equilibrium driven diffusional release mechanism. Confocal images taken after 24 hours showed slightly more concentrated protein on/around the porous surfaces of PGX gels with proteins distributed more homogenously throughout the non-PGX gels, consistent with the internal micro/nanofibrous morphology of the PGX-gels versus the more homogeneous internal morphology of the unprocessed gels.

3.4.5 *Cytotoxicity*

The in vitro cytotoxicity of alginate gel formulations was assessed using an MTS assay and 3T3 mouse fibroblasts cells. The results of the assay indicated that none of the gel formulations exhibit significant cytotoxicity. In fact, it was noted that both $CaCO_3$ and $CaCl_2$ crosslinked gels were shown to significantly increase cell proliferation ($p < 0.05$ in comparison to the positive control), consistent with the addition of calcium ions stimulating the calcium signalling pathway as discussed in section 3.1.4.

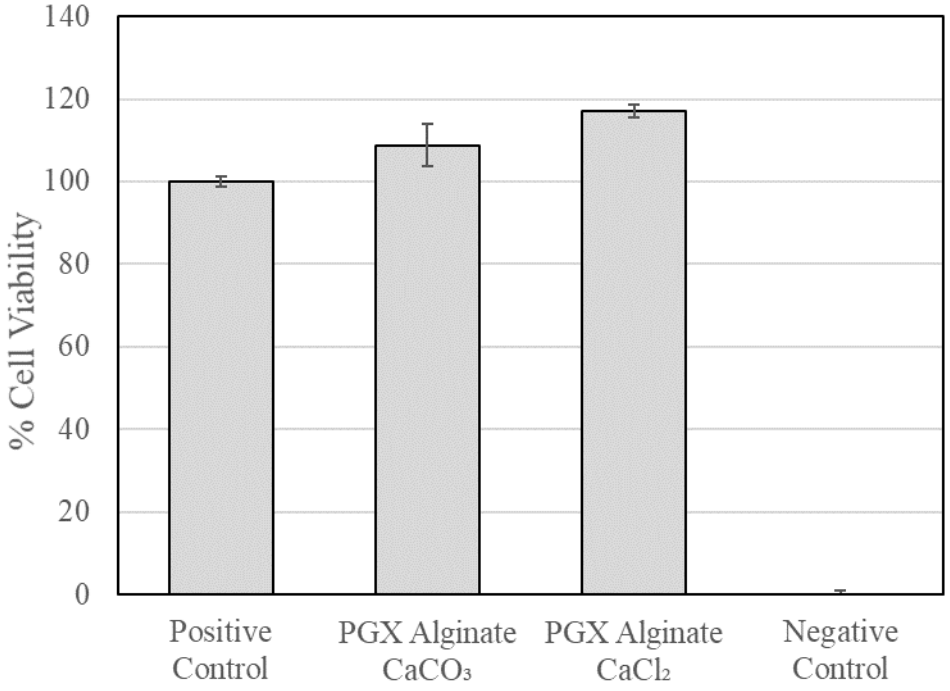

Figure 70: Relative viability of 3T3 mouse fibroblasts after exposure to $CaCO_3$ or $CaCl_2$-crosslinked PGX alginate gel formulations for 24 hours.

3.5 Conclusions

Gel formulations with multi-scale, interconnected pore structures have been developed using PGX-processed chitosan and alginate precursor polymers. The reaction kinetics of these hydrogel formulations were tuned by varying the time, temperature, pH, and crosslinker

concentrations used to prepare the gels, and the structures of the resulting hydrogels analyzed through SEM, HiM, and confocal microscopy to determine the amount of PGX-structure remaining after crosslinking and hydration. In cases in which crosslinking occurred relatively quickly, macroporosity was maintained while nano-scale fibres and pore networks were lost; for more slowly crosslinking systems, minimal differences were observed relative to conventional hydrogel systems in most cases.

Hydrogel formulations were also shown to exhibit tunability in elastic storage moduli as a function of crosslinker concentration and/or reaction conditions, exhibiting plateau G' values ranging from 2-40 kPa. This broad range of elastic storage modulus values could make these gel formulations applicable for a wide range of potential tissue replacements, as seen in Figure 71.

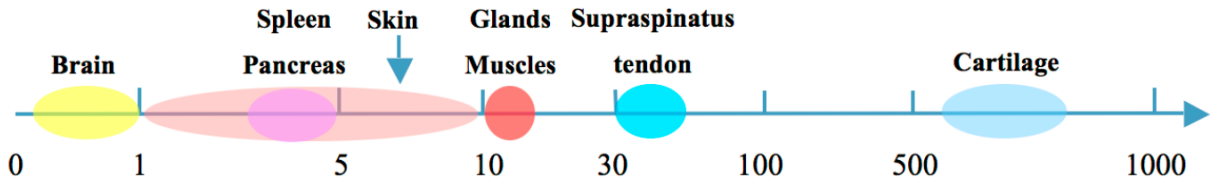

Figure 71: Observed elastic moduli from various native human tissues. Reproduced from [143].

Metabolic assays conducted on both chitosan and alginate hydrogels showed no statistically significant cytotoxicity after scaffolds were purified; however, residual glutaraldehyde in unpurified chitosan scaffolds was shown to have a significant cytotoxic effect. To eliminate the need for dialysis prior to in vivo applications, a preliminary investigation into the use of an aldehyde-functionalized oligomeric POEGMA crosslinker was pursued. This long-chain crosslinker was shown to significantly improve cell viability when exposed to unpurified hydrogel scaffolds, but further effort is required to achieve the same mechanical strength as the glutaraldehyde-crosslinked formulations.

Chapter 4 – Impregnation/Release from PGX Hydrogel Scaffolds

Conventionally, the preparation of drug loaded polymer matrices was a multi-step process consisting of three primary stages: (1) dissolution of the active pharmaceutical ingredient into an appropriate solvent, (2) submersion of the polymer matrix into the drug loaded solvent and subsequent diffusion of drug into the polymer scaffold, (3) removal of the polymer matrix from solution and elimination of residual solvent and unbound solute from the network [144]. Not only is this a time-consuming process, but it often leaves residual solvent behind in the scaffold that can introduce issues with in vivo cytotoxicity and effectively influence drug release kinetics.

Supercritical fluids have emerged as an obvious alternative to this passive diffusion method of drug loading, allowing for the processing of materials at ambient temperatures and high pressures (10-20 MPa), and without the use of organic solvents [145]. Particularly in the case of poorly water-soluble organic molecules, using $scCO_2$ as the mobile phase provides the distinct advantage of being able to solubilize a chemical compound, transport it through the impregnation system, and deposit it into a controlled polymer matrix without disrupting the pore structure or leaving behind residual organics/surfactants [146].

An additional advantage of using $scCO_2$ in the impregnation of small molecules is the ability of the supercritical fluid to purify drug/bioactive components and isolate them in nanocrystalline or micronized form. As a compressible gas like $scCO_2$ solubilizes a small molecule under high pressure, the small molecule will become dispersed throughout the fluid (as in a liquid solution). The subsequent expansion of the supercritical fluid causes a rapid supersaturation and reprecipitation of the solute, nucleating the formation of many tiny solute particles throughout the system [147]. The larger surface-to-volume ratios of these micron-sized particles offer significantly more favourable solubility/mass transfer kinetics relative to larger

drug crystallites. For example, Kerc et. al. micronized nifedipine, felodipine, and fenofibrate and observed dissolutions rates that were 5-10x higher than physically incorporated drugs not treated with $scCO_2$ [147].

Ni et. al. investigated the use of $scCO_2$ for impregnating ibuprofen into mesoporous silica without the use of co-solvents. They determined that scCO2 was an effective and clean solvent for deposition of ibuprofen, with maximum drug loadings of 41.96 wt.% [148]. By leveraging a similar impregnation process in combination with the high porosity of PGX-processed biopolymers, there is significant potential to develop hydrogels with unusually high loading capacities of highly available hydrophobic drugs.

4.1 Materials and Methods

4.1.1 *Materials*

Sodium alginate (alginic acid sodium salt, Sigma Aldrich), chitosan with molecular weights of 310,000-375,000 Da (deacetylated chitin, Sigma Aldrich, ≥ 75 % deacetylated), methacrylated starch from corn, and methacrylated pectin were processed using the PGX system as previously described in section 2.2.2.6. Methacrylation reactions on starch (Sigma Aldrich, practical grade) and pectin from citrus peel (Sigma Aldrich, Galacturonic acid ≥ 74.0 %) were conducted using sodium carbonate (Sigma Aldrich, BioXtra, >99.0%) and methacrylic anhydride (Sigma Aldrich, 94%) to allow for potential photocrosslinking with Irgacure 2959. 1-(4-(2-Hydroxyethoxy)-phenyl)-2-hydroxy-2-methyl-1-propane-1-one (Ciba® Irgacure 2959, Ciba Specialty Chemicals) was impregnated onto PGX-processed methacrylated polymer scaffolds to evaluate the potential of photocrosslinking reactions, while α-Methyl-4-(isobutyl)phenylacetic acid, (±)-2-(4-Isobutylphenyl)propanoic acid (Ibuprofen, Sigma Aldrich, ≥ 98 % by GC) was

impregnated onto PGX-processed chitosan and alginate scaffolds which were subsequently gelled and used as drug delivery vehicles. All impregnations were conducted using compressed CO_2 with a liquid withdrawal tube (Air Liquide Canada, 99.5%). Solvents required for HPLC separations of ibuprofen were Milli-Q grade distilled and deionized water, glacial acetic acid (LabChem Inc, ACS Grade, ≥ 99.7%), and acetonitrile (Fisher Scientific, LC/MS Grade, 99.9%).

4.1.2 *Methods*

4.1.2.1 *Methacrylation of Starch and Pectin*

Starch and pectin samples were functionalized with a methacrylate group prior to PGX-processing to allow for photocrosslinking with Irgacure 2959. This reaction was conducted by dissolving 50 grams of polymer to 7.5wt% in DIW at 80°C and allowing it to stir for 10 minutes. Sodium carbonate was added to 0.1wt% to assist in the dissolution process and the pH of the solution was adjusted to ~10.4 using 1M NaOH. Methacrylic anhydride was subsequently added over 1 hour through 10 additions of 475 µL while maintaining pH at ~ 10.4 using 1M NaOH. Once additions of methacrylic anhydride were complete, pH was adjusted to 11 and the reaction was stirred for an additional 30 minutes, at which point the solution was neutralized with 1M HCl and transferred into dialysis tubing. Reaction products were dialyzed against DIW for a minimum of 6 (6+ hour) cycles and lyophilized to dryness.

4.1.2.2 *Standard Impregnation Method Using PGX*

To prepare for a standard impregnation run, the PGX system was reconfigured to incorporate a continuous recycle loop of CO_2 through the standard 5L collection vessel. The collection basket for the vessel was fitted with filter pads (as described in section 2.2.2.4) and filled partially with packing material consisting of either marbles or perforated stainless steel

discs. Known masses of the PGX-processed polymer network that was to be impregnated and the small molecule of interest were placed into filter sacs and loaded into the pressure vessel, separated by additional packing material, as illustrated in Figure 72.

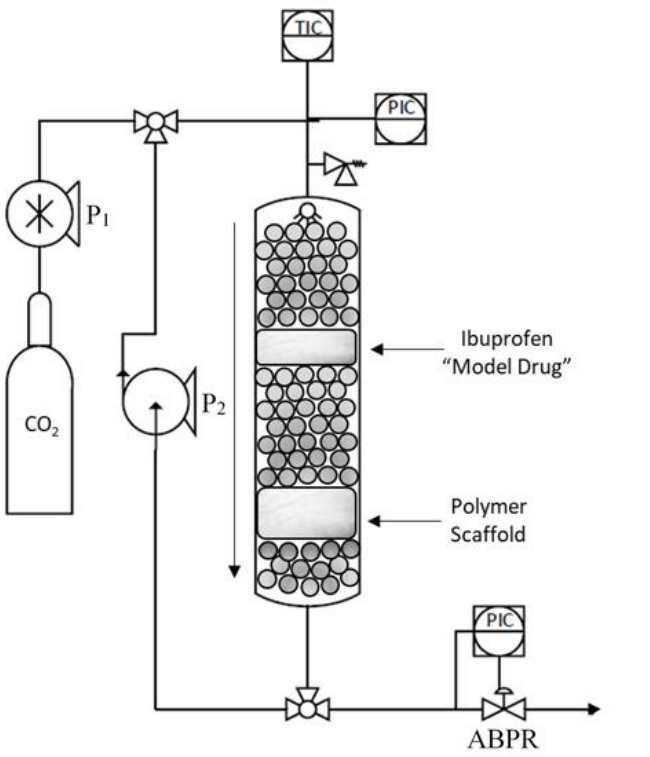

Figure 72: Simplified process flow diagram for PGX system, reconfigured for in situ impregnation of drugs, photoinitiators, or other bioactive molecules.

Once the pressure vessel was loaded and sealed, the automatic back-pressure regulator (ABPR) was closed, the system heated to 50°C and the CO_2 tanks were opened to allow gas into the vessel. The CO_2 pressurization pump (P_1) was subsequently started to pressurize the vessel to 150 bar, creating a pressure and temperature combination at which CO_2 gas exists as a supercritical fluid. When the system had reached the desired temperature and pressure, P_1 was stopped, the vessel was isolated, and the CO_2 recirculation pump (P_2) started at a flowrate of 5 mL/min for 60 – 90 minutes. Following recirculation, the collection vessel was depressurized and the collection basket was removed to recover the impregnated polymer matrix and any

residual active component. The mass of impregnated active molecule was estimated immediately using gravimetric analysis as well as UV/Vis-spectrophotometry, as described in section 4.1.2.3.

4.1.2.3 *Determination of Drug Loading via UV Spectrophotometry*

A known mass (10 mg) of each drug-impregnated sample was placed in a microcentrifuge tube and 2 mL of anhydrous EtOH (in which the drug is very soluble and the carbohydrate is completely insoluble) was added. The sample-containing tubes were placed on an orbital shaker for two hours and then centrifuged at 6000 RPM for 10 minutes to separate solids. The supernatant was subsequently removed, while the pellet was suspended in an additional 2 mL of anhydrous EtOH. The shaking and centrifuging process was repeated to solubilize and separate any residual drug and the supernatants from each respective sample combined. Three replicates of each drug-impregnated polymer were prepared according to this process, and the absorbance of their supernatants analyzed at a wavelength of λ=275nm. Collected absorbance values were compared to a calibration curve of known concentrations (ranging from 0 mg/mL to 4 mg/mL) of ibuprofen in EtOH and a linear calibration curve ($R^2 \geq 0.99$) observed. The weight percentage of drug impregnated in each sample was back-calculated from obtained concentrations values, with the error bars representing the standard error of all replicates collected.

4.1.2.4 *Collection of In Vitro Drug Release Samples*

Ibuprofen-loaded hydrogels were prepared using the gelation methods described in sections 3.2.2.3, 3.2.2.4, 3.2.2.5, and 3.2.2.6, but using drug-loaded precursor carbohydrates instead of pure carbohydrates. Once fully cured, hydrogels were placed in 12-well or 6-well plates filled with 1.5 or 5 mL of buffer solution respectively. At pre-determined time points, 1.5

mL samples were collected from each well and stored. Residual buffer in the well plates was fully removed and replenished with the same volume of fresh buffer. Collected release samples were subsequently filtered using 13mm filter discs (pore size = 0.2 μm, holdup volume after air purge = 28 μL, Supor® 200 hydrophilic polyethersulfone membrane (Acrodisc®)) and transferred into 1.8 mL HPLC vials (VWR). Samples were collected in quadruplicate (i.e. four independent drug loaded gels for each gel formulation) and stored in the dark at 4°C until quantification, as described in section 4.1.2.5.

4.1.2.5 *Quantification of In Vitro Drug Release Kinetics by LC-MS/MS Analysis*

Drug quantification experiments were performed on an LC-MS/MS system consisting of an LTQ Orbitrap XL mass spectrometer (Thermo Scientific) and a 1290 Infinity HPLC (Agilent Technologies). The HPLC system consisted of an autosampler and tray compartment, column oven, binary pump, and diode array UV- detection system, all controlled by XCalibur software (Thermo Scientific). The chromatographic separation was achieved using a Zorbax Extend C-18 column (1.8 μm particle size, 2.1 mm diameter, 50 mm length) (Agilent Technologies). Sample volumes of 5 μL were injected into a full loop injection and separated with a constant flowrate of 200 μL/min. Mobile phase solvents were (A) 0.04% glacial acetic acid in DIW, and (B) HPLC grade acetonitrile, which eluted adsorbed sample through the following gradient: 0-1 min = 3-40%B, 1-2 min = 40-52% B, 2-3 min = 52-70%B, 3-6 min = 70-100%B, 6-10 min = 100%B, 11-15 min = 3%B. The column temperature was maintained at 60°C throughout the experiment.

The mass spectrometry (MS) system was equipped with both linear ion trap and orbitrap mass spectrometer technologies and with an electrospray ionization (ESI) source operating in negative ion mode under a capillary temperature of 275°C, capillary voltage of -6V, source voltage of 3.90 kV, and tube lens voltage of -52.43 V. Helium was used as the auxiliary gas and

nitrogen as the sheath gas under flowrates of 10 and 20 arbitrary units, respectively. MS spectra were recorded in the range of 55-500 m/z, with two scan events: (1) a full scan in Fourier Transform Mass Spectrometry (FTMS) mode, and (2) a data-dependent scan, which selected the most intense ion from the first scan to obtain the MS/MS spectra. Normalized collision energy was optimized at 25%.

For quantification of analytes, total ion chromatogram (TIC) mode was employed to isolate the primary fragment ion at 205.1 g/mol with no applied collision induced dissociation energy and a mass tolerance of 500 mmu. Subsequently, a collision-induced dissociation energy of 20 eV was applied to the primary fragment to verify that it originated from the molecule of interest by isolating the secondary fragment ion of ibuprofen at 159.4 g/mol. Chromatogram peaks were integrated and compared to standard ibuprofen solutions with known concentrations ranging from 0 – 21 μg/mL, with the integration areas correlating linearly with concentration ($R^2 \geq 0.99$). Drug release samples with integration areas outside of the calibration range were diluted 1:1 with DIW and the diluted samples re-analyzed. The resulting drug release was back-calculated from integral area values and presented as a cumulative mass release, with error bars representing the standard error from all replicates analyzed.

4.2 Results and Discussion

In order for successful drug/bioactive impregnation to be possible, three conditions must be met. First, the solute must have sufficient solubility in scCO2 to allow for solubilization and transport through the vessel. Second, the polymer must have adequately large surface area/pore volume, or be sufficiently swellable in scCO2, to allow for the $scCO_2$ borne solute to penetrate throughout the network and participate in surface interactions with the polymer. Finally, the partitioning coefficient (i.e. the equilibrium ratio of active molecule in the $scCO_2$ phase to that in

the polymer matrix [146]) must be favourable enough to allow for a sufficient quantity of active ingredient to be deposited on the polymer scaffold. In reality, these factors are nearly impossible to decouple, and work in tandem to determine the success of an impregnation process.

4.2.1 *Impregnation of Irgacure 2959 Photoinitiator*

Irgacure 2959 is a highly efficient radical photo initiator, which is known to react with methacrylate functional groups to facilitate UV-cured photocrosslinking reactions. It was hypothesized that the speed at which free-radical reactions occur, coupled with the established history of the success of such reactions to crosslink methacrylated carbohydrate materials [149], could make this initiator a promising candidates for the fast and covalent stabilization of PGX processed materials. As such, the first set of impregnations attempted involved the deposition of Ciba Irgacure® 2959 onto various methacrylated-carbohydrate scaffolds, with the impregnation achieved (presented on a wt% basis relative to the polymer scaffold) shown in Figure 73.

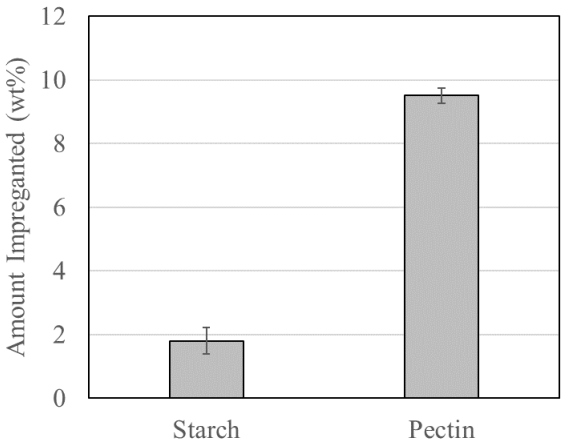

Figure 73: Weight percentage of Irgacure 2959 impregnated onto methacrylated and PGX-processed starch and pectin scaffolds.

The amount of Irgacure 2959 impregnated in the pectin scaffold is almost five times that impregnated into the beta-glucan and starch materials, a result that can largely be attributed to the significantly larger surface area present on PGX-processed pectin scaffolds when compared

with starch. This provides significantly greater opportunity for Irgacure 2959 to interact with the surface of pectin, resulting in higher adsorption and overall initiator loading.

4.2.2 *Impregnation of Model Drug*

The use of the PGX impregnation system was next investigated for depositing a hydrophobic model drug onto chitosan and alginate scaffolds. The model drug chosen for these trials was ibuprofen, based on its poor solubility in water (21 mg/L, logP = 3.97) and inadequate drug dissolution rates in its typical crystalline form, making it very difficult to incorporate into hydrophilic polymer systems at any appreciable concentration.

Loading of ibuprofen onto PGX-processed and unprocessed alginate, as well as PGX-processed chitosan samples (using two different depressurization speeds) was assessed, with the results shown in Figure 74.

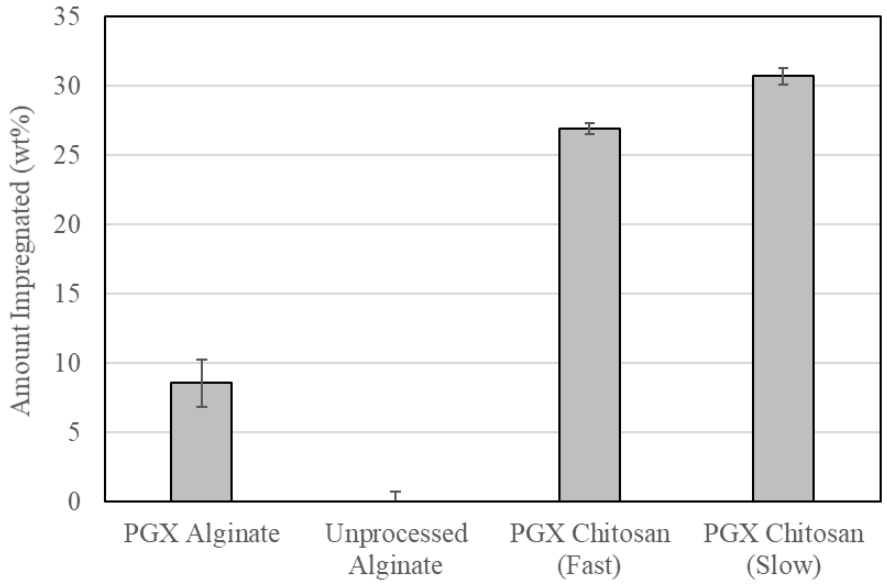

Figure 74: Weight percentage of Ibuprofen impregnated onto alginate and chitosan scaffolds using different CO_2 depressurization rates

Two primary observations may be made from this impregnation data. First, the impregnation efficiency of drug into the PGX chitosan scaffold is significantly higher than that into the PGX alginate scaffold despite their relatively similar surface areas of 165 ± 27 and 192 ± 37 respectively. While it is difficult to predict the pH during an impregnation process, it is expected that the basic amino functional groups on chitosan participate in acid-base interactions with the acidic carboxyl groups on ibuprofen, contributing to the higher drug loadings observed in the chitosan matrices.

Second, the impregnation efficiency into the PGX polymer scaffold is significantly higher than that into the unprocessed scaffold (which exhibited virtually no impregnated drug). This result is attributed entirely to the low surface area and negligible porosity of unprocessed alginate coupled with the apparent inability of $scCO_2$ to swell alginate reversibly. These factors prevented drug from penetrating into the polymer matrix and participating in chemical or physical surface interactions, thereby limiting the overall drug loading potential.

4.2.3 *Drug Release from Impregnated Scaffolds*

4.2.3.1 *Drug Release Kinetics from PGX-Chitosan Hydrogel Scaffolds*

Gels were prepared from ibuprofen-loaded chitosan samples (all of which had been previously PGX processed) according to the process described in sections 3.2.2.3 and 3.2.2.4. Drug release kinetics were subsequently collected from these scaffolds, which were maintained in infinite sink conditions throughout the release period by frequent replacements of buffer solution. The resulting mass of released drug was plotted as a cumulative total against time, as seen in Figure 75, with logarithmic fits shown in Figure 76.

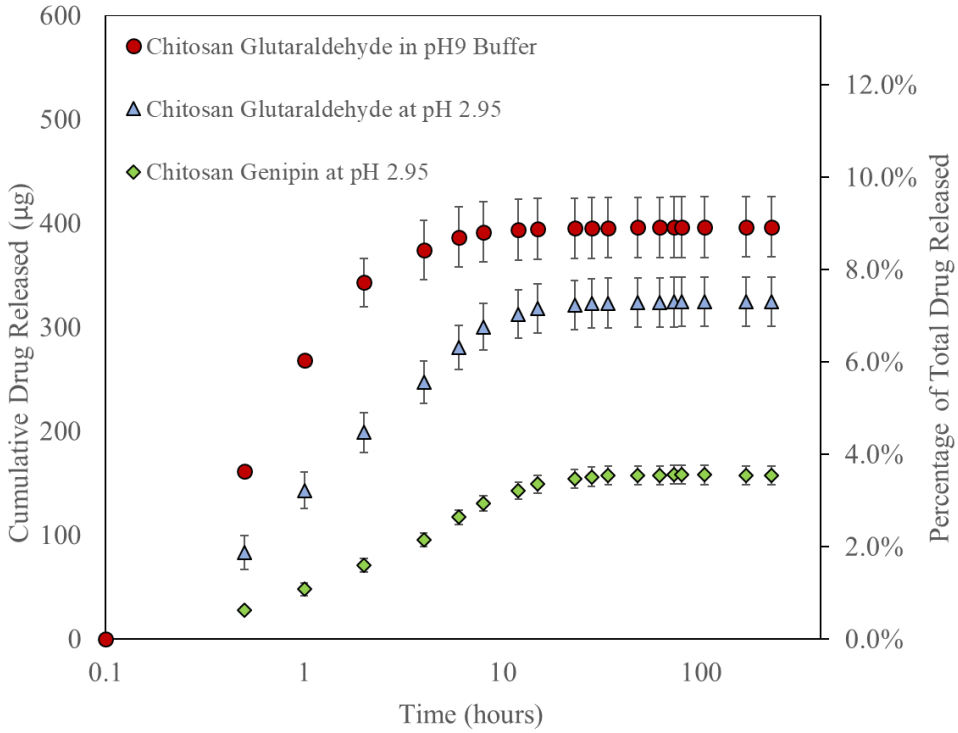

Figure 75: Semi-log plot of cumulative drug release of ibuprofen from impregnated gel scaffolds of 12.5 mm diameter and 1.5 mm height (n=4) as a function of time.

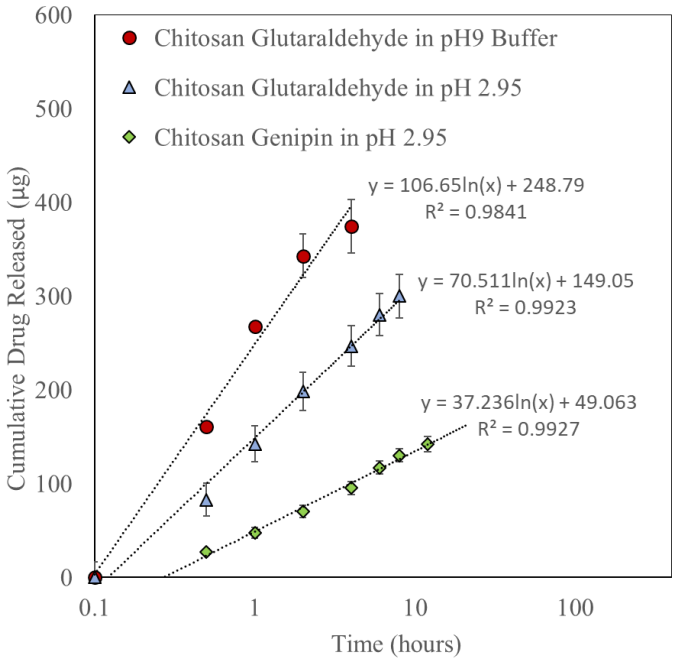

Figure 76: Semi-log plot with equations of fit for initial drug release of ibuprofen from chitosan scaffolds

The initial burst release of drug lasted for approximately twenty hours and exhibited a first-order Fickian release rate with fits having r^2 values > 0.99, suggesting that the release

mechanism was largely diffusion-controlled. The largest release was observed from the glutaraldehyde-crosslinked gels at pH 9, followed by glutaraldehyde-crosslinked gels at pH 2.95, and then genipin-crosslinked gels. Average cumulative masses of drug released per gel disc were 529 μg, 324 μg, and 180 μg, respectively, corresponding to 8.6 ± 0.008%, 5.2 ± 0.005%, and 2.9 ± 0.003% of the total loaded drug. These release results are consistent with the swelling ratios (and thus expected crosslinking extents) of the chitosan gels (Figure 51), with higher cumulative drug release observed for scaffolds that typically have a lower degree of crosslinking. Furthermore, higher cumulate release amounts were observed for scaffolds that are expected to have higher initial porosity (i.e. faster crosslinking and better maintenance of PGX morphology, as shown in Figure 47, Figure 48, Figure 49, and Figure 50).

The very small cumulative release fractions observed are assumed to be the result of the acid-base interactions between the carboxylic acid moiety on ibuprofen and the amino-residues on the backbone of chitosan, resulting in affinity binding (particularly given the large internal surface areas available in the PGX gels) and thus significantly hindered release. However, it would be interesting to track release kinetics from these scaffolds over an extended period, as it is suspected that the presence of these acid-base interactions could provide a sustained release of ibuprofen on the timescale of weeks to months (particularly as polymers degrade).

4.2.3.2 *Drug Release Kinetics from PGX-Alginate Hydrogel Scaffolds*

Gels were also prepared from ibuprofen-loaded PGX alginate samples according to the process described in sections 3.2.2.5 and 3.2.2.6, and drug release kinetics were tracked in the same manner as from the chitosan gels. The resulting mass of released drug was plotted as a cumulative total against time, as seen in Figure 77, with linear fits shown in Figure 78.

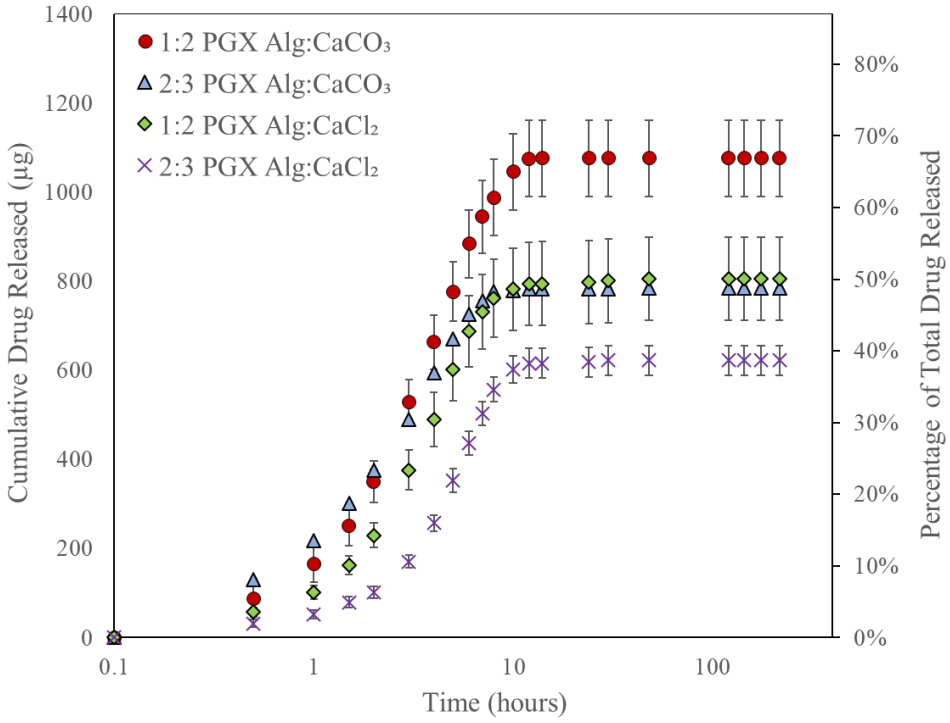

Figure 77: Semi-log plot of cumulative drug release of ibuprofen from a single impregnated alginate gel scaffold (12.5 mm diameter by 1.5 mm height) as a function of time.

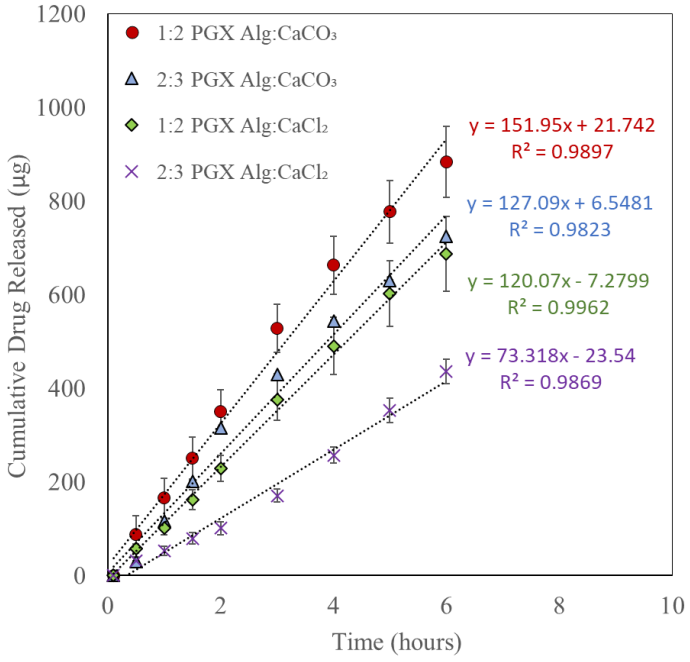

Figure 78: Equations of fit for the initial near zero-order drug release of ibuprofen from alginate scaffolds

The release of drug from the alginate scaffolds persisted for approximately ten hours and exhibited near zero-order release kinetics (i.e. maintaining a relatively constant drug release rate) throughout the first 8 hours of the trial. Interestingly, a larger release of drug was observed for gels with theoretically higher degrees of crosslinking, with 1:2 Alg:$CaCO_3$ and 1:2 Alg:$CaCl_2$ exhibiting cumulative release ratios of 69.3 ± 0.76% and 48.8 ± 0.50% of total drug respectively, while less crosslinked gel formulations, 2:3 Alg:$CaCO_3$ and 2:3 Alg:$CaCl_2$, exhibited cumulative releases of 48.7 ± 0.50% and 40.2 ± 0.44% of the total loaded ibuprofen. A plausible explanation for this release behaviour is that, during the gelation process, gels with lower molar crosslinker concentrations (i.e. 2:3 Alg:Ca^{2+}) produce less CO_2 gas (derived from the dissolution of calcium carbonate) making it more difficult for bubbles to spatially interact and/or coalesce, resulting in less interconnected pore networks and thus making drug diffusion from the scaffold slower and more challenging despite a theoretically lower crosslinking extent. Overall though, release from alginate is substantially faster than from chitosan due to the absence of acid-base interactions between the loaded drug and the alginate scaffold.

4.3 Conclusions

The PGX system has the potential to provide a significant advantage over other drug/active molecule impregnation methods by successfully enabling the loading of large fractions of active molecules into dry scaffolds without disrupting the pore structures or requiring subsequent solvent exchange/purifications steps. Overall, the success of such impregnation methods was shown to depend largely on the surface area of the polymer scaffold onto which the active molecule was being loaded; however, the impregnations (and subsequent drug release) were also shown to be strongly influenced by chemical and physical interactions between the active molecule and the polymer backbone. A summary of the amounts of active

successfully impregnated into a variety of polymer scaffolds (originally presented in Figure 73 and Figure 74) is provided in Table 11.

Table 11: Summary of impregnation amounts of Irgacure 2959 and/or ibuprofen into a variety of polymeric scaffolds

Polymer Scaffold	Active Molecule	Amount Impregnated (wt%)
Starch	Irgacure 2959	1.8 ± 0.41
Pectin	Irgacure 2959	9.5 ± 0.23
Chitosan	Ibuprofen	30.7 ± 0.58
Alginate	Ibuprofen	8.6 ± 1.7

Depending on the nature of the scaffold and the nature of the drug, different loading and release kinetics could be achieved. Using ibuprofen as a model drug, impregnation into chitosan PGX matrices was shown to be highly efficient due to the potential for acid-base interactions with the carboxylated drug, while observed drug loadings into PGX alginate matrices was substantially lower. Subsequently, chitosan gel formulations exhibited first-order release kinetics of a relatively small fraction of impregnated drug over 300 hours (<10%), suggesting that chitosan scaffolds could enable sustained release of ibuprofen on a timescale of weeks to months. In contrast, alginate gels exhibited near zero-order release rate for the first eight hours of the trial, during which time 40-70% of the impregnated drug was released. In this context, by altering the composition of the PGX scaffold, various dosing (loading) and release kinetics may be achieved, making this approach of potential interest for fabricating clinically-relevant drug delivery scaffolds.

Chapter 5 – Nozzle Reconfiguration for Co-Extrusion and In Situ Gelation/Stabilization of PGX-Morphologies

The primary goal of this work was to utilize the PGX process to create structured, macroporous hydrogels. This was done through a variety of post-processing crosslinking chemistries applied to PGX-processed polymer, as describe in Chapter 3; however, these post-processing crosslinking methods required the use of anti-solvents and solid-state chemistries to maintain PGX morphology, and often necessitated the addition of subsequent solvent exchanges and/or time-consuming purification steps. In addition, increasing the degree of solvation of the pre-formed PGX network increased the capacity for crosslinking, but resulted in an increased loss of PGX structure, reducing the benefits of using PGX to create pre-defined macroporosity.

In contrast, the ability to form in situ-crosslinked aerogels during PGX processing could eliminate the need for additional reaction or purification steps, and thus, both significantly increase process throughput as well as ensure that the high surface area PGX product structure is maintained upon gelation. Furthermore, the PGX system and all of its components are sealed and sterilized with anhydrous EtOH, meaning that the aerogel products themselves would be inherently sterile upon production, eliminating the need for material sterilization prior to seeding cells into the stabilized scaffold or using the scaffold as wound healing matrices.

5.1 Materials and Methods

5.1.1 *Materials*

Co-extrusion/in situ crosslinking experiments were conducted using (1) sodium alginate (alginic acid sodium salt, Sigma Aldrich) crosslinked in situ with anhydrous calcium chloride (Sigma Aldrich, granular ≤7.0 mm, ≥ 93.0% purity), and (2) poly(oligoethylene glycol

methacrylate) (POEGMA) functionalized with hydrazide and aldehyde groups. Reactive POEGMA polymers were prepared using oligo(ethylene glycol) methyl ether methacrylate with a number average molecular weight of 500 g/mol (OEGMA500, Sigma Aldrich, ≥ 95%), di(ethylene glycol) methyl ether methacrylate (MEO2MA, Sigma Aldrich, ≥ 95%), 2,2-azobisisobutryic acid dimethyl ester (AIBMe initiator, Wako Chemicals, ≥ 98.5%), acrylic acid (Sigma Aldrich, ≥ 99%), thioglycolic acid (TGA, Sigma Aldrich, ≥ 98%), N-(2,2-dimethoxyethyl)methacrylamide (DMEMAm, McMaster University, ≥ 99%), adipic acid dihydrazide (ADH, AK Scientific Inc., 99%), N'-ethyl-N-(3-dimethylaminopropyl)-carbodiimide (EDC, AK Scientific Inc., 99%). OEGMA500 and MEO2MA were purified prior to use by passing them through separate columns packed with basic aluminum oxide to remove inhibitors (methyl ether hydroquinone and butylated hydroxytolune). DMEMAm was synthesis in-house using the materials and methods reported by Smeets et. al [81]. Hydrochloric acid (HCl, 1M) and sodium hydroxide (NaOH, 1M) were obtained from LabChem Inc. (Pittsburgh, PA). All experiments used Milli-Q grade distilled deionized water (DIW). When necessary, dialysis tubing (Thermo Fisher Scientific, 3.5 kDa) was used for purifications.

5.1.2 *Methods*

5.1.2.1 *Synthesis of Hydrazide-Functionalized POEGMA*

Hydrazide-functionalized poly(oligoethylene glycol methacrylate) (POEGMA) was prepared by adding purified MEO_2MA (4.0 grams, 20 mmol), purified $OEGMA_{500}$ (12.0 grams, 25 mmol), 2,2-azobisisobutyric acid dimethyl ester (AIBMe) initiator (148 mg, 0.65 mmol), acrylic acid monomer (1.44 grams, 20 mmol), and thioglycolic acid (TGA) chain-transfer agent (8 uL, 0.10 mmol) to a 250 mL single-necked round-bottom flask. Dioxane (80 mL) was added, after which the flask was purged with nitrogen for at least 30 minutes by bubbling nitrogen

through a needle into the reaction solution. Once purged, the flask was sealed and submerged in an oil bath at 75°C for four hours under constant stirring. Upon completion of the reaction, the solvent was removed via rotary evaporation to yield poly(oligo ethylene glycol methacrylate-co-acrylic acid).

Conversion of the carboxylic acid groups on the acrylic acid monomers to hydrazides was done by carbodiimide-mediated conjugation of an excess of adipic acid dihydrazide (ADH). To do so, 14g of poly(oligoethylene glycol methacrylate-co-acrylic acid) polymer was dissolved in 250 mL of DIW and transferred to a 1000 mL round-bottom flask. ADH (17.6 grams, 100 mmol) was dissolved, along with any residual polymer, in the original 250 mL round-bottom flask to a total volume of 250 mL and then added to the 1000 mL flask, after which the pH was adjusted to 4.75 using 0.1 M hydrochloric acid (HCl). Finally, EDC (6.4 grams, 33 mmol) was dissolved in 100 mL of DIW, and added slowly to the reaction solution, with the pH maintained at 4.75 for 4 hours (or until the pH stopped changing) by dropwise addition of 0.1M HCl. The solution was left to stir for an additional 12 hours, dialyzed against DIW for a minimum of 6 (6+ hour) cycles, and lyophilized to dryness. Once dry, the final polymer was dissolved to 20 wt% in phosphate buffered saline (PBS) solution for storage.

The resulting hydrazide-functionalized poly(oligoethylene glycol methacrylate) product was termed "$PO_{55}H_{30}$" to represent its theoretical composition (55 mol% long chain monomer, with 30% functional hydrazide units).

5.1.2.2 *Synthesis of Aldehyde-Functionalized POEGMA*

Aldehyde-functionalized poly(oligoethylene glycol methacrylate) (POEGMA) was prepared by adding purified MEO_2MA (4.0 grams, 20 mmol), purified $OEGMA_{500}$ (12.0 grams, 25 mmol), 2,2-azobisisobutyric acid dimethyl ester (AIBMe) initiator (148 mg, 0.65 mmol),

DMEMAm monomer (3.6 grams, 20 mmol), and thioglycolic acid (TGA) chain-transfer agent (8 uL, 0.10 mmol) to a 250 mL single-necked round-bottom flask. Dioxane (80 mL) was added, after which the flask was purged with nitrogen for at least 30 minutes by bubbling nitrogen through a needle into the reaction solution. Once purged, the flask was sealed and submerged in an oil bath at 75^{o}C for four hours under constant stirring. Upon completion of the reaction, the solvent was removed via rotary evaporation, to yield poly(oligo ethylene glycol methacrylate-co-DMEMAm).

Subsequent conversion of the acetal groups on the DMEMAm monomers to aldehydes was done using acid-mediated hydrolysis by dissolving 14g of the pre-polymer in 400 mL of 0.5M HCl and stirring for 24 hours. The product was subsequently dialyzed against DIW for a minimum of 6 (6+ hour) cycles and lyophilized to dryness. Once dry, the final polymer was dissolved to 20 wt% in phosphate buffered saline solution for storage.

The resulting aldehyde-functionalized poly(oligoethylene glycol methacrylate) product was termed "$PO_{55}A_{30}$" to represent its theoretical composition (55 mol% long chain monomer, with 30% functional aldehyde units).

5.1.2.3 *Apparatus and Techniques*

To prepare for a coextrusion or in situ crosslinking trial, the PGX system was reconfigured to incorporate two aqueous feeds, as illustrated in Figure 79. This involved the introduction of an additional high-pressure packed plunger metering pump (LEWA-Nikkiso America), a secondary aqueous feedline, and a mixing tee coupled with an in-line static mixer, through which aqueous feeds were combined and effectively mixed prior to drying. Isolation valves were installed on either side of the mixing tee to control flow and pressure within the aqueous feed lines, while an ethanol quench was incorporated to slow and/or prevent potentially

hazardous buildups of polymer due to gelation of components prior to injection into the collection vessel.

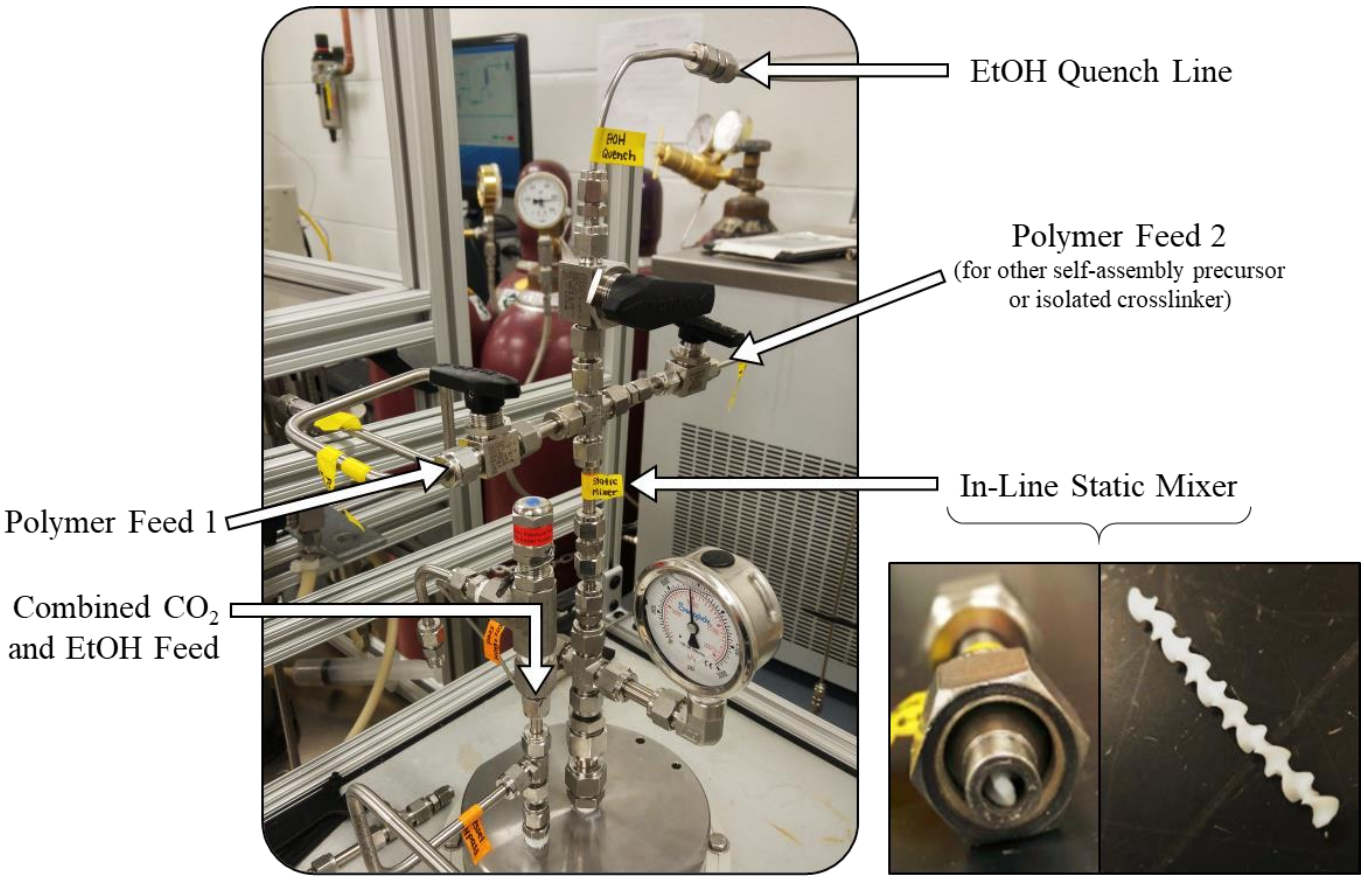

Figure 79: Diagram illustrating the reconfiguration of the PGX apparatus for the incorporation of a second polymer or crosslinker feed, allowing for in situ self-assembly and/or crosslinking reactions.

The success of an in-situ gelation is largely dependent on the tuning of gelation kinetics to match those of the process flowrates and mixing conditions. In the design of these trials, solutions were assumed to be well-mixed immediately upon entering the mixing tee, after which the gel solution was required to flow through 34 cm of tubing prior to entering the vessel. At a polymer flowrate of approximately 15 g/min and inner tube diameter of 0.18" (0.46 cm), passage of the mixed polymer through the tubing and into the vessel would occur in approximately 15 seconds. As such, gelation kinetics were tuned to fully crosslink within 15-20 seconds of

mixing, such that gelation would occur immediately after pumping of the polymer solution into the collection vessel.

5.2 Results and Discussion

5.2.1 *In-Situ Crosslinking of POEGMA*

The first in situ crosslinking trial involved the self-assembly reaction of aldehyde and hydrazide-functionalized POEGMA polymers. These precursor polymers are known to undergo rapid gelation through the spontaneous formation of hydrazone bonds upon mixing, as shown in Figure 2 and Figure 80.

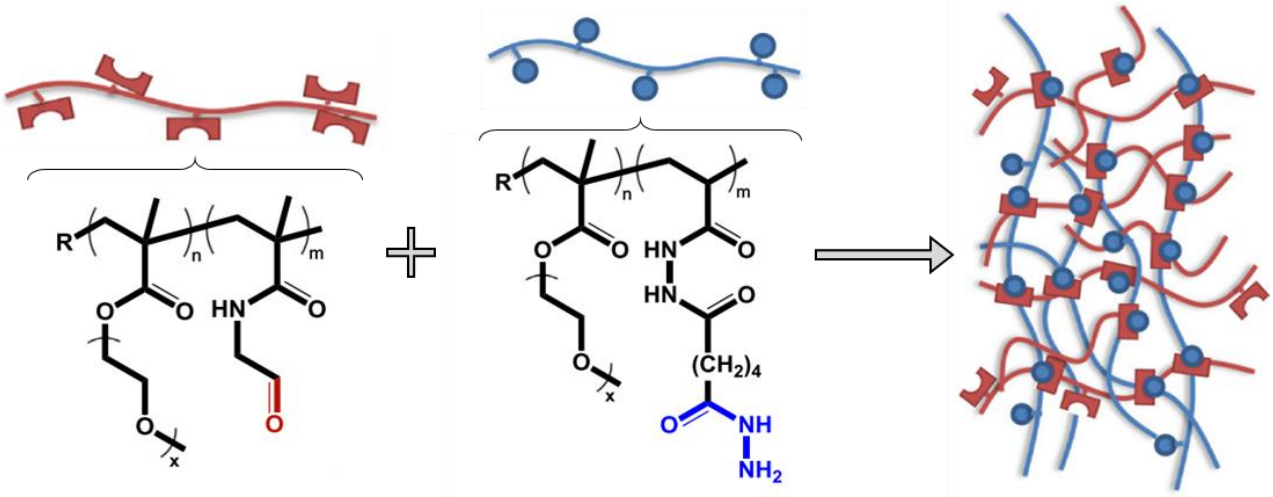

Figure 80: Reaction scheme for self-assembled crosslinking of hydrazide (blue) and aldehyde (red) functionalized POEGMA precursors. Reproduced with permission [52]. Copyright © 2018, Elselvier.

The resulting gels are characterized by their unique ability to exhibit different properties, ranging from highly protein repellant to thermoresponsive, based on the length of the OEGMA side chain. Thermoresponsive properties are achieved based on the unique ability of these gels to become more hydrophobic as temperature increases, driving significant deswelling behaviour

at the volume phase transition temperature (VPTT), at which this hydrophilic-hydrophobic transition occurs [52]. These properties are desirable, particularly in drug-delivery and tissue engineering applications, in that the hydrophilic-hydrophobic interfacial switch and deswelling ability can facilitate tunable cell adhesion [52] or pulsatile drug release [150]. By harnessing the multi-scale porosity of PGX-generated morphologies in combination with this thermal sensitivity, multifunctional hydrogels with great potential in biomedical applications could be obtained.

Typically, PGX-processing is limited to high molecular weight carbohydrate polymers that are soluble in water and insoluble in EtOH. In contrast, POEGMA precursor polymers are soluble in both water and EtOH, resulting in complete solubility in the ternary PGX solvent system. Thus, the potential exists for POEGMA polymers to be washed completely through the PGX system into waste (as opposed to precipitating in the collection vessel), unless gelation occurs precisely in the minutes after injection into the collection vessel. However, the effect of an EtOH co-solvent on gelation kinetics was unknown. As such, gelation times were tested at varying concentrations and ethanol contents, as shown in Table 12 to determine whether spontaneous crosslinking would occur after mixing with EtOH and CO_2.

Table 12: Observed solubility and gelation time kinetics of self-gelling hydrazide and aldehyde-functionalized POEGMA with varying H_2O:EtOH solvent ratios.

Mass $PO_{55}A_{30}$ (mg/mL)	Mass $PO_{55}H_{30}$ (mg/mL)	Solvent Ratio H_2O:EtOH	Gelation Time	Observations
200	0	1:0	N/A	No gelation/precipitation or viscosity changes observed
200	0	0:1	N/A	
0	200	1:0	N/A	
0	200	0:1	N/A	
200	200	1:0	Instant	Transparent gel formed immediately upon mixing.
150	150	1:0	15 secs	Gel is transparent and shows no fluidity after 20 secs
100	100	1:0	40 secs	Gel is transparent and shows no fluidity after 40 secs
100	100	4:1	80 secs	Viscosity increase observed at 60 secs with no fluidity after 80 secs
100	100	3:1	20 min	Viscosity increase observed at 15 min with no fluidity after 20 min. Resulting gel was very weak.
100	100	2:1	N/A	No gelation/precipitation or viscosity changes observed
100	100	1:2	N/A	No gelation/precipitation or viscosity changes observed

Based on these solubility trials, it was determined that gelation was severely inhibited upon mixing with ethanol in the nozzle of the collection vessel (particularly at EtOH:H_2O ratios of 1:3 or higher). Hence, instantaneous gelation immediately prior to injection through the nozzle was targeted, requiring a post-mixing residence time of approximately 15 seconds, as observed with 150 mg/mL solutions of the two reactive polymers.

The total aqueous flowrate was held constant at 15 g/min, consisting of 7.5 g/min each of both precursor solution. The resulting process analytics are shown in Table 13 and generated polymer morphologies illustrated in Figure 81. Unfortunately, the outgassing process required

for BET surface area analysis uses high temperatures (>100ºC) and vacuum pressure to remove water from the polymer sample. After completion of outgassing, samples were observed to have yellowed and collapsed, leading to the conclusion that the polymer had been degraded and lost a significant portion of its original surface area. To avoid this problem, we recommend using a lower outgassing temperature for future trials.

Table 13: Key metrics associated with in situ self-assembled POEGMA macroporous hydrogels

Sample ID	In Situ Self-Assembled POEGMA
Bulk Density	0.292 g/mL
Process Efficiency	12.2%
Generated Surface Area*	3.07 ± 1.32 m^2/g

***** Pore structure was destroyed during outgassing processes due to temperature sensitivity. Actual surface is area is likely significantly higher.

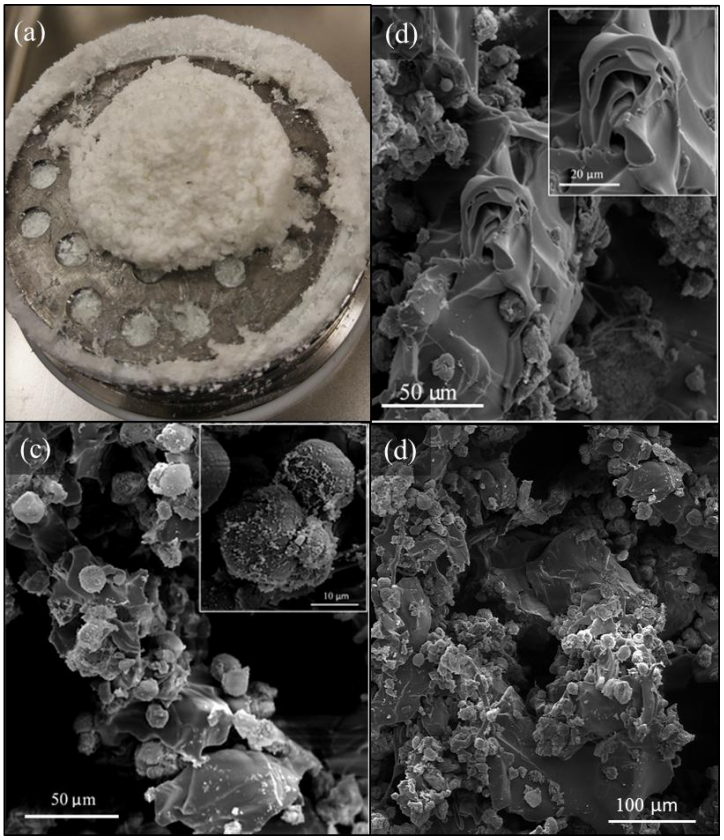

Figure 81: Morphology of PGX in situ crosslinked POEGMA polymer observed in (a) photograph (b) SEM Images at 1000x [4000x] magnification (c) SEM images at 800x [2000x] magnification (d) SEM image at 500x magnification

The low process efficiency observed for this process was attributed to the challenges encountered related to flowrate control. While the hydrazide-functionalized polymer was consistently flowing at 7.5 mL/min, the pump responsible for feeding the aldehyde-functionalized precursor experienced issues holding pressure, and therefore is assumed to have delivered an inaccurate flow of polymer. As such, ratios of each precursor were likely variable during the process, resulting in incomplete gelation and causing a significant fraction of un-crosslinked polymer to be washed through the system and collected in waste (based on its solubility in the supercritical fluid). The remaining POEGMA gel was obtained in a pseudo-dry state, which was subsequently dried in a desiccator and further analyzed. Observation of SEM images showed that the collected polymeric gel was a composite scaffold of coagulated particles and micron-sized lamellar sheets separated by macropores (Figure 81(b)). This result is consistent with a portion of the polymer crosslinking as it passed through the nozzle/entered the vessel, creating gel droplets/microbeads, while the remaining porting of polymer gelled in layers as it was deposited at the bottom of the vessel. However, this in situ crosslinking trial would have to repeated with a more consistent pump to determine with certainty the mechanisms by which the polymer is precipitated/gelled.

The presence of stable crosslinks within the collected polymer fraction was verified by measuring the swelling kinetics of the polymer in 10 mM phosphate buffer solution, the results of which are shown in Figure 82.

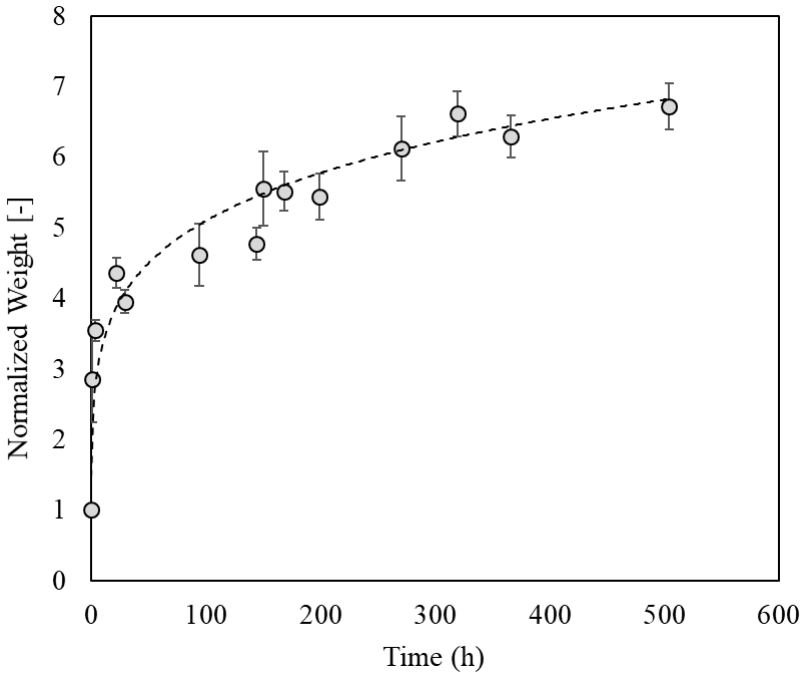

Figure 82: Swelling kinetics of in situ crosslinked POEGMA aerogel, collected in 10 mM PBS at 37°C and shown here with a line that is simply noted as a guide to the eye.

While uncrosslinked POEGMA is readily soluble in aqueous solution, the processed POEGMA hydrogel effectively swelled and resisted dissolution for a period of over 20 days with no sign of degradation, providing clear evidence of successful gelation. The average water content of these in situ crosslinked POEGMA gels was measured to be 90.2 ± 4.3% at equilibrium swelling, which is very similar to the equivalent (non-PGX processed) formulation that typically displays a water content of 90-95% at equilibrium swelling [151].

5.2.2 *In Situ Crosslinking of Sodium Alginate*

Subsequently, in situ gelation techniques were applied to sodium alginate, which forms crosslinks by tightly chelating to free calcium ions in solution (discussed in greater detail in section 3.1.3). To avoid the flow control problems experienced in section 5.2.1, calcium chloride

($CaCl_2$) crosslinker was dissolved in the standard ethanol flow, as opposed to being pumped through a secondary aqueous feed.

In contrast to the POEGMA polymers, which gelled over a period of seconds to minutes, alginate solutions are known to crosslink almost instantaneously upon contact with free calcium ions. Furthermore, the gas expanded ethanol stream containing calcium ions was combined with the aqueous polymer stream in the nozzle cap (immediately before injection into the pressure vessel), according to the standard PGX operating process. This mixing element, followed by subsequent injection into the vessel, eliminated the need for fine-tuning of the crosslinking kinetics to confine gelation to a certain location within the apparatus. As such, the aqueous solution and gas expanded ethanol ratios remained unchanged from those described in section 2.2.2.6. The resulting process analytics are shown in Table 14 with photographs of the generated polymer morphologies illustrated in Figure 83.

Table 14: Important metrics collected from the processing and subsequent analysis of in situ crosslinked PGX calcium alginate aerogel

Sample ID	In Situ Crosslinked Calcium Alginate
Bulk Density	0.0083 g/mL
Process Efficiency	99%
Generated Surface Area	631 ± 43 m^2/g

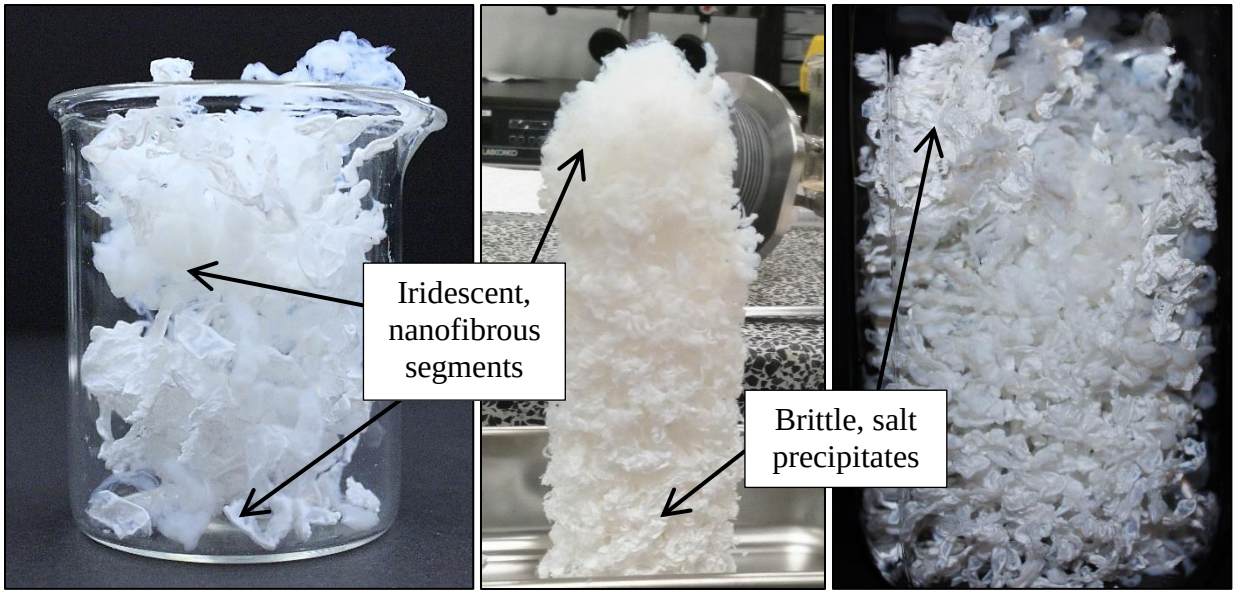

Figure 83: Photographs of in situ crosslinked calcium alginate aerogel, showing flexible nanofibrous segments and brittle, salt-coated components.

Unlike POEGMA, both alginate and $CaCl_2$ are insoluble in gas expanded $EtOH/H_2O$ and will rapidly precipitate upon mixing, resulting in extremely high polymer recoveries and surface areas. In fact, the measured surface areas of PGX in situ crosslinked alginate were comparable to conventional silica aerogels (which possess typical surface areas of 600-1000 m^2/g), while the measured bulk density was an order of magnitude lower than conventional silica aerogels, that have typical bulk densities of 0.03-0.35 g/mL [152].

Observation of the PGX-generated alginate aerogel showed distinct sections of extremely low-density, iridescent cloud-like material that appeared blue when observed from certain angles. It is hypothesized that the bluish tint of the iridescent materials originates from the scattering of light at the same magnitude as visible blue light, indicating the existence of nanofibers in the range of 450-500 nm. This hypothesis was confirmed through helium ion microscopy imaging of low-density components that directly show fibres in the range of ~500 nm, as seen in Figure 84.

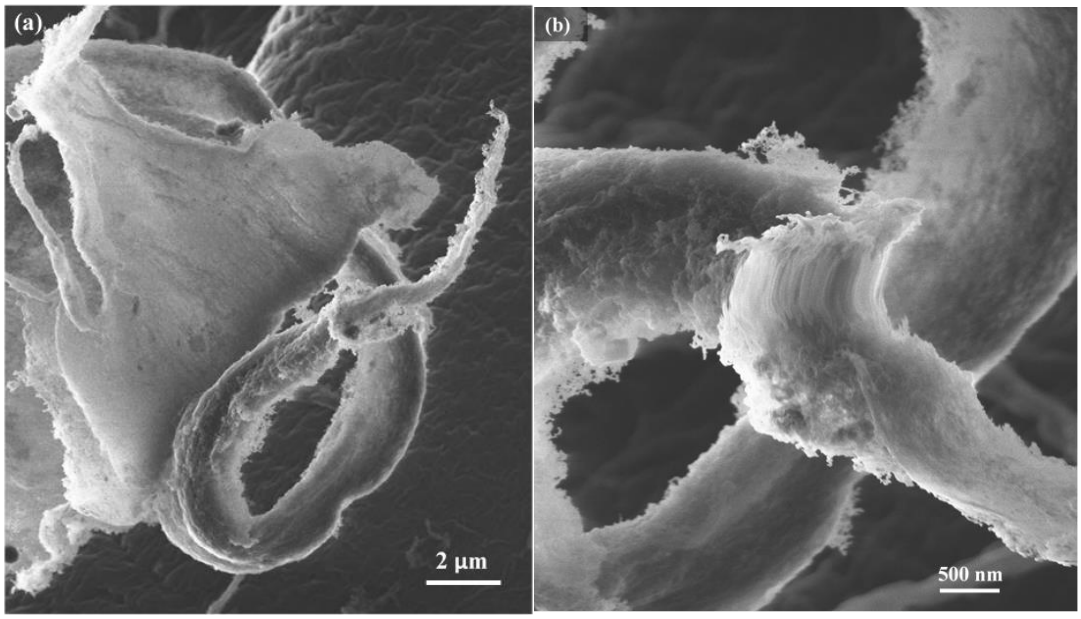

Figure 84: Helium ion microscopy images of the low-density section of in situ crosslinked calcium alginate aerogel, showing nanofibrous structures with diameters of approx. 500 nm.

In contrast, other sections of the precipitated scaffold appeared as brittle, white, and crystalline precipitates. These precipitates were likely formed from H_2O/CO_2-insoluble calcium salts exceeding the crosslinking capacity of alginate and, as a result, were not ionically bound during the crosslinking reactions. The exact mass of precipitated salts deposited on the calcium alginate scaffold was quantified by dialysis of calcium alginate gels against DIW (during which unbound salts dissolved and crosslinked gel remained stable) and subsequent lyophilization of the remaining calcium alginate scaffold, suggesting that the scaffolds contained 18.1 ± 1.4 wt% precipitated calcium salts. While macropores remain, the precipitated salts likely affected the mesoporosity of the aerogel network in regions and would certainly result in osmotic imbalances if cells were directly incorporated into the scaffold without purification. In subsequent in situ gelling trials of alginate, the concentration of calcium salt in the crosslinking stream could easily be decreased to reduce the fraction of precipitated salts and minimize concerns regarding osmotic imbalances and decreased porosity.

To confirm the effectiveness of simultaneously processing and crosslinking alginate in the PGX system, the swelling kinetics of the macroporous scaffold were investigated in 10 mM HEPES buffered saline solution (again chosen instead of phosphate buffer to eliminate the extraction of Ca^{2+} from the scaffold and subsequent calcium phosphate precipitation), the results of which are shown in Figure 85.

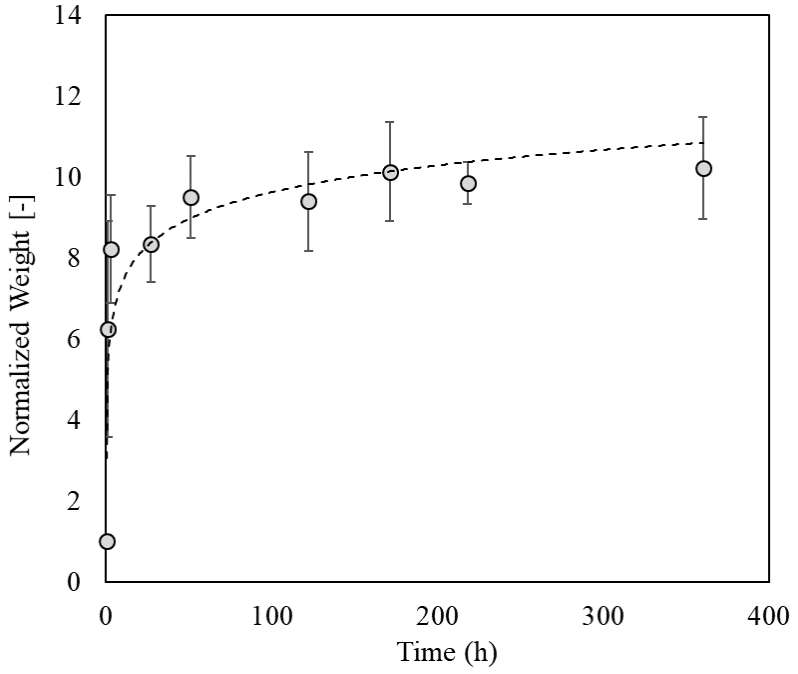

Figure 85: Swelling kinetics of in situ crosslinked calcium alginate aerogel collected in 10 mM HEPES buffer at 37°C and a line that is simply noted as a guide to the eye.

Similar to POEGMA, the alginate polymer is readily soluble in aqueous solution in its uncrosslinked state. However, when the in situ crosslinked material was placed in buffer solution under gentle mechanical agitation, it resisted dissolution for a period of 16 days with no sign of degradation. During swelling trials, the dry scaffold's pores were observed to fill with water, exhibiting a water content of 85.1 ± 1.9% at equilibrium swelling. This is consistent with alginate scaffolds crosslinked in excess $CaCl_2$ using the post-processing method, which have typical water contents of 81.5 ± 1.5%.

5.3 Conclusions

Two in situ gelation methods were investigated: (1) the incorporation of a second aqueous feed for the timed gelation of aldehyde and hydrazide-functionalized POEGMAs, and (2) the addition of a calcium salt into the ethanol feed to gel alginate instantaneously upon co-extrusion into the collection vessel. The measured bulk densities of crosslinked POEGMA and alginate scaffolds were 0.292 g/mL and 0.0038 g/mL respectively, and both structures exhibited stability in aqueous media for over 16 days with no indication of degradation. When not covered by precipitated salts, in situ crosslinked alginate was shown to be composed of bunches of fibers in the range of several hundred nanometres and exhibited surface areas >600 m^2/g, which is comparable to conventional silica aerogels. Due to the high level of interconnectivity in PGX morphologies, it is expected that (once the process is tuned to eliminate precipitated salts) these alginate aerogels would exhibit stronger and more elastic properties without the requirement of toxic and/or expensive additives. The presence of ionic salts in such an interconnected network could limit the functionality of these scaffolds in insulating applications, where the lack of conductivity/interconnectivity inhibits thermal transport [153], but could open up numerous possibilities for their application as conductive macroporous materials.

Chapter 6 – Conclusions and Future Directions

6.1 Summary of Contributions

This work has provided the basis for a great deal of other research into the use of PGX-processing to generate macroporous structured hydrogels, particularly in wound healing, drug delivery, and tissue engineering applications. In particular, this thesis has significantly contributed to the understanding of the PGX processing technology, establishing both in situ and post-processing methods of stabilizing PGX-generated polymer structures into bulk hydrogels, and the use of PGX-technology for impregnating drugs and other bioactives into PGX-processed polymer scaffolds.

First, the tunability of the PGX-processing system was explored by processing starch and pectin polymers at a variety of operating conditions. The resulting morphologies were assessed through brightfield microscopy and BET analysis to determine the effects of mixing distance, operating point, polymer molecular weight and polymer concentration on the polymer morphologies produced. More aggressive mixing/precipitation systems were achieved by using higher anti-solvent ratios (operating point #1), more turbulent mixing regimes (larger mixing distances), and higher shear forces (smaller nozzle gaps), and were found to produce finer precipitates with generally higher surface areas. Higher surface areas and smaller particulates/fibres were also obtained by degrading the polymer backbone and PGX-processing the lower molecular weight oligomers, or pumping polymer into the system at a lower concentration in aqueous solution. Conversely, less aggressive precipitation systems with higher water and CO_2 concentrations (operating point #2) were found to provide significantly aggregated systems of coalesced particles.

In all cases, PGX processing was shown to produce polymer scaffolds with significantly larger surface areas and pore volumes than their unprocessed precursors. Furthermore, different polymers were shown to produce significantly different structures, with processed starches consistently generating particulate structures, while pectin, alginate, and chitosan were shown to generate highly interconnected fibrous networks with fibre diameters dependent on the processing conditions. The inability of starch to form fibres was thought to be the result of its preference to form semi-crystalline granules, with moderated re-crystallization/retrogradation occurring as the starch is cooled and re-precipitated in the collection vessel. As such, it was extremely difficult to formulate conclusions regarding the mixing and precipitation kinetics occurring by looking primarily at starch, as the tendency for starch to form granule structures conflicted with the ability to isolate variables on the processing system.

The ultimate objective in the use of the PGX system for processing biopolymers, was to stabilize the PGX-generated morphologies to obtain covalently/ionically-crosslinked aerogels or hydrogels for extended use in diverse applications. This was done through two different methods: (1) post-processing crosslinking using unfavourable solvents and (semi)solid-state chemistries, and (2) in situ self crosslinking during PGX processing.

Post-processing gelation techniques were developed using PGX-processed chitosan and alginate precursors, with the resulting hydrogels exhibiting multi-scale interconnected pore structures. The reaction kinetics of these hydrogel formulations were tuned by varying time, temperature, pH, and crosslinker concentrations, to determine which conditions were most suitable for the maintenance of PGX-morphologies in a stabilized and hydrated state. In many cases, macroporosity was maintained while nano-scale fibres and pore networks were lost; in other cases, longer solubilization time prior to effective crosslinking resulted in the loss of all of

the original PGX structure. All formulations were shown to possess tunability in elastic storage moduli as a function of crosslinker concentration and/or reaction conditions, exhibiting plateau G' values ranging from 2-40 kPa. As such, great potential exists for gel formulations to be used as possible synthetic replacements for a wide range of native tissues.

Protein uptake experiments on all hydrogel scaffolds indicated that gels formulated from PGX-processed precursors exhibiting loadings primarily via adsorption (due to their large internal surface areas) while their non-PGX equivalents were found to swell and uptake proteins primarily through absorption. Metabolic assays conducted on chitosan and alginate hydrogels showed no statistically relevant cytotoxicity after purification of scaffolds through four rounds of dialysis; however, residual glutaraldehyde-crosslinker in unpurified chitosan scaffolds was shown to have a significant cytotoxic effect. To eliminate the need for dialysis prior to in vivo applications, a preliminary investigation into the use of an aldehyde-functionalized POEGMA long-chain crosslinker was pursued. This long-chain crosslinker was shown to significantly improve cell viability, but further effort is required to achieve the same mechanical strength as the glutaraldehyde-crosslinked formulations. In contrast, free calcium ions from unpurified calcium alginate gels were shown to promote cell proliferation in vitro, which could potentially assist in the regeneration of healthy tissues at a wound site.

In all post-processing crosslinking methods, the use of anti-solvents, solid-state chemistries, and/or rapid gelation kinetics was required to maintain PGX morphology. To eliminate the need for these less efficient and time-consuming processes, new methods of stabilizing PGX-processed biopolymers in situ (i.e. during PGX processing) were developed by reconfiguring the PGX apparatus to incorporate two aqueous feeds, enabling the simultaneous pumping of polymer and crosslinker (or two self-assembling polymers) into the collection vessel.

Successful in situ crosslinking reactions were completed using aldehyde and hydrazide-functionalized POEGMA (which could crosslink in situ via hydrazone chemistry as they were extruded into the PGX vessel) and calcium-crosslinked alginate, which rapidly gelled as soon as the polymer feed and the calcium-ion feed were combined. The successful crosslinking of these two polymers was verified by both gels exhibiting no observed degradation over the course of a 400+ hour incubation in pH 7.4 buffer solution.

Finally, the ability of the PGX-system to impregnate active molecules into a pre-processed scaffold using $scCO_2$ was evaluated. The success of these impregnation methods was shown to depend largely on the surface area of the polymer scaffold onto which the active molecule was being loaded, but chemical and physical interactions between the active molecule and the polymer backbone were also shown to enhance drug loading in the case of ibuprofen and chitosan. Ibuprofen release from alginate scaffolds exhibited near zero-order kinetics, with 40-70% of the impregnated drug released; in contrast, release from chitosan gels was significantly slower, with only 3-9% of the total drug released from the scaffold over 200+ hours. We hypothesized that this inhibited release is due to acid-base interactions between the ibuprofen and chitosan, resulting in an initial release of unbound/weakly bound drug followed by a release plateau (although it is hypothesised that sustained release of ibuprofen would be observed if examined on a much longer timescale).

6.2 Future Directions

Many aspects of this work have great potential to be expanded and improved upon, including the further stabilization of scaffolds for use in other applications, the investigation of a larger range of bioactive molecules for impregnation and release, and the application of the developed hydrogel scaffolds for in vivo wound healing. In particular, the following areas of

research will be pursued with the aim of further leveraging the properties of PGX-processed biopolymer scaffolds.

6.2.1 *Extended Drug Release and In Vivo Wound Healing Model*

The drug release kinetics from ibuprofen-loaded chitosan hydrogels will be studied over a significantly longer time period to assess the potential for facilitating greatly extended release profiles over the course of weeks to months. The ability of ibuprofen-loaded alginate scaffolds to actively contribute to in vivo wound healing will subsequently be explored using a murine burn wound model on BALB/c mice, while both ibuprofen-loaded and cell encapsulated chitosan scaffolds will be evaluated for use as tissue engineering scaffolds in an excised wound model.

6.2.2 *Reinforcement of Alginate Hydrogels via Covalent Crosslinking*

Calcium-ion crosslinked alginate gels are known to go through a series of ion-exchanges over time, causing gels to lose their mechanical stability and, ultimately, degrade. As such, covalent stabilization methods for alginate hydrogel scaffolds will be explored to produce gels with higher and more consistent mechanical strengths, as well as increased resistance to degradation. This will be done by first performing a rapid crosslinking reaction using calcium (to fix as much as possible of the PGX morphology in place) and subsequently exposing the gels to (a) a short-chain crosslinker like adipic acid dihydrazide, and (b) a long-chain, multi-functional crosslinker like PEGDA, hydrazide-functionalized poly(acrylamide), and/or hydrazide-functionalized POEGMA. Once covalently crosslinked, calcium ions will be removed from the scaffold via chelation using EDTA and the mechanical strength and degradation times will be tuned by modifying the degree of functionality of long-chain crosslinker molecules.

6.2.3 *Investigation into Other Hydrophobic Drugs and Impregnation*

The impregnation and release of a range of other $scCO_2$-soluble, hydrophobic drugs will be investigated and compared to the already analyzed drug loading and release kinetics for ibuprofen (Chapter 4). Subsequently, modifications will be made to existing hydrogel scaffolds (e.g. functionalizing a particular tag onto the polymer backbone) to introduce affinity binding sites to functional moieties on impregnated drugs and thus introduce a degree of tuneability to the drug release kinetics. The impregnation method will be engineered to optimize drug loadings by varying circulation time, circulation speed, loaded mass of drug, and depressurization speed. The incorporation of bioactives directly into the spray-drying process (after elimination of water and ethanol from the system) will be attempted to avoid the depressurization/re-pressurization step required to load drug prior to starting an impregnation.

6.2.4 *Graft Co-Polymerizations*

A ceric ammonium nitrate (CAN) modification will be performed in nitric acid enabling in situ generation of radicals directly on the polymer backbone that can subsequently be used to initiate a grafting reaction. Two different grafting chemistries will be pursued: (1) grafting of methyl methacrylate or butyl methacrylate to encase the soft hydrogel in a hard polymer coating, useful for reinforcing the porous structure and allowing for potential applications in high pressure bioseparations and (2) grafting of thermoresponsive poly(N-isopropylacrylamide) (PNIPAM) or POEGMA that can exhibit an LCST (i.e. switchable hydrophobicity upon heating or cooling), useful for pulsatile drug release or producing scaffolds with tunable cell adhesion.

6.2.5 *Composite Scaffolds*

The ability to create unique PGX morphologies by producing composite scaffolds combining more than one polymer has been previously demonstrated using the PGX, as shown in Figure 86 and Figure 87.

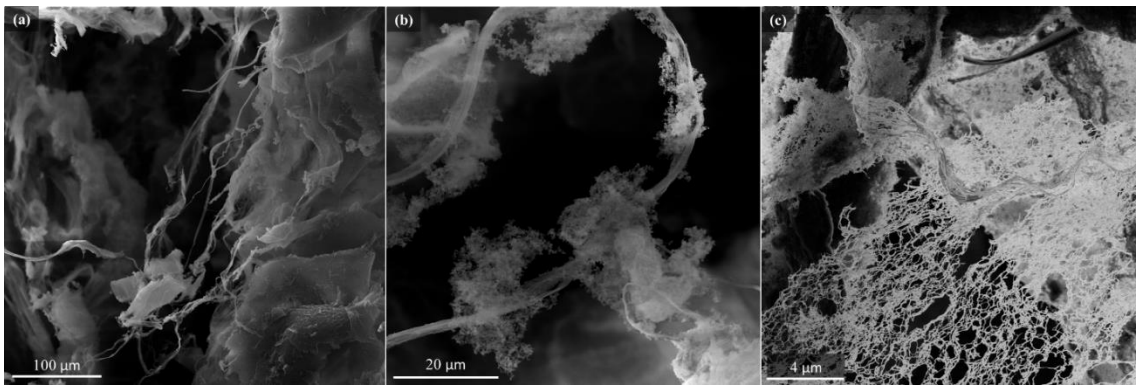

Figure 86: Images of PGX-processed composite scaffold composed of 50:50 chitosan:alginate complex by (a) SEM at 500x magnification, (b) SEM at 3000x magnification, and (c) HiM

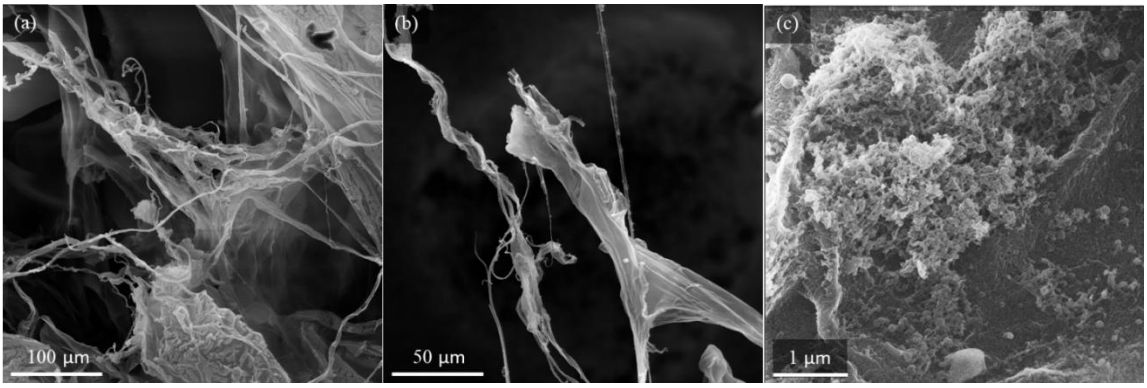

Figure 87: Images of PGX-processed composite scaffold composed of 50:50 low methoxy pectin:alginate by (a) SEM at 500x magnification, (b) SEM at 1000x magnification, and (c) HiM

Since alginate is a component of both blends shown above, calcium-ion crosslinking (perhaps coupled with the covalent crosslinking methods proposed in section 6.2.2), will be employed to stabilize these scaffolds as hydrogels. Such composite blends may enable the leveraging of the combined properties of both polymers, such as the haemostatic properties of chitosan with the efficient calcium delivery and resulting cell signalling of calcium alginate to

improve the overall function of these scaffolds in a wound healing application. The co-processing of composites containing chitosan or alginate with beta-glucan, which has intrinsic anti-inflammatory properties, will also be explored for potential wound healing applications.

References

[1] E. M. Ahmed, "Hydrogel: Preparation, characterization, and applications: A review," (in English), *Journal of Advanced Research,* vol. 6, no. 2, pp. 105-121, Mar 2015.

[2] S. Naahidi *et al.*, "Biocompatibility of hydrogel-based scaffolds for tissue engineering applications," (in English), *Biotechnology Advances,* vol. 35, no. 5, pp. 530-544, Sep-Oct 2017.

[3] M. R. Guilherme *et al.*, "Superabsorbent hydrogels based on polysaccharides for application in agriculture as soil conditioner and nutrient carrier: A review," (in English), *European Polymer Journal,* vol. 72, pp. 365-385, Nov 2015.

[4] Z. Liu, Z. J. Xia, L. Y. Fan, H. Xiao, and C. X. Cao, "An ionic coordination hybrid hydrogel for bioseparation," (in English), *Chemical Communications,* vol. 53, no. 43, pp. 5842-5845, May 28 2017.

[5] T. R. Hoare and D. S. Kohane, "Hydrogels in drug delivery: Progress and challenges," (in English), *Polymer,* vol. 49, no. 8, pp. 1993-2007, Apr 15 2008.

[6] C. F. Echeverria, Susete; Godinho, Maria; Borges, Joao; Soares, Paula;, "Functional Stimuli-Responsive Gels: Hydrogels and Microgels," *Gels,* vol. 454, 2018.

[7] M. Arruebo, "Drug delivery from structured porous inorganic materials," *Wiley Interdiscip Rev Nanomed Nanobiotechnol,* vol. 4, no. 1, pp. 16-30, Jan-Feb 2012.

[8] I. Bruzauskaite, D. Bironaite, E. Bagdonas, and E. Bernotiene, "Scaffolds and cells for tissue regeneration: different scaffold pore sizes-different cell effects," *Cytotechnology,* vol. 68, no. 3, pp. 355-69, May 2016.

[9] S. P. Lee, Michael; Wasko, Scott; Lau, Grace; Po-Yu, Chen; Novitskaya, Ekaterina; Tomsia, Antoni; Adah, Almutairi; Meyers, Marc; McKittrick, Joanna;, "Potential Bone Replacement Materials Prepared by Two Methods," *MRS Online Proceedings Library Archive,* vol. 1418, pp. 177-188, 2012.

[10] K. J. De France, F. Xu, and T. Hoare, "Structured Macroporous Hydrogels: Progress, Challenges, and Opportunities," *Adv Healthc Mater,* vol. 7, no. 1, Jan 2018.

[11] J. T. Delaney, A. R. Liberski, J. Perelaer, and U. S. Schubert, "Reactive inkjet printing of calcium alginate hydrogel porogens-a new strategy to open-pore structured matrices with controlled geometry," (in English), *Soft Matter,* vol. 6, no. 5, pp. 866-869, 2010.

[12] R. T. Tran, E. Naseri, A. Kolasnikov, X. Bai, and J. Yang, "A new generation of sodium chloride porogen for tissue engineering," *Biotechnol Appl Biochem,* vol. 58, no. 5, pp. 335-44, Sep-Oct 2011.

[13] M. Dadsetan *et al.*, "Effect of hydrogel porosity on marrow stromal cell phenotypic expression," *Biomaterials,* vol. 29, no. 14, pp. 2193-202, May 2008.

[14] G. H. Yu and Y. B. Fan, "Preparation of poly(D,L-lactic acid) scaffolds using alginate particles," (in English), *Journal of Biomaterials Science-Polymer Edition,* vol. 19, no. 1, pp. 87-98, 2008.

[15] J. Kim, M. J. Yaszemski, and L. Lu, "Three-dimensional porous biodegradable polymeric scaffolds fabricated with biodegradable hydrogel porogens," *Tissue Eng Part C Methods,* vol. 15, no. 4, pp. 583-94, Dec 2009.

[16] G. H. Wu and S. H. Hsu, "Review: Polymeric-Based 3D Printing for Tissue Engineering," *J Med Biol Eng,* vol. 35, no. 3, pp. 285-292, 2015.

[17] S. Derakhshanfar, R. Mbeleck, K. Xu, X. Zhang, W. Zhong, and M. Xing, "3D bioprinting for biomedical devices and tissue engineering: A review of recent trends and advances," *Bioact Mater,* vol. 3, no. 2, pp. 144-156, Jun 2018.

[18] T. Boland, V. Mironov, A. Gutowska, E. A. Roth, and R. R. Markwald, "Cell and organ printing 2: fusion of cell aggregates in three-dimensional gels," *Anat Rec A Discov Mol Cell Evol Biol,* vol. 272, no. 2, pp. 497-502, Jun 2003.

[19] K. Jakab, C. Norotte, F. Marga, K. Murphy, G. Vunjak-Novakovic, and G. Forgacs, "Tissue engineering by self-assembly and bio-printing of living cells," *Biofabrication,* vol. 2, no. 2, p. 022001, Jun 2010.

[20] I. T. Ozbolat and M. Hospodiuk, "Current advances and future perspectives in extrusion-based bioprinting," *Biomaterials,* vol. 76, pp. 321-43, Jan 2016.

[21] G. P. B. Pfeifer, A.;, "Mutations induced by ultraviolet light," *Mutation Research/Fundamental and Molecular Mechanisms of Mutagenesis,* vol. 571, no. 1-2, pp. 19-31, 2005.

[22] W. Zongjie, T. Zhenlin, J. Xian, J. F. Holzman, F. Menard, and K. Keekyoung, "Visible light-based stereolithography bioprinting of cell-adhesive gelatin hydrogels," *Conf Proc IEEE Eng Med Biol Soc,* vol. 2017, pp. 1599-1602, Jul 2017.

[23] Z. Wang *et al.*, "Visible Light Photoinitiation of Cell-Adhesive Gelatin Methacryloyl Hydrogels for Stereolithography 3D Bioprinting," *ACS Appl Mater Interfaces,* Aug 1 2018.

[24] L. A. Hockaday *et al.*, "Rapid 3D printing of anatomically accurate and mechanically heterogeneous aortic valve hydrogel scaffolds," *Biofabrication,* vol. 4, no. 3, p. 035005, Sep 2012.

[25] N. Annabi *et al.*, "Controlling the porosity and microarchitecture of hydrogels for tissue engineering," *Tissue Eng Part B Rev,* vol. 16, no. 4, pp. 371-83, Aug 2010.

[26] K. M. B. Huh, Namjin; Park, Kinam;, "Enhanced Swelling Rate of Poly(ethylene glycol)-Grafted Superporous Hydrogels," *Journal of Bioactive and Compatible Polymers,* vol. 20, no. 3, pp. 231-243, 2005.

[27] T. K. Kim, J. J. Yoon, D. S. Lee, and T. G. Park, "Gas foamed open porous biodegradable polymeric microspheres," *Biomaterials,* vol. 27, no. 2, pp. 152-9, Jan 2006.

[28] F. Dehghani and N. Annabi, "Engineering porous scaffolds using gas-based techniques," *Curr Opin Biotechnol,* vol. 22, no. 5, pp. 661-6, Oct 2011.

[29] N. Annabi, S. M. Mithieux, A. S. Weiss, and F. Dehghani, "Cross-linked open-pore elastic hydrogels based on tropoelastin, elastin and high pressure CO2," *Biomaterials,* vol. 31, no. 7, pp. 1655-65, Mar 2010.

[30] T. S. Zhang, Michael;, "Doubly-crosslinked, emulsion-templated hydrogels through reversiblemetal coordination," *Polymers,* vol. 126, pp. 386-394, 2017.

[31] S. W. Zou, Z. J. Wei, Y. Hu, Y. H. Deng, Z. Tong, and C. Y. Wang, "Macroporous antibacterial hydrogels with tunable pore structures fabricated by using Pickering high internal phase emulsions as templates," (in English), *Polymer Chemistry,* vol. 5, no. 14, pp. 4227-4234, 2014.

[32] P. Krajnc, D. Stefanec, and I. Pulko, "Acrylic acid "reversed" polyHIPEs," (in English), *Macromolecular Rapid Communications,* vol. 26, no. 16, pp. 1289-1293, Aug 19 2005.

[33] T. L. Henderson, Katharina; Haylock, David; McLean, Keith; O'Connor, Andrea;, "Cryogels for biomedical applications," *Journal of Materials Chemistry B,* vol. 1, pp. 2682-2695, 2013.

[34] G. C. Ingavle *et al.*, "Affinity binding of antibodies to supermacroporous cryogel adsorbents with immobilized protein A for removal of anthrax toxin protective antigen," *Biomaterials,* vol. 50, pp. 140-53, May 2015.

[35] M. Jurga *et al.*, "The performance of laminin-containing cryogel scaffolds in neural tissue regeneration," *Biomaterials,* vol. 32, no. 13, pp. 3423-34, May 2011.

[36] Y. Hiramure, K. Suga, H. Umakoshi, J. Matsumoto, and K. Shiomori, "Preparation and Characterization of Poly-N-isopropylacrylamide Cryogels containing Liposomes and Their Adsorption Properties of Tryptophan," (in English), *Solvent Extraction Research and Development-Japan,* vol. 25, no. 1, pp. 37-46, 2018.

[37] A. M. Thomas and L. D. Shea, "Cryotemplation for the Rapid Fabrication of Porous, Patternable Photopolymerized Hydrogels," *J Mater Chem B,* vol. 2, no. 28, pp. 4521-4530, Jul 28 2014.

[38] W. B. Wan, Dawn; Yang, Lifang; Mak, Helium;, "Poly(Vinyl Alcohol) Cryogels for Biomedical Applications," *Advances in Polymer Science,* vol. 263, pp. 283-321, 2014.

[39] V. I. Lozinsky, I. Y. Galaev, F. M. Plieva, I. N. Savina, H. Jungvid, and B. Mattiasson, "Polymeric cryogels as promising materials of biotechnological interest," *Trends Biotechnol,* vol. 21, no. 10, pp. 445-51, Oct 2003.

[40] N. E. Vrana *et al.*, "Cell encapsulation and cryostorage in PVA-gelatin cryogels: incorporation of carboxylated e-poly-L-lysine as cryoprotectant," (in English), *Journal of Tissue Engineering and Regenerative Medicine,* vol. 6, no. 4, pp. 280-290, Apr 2012.

[41] A. De Mori, M. P. Fernandez, G. Blunn, G. Tozzi, and M. Roldo, "3D Printing and Electrospinning of Composite Hydrogels for Cartilage and Bone Tissue Engineering," (in English), *Polymers,* vol. 10, no. 3, Mar 2018.

[42] X. M. Shi *et al.*, "Electrospinning of Nanofibers and Their Applications for Energy Devices," (in English), *Journal of Nanomaterials,* 2015.

[43] E. D. Boland, G. E. Wnek, D. G. Simpson, K. J. Pawlowski, and G. L. Bowlin, "Tailoring tissue engineering scaffolds using electrostatic processing techniques: A study of poly(glycolic acid) electrospinning," (in English), *Journal of Macromolecular Science-Pure and Applied Chemistry,* vol. 38, no. 12, pp. 1231-1243, 2001.

[44] J. Deitzel *et al*. "Controlled Deposition and Collection of Electro-spun Poly(ethylene oxide) Fibers", *Polymer*, 2001.

[45] A. Hasan *et al.*, "Electrospun scaffolds for tissue engineering of vascular grafts," *Acta Biomater,* vol. 10, no. 1, pp. 11-25, Jan 2014.

[46] S. M. Lin and L. X. Gu, "Influence of Crosslink Density and Stiffness on Mechanical Properties of Type I Collagen Gel," (in English), *Materials,* vol. 8, no. 2, pp. 551-560, Feb 2015.

[47] A. N. Stachowiak, A. Bershteyn, E. Tzatzalos, and D. J. Irvine, "Bioactive hydrogels with an ordered cellular structure combine interconnected macroporosity and robust mechanical properties," (in English), *Advanced Materials,* vol. 17, no. 4, pp. 399-+, Feb 23 2005.

[48] B. Tarus, N. Fadel, A. Al-Oufy, and M. El-Messiry, "Effect of polymer concentration on the morphology and mechanical characteristics of electrospun cellulose acetate and poly (vinyl chloride) nanofiber mats," (in English), *Alexandria Engineering Journal,* vol. 55, no. 3, pp. 2975-2984, Sep 2016.

[49] A. Bin Imran, T. Seki, and Y. Takeoka, "Recent advances in hydrogels in terms of fast stimuli responsiveness and superior mechanical performance," (in English), *Polymer Journal,* vol. 42, no. 11, pp. 839-851, Nov 2010.

[50] M. K. C. Hrnčič, Darija; Verboten, Mojca Tancer; Knez, Željko;, "Application of supercritical and subcritical fluids in food processing," *Food Quality and Safety,* vol. 2, no. 2, pp. 59-67, 2018.

[51] J. Li and D. J. Mooney, "Designing hydrogels for controlled drug delivery," *Nat Rev Mater,* vol. 1, no. 12, Dec 2016.

[52] N. M. Smeets, E. Bakaic, M. Patenaude, and T. Hoare, "Injectable poly(oligoethylene glycol methacrylate)-based hydrogels with tunable phase transition behaviours: physicochemical and biological responses," *Acta Biomater,* vol. 10, no. 10, pp. 4143-55, Oct 2014.

[53] M. P. Simpson, Justin; Katare, Yogesh; Kooner, Sharnpreet, Kooner; Smeets, Niels; Mishra, Ram; Hoare, Todd;, "Microgels as vehicles for effective delivery of hydrophobic drugs to the brain," in *10th World Biomaterials Congress*, Montreal, Canada, 2016: Fronteirs.

[54] Y. Fu and W. J. Kao, "Drug release kinetics and transport mechanisms of non-degradable and degradable polymeric delivery systems," *Expert Opin Drug Deliv,* vol. 7, no. 4, pp. 429-44, Apr 2010.

[55] E. B. Holowka, S.K., "Controlled-Release Systems," in *Drug Delivery: Materials Design and Clinical Perspective*New York: Springer-Verlag New York, 2014, pp. 7-62.

[56] P. Andrade-Vivero, E. Fernandez-Gabriel, C. Alvarez-Lorenzo, and A. Concheiro, "Improving the loading and release of NSAIDs from pHEMA hydrogels by copolymerization with functionalized monomers," (in English), *Journal of Pharmaceutical Sciences,* vol. 96, no. 4, pp. 802-813, Apr 2007.

[57] L. Padrela, M. A. Rodrigues, A. Duarte, A. M. A. Dias, M. E. M. Braga, and H. C. de Sousa, "Supercritical carbon dioxide-based technologies for the production of drug nanoparticles/nanocrystals - A comprehensive review," *Adv Drug Deliv Rev,* Jul 17 2018.

[58] A. C. Gonzalez, T. F. Costa, Z. A. Andrade, and A. R. Medrado, "Wound healing - A literature review," *An Bras Dermatol,* vol. 91, no. 5, pp. 614-620, Sep-Oct 2016.

[59] R. G. Frykberg and J. Banks, "Challenges in the Treatment of Chronic Wounds," *Adv Wound Care (New Rochelle),* vol. 4, no. 9, pp. 560-582, Sep 1 2015.

[60] T. J. Koh and L. A. DiPietro, "Inflammation and wound healing: the role of the macrophage," (in English), *Expert Reviews in Molecular Medicine,* vol. 13, Jul 11 2011.

[61] M. Xue and C. J. Jackson, "Extracellular Matrix Reorganization During Wound Healing and Its Impact on Abnormal Scarring," *Adv Wound Care (New Rochelle),* vol. 4, no. 3, pp. 119-136, Mar 1 2015.

[62] A. M. Szpaderska and L. A. DiPietro, "Inflammation in surgical wound healing: friend or foe?," *Surgery,* vol. 137, no. 5, pp. 571-3, May 2005.

[63] A. D. Dardenne, B. C. Wulff, and T. A. Wilgus, "The alarmin HMGB-1 influences healing outcomes in fetal skin wounds," *Wound Repair Regen,* vol. 21, no. 2, pp. 282-91, Mar-Apr 2013.

[64] C. C. Yates, P. Hebda, and A. Wells, "Skin wound healing and scarring: fetal wounds and regenerative restitution," *Birth Defects Res C Embryo Today,* vol. 96, no. 4, pp. 325-33, Dec 2012.

[65] N. X. Landen, D. Q. Li, and M. Stahle, "Transition from inflammation to proliferation: a critical step during wound healing," (in English), *Cellular and Molecular Life Sciences,* vol. 73, no. 20, pp. 3861-3885, Oct 2016.

[66] B. Brune *et al.*, "Redox control of inflammation in macrophages," *Antioxid Redox Signal,* vol. 19, no. 6, pp. 595-637, Aug 20 2013.

[67] S. G. Kumbar, S. P. Nukavarapu, R. James, L. S. Nair, and C. T. Laurencin, "Electrospun poly(lactic acid-co-glycolic acid) scaffolds for skin tissue engineering," (in English), *Biomaterials,* vol. 29, no. 30, pp. 4100-4107, Oct 2008.

[68] B. J. Kim *et al.*, "Accelerated skin wound healing using electrospun nanofibrous mats blended with mussel adhesive protein and polycaprolactone," (in English), *Journal of Biomedical Materials Research Part A,* vol. 105, no. 1, pp. 218-225, Jan 2017.

[69] A. R. Del Bakhshayesh *et al.*, "Recent advances on biomedical applications of scaffolds in wound healing and dermal tissue engineering," (in English), *Artificial Cells Nanomedicine and Biotechnology,* vol. 46, no. 4, pp. 691-705, 2018.

[70] L. E. Dickinson and S. Gerecht, "Engineered Biopolymeric Scaffolds for Chronic Wound Healing," *Front Physiol,* vol. 7, p. 341, 2016.

[71] Y. Li, Y. Han, X. Wang, J. Peng, Y. Xu, and J. Chang, "Multifunctional Hydrogels Prepared by Dual Ion Cross-Linking for Chronic Wound Healing," *ACS Appl Mater Interfaces,* vol. 9, no. 19, pp. 16054-16062, May 17 2017.

[72] X. Wang, T. Lou, W. Zhao, G. Song, C. Li, and G. Cui, "The effect of fiber size and pore size on cell proliferation and infiltration in PLLA scaffolds on bone tissue engineering," *J Biomater Appl,* vol. 30, no. 10, pp. 1545-51, May 2016.

[73] B. Du, C. Y. Lin, Z. X. Bian, and B. J. Xu, "An insight into anti-inflammatory effects of fungal beta-glucans," (in English), *Trends in Food Science & Technology,* vol. 41, no. 1, pp. 49-59, Jan 2015.

[74] M. S. Pogorielov, Vitalii;, "Chitosan as a Hemostatic Agent: Current State," *European Journal of Medicine. Series B.,* vol. 2, no. 1, pp. 24-33, 2015.

[75] V. O. O. Goodship, Erich;, *Polymer Processing with Supercritical Fluids* (Rapra Review Reports, no. 8). Shawbury, Shropshire, United Kingdom: Rapra Technology, 2004.

[76] S. Cotugno *et al.*, "Characterization of microcellular biodegradable polymeric foams produced from supercritical carbon dioxide solutions," (in English), *Industrial & Engineering Chemistry Research,* vol. 44, no. 6, pp. 1795-1803, Mar 16 2005.

[77] M. Sauceau, J. Fages, A. Common, C. Nikitine, and E. Rodier, "New challenges in polymer foaming: A review of extrusion processes assisted by supercritical carbon dioxide," (in English), *Progress in Polymer Science,* vol. 36, no. 6, pp. 749-766, Jun 2011.

[78] S. H. Alavi, B. K. Gogoi, M. Khan, B. J. Bowman, and S. S. H. Rizvi, "Structural properties of protein-stabilized starch-based supercritical fluid extrudates," (in English), *Food Research International,* vol. 32, no. 2, pp. 107-118, 1999.

[79] S. H. Zheng, Xiaohui; Ibrahim, Abdul-Rauf; Tang, Daoting; Tan, Yuquan; Li, Jun;, "Supercritical Fluid Drying: Classifications and Applications," *Recent Patents on Chemical Engineering,* vol. 3, pp. 230-244, 2010.

[80] I. De Marco and E. Reverchon, "Supercritical carbon dioxide plus ethanol mixtures for the antisolvent micronization of hydrosoluble materials," (in English), *Chemical Engineering Journal,* vol. 187, pp. 401-409, Apr 1 2012.

[81] A. M. Scurto, K. Hutchenson, and B. Subramaniam, "Gas-Expanded Liquids: Fundamentals and Applications," (in English), *Gas-Expanded Liquids and near-Critical Media: Green Chemistry and Engineering,* vol. 1006, pp. 3-37, 2009.

[82] P. G. Jessop and B. Subramaniam, "Gas-expanded liquids," (in English), *Chemical Reviews,* vol. 107, no. 6, pp. 2666-2694, Jun 2007.

[83] A. A. A. Halim, Z. Mohammed Suleiman; Kadir, Habsah Abdul; Tayyab, Saad;, "Alcohol-induced structural transitions in the acid-denatured Bacillus licheniformis α-amylase," *Journal of Saudi Chemical Society,* vol. 21, no. 1, pp. s349-s358, 2017.

[84] N. E. Durling, O. J. Catchpole, S. J. Tallon, and J. B. Grey, "Measurement and modelling of the ternary phase equilibria for high pressure carbon dioxide-ethanol-water mixtures," (in English), *Fluid Phase Equilibria,* vol. 252, no. 1-2, pp. 103-113, Mar 1 2007.

[85] A. Raguin and O. Ebenhoh, "Design starch: stochastic modeling of starch granule biogenesis," (in English), *Biochemical Society Transactions,* vol. 45, pp. 885-893, Aug 15 2017.

[86] E. C. O'Neill and R. A. Field, "Underpinning Starch Biology with in vitro Studies on Carbohydrate-Active Enzymes and Biosynthetic Glycomaterials," *Front Bioeng Biotechnol,* vol. 3, p. 136, 2015.

[87] A. M. Smith, "The biosynthesis of starch granules," *Biomacromolecules,* vol. 2, no. 2, pp. 335-41, Summer 2001.

[88] M. Schirmer, M. Jekle, and T. Becker, "Starch gelatinization and its complexity for analysis," (in English), *Starch-Starke,* vol. 67, no. 1-2, pp. 30-41, Jan 2015.

[89] S. J. Wang, C. L. Li, L. Copeland, Q. Niu, and S. Wang, "Starch Retrogradation: A Comprehensive Review," (in English), *Comprehensive Reviews in Food Science and Food Safety,* vol. 14, no. 5, pp. 568-585, Sep 2015.

[90] A. R. Allwyn Sundar Raj, S.; Jayabalan, R.; Ranganathan, T.V.;, "A Review on Pectin: Chemistry due to General Properties of Pectin and its Pharmaceutical Uses," *Scientific Reports,* vol. 1, no. 12, 2012.

[91] A. Strom, E. Schuster, and S. M. Goh, "Rheological characterization of acid pectin samples in the absence and presence of monovalent ions," (in English), *Carbohydrate Polymers,* vol. 113, pp. 336-343, Nov 26 2014.

[92] D. Elieh-Ali-Komi and M. R. Hamblin, "Chitin and Chitosan: Production and Application of Versatile Biomedical Nanomaterials," *Int J Adv Res (Indore),* vol. 4, no. 3, pp. 411-427, Mar 2016.

[93] J. K. F. Suh and H. W. T. Matthew, "Application of chitosan-based polysaccharide biomaterials in cartilage tissue engineering: a review," (in English), *Biomaterials,* vol. 21, no. 24, pp. 2589-2598, Dec 2000.

[94] S. Dumitriu, "Polymeric Biomaterials." New York, NY: Marcel Dekker, Inc., 2002, p.^pp. Pages.

[95] A. Jimtaisong and N. Saewan, "Utilization of carboxymethyl chitosan in cosmetics," (in English), *International Journal of Cosmetic Science,* vol. 36, no. 1, pp. 12-21, Feb 2014.

[96] Q. Z. Wang *et al.*, "Protonation constants of chitosan with different molecular weight and degree of deacetylation," (in English), *Carbohydrate Polymers,* vol. 65, no. 2, pp. 194-201, Jul 25 2006.

[97] V. Zargar, M. Asghari, and A. Dashti, "A Review on Chitin and Chitosan Polymers: Structure, Chemistry, Solubility, Derivatives, and Applications," (in English), *Chembioeng Reviews,* vol. 2, no. 3, pp. 204-226, Jun 2015.

[98] M. N. V. R. Kumar, R. A. A. Muzzarelli, C. Muzzarelli, H. Sashiwa, and A. J. Domb, "Chitosan chemistry and pharmaceutical perspectives," (in English), *Chemical Reviews,* vol. 104, no. 12, pp. 6017-6084, Dec 2004.

[99] F.-M. H. Hsieh, Chih; Lin, Tsair-Fuh; Chen, Yan-Ming; Lin, Jui-Che;, "Study of sodium tripolyphosphate-crosslinked chitosan beads entrapped with Pseudomonas putida for phenol degradation," *Process Biochemistry,* vol. 43, no. 1, pp. 83-92, 2008.

[100] H. K. Jonassen, Anna-Lena; Hiorth, Marianne, "Stability of Chitosan Nanoparticles Cross-Linked with Tripolyphosphate," *Biomacromolecules,* vol. 13, no. 11, pp. 3747-3756, 2012.

[101] K. Y. Lee, W. S. Ha, and W. H. Park, "Blood compatibility and biodegradability of partially N-acylated chitosan derivatives," *Biomaterials,* vol. 16, no. 16, pp. 1211-6, Nov 1995.

[102] S. Hirano, H. Tsuchida, and N. Nagao, "N-acetylation in chitosan and the rate of its enzymic hydrolysis," *Biomaterials,* vol. 10, no. 8, pp. 574-6, Oct 1989.

[103] M. I. Oliveira, S. G. Santos, M. J. Oliveira, A. L. Torres, and M. A. Barbosa, "Chitosan drives anti-inflammatory macrophage polarisation and pro-inflammatory dendritic cell stimulation," *Eur Cell Mater,* vol. 24, pp. 136-52; discussion 152-3, Jul 24 2012.

[104] G. Peluso *et al.*, "Chitosan-Mediated Stimulation of Macrophage Function," (in English), *Biomaterials,* vol. 15, no. 15, pp. 1215-1220, Dec 1994.

[105] F. Croisier and C. Jerome, "Chitosan-based biomaterials for tissue engineering," (in English), *European Polymer Journal,* vol. 49, no. 4, pp. 780-792, Apr 2013.

[106] S. Y. Ong, J. Wu, S. M. Moochhala, M. H. Tan, and J. Lu, "Development of a chitosan-based wound dressing with improved hemostatic and antimicrobial properties," (in English), *Biomaterials,* vol. 29, no. 32, pp. 4323-4332, Nov 2008.

[107] N. R. Sudarshan, D. G. Hoover, and D. Knorr, "Antibacterial Action of Chitosan," (in English), *Food Biotechnology,* vol. 6, no. 3, pp. 257-272, 1992.

[108] S. Wittaya-areekul, J. Kruenate, and C. Prahsarn, "Preparation and in vitro evaluation of mucoadhesive properties of alginate/chitosan microparticles containing prednisolone," *Int J Pharm,* vol. 312, no. 1-2, pp. 113-8, Apr 7 2006.

[109] J. Smith, E. Wood, and M. Dornish, "Effect of chitosan on epithelial cell tight junctions," (in English), *Pharmaceutical Research,* vol. 21, no. 1, pp. 43-49, Jan 2004.

[110] K. S. Bhise, R. S. Dhumal, A. R. Paradkar, and S. S. Kadam, "Effect of drying methods on swelling, erosion and drug release from chitosan-naproxen sodium complexes," (in English), *Aaps Pharmscitech,* vol. 9, no. 1, pp. 1-12, Mar 2008.

[111] A. P. Stephen, G.; Williams, P., *Food Polysaccharides and Their Applications*. Boca Raton, Florida: Taylor & Francis Group, 2006.

[112] J. T. Oliveira and R. L. Reis, "Polysaccharide-based materials for cartilage tissue engineering applications," *J Tissue Eng Regen Med,* vol. 5, no. 6, pp. 421-36, Jun 2011.

[113] Y. Yuguchi, A. Hasegawa, A. M. Padol, K. I. Draget, and B. T. Stokke, "Local structure of Ca(2+) induced hydrogels of alginate-oligoguluronate blends determined by small-angle-X-ray scattering," *Carbohydr Polym,* vol. 152, pp. 532-540, Nov 5 2016.

[114] F. Lotfipour, S. Mirzaeei, and M. Maghsoodi, "Evaluation of the effect of CaCl2 and alginate concentrations and hardening time on the characteristics of Lactobacillus

acidophilus loaded alginate beads using response surface analysis," *Adv Pharm Bull,* vol. 2, no. 1, pp. 71-8, 2012.

[115] E. A. Growney Kalaf, R. Flores, J. G. Bledsoe, and S. A. Sell, "Characterization of slow-gelling alginate hydrogels for intervertebral disc tissue-engineering applications," *Mater Sci Eng C Mater Biol Appl,* vol. 63, pp. 198-210, Jun 2016.

[116] K. Y. Lee and D. J. Mooney, "Alginate: properties and biomedical applications," *Prog Polym Sci,* vol. 37, no. 1, pp. 106-126, Jan 2012.

[117] M. L. Zaitoun, C., "Chelating behavior between metal ions and EDTA in sol-gel Matrix," *Journal of Physical Chemistry,* vol. 101, no. 10, pp. 1857-1860, 1997.

[118] D. Morgan, "Alginate Dressings," *Journal of Tissue Viability,* vol. 7, no. 1, pp. 4-9, 1996.

[119] T. Gilchrist and A. M. Martin, "Wound treatment with Sorbsan--an alginate fibre dressing," *Biomaterials,* vol. 4, no. 4, pp. 317-20, Oct 1983.

[120] M. J. Berridge, "Calcium signalling and cell proliferation," *Bioessays,* vol. 17, no. 6, pp. 491-500, Jun 1995.

[121] L. A. Munaron, S.; Lovisolo, D.;, "Intracellular calcium signals and control of cell proliferation: how many mechanisms?," *Journal of Cellular and Molecular Medicine,* vol. 8, no. 2, pp. 161-168, 2004.

[122] S. Thomas, "Alginate dressings in surgery and wound management--Part 1," *J Wound Care,* vol. 9, no. 2, pp. 56-60, Feb 2000.

[123] B. Balakrishnan, M. Mohanty, A. C. Fernandez, P. V. Mohanan, and A. Jayakrishnan, "Evaluation of the effect of incorporation of dibutyryl cyclic adenosine monophosphate in an in situ-forming hydrogel wound dressing based on oxidized alginate and gelatin," *Biomaterials,* vol. 27, no. 8, pp. 1355-61, Mar 2006.

[124] S. Y. Rabbany *et al.*, "Continuous delivery of stromal cell-derived factor-1 from alginate scaffolds accelerates wound healing," *Cell Transplant,* vol. 19, no. 4, pp. 399-408, 2010.

[125] T. Boontheekul, H. J. Kong, and D. J. Mooney, "Controlling alginate gel degradation utilizing partial oxidation and bimodal molecular weight distribution," *Biomaterials,* vol. 26, no. 15, pp. 2455-65, May 2005.

[126] B. Y. Shin, B. G. Cha, J. H. Jeong, and J. Kim, "Injectable Macroporous Ferrogel Microbeads with a High Structural Stability for Magnetically Actuated Drug Delivery," *ACS Appl Mater Interfaces,* vol. 9, no. 37, pp. 31372-31380, Sep 20 2017.

[127] S. Maiti, K. Singha, S. Ray, P. Dey, and B. Sa, "Adipic acid dihydrazide treated partially oxidized alginate beads for sustained oral delivery of flurbiprofen," *Pharm Dev Technol,* vol. 14, no. 5, pp. 461-70, 2009.

[128] *HEPES-Buffered Saline*, 2006.

[129] S. K. K. Bajpai, Narendra;, "Swelling and drug release behaviour of calcium alginate/poly(sodium acrylate) hydrogel beads," *Designed Monomers and Polymers,* vol. 19, no. 1, pp. 89-98, 2015.

[130] Q. X. Wu, D. Q. Lin, and S. J. Yao, "Design of chitosan and its water soluble derivatives-based drug carriers with polyelectrolyte complexes," *Mar Drugs,* vol. 12, no. 12, pp. 6236-53, Dec 19 2014.

[131] Y. Y. Xin, Jinying;, "Schiff's Base as a Stimuli-Responsive Linker in Polymer Chemistry," *Polymer Chemistry,* vol. 3, no. 11, pp. 3045-3055, 2012.

[132] C. d. S. da Silva, Daniel; Modolo, Luzia; Alves, Rosemeire; Resende, Maria; Martins, Cleide; Fatima, Angela;, "Schiff Bases: A short review of their antimicrobial activities," *Journal of Advanced Research,* vol. 2, pp. 1-8, 2011.

[133] I. Migneault, C. Dartiguenave, M. J. Bertrand, and K. C. Waldron, "Glutaraldehyde: behavior in aqueous solution, reaction with proteins, and application to enzyme crosslinking," *Biotechniques,* vol. 37, no. 5, pp. 790-6, 798-802, Nov 2004.

[134] M. E. Nimni, D. Cheung, B. Strates, M. Kodama, and K. Sheikh, "Chemically modified collagen: a natural biomaterial for tissue replacement," *J Biomed Mater Res,* vol. 21, no. 6, pp. 741-71, Jun 1987.

[135] J. Kawahara, T. Ohmori, T. Ohkubo, S. Hattori, and M. Kawamura, "The Structure of Glutaraldehyde in Aqueous-Solution Determined by Ultraviolet-Absorption and Light-Scattering," (in English), *Analytical Biochemistry,* vol. 201, no. 1, pp. 94-98, Feb 14 1992.

[136] Y. S. Kim, C. J. Lee, and J. Y. Ma, "Enhancement of active compound, genipin, from Gardeniae Fructus using immobilized glycosyl hydrolase family 3 beta-glucosidase from Lactobacillus antri," (in English), *Amb Express,* vol. 7, Mar 16 2017.

[137] R. Muzzarelli, "Genipin-crosslinked chitosan hydrogels as biomedical and pharmaceutical aids," *Carbohydrate Polymers,* vol. 77, pp. 1-9, 2009.

[138] P. C. Denton, Barbara; Roberts, Matthew; Forbes, Ben; Seton, Linda; Madden, Judith; Enoch, Steve; McAuley, William; Saleem, Imran; Lawrence, Jayne; Moss, Gary; Russell, Craig; Afzal, Mohammed;, *Pharmaceutics: the science of medicine design*. Oxford, United Kingdom: Oxford University Press, 2013.

[139] M. A. Kiselev, A. Gryzunov Iu, G. E. Dobretsov, and M. N. Komarova, "[Size of a human serum albumin molecule in solution]," *Biofizika,* vol. 46, no. 3, pp. 423-7, May-Jun 2001. Razmer molekuly syvorotochnogo al'bumina cheloveka v rastvore.

[140] S. Aldrich. (September 7). *Product Information: Fibrinogen from human plasma*. Available: https://www.sigmaaldrich.com/content/dam/sigma-aldrich/docs/Sigma/Product_Information_Sheet/f4883pis.pdf

[141] C. M. Laroche, Phillipe;, "A novel alginate from the brown seaweed Sargassum turbinaroides (Sargassae).", vol. 2, Current Topics on Bioprocesses in Food IndustryNew Delhi, India: Asiatech Publisher, Inc., 2009, pp. 227-242. [Online]. Available.

[142] C. M. Kuo, Peter;, "Ionically crosslinked alginate hydrogels as sca!olds for tissue engineering: Part 1. Structure, gelation rate and mechanical properties," *Biomaterials,* vol. 22, pp. 511-521, 2001.

[143] J. Liu, H. Zheng, P. S. Poh, H. G. Machens, and A. F. Schilling, "Hydrogels for Engineering of Perfusable Vascular Networks," *Int J Mol Sci,* vol. 16, no. 7, pp. 15997-6016, Jul 14 2015.

[144] A. R. Duarte *et al.*, "Impregnation of an intraocular lens for ophthalmic drug delivery," *Curr Drug Deliv,* vol. 5, no. 2, pp. 102-7, Apr 2008.

[145] S. J. Macnaughton, I. Kikic, N. R. Foster, P. Alessi, A. Cortesi, and I. Colombo, "Solubility of anti-inflammatory drugs in supercritical carbon dioxide," (in English), *Journal of Chemical and Engineering Data,* vol. 41, no. 5, pp. 1083-1086, Sep-Oct 1996.

[146] S. L. Ma, Z. W. Lu, Y. T. Wu, and Z. B. Zhang, "Partitioning of drug model compounds between poly(lactic acid)s and supercritical CO2 using quartz crystal microbalance as an in situ detector," (in English), *Journal of Supercritical Fluids,* vol. 54, no. 2, pp. 129-136, Aug 2010.

[147] J. Kerc, S. Srcic, Z. Knez, and P. Sencar-Bozic, "Micronization of drugs using supercritical carbon dioxide," (in English), *International Journal of Pharmaceutics,* vol. 182, no. 1, pp. 33-39, May 10 1999.

[148] M. Ni, Q. Q. Xu, and J. Z. Yin, "Preparation of controlled release nanodrug ibuprofen supported on mesoporous silica using supercritical carbon dioxide," (in English), *Journal of Materials Research,* vol. 27, no. 22, pp. 2902-2910, Nov 2012.

[149] J. Pavlinec, "Photocrosslinking Polymerization of Methacrylate Modified Triethoxysilanes Polycondensates and Multifunctional Methacrylates," *Macromolecular Materials and Engineering,* vol. 288, no. 10, pp. 789-797, 2003.

[150] C. M. Nolan, M. J. Serpe, and L. A. Lyon, "Pulsatile release of insulin from Layer-by-Layer assembled microgel thin films," (in English), *Macromolecular Symposia,* vol. 227, pp. 285-294, Jul 2005.

[151] T. B. Hoare, Emilia; Smeets, Niels; Deng, Xudong;, "Poly(oligoethylene glycol methacrylate) hydrogel compositions and methods of use thereof," United States, 2016.

[152] J. J. Gurav, In-Keun; Park, Hyung-Ho; Kang, Eul Son; Nadargi, Digambar;, "Silica Aerogel: Synthesis and Applications," *Journal of Nanomaterials,* vol. 2010, pp. 1-11, 2010.

[153] P. S. Thapliyal, Kirti;, "Aerogels as Promising Thermal Insulating Materials: An Overview," *Journal of Materials,* vol. 2014, pp. 1-10, 2014.

Appendix

Calibration Curves for UV-Vis Analysis of Ibuprofen/Irgacure 2959

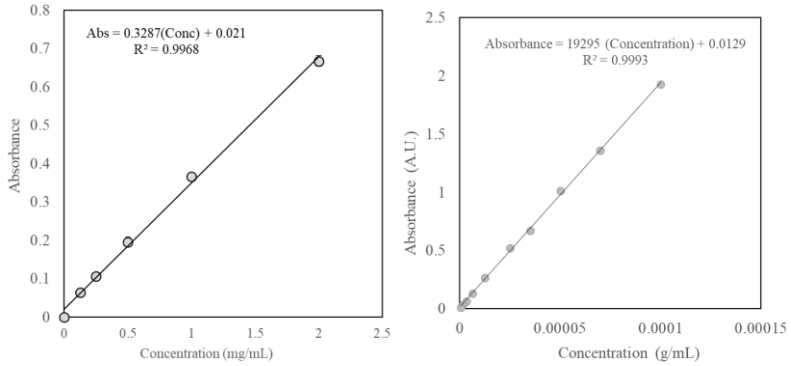

Figure 88: UV-Vis calibration curves for Ibuprofen (left) and Irgacure 2959 (right) in EtOH

Calibration Curves for Protein Studies

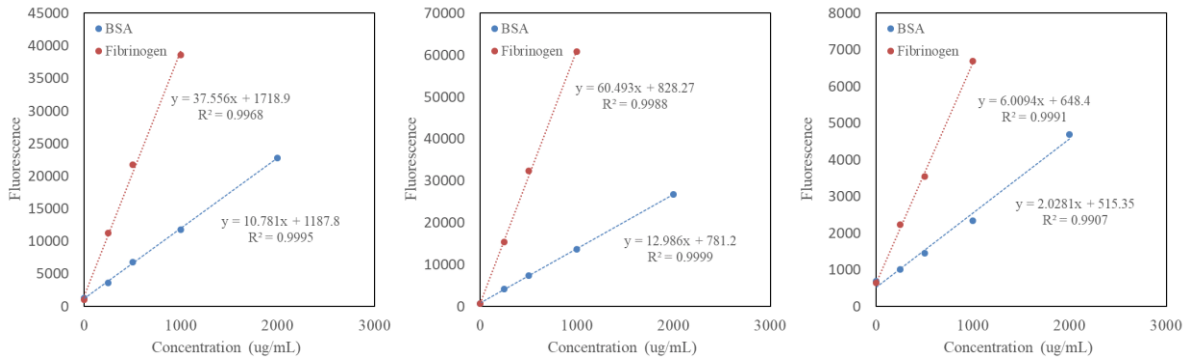

Figure 89: Fluorescence calibration curves for chitosan gel trial after 24 hours (left), 72 hours (middle), and 72-hour release (right).

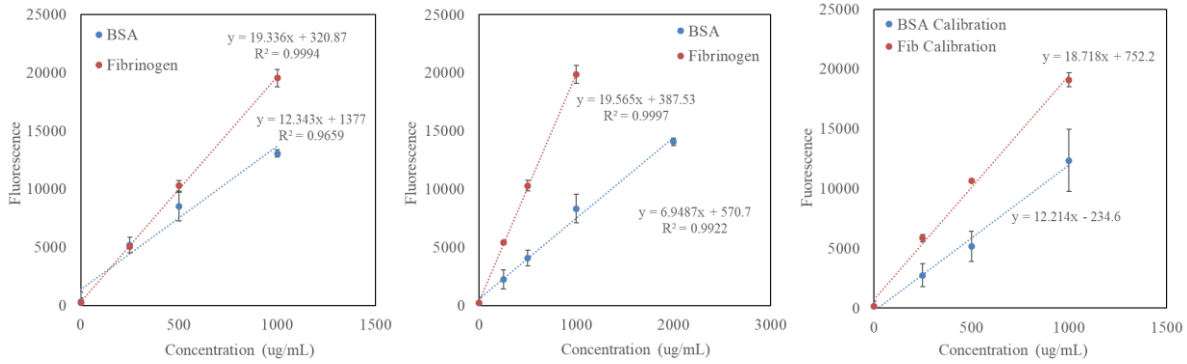

Figure 90: Fluorescence calibration curves for alginate gel trial after 24 hours (left), 72 hours (middle), 72-hour release (right).

Calibration Curves for Ibuprofen on LC-MS/MS

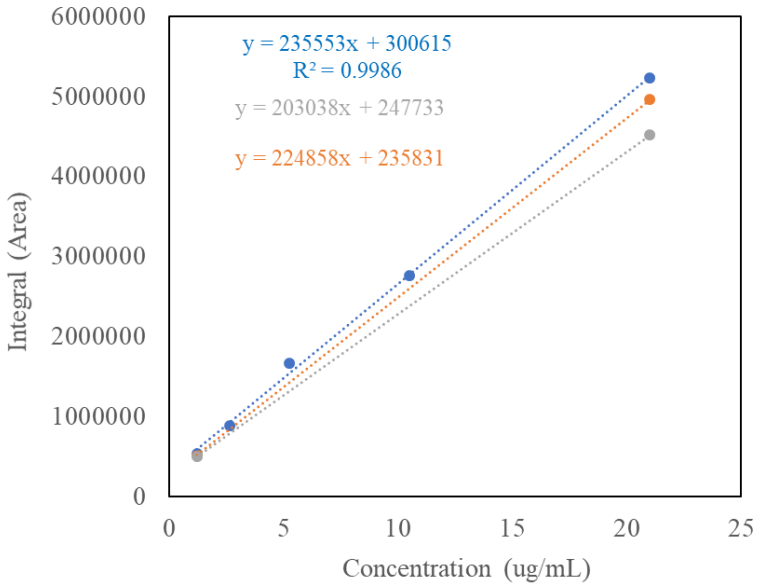

Figure 91: Representative calibration curves for one set of drug release data (with calibrations recorded three times throughout a single drug release analysis)

Representative Isotherm for BET Analysis

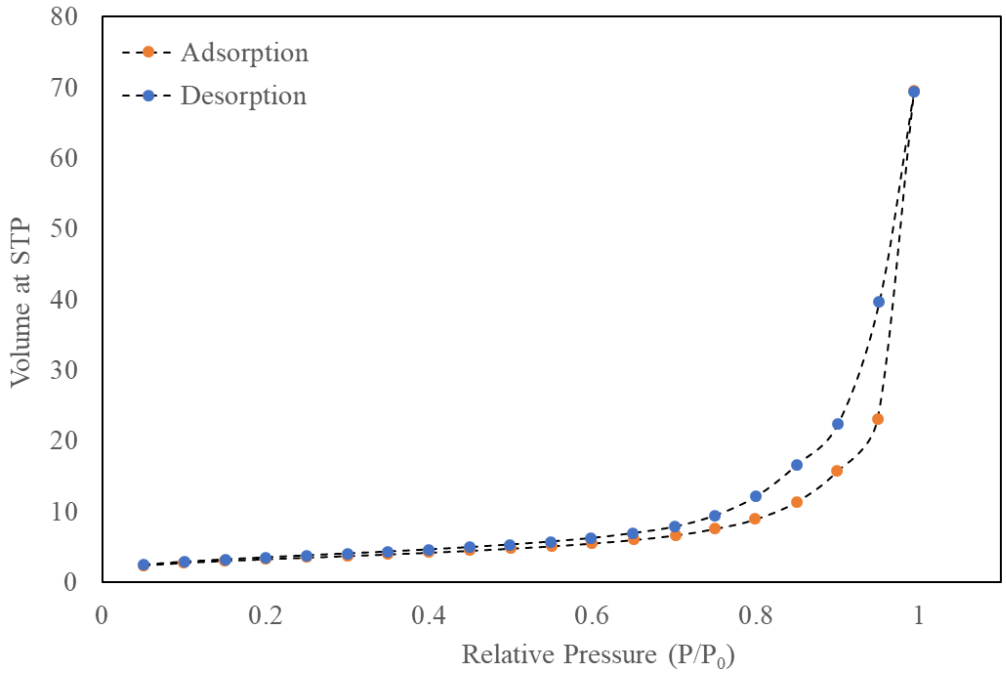

Figure 92: Representative adsorption and desorption isotherms from BET analysis of PGX processed polymer scaffold